Final Report:

Acoustic Fatigue Life Prediction for Nonlinear Structures with Multiple Resonant Modes

NASA Grant #NAG-1-978

April 1989 - March 1992

LANGLEY
GRANT

IN-39-CR

104860

P-157

R. N. Miles
Department of Mechanical and Industrial Engineering
State University of New York
P. O. 6000
Binghamton, NY 13902-6000

Abstract

This report documents an effort to develop practical and accurate methods of estimating the fatigue lives of complex aerospace structures subjected to intense random excitations. The emphasis of the current program is to construct analytical schemes of performing fatigue life estimates for structures that exhibit nonlinear vibration behavior and that have numerous resonant modes contributing to the response.

(NASA-CR-190471) ACOUSTIC FATIGUE LIFE PREDICTION FOR NONLINEAR STRUCTURES WITH MULTIPLE RESONANT MODES Final Report, Apr. 1989 - Mar. 1992 (State Univ. of New York) 157 p

N92-30988

Unclas

G3/39 0104860

I. Introduction

This report describes results obtained over a three year period under funding from the Structural Acoustics Branch at NASA Langley Research Center. The goal of this effort has been to develop methods for predicting the acoustic fatigue lives of aerospace structures. An attempt has been made to focus on certain technology areas that this investigator believes are in most need of further development. The two main issues that have been addressed are 1) how to properly account for the effects of broadband random loading in acoustic fatigue studies and 2) how to include nonlinear effects due to intense excitations in acoustic fatigue predictions.

In acoustic fatigue studies it is important to be able to account for very complicated stress and strain time histories because acoustic loads often contain components over a broad range of frequencies. As a result, a large number of resonant modes can be excited. As will be discussed in the following, although acoustic fatigue problems are often characterized by extremely broadband loads, (in contrast to most fatigue problems) it is common practice to idealize structures as having a single degree of freedom. In this case, the response is narrowband. This greatly simplifies fatigue predictions but it is not consistent with observations.

To aid in the development of 'consistent' fatigue prediction procedures, several sections are devoted to the problem of identifying the proper damage cycle counting method for acoustic fatigue predictions. The Rainflow cycle counting method is discussed in detail and methods are developed to aid in its implementation.

Nonlinear effects are often important in acoustic fatigue studies because it is the high level excitations that cause the most damage. Nonlinear structural response can have a significant impact on acoustic fatigue life in service as well as in tests. Acoustic fatigue testing is often performed using artificially high excitation levels in order to accelerate the rate of damage accumulation. Accelerated testing is necessary when trying to determine the fatigue characteristics of a structure that is expected to be useful for 20 years. When nonlinear behavior contributes to the structural response, the fatigue mechanisms can be modified significantly.

In order to account for nonlinearities in fatigue predictions it is necessary to obtain a time domain simulation of the response. In a nonlinear structure with a large number of resonant modes, as often considered in acoustic fatigue studies, it is not computationally practical to perform a detailed time domain simulation of the random response. In this report, a numerical procedure is developed which permits a fatigue prediction for a nonlinear structure to be performed with roughly the same numerical effort as for a linear structure having the same number of degrees of freedom. The procedure is applied to nonlinear beams and plates and fatigue predictions are found to agree closely with results of more computationally intense conventional methods.

Acknowledgements

This effort has been given financial and technical support by Dr. S. Rizzi and Dr. C. A. Powell at NASA Langley Research Center. Their contributions to this work are gratefully acknowledged. This study was initiated with many very helpful suggestions by Dr. J. Mixson who retired at the beginning of the project.

Much of the work described in the following has been conducted by Dr. J. Q. Sun, W. Bao, M. Garrison, and Y. Xu of the Department of Mechanical and Industrial Engineering at SUNY Binghamton. They have all made major contributions to this effort.

Publications Resulting From This Award

The following papers which are either published or in press are a direct result of this study. Two additional papers will be submitted for publication in the near future.

[1] J. Q. Sun and R. N. Miles 1991 *Journal of Sound and Vibration* **150**, 531–535. Acoustic Fatigue Life Prediction for Nonlinear Structures.

[2] R. N. Miles 1992 *Journal of Sound and Vibration* **153**, 376–386. Effect of Spectral Shape on Acoustic Fatigue Life Predictions.

[3] R. N. Miles 1992 *Journal of Sound and Vibration* **in press**, . Spectral Response of a Bilinear Oscillator.

[4] R. N. Miles and S. Bigelow 1992 *Journal of Sound and Vibration* **in press**, . Random Vibration of a Beam with a Stick-Slip End Condition.

II.1 Basics of Fatigue Life Estimation - Peak Counting

For the present study we will assume that the relation between the stress amplitude, S, and the number of cycles to failure N, may be approximated by the well known relation,

$$N = \frac{c}{S^b} \tag{II.1.1}$$

where c and b are experimentally obtained constants for a given material. For the present discussion it will be assumed that the number of fatigue cycles experienced by the structure is equal to the number of positive stress peaks, or stress reversals, that occur over time. This approach has been used in a number of acoustic fatigue studies. An alternative cycle counting method, Rainflow cycle counting, will be described in later sections and will be compared to the older peak counting scheme.

The assumption that damage occurs at each positive stress peak may be conveniently combined with the Palmgren-Miner linear damage accumulation rule [1] to produce fatigue life estimates. In this theory, the damage, D_i, caused by stress reversals at the stress level S_i is

$$D_i(S_i) = \frac{n(S_i)}{N(S_i)}, \tag{II.1.2}$$

where $n(S_i)$ is the number of stress reversals experienced by the structure at the stress level S_i and $N(S_i)$ is the number of reversals required to cause failure at this stress level. The total damage, D_m, will be the sum of the damage at all stress levels that occur,

$$D_m = \sum_i D_i(S_i) = \sum_i \frac{n(S_i)}{N(S_i)}. \tag{II.1.3}$$

From equation (II.1.1),

$$N(S_i) = \frac{c}{S_i^b}, \tag{II.1.4}$$

so that equation (II.1.3) becomes

$$D_m = \frac{1}{c} \sum_i n(S_i) S_i^b. \tag{II.1.5}$$

The form of equation (II.1.1) assumes that all stress peaks occur at positive stress levels as would be the case for sinusoidal loading. When a resonant system is subjected to random loading, however, we must allow for the possibility of stress peaks at negative stresses which make positive contributions to the accumulated damage. To account for this, we will take the absolute value of the stress level, S_i, so that equation (II.1.5) becomes

$$D_m = \frac{1}{c} \sum_i n(S_i) |S_i|^b. \tag{II.1.6}$$

Failure is predicted to occur when $D_m = 1$.

Since the response and rate of damage accumulation in the structure are assumed to be random, the fatigue life may be estimated from the expected value of the rate of damage accumulation. If $m(S)$ is the rate of occurrence of a peak with level S, and if $p_{peak}(S)$ is the probability density for response peaks, then the expected value of the damage rate, $\Delta(S)$, may be written as

$$\mathrm{E}[\Delta] = \int_{-\infty}^{\infty} m(S)\frac{|S|^b}{c}p_{peak}(S)dS. \tag{II.1.7}$$

The assumption that the response process is stationary gives the mean fatigue life as

$$T = \frac{1}{\mathrm{E}[\Delta]}. \tag{II.1.8}$$

From equations (II.1.7) and (II.1.8) the problem of estimating fatigue life in a random system is one of properly determining the rate at which peaks occur, $m(S)$, and the peak probability density, $p_{peak}(S)$. The goal of the present study is to develop practical and accurate methods of applying equations (II.1.7) and (II.1.8) to structures with multiple resonant modes and where the response levels are sufficiently high to elicit nonlinear response.

To illustrate the application of equations (II.1.7) and (II.1.8) consider the problem of predicting the fatigue life of a linear system having one resonant frequency and that is driven with Gaussian white noise,

$$\ddot{x} + \omega_o^2 x + \beta\dot{x} = f(t). \tag{II.1.9}$$

In a linear system the stress is linearly related to the displacement, x by $S = Kx$, where the constant, K depends on material and geometrical properties. It may be shown that for Gaussian input, the response of the linear system will be Gaussian. It is also known that for a Gaussian random process, the peak probability density depends on the response spectrum.

Assume that the response of a one degree of freedom oscillator is a narrowband process. Then the probability density for peaks in the time domain response is the Rayleigh density,

$$p_{peak}(S) = \frac{S}{\sigma_S^2}e^{-\frac{S}{2\sigma_S^2}}, \tag{II.1.10}$$

where σ_S^2 is the mean square stress. Also assume that the rate at which peaks occur is a constant and equal to the natural frequency of the oscillator,

$$m(S) = \frac{\omega_o}{2\pi}. \tag{II.1.11}$$

Substituting equations (II.1.10) and (II.1.11) into equation (II.1.7) and carrying out the integration gives

$$\mathrm{E}[\Delta] = \frac{\omega_o}{2\pi c}(\sqrt{2}\sigma_S)^b\Gamma(\frac{b+2}{2}), \tag{II.1.12}$$

where the Gamma function is defined by

$$\Gamma(y) = 2\int_0^\infty x^{2y-1}e^{-x^2}dx, \quad \text{for } y > 0. \qquad \text{(II.1.13)}$$

Equation (II.1.12) was first obtained by Miles [2].

II.2. Linear Systems with Multiple Degrees of Freedom

In the case of a single degree of freedom system as discussed in the previous section, it is relatively straight-forward to estimate the rate at which damaging events occur in the system. It is quite reasonable to assume that one damaging event occurs for each cycle of the oscillation. Unfortunately, when the system has multiple frequency components in its response, as in a multi-mode structure, the task of estimating the rate of damaging occurrences is very difficult. In the present section an example is given of the classical approach to estimate the damage rate in a beam with multiple resonant modes. Improvements on this method will be discussed in subsequent sections.

The main difficulty in estimating fatigue life in multi-mode systems is illustrated in figures II.2.1 through II.2.3. These figures show predicted stress in the time domain for a beam having one, two, and three resonant modes. The spectra of the stress response for each case are shown in figure II.2.4. Figures II.2.1 through II.2.3 show that as the number of modes in the structure is increased, the time domain response becomes increasingly complicated. If we were to define a damaging event to be the occurrence of a positive stress peak, or where the stress reaches a maximum value in time and then decreases, then it is clear from the figures that when three modes contribute to the response the rate at which damage is accumulated is greater than in the single mode system.

While it is clear that the time domain response is profoundly influenced by the number of modes in a system and that this should in some way affect the fatigue life, it is not a simple matter to determine exactly how the damage rate increases with the number of modes. When the time history is complicated as in figure II.2.3, we must make assumptions about what causes damage and then attempt to estimate the rate at which the damaging event occurs. The problem of selecting a proper definition of a damaging event has not received sufficient attention in recent acoustic fatigue research. This will be addressed in more detail in the following sections.

In the current section, applications of two different definitions of damaging event are investigated; one in which damage is assumed to occur for each stress peak and one where damage results only from the highest positive stress peak between each zero crossing. For a linear beam with multi-mode response, approximate analytical solutions for the damage rate and fatigue life are developed and compared to estimates obtained using numerical simulations for each assumed definition of damaging event.

The structure studied here consists of a base excited beam with clamped boundaries. The ends of the beam are thus assumed to have zero slope and prescribed random transverse displacement. The axial deflections at the beam ends are assumed to be zero. The assumption of linear response allows us to express the forced vibration in terms of a superposition of the eigenfunctions and natural frequencies of the beam. The equation governing the transverse deflection, $W(x,t)$ is

$$\rho A\ddot{W} + EI\frac{\partial^4 W}{\partial x^4} + \eta\dot{W} = -\rho A\ddot{W}_o(t), \tag{II.2.1}$$

where ρ is the mass density, A is the cross section area, I is the moment of inertia, E is Young's modulus, and η is a viscous damping coefficient. $\ddot{W}_o(t)$ is the random acceleration that is prescribed at the ends of the beam and is assumed to be Gaussian with zero mean and a constant single sided power spectral density $G_{\ddot{W}_o}$ with units of $(\ddot{W}_o)^2$/Hertz. Equation (II.2.1) is derived in section (II.2.4) and is equivalent to equation (II.4.23) with the nonlinear coefficient, $c(t)$ set equal to zero. To solve for the response by modal analysis, let

$$W(x,t) = \sum_{i=1}^{\infty} \alpha_i(t)\phi_i(x), \tag{II.2.2}$$

where the $\phi_i(x)$ are the beam eigenfunctions and $\alpha_i(t)$ are unknown functions of time.

For a beam with clamped ends, the eigenfunctions are given by

$$\phi_i(x) = \cos(p_i x/l) - \cosh(p_i x/l) + D_i\big(\sin(p_i x/l) - \sinh(p_i x/l)\big) \tag{II.2.3}$$

where p_i and D_i are given in the table below for the first six eigenfunctions.

i	p_i	D_i
1	4.730040745	-0.982502215
2	7.853204624	-1.000777312
3	10.99560784	-0.999966450
4	14.13716549	-1.000001450
5	17.27875966	-1.000000000
6	20.42035225	-1.000000000

Table II.2.1 Eigenfunction Coefficients for a Clamped Beam.

Substitution of equation (II.2.2) into (II.2.1) leads to a set of equations for the unknown $\alpha_i(t)$,

$$\ddot{\alpha}_i + \zeta\dot{\alpha}_i + \omega_i^2\alpha_i = F_i\ddot{W}_o(t), \quad i = 1, 2, \ldots, \infty, \tag{II.2.3}$$

where

$$\omega_i^2 = \frac{EI}{\rho A}\left(\frac{p_i}{l}\right)^4, \quad (I = \frac{bh^3}{12}),$$

$$\zeta = \frac{\eta}{\rho A},$$

$$F_i = -\frac{1}{l}\int_0^l \phi_i(x)dx.$$

b is the beam width and h is the thickness. The solution of equation (II.2.3) can be obtained as

$$\alpha_i(t) = \alpha_i^o(t) + \frac{F_i}{\omega_{d_i}} \int_0^t e^{-\frac{\zeta}{2}(t-\tau)} \sin(\omega_{d_i}(t-\tau)) \ddot{W}_o(\tau) d\tau \tag{II.2.4}$$

where $\omega_{d_i}^2 = \omega_i^2 - \zeta^2/4$, and $\alpha_i^o(t)$ is the transient solution due to a non-zero initial condition. Since the transient solution decays in time, it has no effect on the steady-state response. We shall then take $\alpha_i^o(t) = 0$ in the subsequent discussion. The normal strain of the beam in x direction is given by

$$\epsilon_{xx} = -y \frac{\partial^2 W(x,t)}{\partial x^2} = \sum_{i=1}^{\infty} \left(-y \frac{\partial^2 \phi_i(x)}{\partial x^2} \right) \alpha_i(t). \tag{II.2.5}$$

The maximum strain occurs at the top or bottom surface at each end of the beam, $y = h/2$ and $x = 0$ or l. Let

$$a_i = -\frac{h}{2} \frac{\partial^2 \phi_i(0)}{\partial x^2}. \tag{II.2.6}$$

The maximum strain is written as

$$\epsilon = \sum_{i=1}^{\infty} a_i \alpha_i(t), \tag{II.2.7}$$

The maximum strain rate is given by

$$\dot{\epsilon} = \sum_{i=1}^{\infty} a_i \dot{\alpha}_i(t), \tag{II.2.8}$$

Equations (II.2.7) and (II.2.8) are often truncated to a finite summation in real computation, leading to

$$\epsilon = \sum_{i=1}^{N} a_i \alpha_i(t), \quad \dot{\epsilon} = \sum_{i=1}^{N} a_i \dot{\alpha}_i(t), \tag{II.2.9}$$

where N is a finite integer.

It can be shown that the maximum strain ϵ and strain rate $\dot{\epsilon}$ given by the truncated series are stationary Gaussian processes. The first and second order statistics of ϵ and $\dot{\epsilon}$ completely determine the process, and can be obtained as follows

$$\begin{aligned} \mathrm{E}[\epsilon] &= \mathrm{E}[\dot{\epsilon}] = 0, \\ \mathrm{E}[\epsilon^2] &= \sum_{i=1}^{N} \sum_{j=1}^{N} a_i a_j \mathrm{E}[\alpha_i(t) \alpha_j(t)], \\ \mathrm{E}[\dot{\epsilon}^2] &= \sum_{i=1}^{N} \sum_{j=1}^{N} a_i a_j \mathrm{E}[\dot{\alpha}_i(t) \dot{\alpha}_j(t)], \\ \mathrm{E}[\epsilon \dot{\epsilon}] &= \sum_{i=1}^{N} \sum_{j=1}^{N} a_i a_j \mathrm{E}[\alpha_i(t) \dot{\alpha}_j(t)], \end{aligned} \tag{II.2.10}$$

where

$$\mathrm{E}[\alpha_i(t)\alpha_j(t)] = \frac{F_iF_jG_{\bar{W}_o}}{2\omega_{d_i}\omega_{d_j}}\int_0^t e^{-\zeta\tau}\sin\omega_{d_i}\tau\sin\omega_{d_j}\tau d\tau,$$

$$\mathrm{E}[\dot{\alpha}_i(t)\dot{\alpha}_j(t)] = \frac{F_iF_jG_{\bar{W}_o}}{2}\int_0^t e^{-\zeta\tau}\left\{\cos\omega_{d_i}\tau\cos\omega_{d_j}\tau - \frac{\zeta}{2\omega_{d_j}}\cos\omega_{d_i}\tau\sin\omega_{d_j}\tau\right.$$
$$\left.-\frac{\zeta}{2\omega_{d_i}}\sin\omega_{d_i}\tau\cos\omega_{d_j}\tau + \frac{\zeta^2}{4\omega_{d_i}\omega_{d_j}}\sin\omega_{d_i}\tau\sin\omega_{d_j}\tau\right\}d\tau,$$

$$\mathrm{E}[\alpha_i(t)\dot{\alpha}_j(t)] = \frac{F_iF_jG_{\bar{W}_o}}{2\omega_{d_i}}\int_0^t e^{-\zeta\tau}\left\{\sin\omega_{d_i}\tau\cos\omega_{d_j}\tau - \frac{\zeta}{2\omega_{d_j}}\sin\omega_{d_i}\tau\sin\omega_{d_j}\tau\right\}d\tau,$$

and E[·] is the expected value. It can be shown that in the steady-state as $t \to \infty$, we have

$$\begin{aligned}\sigma_\epsilon^2 &= \mathrm{E}[\epsilon^2] = \sum_{i=1}^{N}\sum_{j=1}^{N}\frac{\zeta a_ia_jF_iF_jG_{\bar{W}_o}}{[\zeta^2+(\omega_{d_i}-\omega_{d_j})^2][\zeta^2+(\omega_{d_i}+\omega_{d_j})^2]},\\ \sigma_{\dot{\epsilon}}^2 &= \mathrm{E}[\dot{\epsilon}^2] = \sum_{i=1}^{N}\sum_{j=1}^{N}\frac{\zeta a_ia_jF_iF_jG_{\bar{W}_o}(\omega_i^2+\omega_j^2)}{2[\zeta^2+(\omega_{d_i}-\omega_{d_j})^2][\zeta^2+(\omega_{d_i}+\omega_{d_j})^2]},\end{aligned} \tag{II.2.11}$$

and

$$\mathrm{E}[\epsilon\dot{\epsilon}] = 0.$$

Having obtained the statistics of the strain and strain rate, ϵ and $\dot{\epsilon}$, we then proceed to estimate the fatigue life of the system. There may be different approaches to this problem dependent on the counting scheme for damaging events that one chooses in applying Miner's rule as discussed in Section II. If we count all the peaks of the strain (or stress) as damaging events, and use the fact that ϵ and $\dot{\epsilon}$ are joint Gaussian variables, we can take advantage of existing methods as presented in reference [3]. To apply the theory, it is necessary to evaluate two parameters: $\mathrm{E}[M_T]$, the average rate at which strain peaks occur, and a parameter, α, which is the ratio of the rate at which zero crossings occur to the rate of strain peaks. The parameter α appears in the probability density function of the strain peaks. $\mathrm{E}[M_T]$ and α are given by

$$\mathrm{E}[M_T] = \frac{\sigma_3}{2\pi\sigma_2}, \quad \alpha = \frac{\sigma_2^2}{\sigma_1\sigma_2}, \tag{II.2.12}$$

where

$$\begin{aligned}\sigma_1^2 &= \int_{-\infty}^{\infty}\Phi_\epsilon(\omega)d\omega,\\ \sigma_2^2 &= \int_{-\infty}^{\infty}\omega^2\Phi_\epsilon(\omega)d\omega,\\ \sigma_3^2 &= \int_{-\infty}^{\infty}\omega^4\Phi_\epsilon(\omega)d\omega,\end{aligned} \tag{II.2.13}$$

$\Phi_\epsilon(\omega)$ is the two sided power spectrum of the strain, and is given by

$$\Phi_\epsilon = \sum_{i=1}^{N} \sum_{j=1}^{N} a_i a_j \Phi_{ij}(\omega), \tag{II.2.14}$$

where

$$\Phi_{ij}(\omega) = \frac{G_{\ddot{W}_o} F_i F_j}{4\pi} H_i(-\omega) H_j(\omega), \tag{II.2.15}$$

and

$$H_i(\omega) = \frac{1}{\omega_i^2 - \omega^2 + \imath\zeta\omega} \qquad (\imath^2 = -1). \tag{II.2.16}$$

$\Phi_{ij}(\omega)$ is the cross power spectrum of α_i and α_j. In the present study, we assume that the random excitation $\ddot{W}_o(t)$ is bandlimited with a cutoff frequency f_c. f_c is taken to be 1000 Hz in the numerical study reported next. This bandlimited assumption is necessary for the convergence of the integral for σ_3^2 in equation (II.2.13).

The probability density function for response peaks is given by

$$\begin{aligned} p_{peak}(\epsilon) = {} & \frac{(1-\alpha^2)^{\frac{1}{2}}}{\sqrt{2\pi}\sigma_1} e^{-\epsilon^2[2\sigma_1^2(1-\alpha^2)]^{-1}} \\ & + \frac{\alpha\epsilon}{2\sigma_1^2} \left\{ 1 + \operatorname{erf}\left[\frac{\epsilon}{\sigma_1}\left(\frac{2}{\alpha^2} - 2\right)^{-\frac{1}{2}}\right] \right\} e^{-\frac{\epsilon^2}{2\sigma_1^2}}, \end{aligned} \tag{II.2.17}$$

where α and σ_1 are defined in equations (II.2.12) and (II.2.13).

In a random process in which there is only one peak for each zero crossing, α will equal to unity and equation (II.2.17) reduces to a Rayleigh density. This is typically considered a narrowband process. A process with an infinite number of peaks for each zero crossing will have α equal to zero and equation (II.2.17) will reduce to the Gaussian density. The process is then said to be broad-band.

To calculate the damage rate as in equation (II.2.7), $m(S)$ is replaced by a constant $\mathrm{E}[M_T]$ and equation (II.2.17) is substituted for the peak density. Since the damage rate in equation (II.2.7) is expressed in terms of stress, S, rather than strain, ϵ, we must also employ the relation $S = E\epsilon$, where E is Young's modulus for the material. The damage rate in terms of an integration over the strain then becomes

$$\mathrm{E}[\Delta] = \int_{-\infty}^{\infty} \mathrm{E}[M_T] \frac{|E\epsilon|^b}{c} p_{peak}(\epsilon) d\epsilon, \tag{II.2.18}$$

with $\mathrm{E}[M_T]$ given in equation (II.2.12) and $p_{peak}(\epsilon)$ given in equation (II.2.17).

The damage rate as estimated by equation (II.2.18) is based on the assumption that damage occurs every time the strain reaches a maximum and then decreases. An alternative to assuming that each peak causes damage is to assume that the damage rate is a narrowband process. The expected value of the damage rate, $\mathrm{E}[\Delta]$ may then be estimated by approximating the strain as a narrowband process. The peak density then corresponds to the Rayleigh density and the rate at which peaks occur is the same as the rate of zero crossings, $n_o(\epsilon)$,

$$n_o(\epsilon) = \frac{\sigma_{\dot{\epsilon}}}{2\pi\sigma_\epsilon} = \frac{\sigma_2}{2\pi\sigma_1} \tag{II.2.19}$$

The average damage rate and fatigue life are then obtained as in equation (II.2.12)

$$\mathrm{E}[D_m] = \frac{n_o(\epsilon)}{c}(\sqrt{2}\sigma_S)^b\Gamma\left(\frac{b+2}{2}\right), \tag{II.2.20}$$

and

$$T = \frac{1}{\mathrm{E}[D_m]}, \tag{II.2.21}$$

where $\sigma_S = E\sigma_\epsilon$, and E is the Young's modulus of the material.

In the numerical results reported herein, the number of terms used in the expansions for the response, equations (II.2.9), is taken to be $N = 6$. Because of the symmetry of the structure, the generalized forces associated with the even modes in equation (II.2.3) are zero,

$$F_2 = F_4 = F_6 = 0. \tag{II.2.22}$$

This indicates that the modes that are anti-symmetric about the middle point ($x = l/2$) of the beam do not contribute to the long-term dynamic response, and hence to the fatigue damage accumulation.

The methods presented above have been applied to estimate the fatigue life of the clamped beam as a function of the level of the random base excitation and as a function of the fatigue exponent, b, in equation (II.2.1). The predictions were performed using the analytical methods discussed above and also by a direct numerical simulation of the random response in the time domain.

Figure II.2.5 shows a comparison of fatigue lives obtained by the analytical method discussed above and by numerical simulation. In this case it is assumed that each stress peak in the time domain causes damage. The figure shows that the numerical and analytical methods give essentially identical results. The effect of including one, two, or three modes in the model is also shown. It is found that with the assumption that each stress peak causes damage, increasing the number of modes tends to reduce the fatigue life. It could be argued that in general, one obtains a nonconservative fatigue life estimate by only accounting for the lowest frequency mode in a structure.

The calculations shown in figure II.2.5 are repeated in figure II.2.6 except that in this case it is assumed that only one damaging event occurs for each time the stress crosses zero with positive slope. Here it is assumed that the damage results only from the highest peak between zero crossings. It is again found that the analytical and numerical methods are in excellent agreement. As in figure II.2.5 increasing the number of modes in the model decreases the fatigue life.

Comparing the results in figures II.2.5 and II.2.6 shows only very small differences between the two damage counting schemes. The close agreement between the elementary counting schemes examined here should not be interpreted as evidence that all damaging event definitions will give identical results. A more detailed comparison of damage counting schemes will be presented in the following sections.

II.3. Effect of Nonlinearity on Fatigue Life (Peak Counting)

In the special case where the response of a nonlinear structure is dominated by a single resonant mode, the methods discussed above can be extended to estimate the fatigue life including nonlinear effects. A single mode model of the displacement response of a base-excited beam with large deflection may be expressed as

$$\ddot{\alpha} + \omega_o^2(\alpha + \hat{\epsilon}\alpha^3) + \beta\dot{\alpha} = f(t), \tag{II.3.1}$$

where α is the response of the first mode so that the beam displacement, $W(x,t)$, is

$$W(x,t) = \alpha(t)\phi(x), \tag{II.3.2}$$

$\phi(x)$ is the corresponding eigenfunction. ω_o is the natural frequency when the deflections are small, β is the damping coefficient and $\hat{\epsilon}$ is a constant which determines the degree of nonlinearity. $f(t)$ is a Gaussian random process. The derivation of equation (II.3.1) is presented in the following section.

The nonlinearity in the beam response is assumed to result from the stretching of the fibers along the beam's neutral axis which occurs when the deflections are large. When large deflections are included in the analysis the stress (or strain) is not linearly related to the displacement. For the nonlinear beam with a single resonant mode, the maximum stress (at the beam end) is found to be

$$S = E\left(\alpha^2\frac{d_1}{l^2} + h\left(\frac{p}{l}\right)^2\alpha\right), \tag{II.3.3}$$

where E is Young's modulus, l is the beam length, h is the thickness and d_1, and p are constants given by $d_1 = 6.1513$ and $p = 4.730$.

For a single mode system described by equations (II.3.1) and (II.3.3), it is possible to apply equations (II.1.7) and (II.1.8) in a fairly rigorous fashion. The result is a nonlinear analog of Miles' linear single degree of freedom analysis shown in equation (II.1.12). It should be emphasized, however, that real structures very rarely behave as single degree of freedom systems and that fatigue life estimates are affected by the number of modes included in the analysis. The main purpose of the present study is to develop accurate and practical methods of applying equation (II.1.7) to multi-mode nonlinear systems.

For the nonlinear system considered here the easiest approach is to express the expected value operation in equation (II.1.7) as an integration over the modal response, α, rather than over the stress, S. This leads to

$$\mathrm{E}[\Delta] = \int_{-\infty}^{\infty} m(S(\alpha))\frac{|S(\alpha)|^b}{c}p_{peak}(\alpha)d\alpha. \tag{II.3.4}$$

It is not a simple matter to derive an exact expression for $p_{peak}(\alpha)$ or $m(S(\alpha))$ in equation (II.3.4) when the input to the system is Gaussian white noise. If it is assumed that there is only one peak for each zero crossing with positive slope (which implies a narrow band process) then $p_{peak}(\alpha)$ and m may be calculated so that equation (II.3.4) becomes

$$\mathrm{E}[\Delta] = \frac{C}{c}\omega_o^2 \int_{-\infty}^{\infty} |S(\alpha)|^b (\alpha + \hat{\epsilon}\alpha^3) e^{-\frac{\alpha^2}{2\sigma^2_{\alpha_o}} - \hat{\epsilon}\frac{\alpha^4}{4\sigma^2_{\alpha_o}}} d\alpha, \tag{II.3.5}$$

where

$$C = \sqrt{2\pi\omega_o^2\sigma^2_{\alpha_o}} \int_{-\infty}^{\infty} e^{-\frac{\alpha^2}{2\sigma^2_{\alpha_o}} - \hat{\epsilon}\frac{\alpha^4}{4\sigma^2_{\alpha_o}}} d\alpha, \tag{II.3.6}$$

and where $\sigma^2_{\alpha_o}$ is the mean square response of $\alpha(t)$ when $\hat{\epsilon}$ is set to zero in equation (II.3.1).

The calculation of the damage rate in equations (II.3.5) and (II.3.6) relies on knowledge of the peak probability density which for the present system is given by

$$p_{peak}(\alpha) = \frac{(\alpha + \hat{\epsilon}\alpha^3)}{\sigma^2_{\alpha_o}} e^{-\frac{1}{\sigma^2_{\alpha_o}}\left(\frac{\alpha^2}{2} + \hat{\epsilon}\frac{\alpha^4}{4}\right)} \tag{II.3.7}$$

This expression may be obtained from the joint probability density of α and $\dot{\alpha}$ if the response is a narrowband process. Unfortunately, the joint density of α and $\dot{\alpha}$ may be obtained only for rather specialized nonlinear systems. Since our goal is to develop a method that is applicable to a wide class of systems, an approximate method of estimating the damage rate will now be described that includes the effects of nonlinearities on α through the method of equivalent linearization [4].

The method of equivalent linearization consists of replacing equation (II.3.1) with an equivalent linear system given by

$$\ddot{\alpha} + \omega_e^2\alpha + \beta\dot{\alpha} + e(\alpha) = f(t), \tag{II.3.8}$$

where ω_e^2 is the equivalent linear frequency and $e(\alpha)$ is an error term. ω_e^2 is chosen so that the mean square of the error is minimized. If the error, $e(\alpha)$, is then neglected, equation (II.3.8) is a simple linear system with a natural frequency that depends on the spectrum level of the excitation. Since the system is linear, its response will be Gaussian for a Gaussian input, $f(t)$. This leads to

$$\omega_e^2 = \frac{\omega_o^2}{2}\left(1 + \sqrt{1 + 12\hat{\epsilon}\sigma^2_{\alpha_o}}\right). \tag{II.3.9}$$

If the single sided power spectral density of $f(t)$ is $G_f(\frac{\omega}{2\pi})$ with units of f^2/Hertz, then

$$\sigma^2_{\alpha_o} = \frac{G_f}{4\omega_o^2\beta}, \tag{II.3.10}$$

where G_f is assumed to be a constant at all frequencies. One may then calculate the mean square response of the equivalent linear system to be

$$\sigma^2_{\alpha_e} = \frac{G_f}{4\omega_e^2\beta}. \tag{II.3.11}$$

With the response of the equivalent linear system assumed to be Gaussian when $e(\alpha)$ is neglected in equation (II.3.8), one may calculate the peak probability density to be a Rayleigh distribution as in equation (II.1.10). The peak density for the equivalent linear system is then

$$p_e(\alpha) = \frac{\alpha}{\sigma_{\alpha_e}^2} e^{-\frac{\alpha^2}{2\sigma_{\alpha_e}^2}}, \tag{II.3.12}$$

where $\sigma_{\alpha_e}^2$ is given in equation (II.3.11).

To evaluate equation (II.3.4), we must also approximate the rate of occurrence of peaks, $m(S(\alpha))$. For the present study this will be taken to be a constant equal to the equivalent linear natural frequency of the oscillator in Hertz, $\omega_e/2\pi$.

By using equivalent linearization, equation (II.3.4) may then be approximated by

$$\mathrm{E}[\Delta] = \frac{\omega_e}{2\pi} \int_0^\infty \frac{|S(\alpha)|^b}{c} \frac{\alpha}{\sigma_{\alpha_e}^2} e^{-\frac{\alpha^2}{2\sigma_{\alpha_e}^2}} d\alpha, \tag{II.3.13}$$

where $S(\alpha)$ is given in equation (II.3.3).

The comparison of equations (II.3.5) and (II.3.13) may be simplified somewhat by defining a normalized random variable,

$$\gamma = \frac{\alpha}{\sigma_o}. \tag{II.3.14}$$

Substitution of equation (II.3.14) into equations (II.3.5) and (II.3.6) gives

$$\mathrm{E}[\Delta]_R = \frac{\omega_o}{c\sqrt{2\pi}} \frac{\int_0^\infty |S(\gamma\sigma_o)|^b \cdot (\gamma + \hat{\epsilon}\sigma_o^2\gamma^3) e^{-\frac{\gamma^2}{2} - \hat{\epsilon}\sigma_o^2\frac{\gamma^4}{4}} d\gamma}{\int_{-\infty}^\infty e^{-\frac{\xi^2}{2} - \hat{\epsilon}\sigma_o^2\frac{\xi^4}{4}} d\xi}, \tag{II.3.15}$$

where the R subscript on E[Δ] denotes the 'rigorous' solution.

Substitution of equation (II.3.14) and the use of equations (II.3.9) and (II.3.10) in equation (II.3.13) give

$$\mathrm{E}[\Delta]_E = \frac{\omega_o}{c2\pi} \int_0^\infty |S(\gamma\sigma_o)|^b \gamma \left(\frac{1}{2}(1 + \sqrt{1 + 12\hat{\epsilon}\sigma_o^2})\right)^{3/2} e^{-\frac{\gamma^2}{4}(1+\sqrt{1+12\hat{\epsilon}\sigma_o^2})} d\gamma, \tag{II.3.16}$$

where the E subscript on E[Δ] denotes the equivalent linearization solution.

Substituting equation (II.3.14) into (II.3.3) and rearranging give

$$S = a_1\sigma_o(\gamma + a\gamma^2), \tag{II.3.17}$$

where

$$a_1 = Eh\left(\frac{p}{l}\right)^2, \tag{II.3.18}$$

and

$$a = \frac{\sigma_o d_1}{hp^2}. \tag{II.3.19}$$

The results of this section may be used to estimate the effects on fatigue life of nonlinear strains in a single mode system and to assess the applicability of equivalent linearization to the nonlinear fatigue problem. Figures II.3.1 and II.3.2 show predicted fatigue lives of a base excited beam for a range of excitation levels and for the damage exponent, b, in equations (II.3.15) and (II.3.16) equal to 4 and 6. The geometrical and material parameters of the beam are identical to those used in the results presented in Section II.2. Excellent agreement is shown between the results of equations (II.3.15) and (II.3.16) for both values of b.

Figures II.3.1 and II.3.2 show the predicted fatigue life with and without the effect of nonlinear axial strain. In the calculations, the nonlinear axial strain was neglected by setting $a = 0$ in equation (II.3.17). In this case the nonlinearity affects the displacement response through equation (II.3.1) but the relation between strain and displacement is assumed to be linear. This is essentially the same approach taken in reference [4]. The figures show that when the full nonlinear strain-displacement relation is used, the added stretching strain substantially reduces the fatigue life at high excitation levels.

The results shown in figures II.3.1 and II.3.2 indicate that nonlinear stiffness in the beam can reduce the response amplitude relative to that of a linear system and hence increase fatigue life. However, the figures also show that the nonlinear stretching strain results in an increase in the damage rate and hence partially cancels the beneficial effect of the reduced displacement.

II.4 Governing Equations For A Nonlinear Beam

The governing equations for a beam will now be developed including what are likely to be the dominant nonlinear effects. The nonlinearities accounted for here are due to axial stretching and friction damping at the boundaries. The ends of the beam are assumed to be clamped in a fixture that allows axial slipping when the axial force exceeds a certain value. For simplicity, this slipping is assumed to occur at only one end, the other end being held rigidly.

The friction damping model has been included in this analysis because it is suspected to be the most likely nonlinear damping mechanism in the beam. When the experimental phase of the current project is complete, data will be available to determine the relative influence of stiffness nonlinearity (due to axial stretching) and damping nonlinearity (due to friction at the boundary). Although the friction damping model is developed in this section, it has not been utilized in a numerical model to assess its influence on fatigue life.

The derivation of the equations of motion will be based on Hamilton's principle,

$$\delta \int_{t_1}^{t_2} (\mathcal{T} - \mathcal{V} + \mathcal{W}) dt = 0, \tag{II.4.1}$$

Where δ is the variational operator, $\mathcal{T}$ is the kinetic energy, $\mathcal{V}$ is the potential energy and $\mathcal{W}$ is the work done by nonconservative forces. The limits of integration, t_1 and t_2 define an arbitrary time interval.

If the beam is subjected to a base acceleration, $\ddot{W}_o(t)$, and if the deflection of the beam mid-line relative to its moving supports is $W(x,t)$, where x is the axial coordinate, then the kinetic energy may be written as

$$\mathcal{T} = \frac{\rho A}{2} \int_0^l (\dot{W}_o(t) + \dot{W}(x,t))^2 dx, \tag{II.4.2}$$

where ρ is the density, A is the constant cross sectional area, l is the beam length, and the dots denote partial differentiation with respect to time, t. It is assumed that the beam is thin so that rotary inertia effects are negligible.

The potential energy will be assumed to consist of contributions due to strain energy in the beam, $\mathcal{V}_s$, and the energy $\mathcal{V}_b$, stored in a linear, axial spring at the boundary at $x = l$. To construct the strain energy, $\mathcal{V}_s$, it will be assumed (as in elementary beam theory) that the strain is dominated by the axial strain, ϵ_{xx}. This leads to

$$\mathcal{V}_s = \frac{b}{2} \int_0^l \int_{-\frac{h}{2}}^{\frac{h}{2}} E\epsilon_{xx}^2 dz dx, \tag{II.4.3}$$

where b is the beam width (assumed to be constant), h is the thickness, E is Young's modulus, and z is the transverse distance relative to be beam mid-line.

Bringing the variational operation inside the integrand of equation (II.4.1) gives

$$\int_{t_1}^{t_2} (\delta\mathcal{T} - \delta\mathcal{V} + \delta\mathcal{W}) dt = 0, \tag{II.4.4}$$

where from equation (II.4.2),

$$\delta\mathcal{T} = \rho A \int_0^l (\dot{W}_o(t) + \dot{W}(x,t)) \delta\dot{W}(x,t) dx, \tag{II.4.5}$$

and, from equation (II.4.3),

$$\delta\mathcal{V} = \delta\mathcal{V}_s + \delta\mathcal{V}_b = b \int_0^l \int_{-\frac{h}{2}}^{\frac{h}{2}} E\epsilon_{xx}\delta\epsilon_{xx} dz dx + \delta\mathcal{V}_b. \tag{II.4.6}$$

In equation (II.4.5) we have used the fact that $\ddot{W}_o(t)$ is prescribed so that its variation is zero. The contributions due to nonconservative forces in $\delta\mathcal{W}$ will be discussed later.

Substituting equation (II.4.5) into equation (II.4.4) and carrying out the integration of $\delta\mathcal{T}$ over time by parts give

$$\int_{t_1}^{t_2} \delta\mathcal{T} dt = -\rho A \int_0^l \int_{t_1}^{t_2} (\ddot{W}_o(t) + \ddot{W}(x,t)) \delta W(x,t) dx dt, \tag{II.4.7}$$

where the variation of $W(x,t)$ is zero at $t = t_1$, and $t = t_2$.

The variation of the strain energy in equation (II.4.6) must be written in terms of convenient displacement coordinates. This is accomplished by expressing the axial strain in terms of $U(x,t)$, which is the axial displacement at $z = 0$, and $W(x,t)$, the transverse displacement at $z = 0$. This gives

$$\epsilon_{xx} = \frac{\partial U(x,t)}{\partial x} - z\frac{\partial^2 W(x,t)}{x^2} + \frac{1}{2}\left(\frac{\partial W(x,t)}{\partial x}\right)^2 . \tag{II.4.8}$$

The last term on the right hand side of equation (II.4.8) accounts for axial stretching which will be important when the deflection is large.

Substituting equation (II.4.8) into equation (II.4.6) gives

$$\delta\mathcal{V}_s = bE\int_0^l \int_{-\frac{h}{2}}^{\frac{h}{2}} (U_x - zW_{xx} + \frac{1}{2}W_x^2)(\delta U_x - z\delta W_{xx} + W_x\delta W_x)dzdx, \tag{II.4.9}$$

where the subscripts denote partial differentiation. Integrating equation (II.4.9) over z gives

$$\delta\mathcal{V}_s = bE\int_0^l (\frac{h^3}{12}W_{xx}\delta W_{xx} + h^2(U_xW_x + \frac{1}{2}W_x^3)\delta W_x(U_x + \frac{1}{2}W_x^2)dx. \tag{II.4.10}$$

The finite stiffness of the beam support in the axial direction may be modeled by an axial spring at $x = l$ having spring constant, k. The potential energy of this spring is

$$\mathcal{V}_b = \frac{1}{2}kU^2(l). \tag{II.4.11}$$

Integrating equation (II.4.10) by parts and including the variation of the boundary potential energy in equation (II.4.11) lead to

$$\begin{aligned}\delta\mathcal{V} = Eb&\left\{\int_0^l\left[\frac{h^3}{12}W_{xxxx} - h\frac{\partial}{\partial x}((U_x + \frac{1}{2}W_x^2)W_x)\right]\delta W dx - \int_0^l h\frac{\partial}{\partial x}(U_x + \frac{1}{2}W_x^2)\delta U dx\right\}\\ &+Eb\left\{\frac{h^3}{12}(W_{xx}\delta W_x|_0^l - W_{xxx}\delta W|_0^l) + h(U_xW_x + \frac{1}{2}W_x^3)\delta W|_0^l\right\}\\ &+Ebh(U_x + \frac{1}{2}W_x^2)\delta U|_0^l + kU(l)\delta U(l).\end{aligned} \tag{II.4.12}$$

The remaining term to be evaluated in Hamilton's principle in equation (II.4.4) is the contribution due to nonconservative forces. This includes the effects of applied forces and damping. It will be assumed that there are no external forces acting other than those that produce the base excitation which is already accounted for in the kinetic energy expression, equation (II.4.2). Two different damping mechanisms will be included in the model. One will be viscous damping which depends only on the velocity at each point along the beam length and the other is due to friction at the support at $x = l$. The model of frictional damping accounts for sticking and slipping depending on the axial force at the boundary. This results in hysteresis which greatly complicates the analysis of the random response.

The variation of the work done by viscous damping (the virtual work) may be modeled as

$$\delta W_v = -\int_0^l \eta \dot{W}(x,t)\delta W(x,t)dx, \tag{II.4.13}$$

where η is the viscous damping coefficient. The negative sign accounts for the fact that damping consists of the removal of energy from the system.

Frictional damping at the support will be modeled as a contact surface with a clamping force N. It is assumed that as long as the magnitude of the axial force is less than a critical value, μN, there is no slipping and the axial force applied by the beam is equal and opposite that of the frictional support. As the axial force at the beam end is increased to μN, however, the contact surface slips and no further increase in axial force is allowed. The stick/slip boundary may then be thought of as a force limiter. The behavior is characterized in three possible states, (1) axial force equal to $-\mu N$ for slipping in negative x direction; (2) zero velocity (no slip) when the magnitude of the axial force is less than μN, and (3) axial force equal to $+\mu N$ for slipping in the positive x direction.

To construct the equations that describe the axial boundary condition let the frictional damping force be denoted by $f_s(U(l), \dot{U}(l))$. The virtual work associated with friction damping is then

$$\delta W_f = f_s(U(l), \dot{U}(l))\delta U(l). \tag{II.4.14}$$

The axial boundary condition at $x = l$ follows from letting $\delta W = \delta W_v + \delta W_f$, then substituting equations (II.4.12) through (II.4.14) into equation (II.4.4) and combining the terms that multiply $\delta U(l)$. Setting the result to zero, we have

$$\left[-Ebh(U_x + \frac{1}{2}W_x^2)|_{x=l} - kU(l) + f_s(U(l), \dot{U}(l))\right]\delta U(l) = 0. \tag{II.4.15}$$

The first term in equation (II.4.15) may be evaluated using the governing equation for axial deflection which may be obtained from equations (II.4.2), (II.4.4), and (II.4.12),

$$Ebh\frac{\partial}{\partial x}(U_x + \frac{1}{2}W_x^2) = 0. \tag{II.4.16}$$

This equation contains no inertia terms because axial kinetic energy was neglected in equation (II.4.2). It is assumed that resonances in the axial direction are outside the frequency range of interest.

Integrating equation (II.1.16) over x gives

$$U_x + \frac{1}{2}W_x^2 = c(t), \tag{II.4.17}$$

where $c(t)$ depends only on time. From equations (II.4.8) and (II.4.17) the axial strain is

$$\epsilon_{xx} = c(t) - z\frac{\partial^2 W(x,t)}{\partial x^2}, \tag{II.4.18}$$

where the first term $c(t)$ is seen to account for axial stretching of the mid-line at $z = 0$, and the second term is the usual bending strain. The stretching of the beam mid-line, $c(t)$ is a constant along the beam length.

Substituting equation (II.4.17) into equation (II.4.15) leads to

$$-Ebhc(t) - kU(l) + f_s(U(l), \dot{U}(l)) = 0. \tag{II.4.19}$$

It is convenient to express this boundary condition in terms of the axial stretching, $c(t)$, and the transverse deflection, $W(x,t)$, by eliminating $U(l)$. This may be accomplished by integrating equation (II.4.17) over x,

$$U(x,t) + \int_0^l \frac{1}{2} W_x^2(\xi,t)d\xi = xc(t) + a(t), \tag{II.4.20}$$

where ξ is a dummy variable and $a(t)$ is a constant of integration. Since the axial displacement is constrained to be zero at $x = 0$, i.e., $U(0,t) = 0$ then from equation (II.4.20), $a(t) = 0$. Evaluating equation (II.4.20) at $x = l$ then gives

$$U(l,t) = lc(t) - \frac{1}{2} \int_0^l W_x^2(\xi,t)d\xi. \tag{II.4.21}$$

Substituting equation (II.4.21) into equation (II.4.19) and rearranging give the friction force in terms of $c(t)$ and $W(x,t)$

$$f_s(c(t), W(x,t)) = (kl + Ebh)c(t) - \frac{k}{2} \int_0^l W_x^2(\xi,t)d\xi. \tag{II.4.22}$$

Equation (II.4.22) must be solved along with the governing equation for $W(x,t)$ which follows from equations (II.4.4), (II.4.7), (II.4.12), (II.4.13) and (II.4.17),

$$\rho A\ddot{W}(x,t) + \frac{Ebh^3}{12} W_{xxxx} - Ebhc(t)W_{xx} + \eta\dot{W} = -\rho A\ddot{W}_o. \tag{II.4.23}$$

Since $W(x,t)$ is the transverse deflection of the beam mid-line relative to the motion of the supporting clamps, it will be assumed that $W(x,t)$ and $W_x(x,t)$ are zero at $x = 0$ and $x = l$. This eliminates the boundary terms for $W(x,t)$ in equation (II.4.12).

Equations (II.4.22) and (II.4.23) must be solved simultaneously for $c(t)$ and $W(x,t)$ with the friction force f_s properly accounted for. Due to the nature of the friction force, an iterative solution procedure must be used. In the present study, the response is simulated in the time domain using Newmark's numerical integration scheme.

II.4 References

[1] M. A. Miner 1945 *Journal of Applied Mechanics* **12**, A159–164. Cumulative damage in fatigue.

[2] J. W. Miles 1954 *Journal of the Aeronautical Sciences* **21**, 753–762. On structural fatigue under random loading.

[3] Y. K. Lin 1967 *Probabilistic Theory of Structural Dynamics.* New York, NY: McGraw-Hill, Inc..

[4] R. N. Miles 1989. *Equivalent linearization for fatigue life estimates of a nonlinear structure* NASA TM 101536.

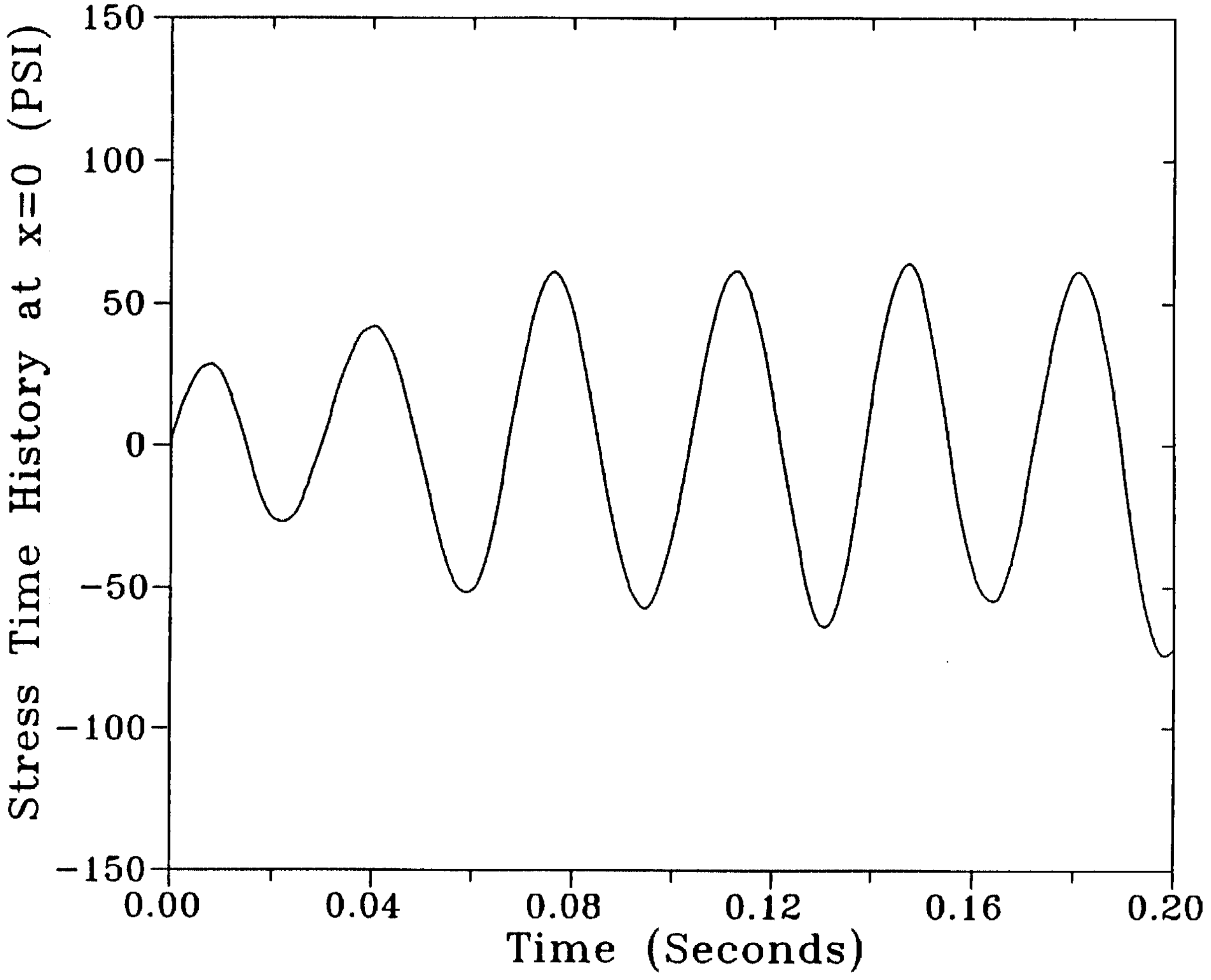

Figure II.2.1 Simulated stress response of a linear beam with one mode.

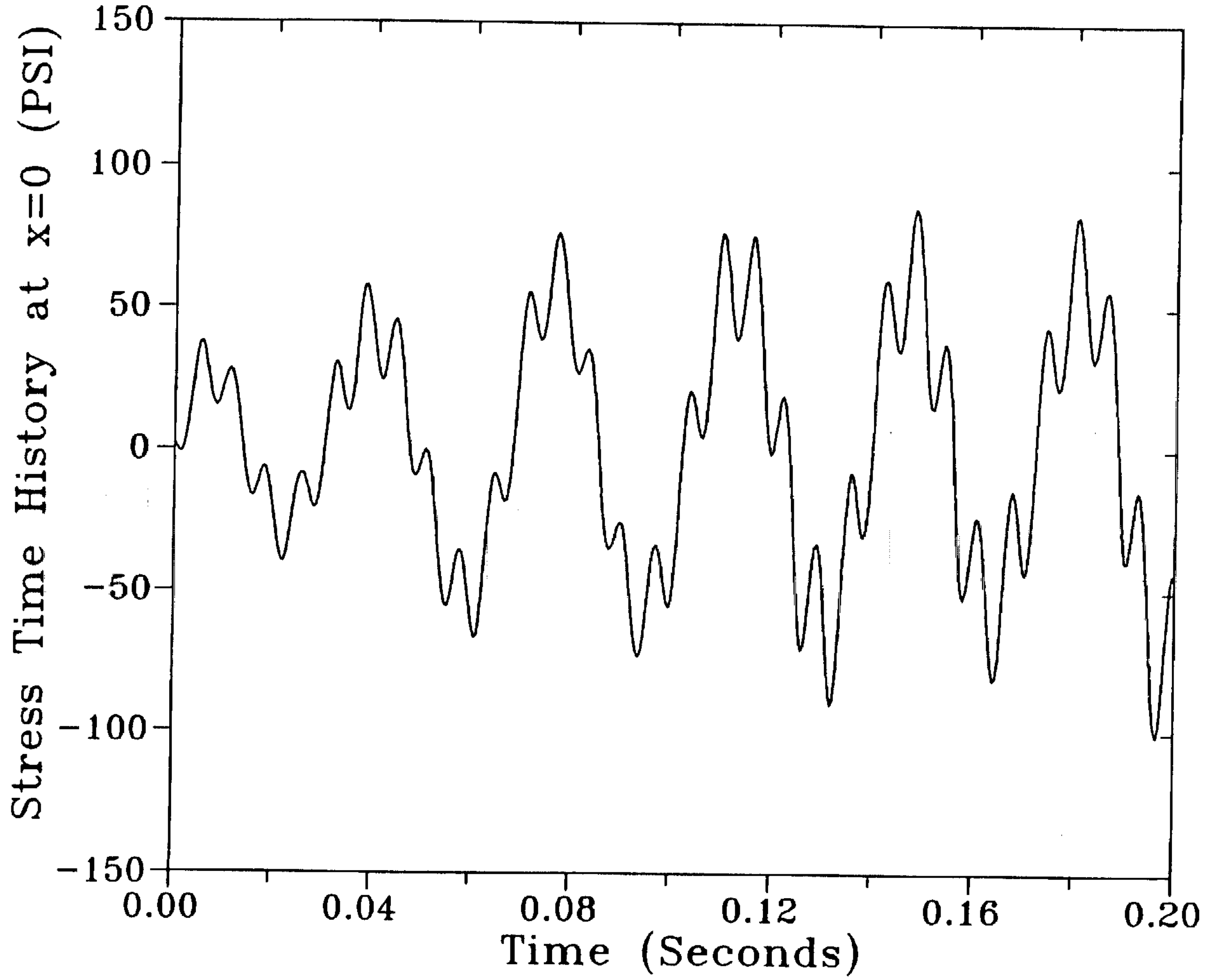

Figure II.2.2 Simulated stress response of a linear beam with two modes.

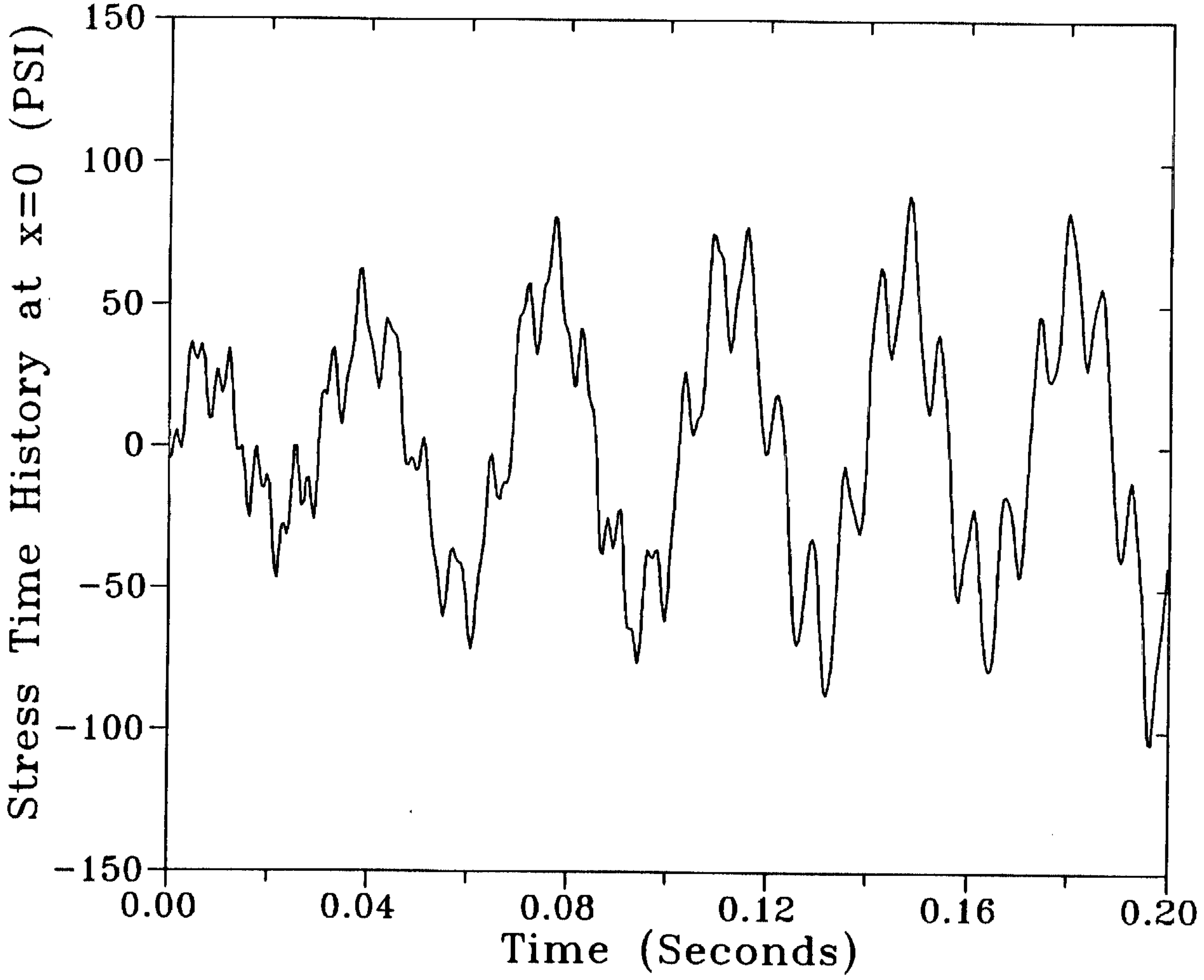

Figure II.2.3 Simulated stress response of a linear beam with three modes.

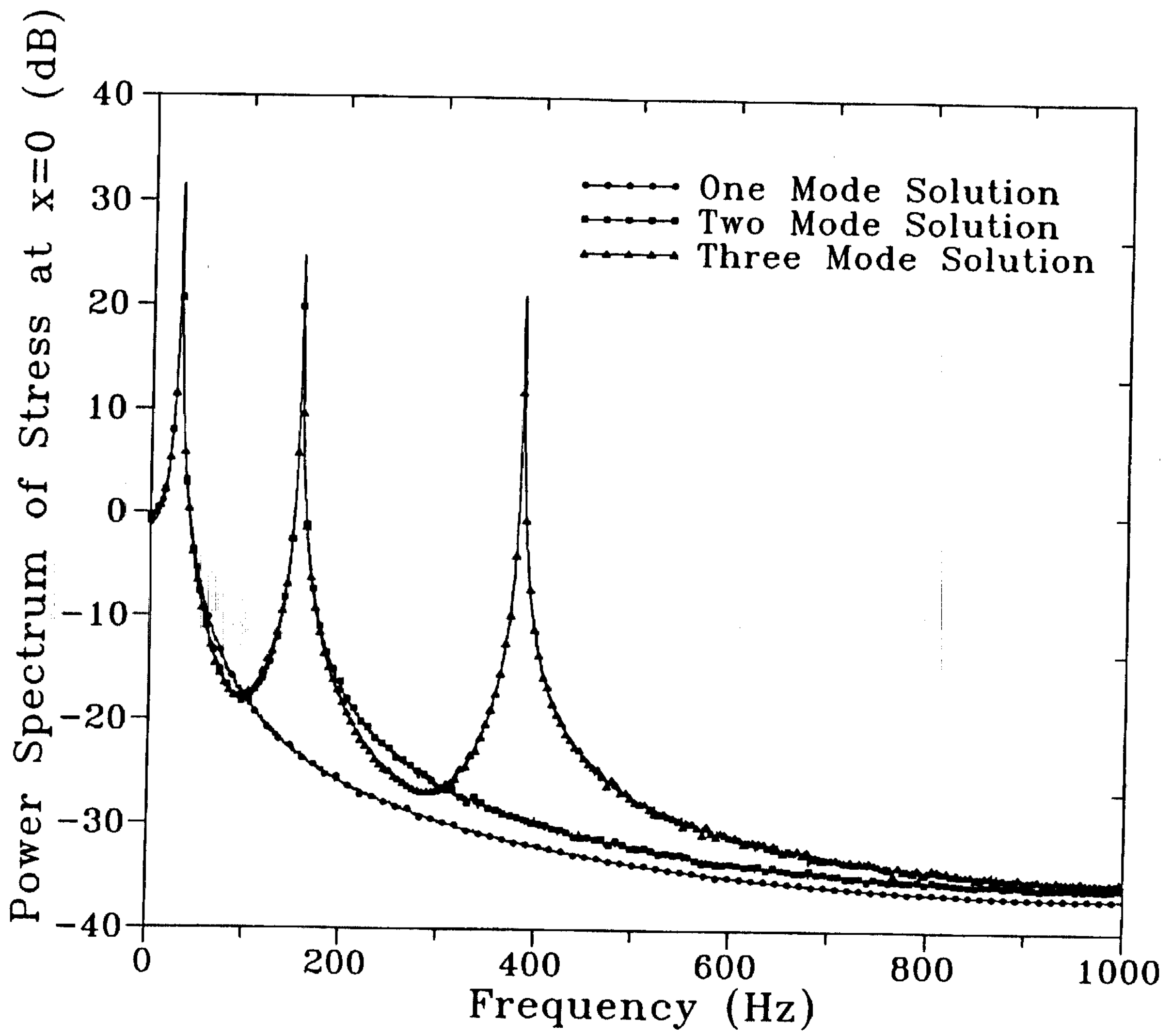

Figure II.2.4 Predicted stress spectra of a linear beam.

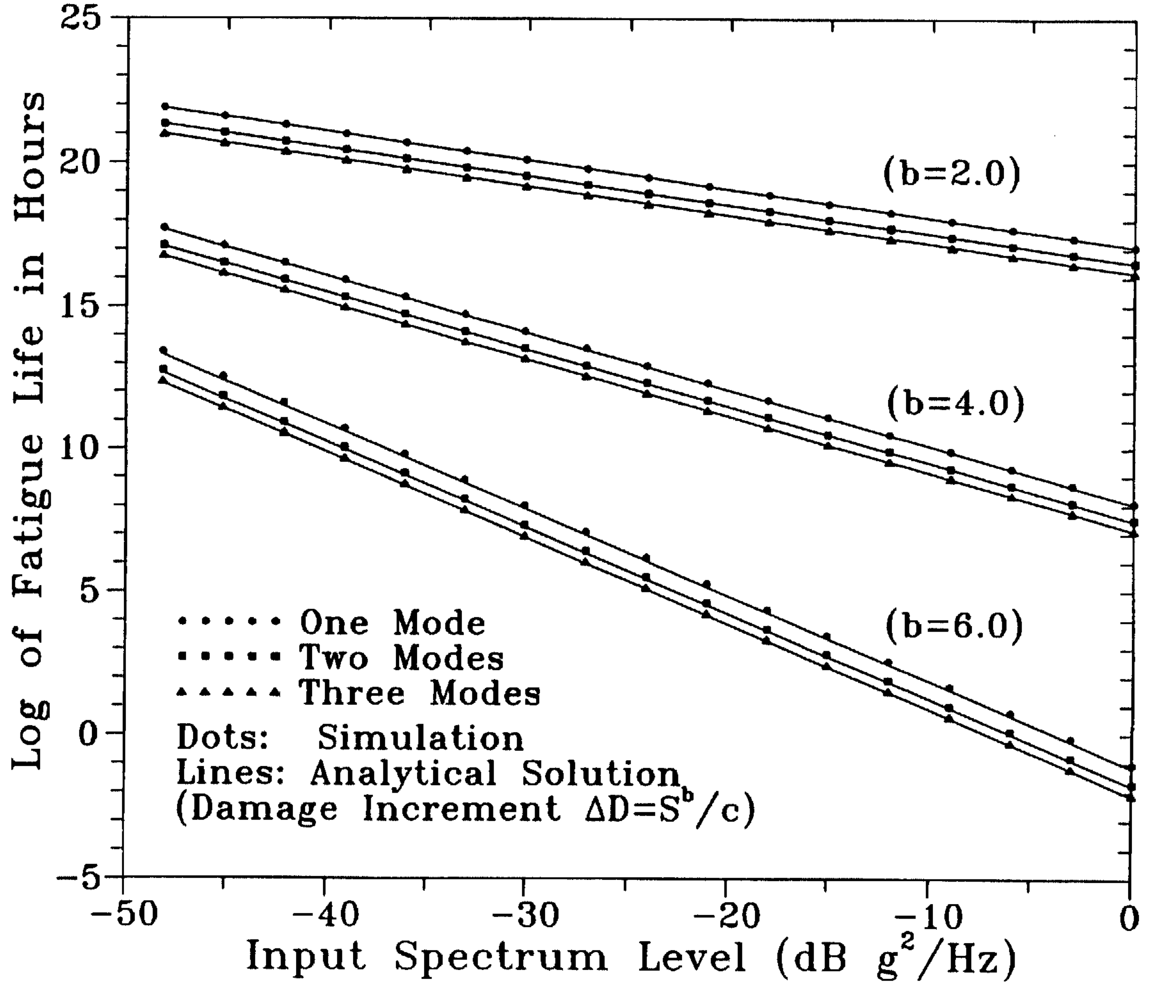

Figure II.2.5
Predicted fatigue life of a linear beam with multiple modes. Damage is assumed to occur for each stress maximum.

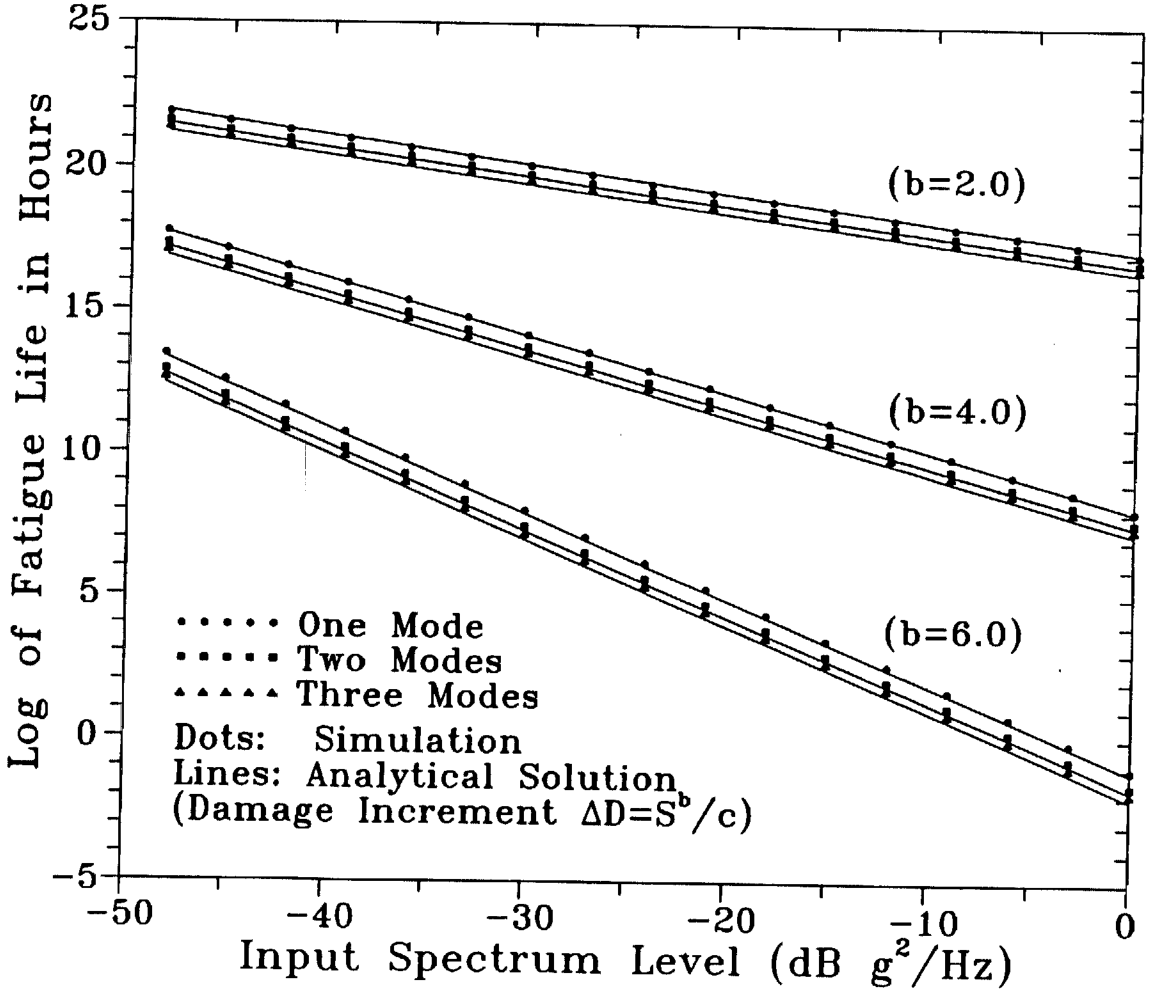

Figure II.2.6

Predicted fatigue life of a linear beam with multiple modes. Damage is assumed to occur due to the largest stress maximum between each zero crossing with positive slope.

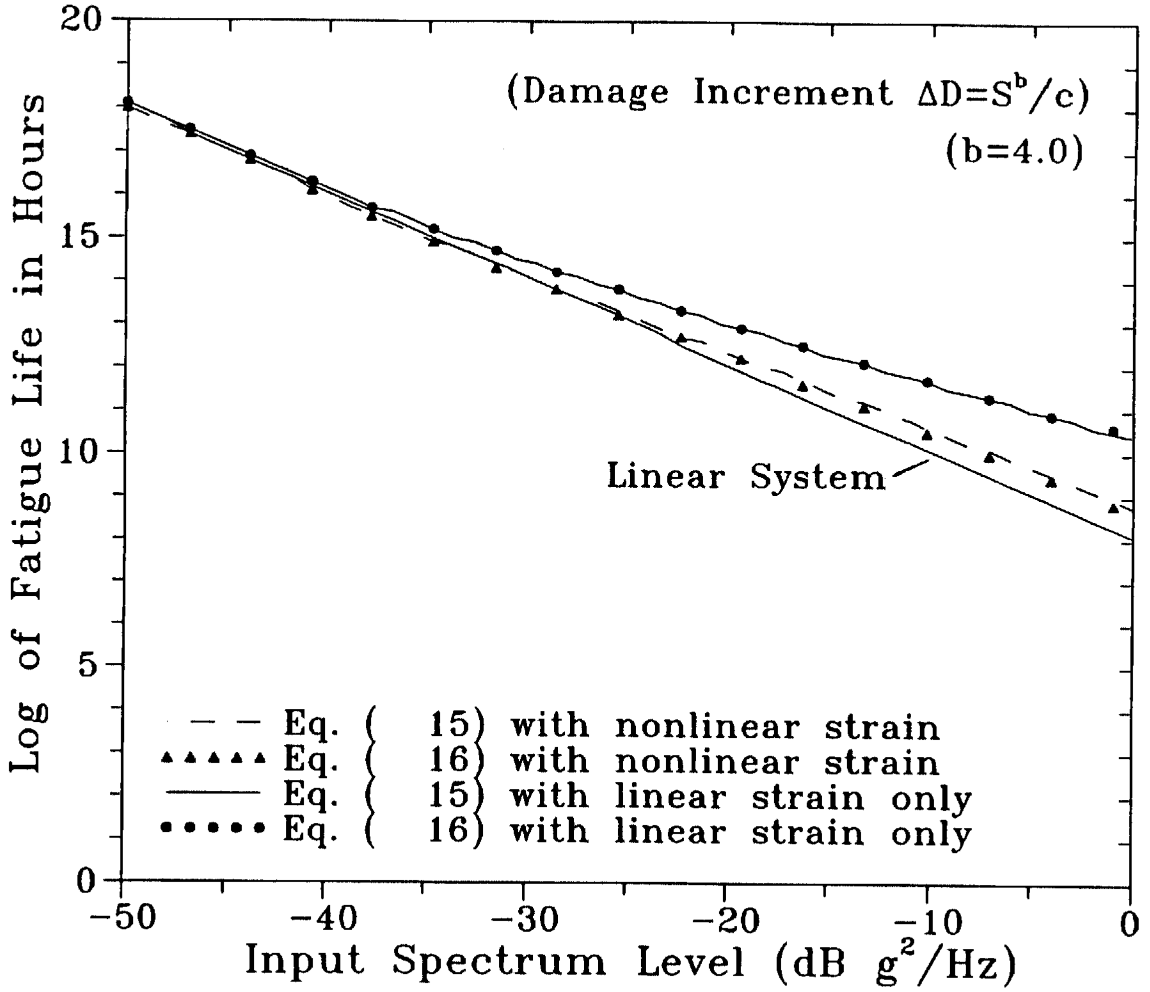

Figure II.3.1 Predicted fatigue life of a nonlinear beam with one resonant mode.

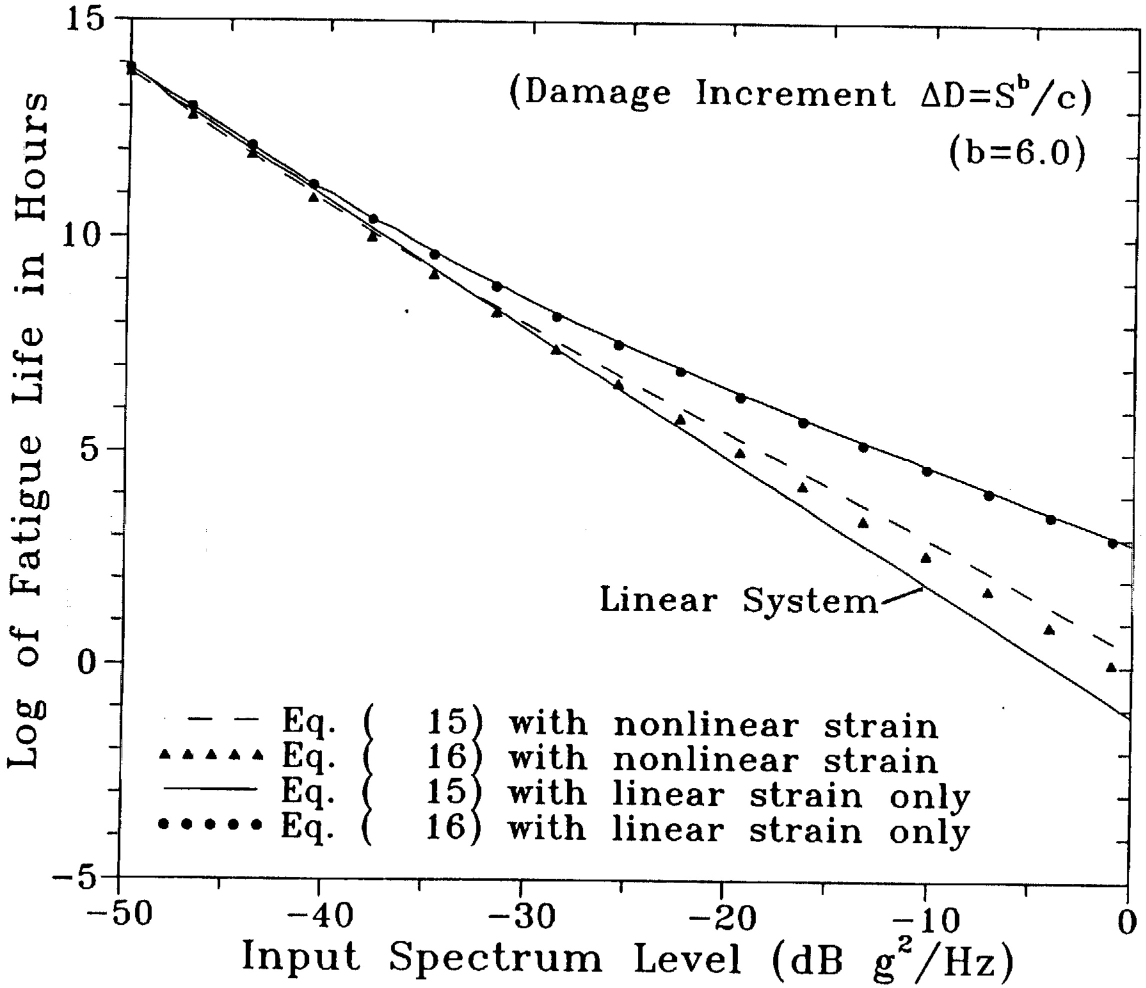

Figure II.3.2 Predicted fatigue life of a nonlinear beam with one resonant mode.

III.1 Rainflow Counting

The methods used in the previous sections for identifying damaging events are appealing because they require statistics of the random response that may be easily computed using exact closed form expressions. In the present section we estimate damage based on a consideration of the mechanical behavior of materials rather than on easily computed statistics. While the resulting procedure does not permit simple analytical expressions to be used to estimate fatigue life, it has been shown to produce more accurate estimates of fatigue life than the methods discussed above.

A great deal of research on fatigue is concerned with estimating the usable lifetime of structures that are subjected to complicated loading. These studies are usually broken into two cases, one where the structure experiences significant plastic deformation and one where the deformation is predominantly elastic. When the strains are sufficiently large to induce plastic deformation, the damage mechanisms are different from the case where elastic behavior predominates. Since the structure lasts considerably longer when the strains are elastic, this situation is referred to as high-cycle fatigue. In studies of acoustic fatigue, the strains are considerably smaller still and damage accumulates very slowly. Acoustic fatigue is a special case of high cycle fatigue.

In contrast to plastic, or low-cycle fatigue, in which damage can be directly measured by observing the growth in crack length, the damage in high-cycle fatigue is microscopic and during the majority of the structure's life, it can only be measured using sophisticated techniques. It is assumed that unobserved damage accumulates over the life of the structure. The time duration for this damage to result in failure is the fatigue life.

Although the strains in high-cycle fatigue are primarily elastic, damage is always associated with inelastic behavior. It must be assumed that while the majority of the material responds elastically, there must be high strains at specific locations within the structure that result in microscopic damage. In acoustic fatigue studies, the deflections, stresses, and strains are estimated with the assumption of elastic response but the damage estimation should be based on considering the strains to be plastic.

It is well known that when a material experiences cyclic plastic deformation, a hysteresis loop is observed in a plot of stress versus strain. While it may not be possible to measure the stress and strain at microscopic areas where damage occurs in high-cycle fatigue, it is reasonable to assume that a hysteresis loop exists. This is the basis of modern damage counting schemes such as Rainflow cycle counting.

Rainflow cycle counting was first proposed by Matsuishi and Endo in 1968 [1]. Prior to this development considerable effort had been made to construct a cycle counting scheme that correlated with a physical understanding of the damage process and with experimental results.

The most often cited work on acoustic fatigue prediction is that of J.W. Miles [2] as discussed in section II. In this paper a remarkably simple formula is presented for estimating the fatigue life of a simple panel subjected to random loading. It is assumed that the strain response is dominated by that of the first resonant mode so that it may be considered to be a narrowband process. This narrowband assumption greatly simplifies the estimation of fatigue life because it may then be claimed that whatever the damage mechanism, there will be a damaging event for each cycle of the oscillating strain or stress. By assuming that the rate at which damage occurs is equal to the oscillation frequency, one can use the probability density for stress maxima to compute the expected value of the fatigue life. The details of the calculation are given in references [2-4].

Although the response of complex structures can rarely be considered a narrowband process, there has been considerable motivation to assume that damage is easily related to some statistic that can be readily calculated. If one assumes that damage occurs each time the stress or strain experiences a maximum or minimum it is possible to employ a similar formulation to that of Miles [2] to estimate fatigue life. An expression for the probability density of strain peaks in a wide-band random process is given in [4]. This result depends on the ratio of the expected number of zero crossings at positive slopes to the expected number of peaks. This quantity is easily computed from the response power spectral density. An example of the application of this approach is given in the previous sections and is also presented in Vaicaitis and Choi [5].

While the assumption that damage occurs for each strain peak has been primarily motivated by its mathematical utility, there have been several attempts to justify it experimentally. Broch [6] conducted an extensive fatigue test using a total of two hundred samples. Half of these samples were driven such that response behaved like a one degree of freedom system and the remaining samples responded as two degree of freedom systems. An attempt was made to control the experiments so that the mean square response levels and the total number of zero crossings were the same for each sample. In the one degree of freedom tests the ratio of the number of zero crossings to the number of peaks, α, was approximately unity and in the two degree of freedom tests the ratio was 0.275. An attempt was made to correlate the data using the known statistics of strain or stress peaks. It was concluded that further work was necessary before firm conclusions could be drawn.

Hillberry [7] conducted a similar comparison of the effect of response bandwidth where one set of data was obtained using narrowband response and the remaining data was broadband. In his broadband data , however, the ratio of the number of zero crossings to the number of peaks was 0.79 which is not significantly different than unity as in the case of narrowband data. Only minor differences were detected in the fatigue lives due to the different loadings. In a later work, Linsley and Hillberry [8] conducted fatigue tests with loadings that had significantly different spectra but identical peak probability densities. It was found that the fatigue lives were very similar even though the response spectra were quite different. They concluded that the peak probability density contained all the necessary information for fatigue predictions.

While Linsley and Hillberry's result [8] is interesting and lends support to the claim that peak counting may be sufficient for fatigue prediction, it is found that two signals that have the same peak probability density could also have similar damage rates as predicted using Rainflow counting. This was observed by Wirsching and Shehata [9] who estimated fatigue lives using Rainflow counting on simulated data sets that had eleven different power spectra. These spectra had α ratios that varied from 0.218 to 0.998 . It was found that the mean and standard deviations of stress cycles as determined by Rainflow counting are directly related to α. The authors conclude that for the purpose of estimating fatigue life, the spectral shape of the response can be characterized by the total power and α. Further justification of this claim is needed.

Since the early seventies, there has been general agreement that for complicated random loading it is necessary to use a scheme such as Rainflow counting to obtain reliable fatigue estimates. This type of procedure is especially helpful in properly accounting for the effects of mean stress superimposed on the fluctuating loads. The mean stress could be the result of very low frequency oscillations such those caused by thermal stress, geometrically nonlinear in-plane strains due to large deflections, or low frequency structural modes. The effect of mean stress could be very important in acoustic fatigue analysis.

The manner in which Rainflow counting accounts for mean stress is illustrated in figure III.1.1 which is taken from reference [10]. The key to the method is to attempt to count closed hysteresis loops. As discussed above, although these stress-strain hysteresis loops may be unobservable due to the difficulty of measuring stress and strain at the locations of damage accumulation, there must be some hysteresis in the structure because damage will never occur if the response is perfectly elastic. Hysteresis loops associated with two rather similar strain time histories are shown in figure III.1.1. In each time history a single large amplitude strain cycle occurs before the strain oscillates at a lower amplitude. The difference in the two time histories shown is that the half cycle preceding the smaller amplitude oscillation is negative in history A and positive in history B. As indicated in the figure, the hysteresis loops corresponding to these cases show that for history A, during the small oscillation cycles there is a positive mean stress, σ_0, and for history B the mean stress is negative during the small amplitude cycles. The damage associated with these two histories is expected to differ substantially because it is known that a positive mean stress can shorten fatigue life and a negative mean stress can lengthen it. It is important to note that older cycle counting schemes (such as simple peak counting) that do not consider the hysteresis loops will predict identical damage rates for these two time histories.

To understand the way Rainflow counting accounts for hysteresis we need to describe the method in detail. There are many excellent descriptions of the approach that are available in the literature. The following is adapted from reference [10].

The Rainflow counting procedure is best visualized by viewing the strain time history with the time axis pointing downward as in figure III.1.2 (adapted from reference [10]). The method gets its name from constructing cycles by imagining rain flowing downward with the strain curve acting like a series of roofs. The first step is to rearrange the time history so that it begins and ends at the strain value of greatest magnitude in the block of data. This rearrangement of the data is justifiable because the response is considered to be a stationary random process. A shift in the time axis will not affect the statistics. It is assumed that rain begins to flow at the beginning of the trace at point A in figure III.1.2 and at each strain reversal in the time history. To identify the closed hysteresis loops a number of rules are applied to the falling rain. The rain is assumed to continue flowing downward unless:

a. The rain began at a local maximum (peak) and falls opposite a local maximum greater than that from which it came.

b. The rain began at a local minimum point (valley) and falls opposite a local minimum point greater (in magnitude) than that from which it came.

c. It encounters a previous rainflow.

Figure III.1.2 illustrates the application of the method. The dots indicate the initiation of rainflow at each reversal in the time history.

A. Rain flows from point A over points B and D and continues to the end of the history (which is point A again) since none of the conditions for stopping rainflow are satisfied.

B. Rain flows from point B over point C and stops opposite point D, since both B and D are local maximums and the magnitude of D is greater than B (rule a above).

C. Rain flows from point C and must stop upon meeting the rainflow from point A (rule c).

D. Rain flows from point D over points E and G and continues to the end of the history since none of the conditions for stopping rainflow are satisfied.

E. Rain flows from point E over point F and stops opposite point G, since both E and G are local minimums and the magnitude of G is greater than E (rule b).

F. Rain flows from point F and must stop upon meeting the flow from point D (rule c).

G. Rain flows from point G over point H and stops opposite point A, since both G and A are local minimums and the magnitude of A is greater than G (rule b).

H. Rain flows from point H and must stop upon meeting the rainflow from point D (rule c).

The events identified above may now be combined to identify complete cycles, or closed hysteresis loops. The rainflow from A to D and from D to A forms a complete cycle. Another cycle is formed by the flow from B to C and from C to the strain level at B (in the line connecting C and D). There are also cycles formed between strain ranges E-F and G-H.

The rainflow process identifies cycles that are associated with closed hysteresis loops as indicated in figure III.1.3. This figure shows the loops that correspond to each cycle. The strain maxima are each located at a tip of a loop. After the strain goes from A to B it decreases to C. As the strain increases from C it reaches the level of B again while on its way to D. The Rainflow counting procedure correctly indicated that there is a hysteresis loop between B and C which is a complete cycle contained within the larger loop between A and D.

Once the cycles and associated strain ranges are identified the, Palmgren-Miner linear damage accumulation rule may be applied [11]. This rule states that we may simply add the incremental damage (or life used up) due to each cycle to estimate the fatigue life. The damage due to one cycle may be expressed as

$$\Delta D_i = \frac{1}{c}\left(\frac{1/2\Delta S_i}{1 - S_{mi}/S_u}\right)^b, \tag{III.1.1}$$

where ΔS_i is the stress range of the cycle, S_{mi} is the mean stress of the cycle, S_u is the ultimate strength of the material, and b and c are constants obtained from a S-N diagram for the material with constant amplitude loading. The manner of incorporating the mean stress in equation (III.1.1) is after Morrow [12]. The total damage is simply

$$D = \sum_i \Delta D_i. \tag{III.1.2}$$

Failure is assumed to occur when $D = 1$.

III.2 Experimental Verification of Rainflow Counting

There have been a number of experimental studies to verify the accuracy of fatigue prediction schemes. In the following, we will describe two reports that address issues that are relevant to acoustic fatigue studies. The two most commonly cited works on the experimental verification of Rainflow counting are those of Dowling [13] and a program conducted by the SAE Cumulative Fatigue Damage Division [14]. In Dowling's study a total of 83 specimens were tested to failure. His main purpose was to construct a fatigue prediction procedure that could account for the effects of the sequence of the strain cycles and could also account for fluctuating mean stresses. A number of complicated load histories were used. Data is presented which indicates that Rainflow counting does a very good job of handling time histories where small, high frequency oscillations are superimposed on top of large amplitude, low frequency oscillations.

Signals that have small fluctuations added to large low frequency oscillations are commonly seen in the response of complex structures where large amplitude low frequency modes coexist with an uncountable number of high frequency resonances. Simplified time histories that have this feature are shown in figure III.2.1 (taken from Dowling [13]). The traces a and b shown in the figure would have identical fatigue lives if simple peak counting were used. Dowling showed that the actual fatigue lives of specimens will differ substantially with these two types of response and that the difference in fatigue life is accurately estimated only if a procedure such as Rainflow counting is used.

Tests were conducted by adding two sine waves to obtain stress and strain histories as shown in figure III.2.2 a (again taken from reference [13]). In these tests the amplitude of the small, high frequency fluctuation was held constant and the amplitude of the low frequency component, $\Delta\epsilon_1$, was varied. Figure III.2.2 b shows that his prediction procedure using Rainflow counting accounts for changes in $\Delta\epsilon_1$ remarkably well.

The data of figure III.2.2 correspond to a low cycle fatigue test where the material experienced significant plastic deformation. This is apparent in the figure because the traces for strain and stress differ substantially. Another set of specimens were tested where the strains were predominantly elastic so that high cycle fatigue mechanisms would be encountered. Typical stress time histories for these tests are shown in figure III.2.3. In this case a high frequency sine wave was superimposed on a lower frequency triangle wave. The amplitudes of the high frequency sine wave and the low frequency triangle wave were held constant. The fatigue lives were measured and predicted for a range of values of the frequency of the triangle wave. Comparisons of the measured and predicted results are shown in the figure. Note that the vertical scale spans only one decade so that the error is roughly a factor of two. This is quite good agreement for a fatigue prediction.

A similar test to that of figure III.2.2 was conducted where the maximum stress range was kept constant, $\Delta\sigma_1 = 100$, but the relative amplitudes of the low frequency and high frequency components were varied. It was found that as the amplitude of the high frequency component was increased, the fatigue life was reduced dramatically. The results are shown in figure III.2.4. It should be noted that simple peak counting would not predict that the amplitude of the high frequency component would have a major effect. This is because the rate at which peaks occur is held constant and the peak amplitude distribution is not changed substantially. Rainflow counting, however, does a remarkably good job of accounting for this.

In the results shown in figures III.2.1 through III.2.4 the stress and strain time histories essentially contain subcycles with varying lower frequency (mean) fluctuations. It is well known that compressive mean stresses reduce damage and that tensile mean stresses increase the rate of damage accumulation. Rainflow counting enables one to account for these two effects for each cycle identified by the procedure as indicated in equation (III.1.1).

A number of other experiments were reported by Dowling [13] which will not be discussed here. These tests included other complicated time histories. He did not, however, conduct a comprehensive evaluation of Rainflow counting for very high cycle fatigue problems with loadings that are as complicated as encountered in acoustic fatigue. One may conclude, however, that Rainflow counting should lead to vastly more accurate estimates of fatigue life than methods that are often used in acoustic fatigue studies.

Another study that is often cited in support of the use of Rainflow counting is a joint effort by the SAE Cumulative Fatigue Damage Division [14]. In this, study three different complex loadings were applied to notched steel specimens. A total of 57 specimens were tested. The load time histories used are shown in figure III.2.5. The time history corresponding to bracket vibration shown in the figure most closely matches that seen in aerospace structures. The response power spectra for these histories were, unfortunately, not presented in the report. A comparison of predicted and measured fatigue lives is shown in figure III.2.6. In these predictions the Rainflow counting method was used to identify cycles as discussed in Section II.

An investigation is described in reference [14] of the effect of mean stress on fatigue life. Predictions were made with and without mean stress included. This was accomplished by either including or neglecting S_m in equation (III.1.1). As discussed above, tensile mean stress is known to reduce fatigue life while compressive mean stress increases it. It was found that for a time history where the average stress was near zero, the reductions and increases in fatigue life due to fluctuating mean stresses tend to cancel out. It is likely then, that for Gaussian time histories with zero mean, the mean stress effect may be safely ignored. When the structure responds nonlinearly, however, such that in-plane stretching strains are significant, the mean stress effect could be quite substantial.

It should be pointed out that the tests conducted by Dowling [13] were conducted on smooth samples with uniaxial loading and the tests discussed in reference [14] were conducted on notched specimens in tension and compression. None of the studies reviewed to date examined fatigue where the primary mode of deflection is in bending as it is in acoustic fatigue. It is possible that this could affect the applicability of these studies to the acoustic fatigue problem.

A large number of other studies have compared experimental fatigue measurements with predictions. We have attempted to limit our attention to those studies that relate to the acoustic fatigue problem. This means that those studies that investigated low cycle fatigue are excluded. Low cycle fatigue is important if acoustic fatigue tests are accelerated by increasing response levels to the point where plastic deformation is significant. This would drastically change the results and care should be taken when high level tests are designed.

III.3 References

[1] M. Matsuishi and T. Endo Fatigue of metals subjected to varying stress. *JSME* Paper presented to Japan Society of Mechanical Engineers, Fukota, Japan.March1968

[2] J. W. Miles On structural fatigue under random loading *Journal of the Aeronautical Sciences* **21**, 753–762. 1954.

[3] R. N. Miles Equivalent linearization for fatigue life estimates of a nonlinear structure. *NASA* TM 101536.January1989

[4] Y. K. Lin Probabilistic Theory of Structural Dynamics *New York, NY.* McGraw-Hill, Inc.: 1967.

[5] R. Vaicaitis and S. T. Choi, 'Acoustic Fatigue of Stiffened Structures', AFWAL-TR-88-3034, Proceedings of the Third International Conference on Recent Advances in Structural Dynamics, University of Southampton, England, July 18-22, 1988.

[6] J. T. Broch, "Peak Distribution Effects in Random Load Fatigue," in *Bruel and Kjaer Technical Review.* B&K (Eds.), 1: 1968, , pp. 119-147.

[7] B. M. Hillberry Fatigue Life of 2024-T3 Aluminum Alloy Under Narrow- and Broad-Band Random Loading *Effects of Environment and Complex Load History on Fatigue Life, ASTM STP* **462**, 167-183. 1970.

[8] R. C. Linsley and B. M. Hillberry Fatigue Life of 2024-T3 Aluminum Under Two Spectra with Identical Peak- Probability Density Function *Probabilistic Aspects of Fatigue ASTM* **511**, 156-167. 1972.

[9] P. H. Wirsching and A. Mohsen Shehata Fatigue Under Wide Band Random Stresses Using the Rain-Flow Method *Journal of Engineering Materials and Technology* **99**, 205-211. 1977.

[10] J. A. Bannantine, J. J. Comer, and J. L. Handrock Fundamentals of Metal Fatigue Analysis *Englewood Cliffs, NJ.* Prentice Hall: 1990.

[11] M. A. Miner Cumulative damage in fatigue *Journal of Applied Mechanics* **12**, A159–164. 1945.

[12] J. Morrow Fatigue Design Handbook. *Advances in Engineering, Vol. 4, Society of the Automotive Engineers* Warrendale, PA.Section 3.2, pp 21-201968

[13] N. E. Dowling Fatigue Failure Predictions for Complicated Stress-Strain Histories *Journal of Materials* **7**, 71-87. 1972.

[14] R. M. Wetzel (ed.) Fatigue under Complex Loading: Analysis and Experiments *Warrendale, PA*. Society of Automotive Engineers: 1977.

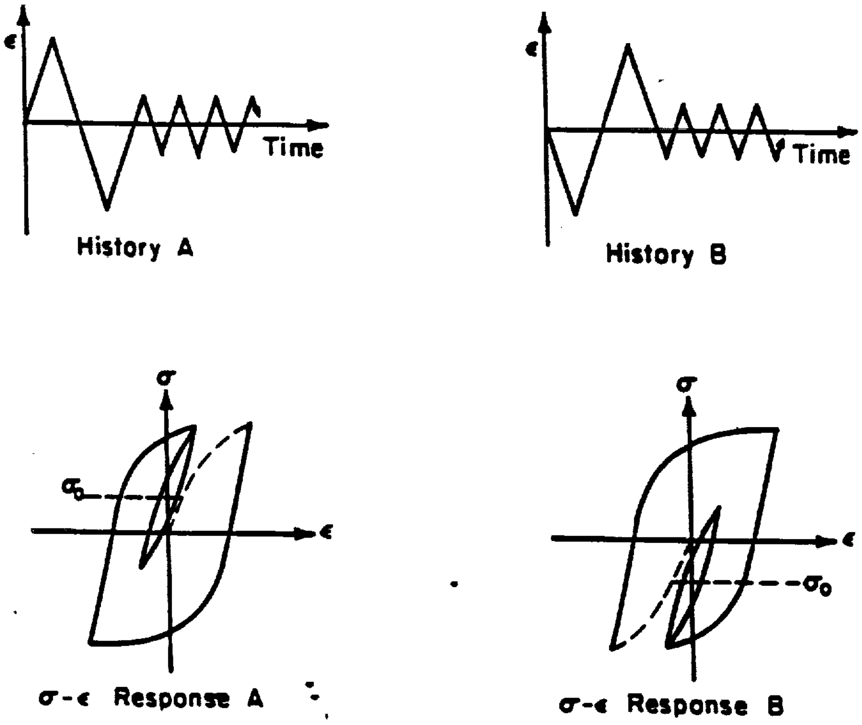

Figure III.1.1

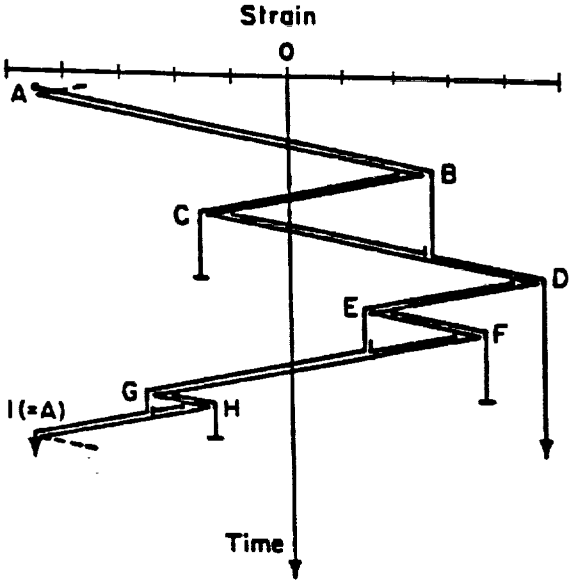

Figure III.1.2

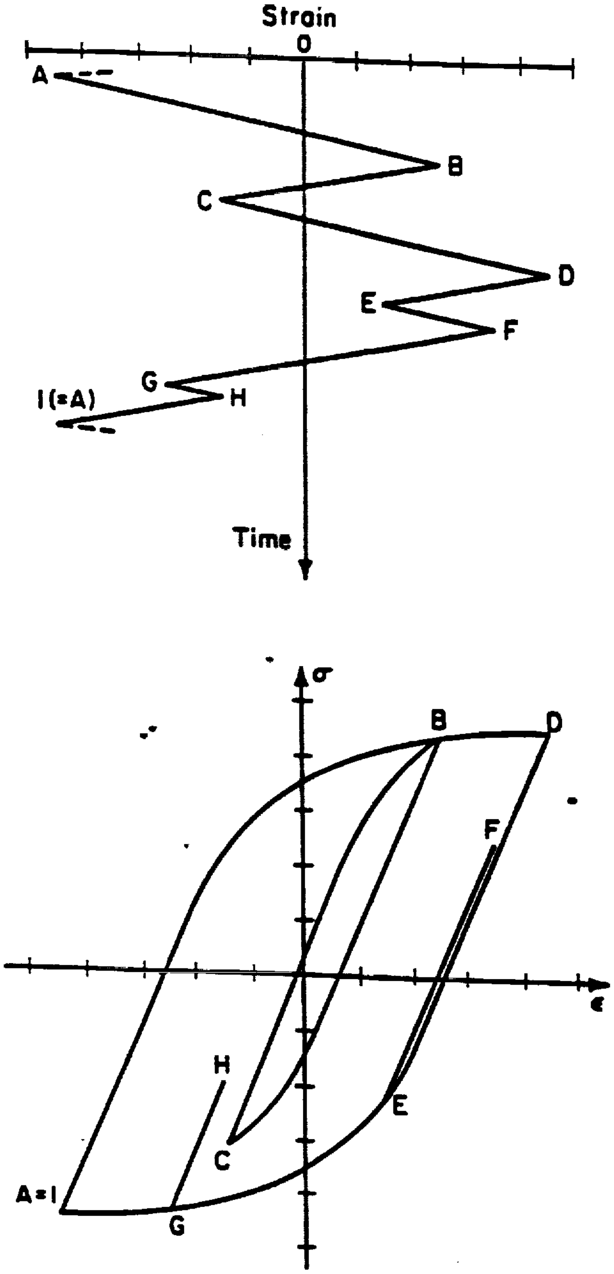

Figure III.1.3

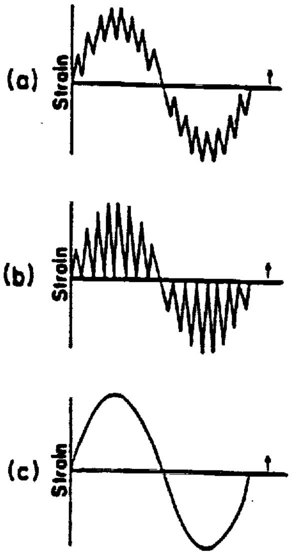

Figure III.2.1

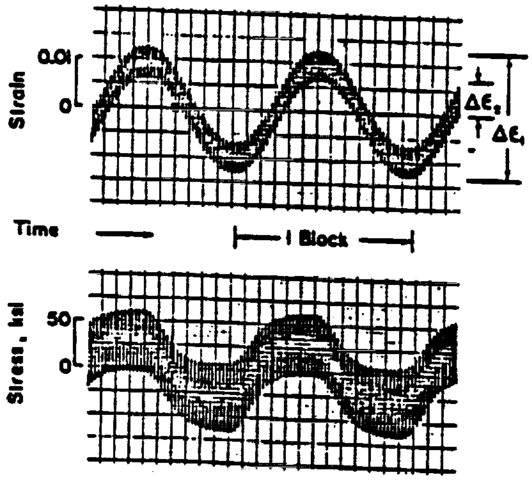

a) Strain – time and stress – time recordings for $\Delta\epsilon_1 = 0.027$

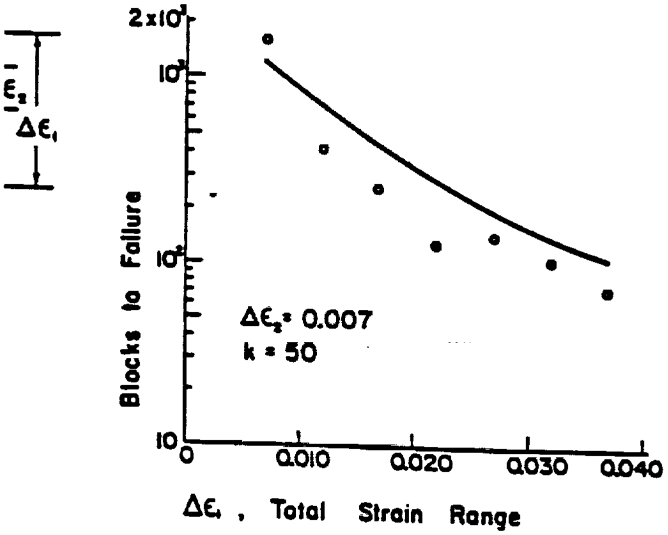

b) Test data and predicted line

Figure III.2.2

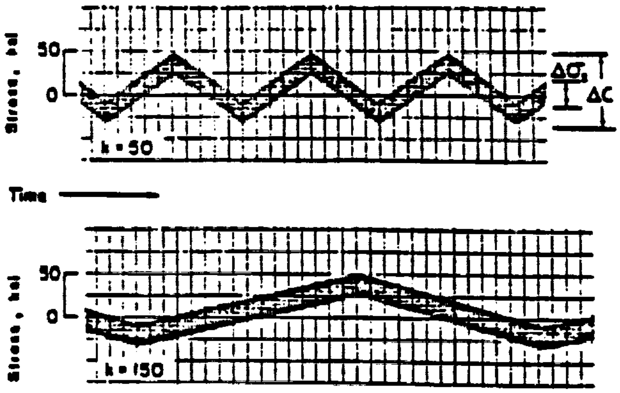

(a) Typical stress - time recordings

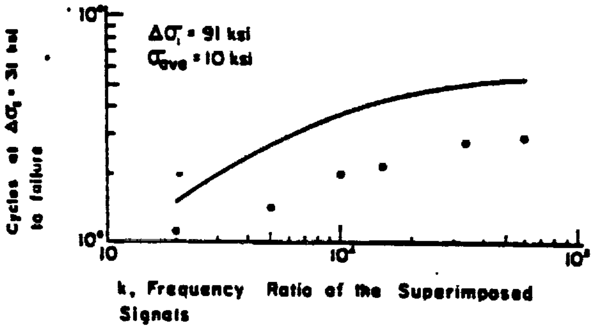

(b) Test data and predicted line

Figure III.2.3

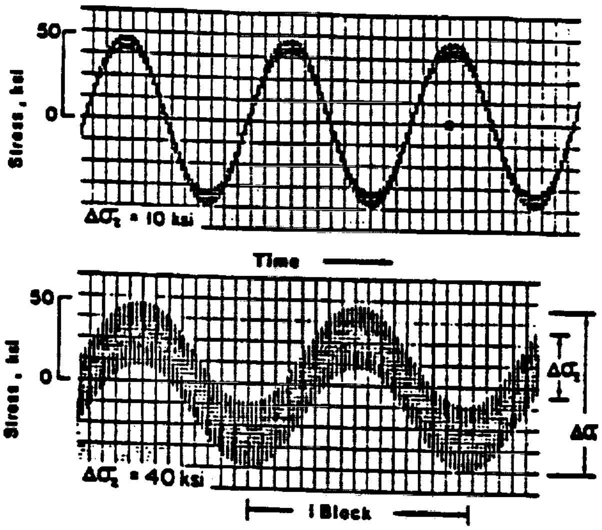

(a) Typical stress – time recordings

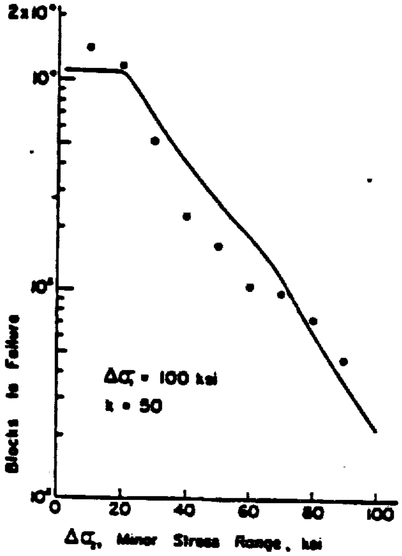

(b) Test data and predicted line

Figure III.2.4

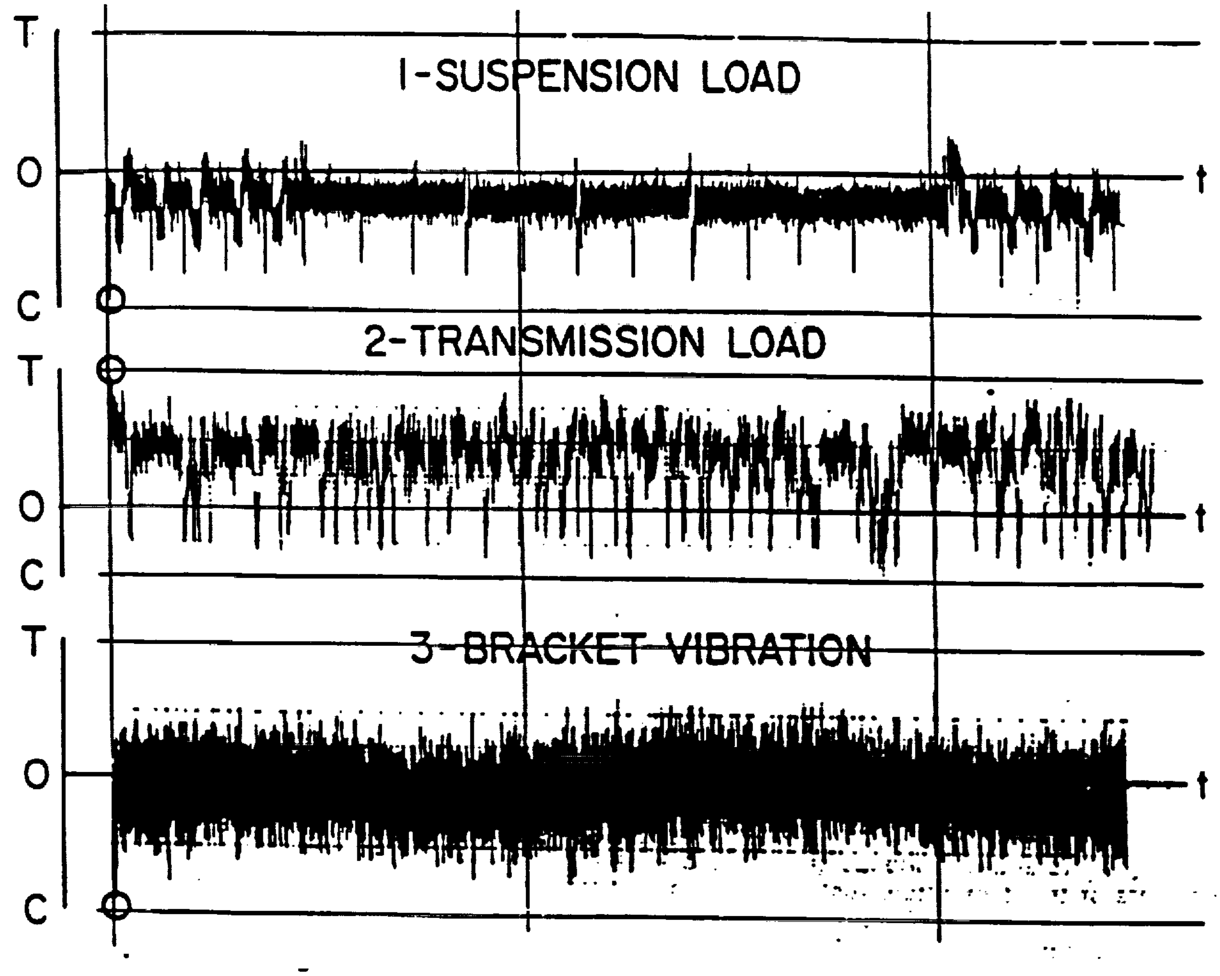

Figure III.2.5

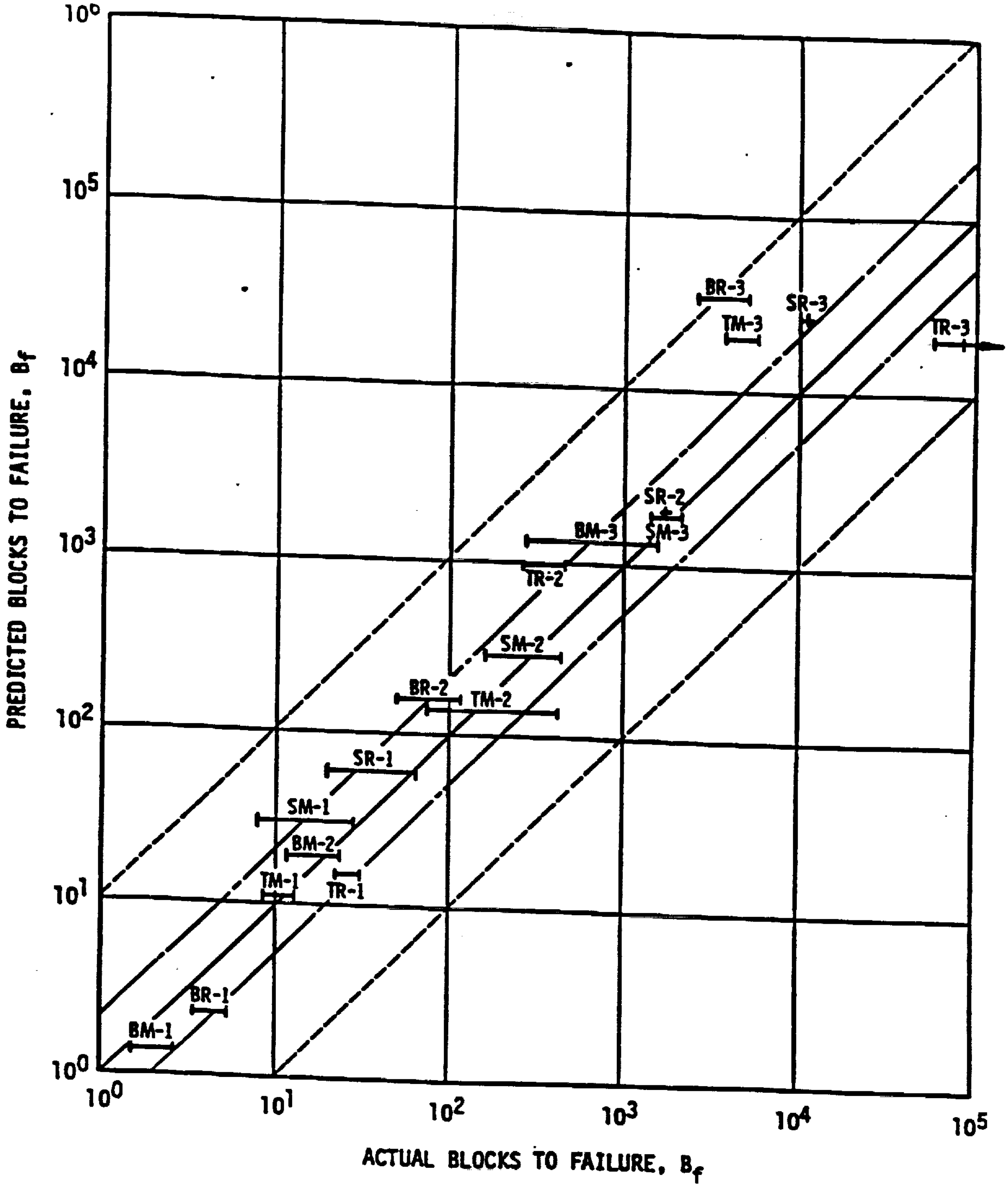

Figure III.2.6

IV. Power Spectral Density of Multi-Mode Systems

In the following sections a comparison is presented of fatigue lives predicted using simple peak counting to those obtained using Rainflow counting. The results presented indicate that when a signal contains significant low frequency oscillations there can be considerable difference between the fatigue lives predicted by the two methods. Further work is needed to compare the methods in typical aerospace applications.

The comparisons of fatigue lives estimated using peak counting and Rainflow counting to be presented in the following were performed using a time domain simulation of the response. An attempt has been made to simulate the response of typical aerospace structures. The method of simulating the time domain signal is presented in section V. The method depends on the response power spectral density. It is possible to accurately simulate the time domain response corresponding to any given power spectrum. In the present study, power spectra are created to model 'typical' structures that have nine resonant modes. The calculation of the response spectrum of a multi-mode system is presented in the present section. By processing the resulting time histories to predict fatigue lives, it is then possible to examine the influence of changes in the response spectrum (such as modifying the relative contribution of various modes) on the fatigue estimated by the two methods.

In the present study, fatigue lives were calculated for systems having nine resonant modes over the frequency range from 0 to 2000 Hertz. As will be discussed in section VI, it is found that by increasing the relative contribution of the lowest frequency mode, substantial differences are observed between the fatigue lives obtained using peak counting and those estimated using Rainflow counting. In every case, peak counting produced shorter lives than did Rainflow counting.

It should be noted that the fatigue estimates using peak counting performed here are not based on the single degree of freedom assumption of reference [2] of section III. Fatigue estimates using the single degree of freedom approach differed from those obtained using Rainflow counting by factors ranging from 48.69 to .0098. This method can be either highly conservative or very nonconservative depending on the system's spectral characteristics.

The primary result of the present comparison is that Rainflow counting produces significantly different fatigue life predictions than simple peak counting. This can also be seen by examining the Rainflow counting method. When low frequency oscillations are present in a signal along with high frequency components, peak counting will produce substantially shorter fatigue lives than Rainflow counting. While this is well known for certain time histories, it has not been demonstrated that Rainflow counting is necessary for time histories that are typically encountered in acoustic fatigue applications. The preliminary results presented here indicate that Rainflow counting is necessary in acoustic fatigue studies.

In the following, expressions are developed for the power spectral density of the response of a system that is subjected to Gaussian white noise excitation and that has a number of resonant modes. This will allow one to construct the power spectrum of the stress or strain response given the system resonant frequencies, modal damping ratios, and the relative contributions of the modes. The results of this section will be used in section V to create power spectra of simple multi-mode systems.

Suppose the deflection at some point can be expressed as

$$W(x,y,t) = \sum_{i=1}^{\infty} \alpha_i(t)\phi_i(x,y), \tag{IV.1}$$

where $\phi_i(x,y)$ are eigenfunctions and $\alpha_i(t)$ are modal responses. In a linear system $\alpha_i(t)$ are solutions to

$$\begin{aligned} \ddot{\alpha}_i + 2\omega_i\xi_i\dot{\alpha}_i + \omega_i^2\alpha_i &= Q_i(t) \qquad ,i = 1,2,...,\infty \\ &= q_i f_o(t). \end{aligned} \tag{IV.2}$$

We will assume that q_i is some constant, $f_o(t)$ is Gaussian white noise, ω_i is the natural frequency of the i^{th} mode, and ξ_i is the damping ratio.

The strain at some point on the structure may be expressed in the form

$$\epsilon(t) = \sum_{i=1}^{\infty} a_i\alpha_i(t), \tag{IV.3}$$

where the a_i indicate the contributions of the various modes.

The solution for $\alpha_i(t)$ in equation (IV.2) is

$$\alpha_i(t) = \int_0^t h_i(\tau')q_i f_o(t-\tau')d\tau' \tag{IV.4}$$

where

$$h_i(\tau') = \frac{e^{-\xi_i\omega_i\tau'}}{\omega_i\sqrt{1-\xi_i^2}} sin\left(\omega_i\sqrt{1-\xi_i^2}\tau'\right), \qquad \tau' > 0. \tag{IV.5}$$

It is assumed that $\alpha_i(t) = 0$ for $t \leq 0$. We may compute the power spectral density of the strain, $\epsilon(t)$, by first computing the strain auto correlation function,

$$R_{\epsilon\epsilon}(\tau) = \mathrm{E}\left[\epsilon(t)\epsilon(t+\tau)\right], \tag{IV.6}$$

where E[·] denotes the expected value. The strain is assumed to be a weakly stationary random process. The power spectral density of $\epsilon(t)$ is then obtained by the Fourier transform of equation (IV.6),

$$\Phi_{\epsilon\epsilon}(\omega) = \frac{1}{2\pi}\int_{-\infty}^{\infty} R_{\epsilon\epsilon}(\tau)e^{-i\omega\tau}d\tau. \tag{IV.7}$$

Substituting equation (IV.3) into equation (IV.6) gives

$$R_{\epsilon\epsilon}(\tau) = \mathrm{E}\Big[\sum_{i=1}^{\infty}\sum_{j=1}^{\infty} a_i a_j \alpha_i(t)\alpha_j(t+\tau)\Big], \tag{IV.8}$$

$$= \sum_{i=1}^{\infty}\sum_{j=1}^{\infty} a_i a_j \mathrm{E}\big[\alpha_i(t)\alpha_j(t+\tau)\big], \tag{IV.9}$$

$$= \sum_{i=1}^{\infty}\sum_{j=1}^{\infty} a_i a_j R_{\alpha_i\alpha_j}(\tau), \tag{IV.10}$$

where

$$R_{\alpha_i\alpha_j}(\tau) = \mathrm{E}[\alpha_i(t)\alpha_j(t+\tau)] \tag{IV.11}$$

is the cross correlation function for $\alpha_i(t)$ and $\alpha_j(t)$. Our assumption that the process is weakly stationary causes this cross correlation function to be independent of t. Substituting equation (IV.10) into equation (IV.7) and rearranging gives

$$\Phi_{\epsilon\epsilon}(\omega) = \frac{1}{2\pi}\sum_{i=1}^{\infty}\sum_{j=1}^{\infty} a_i a_j \int_{-\infty}^{\infty} R_{\alpha_i\alpha_j}(\tau)e^{-i\omega\tau}d\tau, \tag{IV.12}$$

$$= \sum_{i=1}^{\infty}\sum_{j=1}^{\infty} a_i a_j \Phi_{\alpha_i\alpha_j}(\omega), \tag{IV.13}$$

where the cross power spectral density of $\alpha_i(t)$ and $\alpha_j(t)$ is

$$\Phi_{\alpha_i\alpha_j}(\omega) = \frac{1}{2\pi}\int_{-\infty}^{\infty} R_{\alpha_i\alpha_j}(\tau)e^{-i\omega\tau}d\tau \tag{IV.14}$$

Substituting equation (IV.4) into equation (IV.11) gives

$$\begin{aligned} R_{\alpha_i\alpha_j}(\tau) &= \mathrm{E}\Big[\Big(\int_0^t h_i(\tau')q_i f_o(t-\tau')d\tau'\Big)\Big(\int_0^{t+\tau'} h_j(\tau')q_j f_o(t+\tau-\tau')d\tau'\Big)\Big] \\ &= q_i q_j \int_0^t \int_0^{t+\tau'} h_i(\tau')h_j(\tau'')\mathrm{E}\big[f_o(t-\tau')f_o(t+\tau-\tau'')\big]d\tau''\tau' \end{aligned} \tag{IV.15}$$

The excitation, $f_o(t)$, is assumed to be stationary Gaussian white noise so that

$$\mathrm{E}\big[f_o(t-\tau')f_o(t+\tau-\tau'')\big] = 2\pi\Phi_{f_o}\delta(\tau+\tau'-\tau''), \tag{IV.16}$$

where $\delta(\cdot)$ is the Dirac delta function and Φ_{f_o} is the two-sided power spectral density of $f_o(t)$. Substituting equation (IV.16) into equation (IV.15) and integrating over τ'' gives

$$R_{\alpha_i\alpha_j}(\tau) = 2\pi q_i q_j \int_0^{\tau} h_i(\tau')h_j(\tau+\tau')\Phi_{f_o}d\tau'. \tag{IV.17}$$

Because $h_i(\tau')$ is zero for $\tau' \leq 0$, the lower limit of integration may be replaced by $-\infty$. Since we are interested in the stationary cross correlation of α_i and α_j, the upper limit of integration may be replaced by ∞,

$$R_{\alpha_i\alpha_j}(\tau) = 2\pi q_i q_j \int_{-\infty}^{\infty} h_i(\tau')h_j(\tau+\tau')\Phi_{f_o} d\tau'. \tag{IV.18}$$

Substituting equation (IV.18) into equation (IV.14) gives

$$\Phi_{\alpha_i\alpha_j}(\omega) = q_i q_j \Phi_{f_o} \int_{-\infty}^{\infty}\int_{-\infty}^{\infty} h_i(\tau')h_j(\tau+\tau')e^{-i\omega\tau} d\tau' d\tau. \tag{IV.19}$$

Multiplying the integrand by $e^{-i\omega\tau'} \cdot e^{i\omega\tau'}$ gives

$$\Phi_{\alpha_i\alpha_j}(\omega) = q_i q_j \Phi_{f_o} \int_{-\infty}^{\infty}\int_{-\infty}^{\infty} h_i(\tau')e^{i\omega\tau'} h_j(\tau+\tau')e^{-i\omega(\tau+\tau')} d\tau' d\tau. \tag{IV.20}$$

Integrating over τ and then over τ' gives

$$\Phi_{\alpha_i\alpha_j}(\omega) = q_i q_j \Phi_{f_o} H_i^*(\omega) H_j(\omega), \tag{IV.21}$$

where

$$H_j(\omega) = \int_{-\infty}^{\infty} h_j(t)e^{-i\omega\tau} dt, \tag{IV.22}$$

is the complex frequency response function for the jth mode. $H_i^*(\omega)$ is the complex conjugate of $H_i(\omega)$. Substituting equation (IV.5) into equation (IV.22) and carrying out the integration give

$$H_j(\omega) = \frac{1}{\omega_j^2 - \omega^2 + 2\hat{\imath}\omega_j\xi_j\omega}. \tag{IV.23}$$

Substituting equation (IV.21) into equation (IV.12) gives the power spectrum of the strain,

$$\Phi_{\epsilon\epsilon}(\omega) = \Phi_{f_o} \sum_{i=1}^{\infty}\sum_{j=1}^{\infty} a_i a_j q_i q_j H_i^*(\omega) H_j(\omega). \tag{IV.24}$$

In cases where ξ_i is sufficiently small for all i, the double sum in equation (IV.24) will be dominated by the terms in which $i = j$. In this case

$$\Phi_{\epsilon\epsilon}(\omega) \approx \Phi_{f_o} \sum_{i=1}^{\infty} a_i^2 q_i^2 |H_i(\omega)|^2, \tag{IV.25}$$

which is easily computed if the sum is truncated to a reasonable number of modes.

Section V. Simulation of the Random Time Series

Given the power spectral density obtained analytically for a multi-degree- of-freedom system as described in the previous section, or obtained experimentally, one can construct a time series that will have the desired power spectrum. The method is primarily due to Rice [1] and it was modified to be computationally efficient by Yang as discussed by Shinozuka [2]. If $\Phi_s^1(\omega)$ is the single sided power spectrum of the desired signal, $s(t)$, then $s(t)$ may be approximated by [1]

$$s(t) = \sqrt{2}\sum_{n=0}^{N-1}[\Phi_s^1(\omega_n)\Delta\omega]^{1/2} cos(\omega_n t - \phi_n), \tag{V.1}$$

where ϕ_n are uniformly distributed random numbers on the interval from 0 to 2π and

$$\omega_n = n\Delta\omega, \tag{V.2}$$

with

$$\Delta\omega = \omega_{max}/N, \tag{V.3}$$

where ω_{max} is the maximum frequency in the power spectrum $\Phi_s^1(\omega)$, and N is the total number of terms in the summation in equation (V.1).

Equation (V.1) simulates the time series as a distribution of sinusoidal signals having random phases. Unfortunately, this expression requires the computation of a large number of cosine functions at each desired value of the time, t. A considerable improvement in computational efficiency can be obtained by recasting equation (V.1) to allow the use of the Fast Fourier Transform. To accomplish this, note that equation (V.1) may be written as

$$s(t) = Re[\sqrt{2}\sum_{n=0}^{N-1}[\Phi_s^1(\omega_n)\Delta\omega]^{1/2} e^{i\omega_n t} e^{-i\phi_n}], \tag{V.4}$$

where $Re[\cdot]$ denotes the real part and $\hat{\imath}$ is $\sqrt{-1}$.

If the simulated time series, $s(t)$ is needed only at discrete values of time, t, then let

$$s_k = s(t_k) = s(k\Delta t), \tag{V.5}$$

where the time duration between the equally spaced sample times is Δt. Evaluating equation (V.4) at $t = t_k$ gives

$$s(k\Delta t) = Re[\sqrt{2}\sum_{n=0}^{N-1}[\Phi_s^1(\omega_n)\Delta\omega]^{1/2} e^{i\omega_n k\Delta t} e^{-i\phi_n}], \tag{V.6}$$

To satisfy the Nyquist sampling criterion, the time series, $s(t)$ must be sampled at a high enough rate to obtain two samples during one period of the highest frequency component in the original input power spectrum, $\Phi_s^1(\omega)$. This gives

$$\Delta t = \frac{2\pi}{\omega_{max}}\frac{1}{2}. \tag{V.7}$$

Substituting equations (V.3) and (V.7) into equation (V.6) gives

$$s(k\Delta t) = Re[\sqrt{2}\sum_{n=0}^{N-1}[\Phi_s^1(\omega_n)\Delta\omega]^{1/2}e^{-i\phi_n}e^{\frac{ink2\pi}{2N}}], \tag{V.8}$$

Equation (V.8) may be evaluated using a Fast Fourier Transform (FFT) algorithm by noting that given a discrete sequence, a_n, the FFT provides an efficient means of computing A_k, where

$$A_k = \sum_{n=0}^{N-1} a_n e^{-i2\pi kn/N}, \quad \text{for} \quad k = 0, 1, 2, \ldots, N-1. \tag{V.9}$$

Equation (V.8) may be evaluated using a FFT by defining a sequence,

$$\begin{aligned} a_n &= [\Phi_s^1(\omega_n)\Delta\omega]^{1/2}e^{-i\phi_n}, \quad \text{for} \quad n \leq N-1 \\ &= 0, \quad \text{for} \quad n \geq N. \end{aligned} \tag{V.10}$$

Equation (V.8) may then be written as

$$s_k = Re[\sqrt{2}\sum_{n=0}^{2N-1} a_n e^{\frac{ink2\pi}{2N}}], \quad \text{for} \quad k = 0, 1, 2, \ldots, 2N-1, \tag{V.11}$$

where $s_k = s(k\Delta t)$. Because we are taking the real part of the result of the summation, taking the complex conjugate of the right side of equation (V.11) gives

$$s_k = Re[\sqrt{2}\sum_{n=0}^{2N-1} a_n e^{-\frac{ink2\pi}{2N}}], \quad \text{for} \quad k = 0, 1, 2, \ldots, 2N-1. \tag{V.12}$$

This is equivalent to

$$s_k = \sqrt{2}Re[FFT(a_n)], \tag{V.13}$$

where $FFT[\cdot]$ denotes the Fast Fourier Transform. Note that the length of the sequence, a_n is $2N$.

V.1 References

[1] S. O. Rice 1954 Mathematical Analysis of Random Noise in *Selected Papers on Noise and Stochastic Processes.* (Edited by N. Wax) New York, NY: Dover.

[2] M. Shinozuka 1972 *Computers and Structures* **2**, 855–874. Monte carlo solution of structural dynamics.

Section VI. Comparison of Peak Counting and Rainflow Counting

In this section time domain signals having a variety of spectral characteristics are processed to compare the fatigue life predicted using simple peak counting and rainflow counting. The goal is to identify features of the power spectrum that result in significant differences between the two damage counting methods. The methods described in the previous sections permit the construction of random time series corresponding to systems having any given spectral properties. From the discussion of section V one can construct the power spectrum of a resonant system having any number of resonant modes with specified resonant frequencies and modal damping ratios. It is also possible to create a random time series from a power spectrum that is obtained experimentally.

Figures VI.1 through VI.6 show simulated time series and corresponding power spectra for systems modeled using the method of section V. These systems have nine resonant modes in the frequency range from 0 to 2000 Hertz. An attempt was made to create systems having spectral characteristics that mimic those seen in actual aerospace structures. The power spectra are shown in decibels by plotting $10Log_{10}$(power spectrum). Both the actual input power spectrum and the power spectrum computed from the simulated time series are shown. Since the two curves are indistinguishable, it can be seen that the simulation procedure reproduces the desired spectral properties. Figure VI.2 shows the power spectrum corresponding to the time signal in figure VI.1, figure VI.4 contains the spectrum for the signal in figure VI.3, and figure VI.6 shows the spectrum for figure VI.5. As the power spectrum plots show, the time series differ only in the relative contribution of the first resonant mode. The figures showing the time series contain only the first 10 % of the simulated signal.

The simulated time series were processed to estimate the fatigue life using peak counting and Rainflow counting. The ratio of the fatigue lives calculated by each method is shown on each plot. Between 4500 and 5000 damaging events were identified in each case shown. In these calculations the constant, c, in equation (III.1.1) will cancel when the ratio of the fatigue lives are compared. The exponent, b in equation (III.1.1) has been taken to be 6.

In figures VI.1 and VI.2 the first resonant mode has a relatively low amplitude. In this case the ratio of the fatigue lives computed using peak counting to Rainflow counting is .5910. In figures VI.3 and VI.4 the amplitude of the first mode is increased so that the time series shows a significant low frequency component. In this case the ratio of the estimated fatigue lives using the two methods is .1639. As the amplitude of the first mode is increased further as in figures VI.5 and VI.6, the ratio of the estimated fatigue lives reduces to .1333. The fatigue life predicted using Rainflow counting is then greater than that estimated by peak counting by roughly a factor of 7.5. When low frequency oscillations are present in the signal, peak counting significantly underestimates the fatigue life.

Figure VI.1 Power Spectral Density

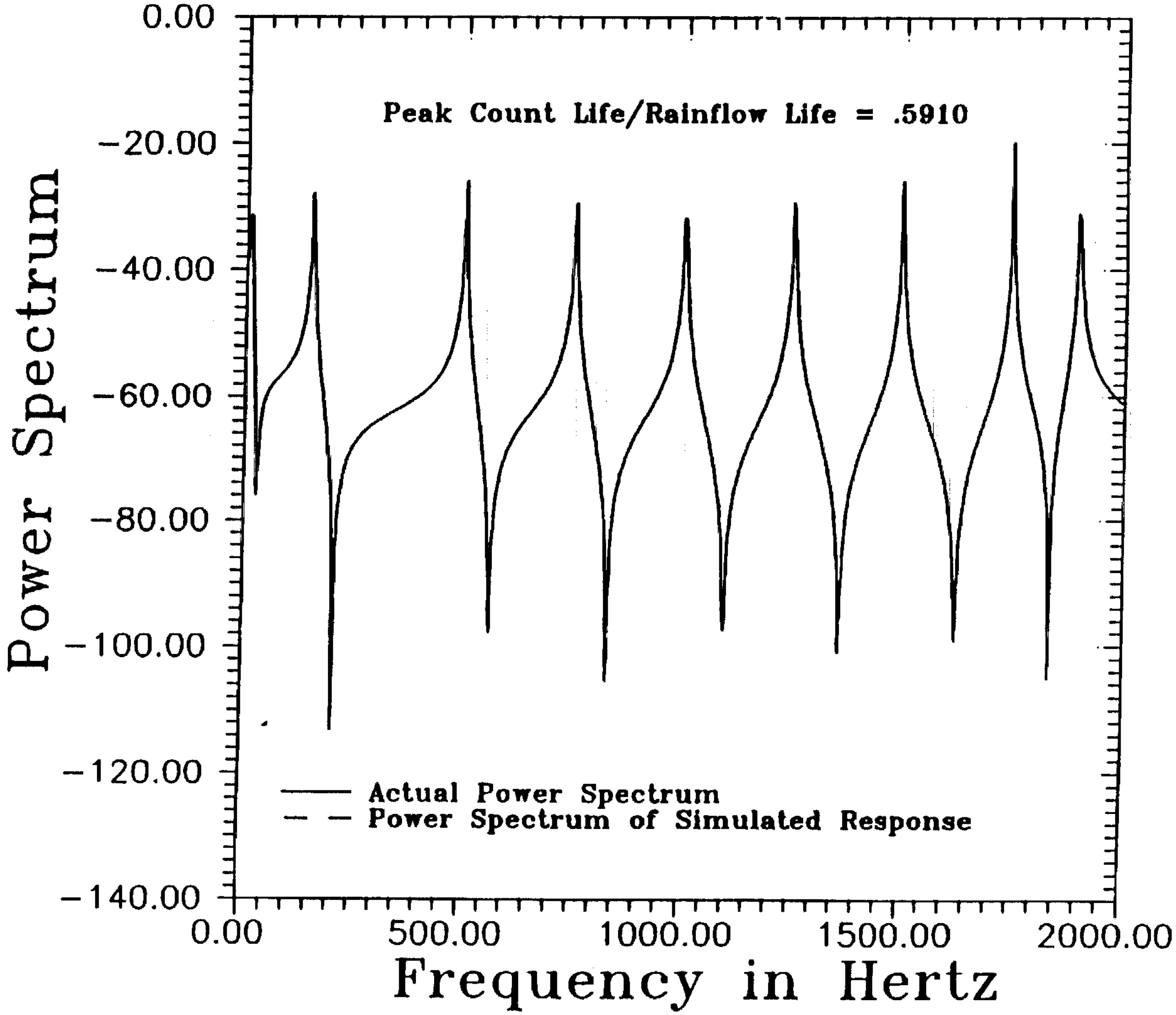

Figure VI.2 Simulated Time History

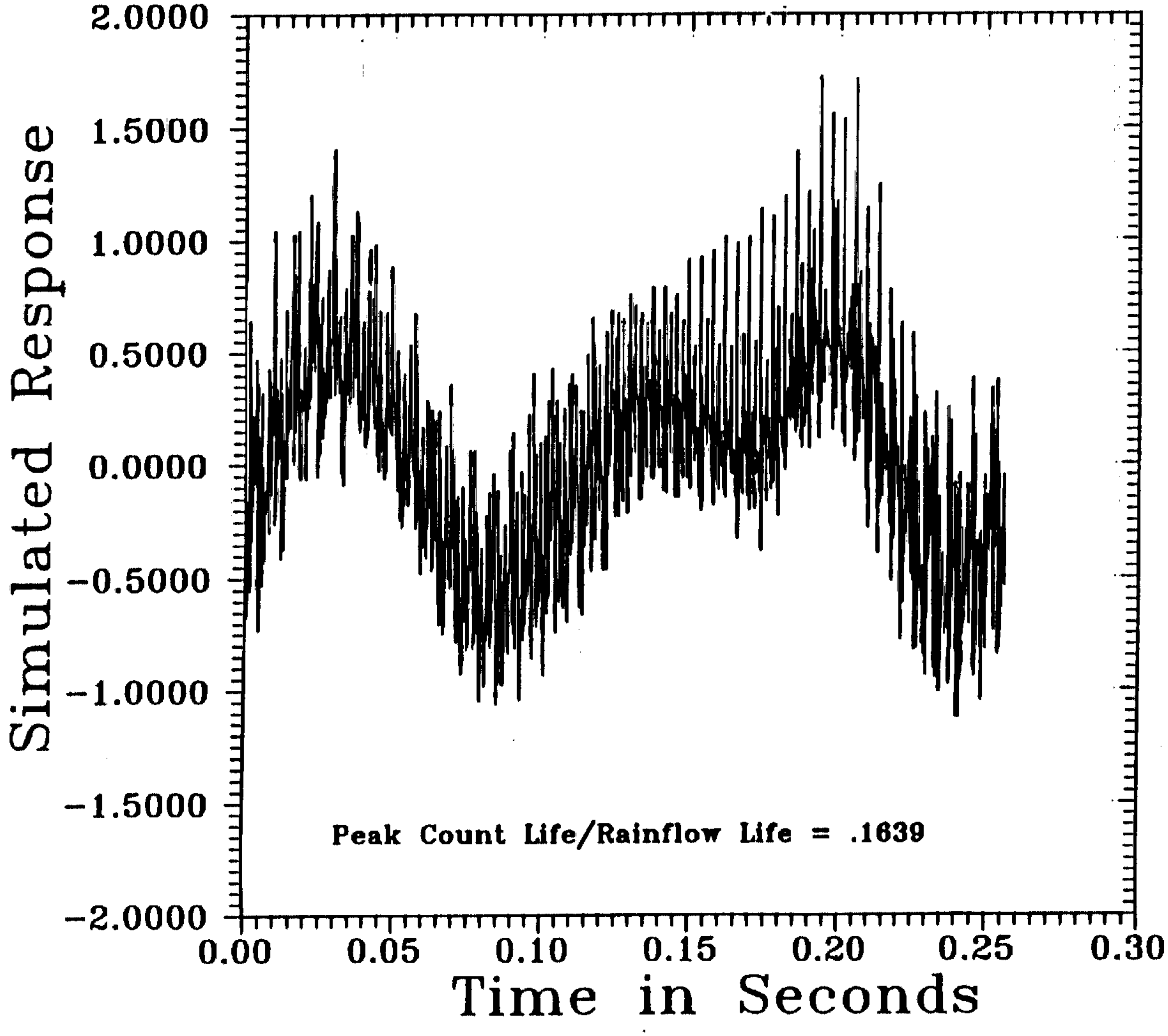

Figure VI.3 Power Spectral Density

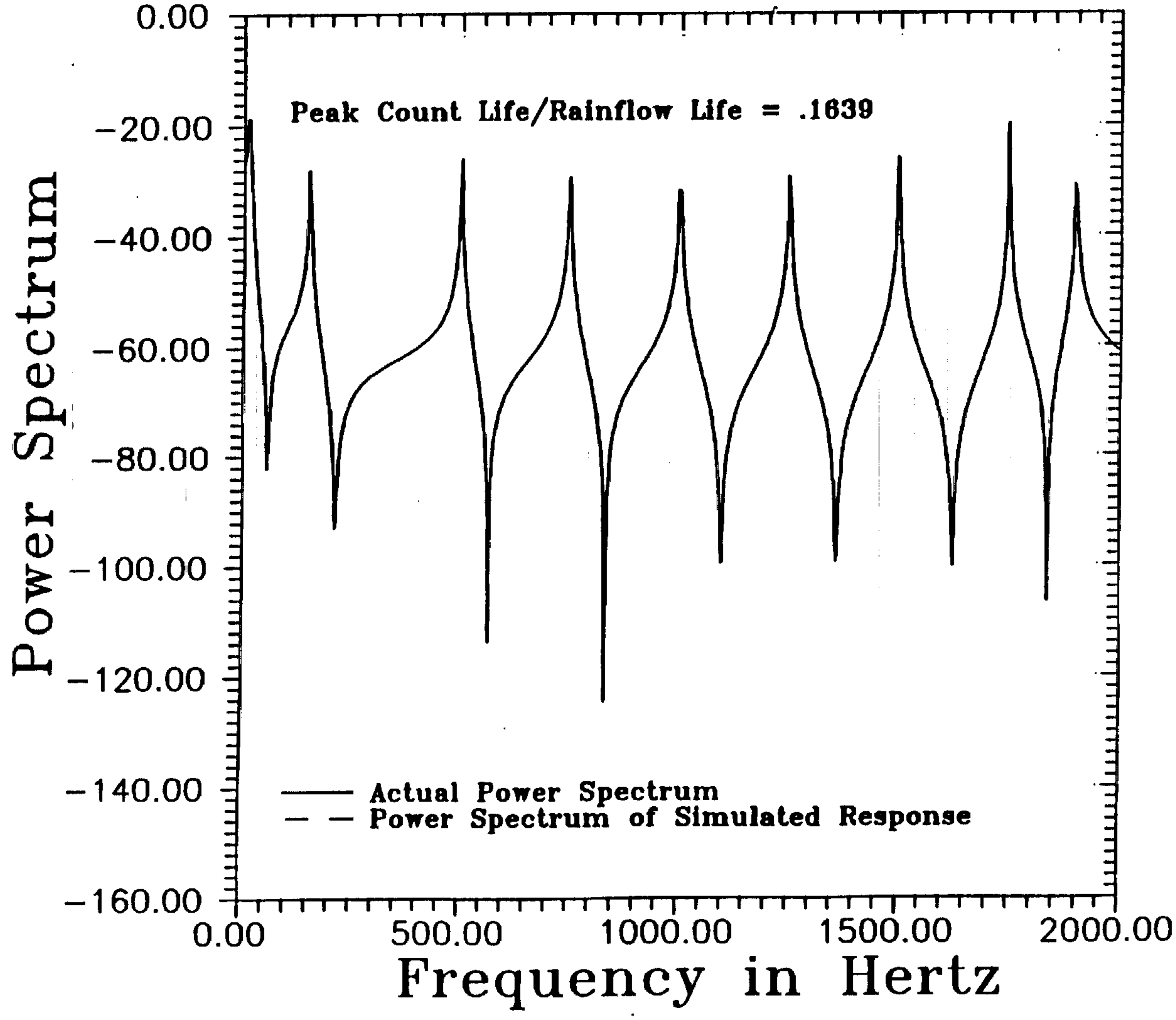

Figure VI.4 Simulated Time History

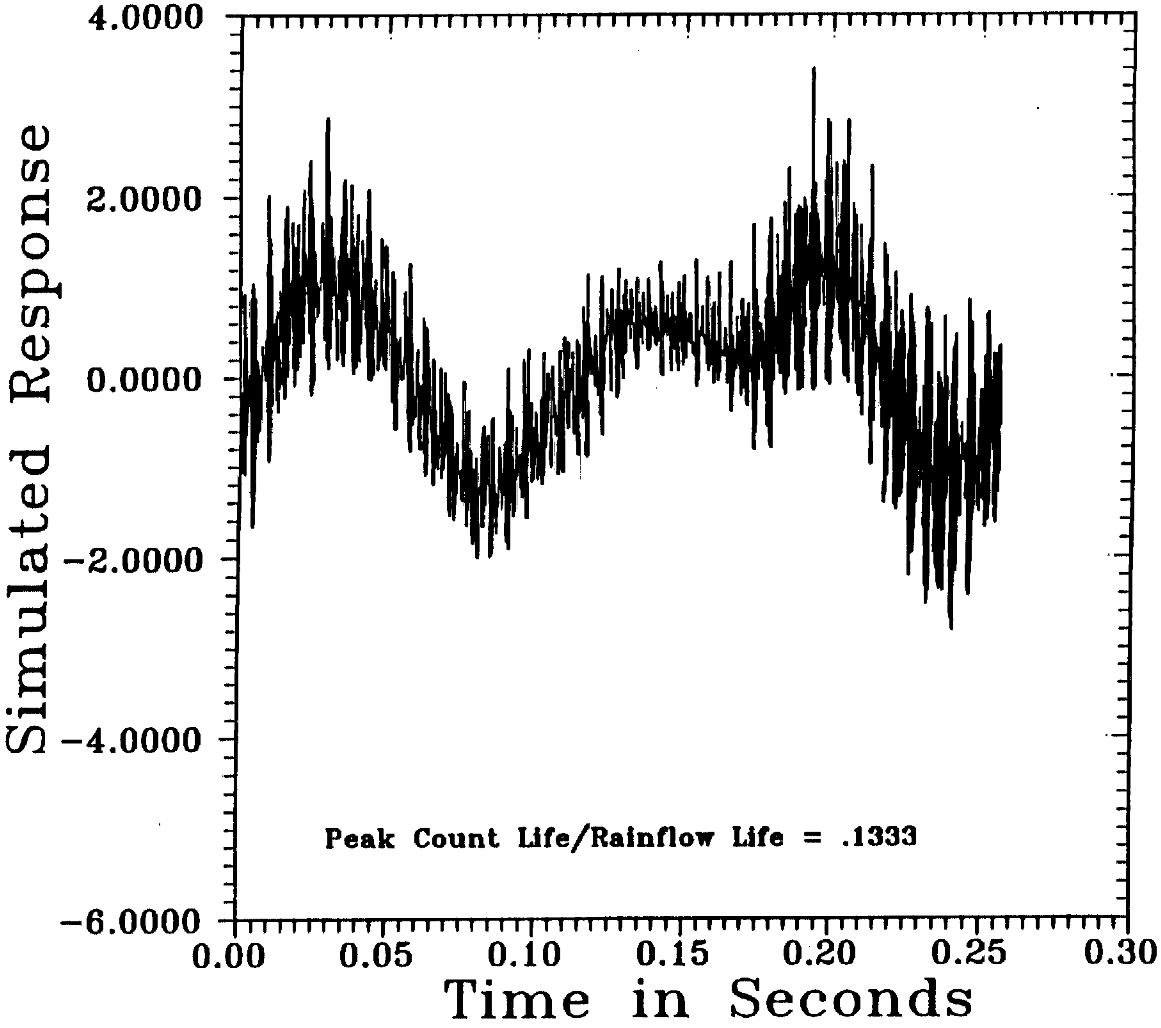

Figure VI.5 Power Spectral Density

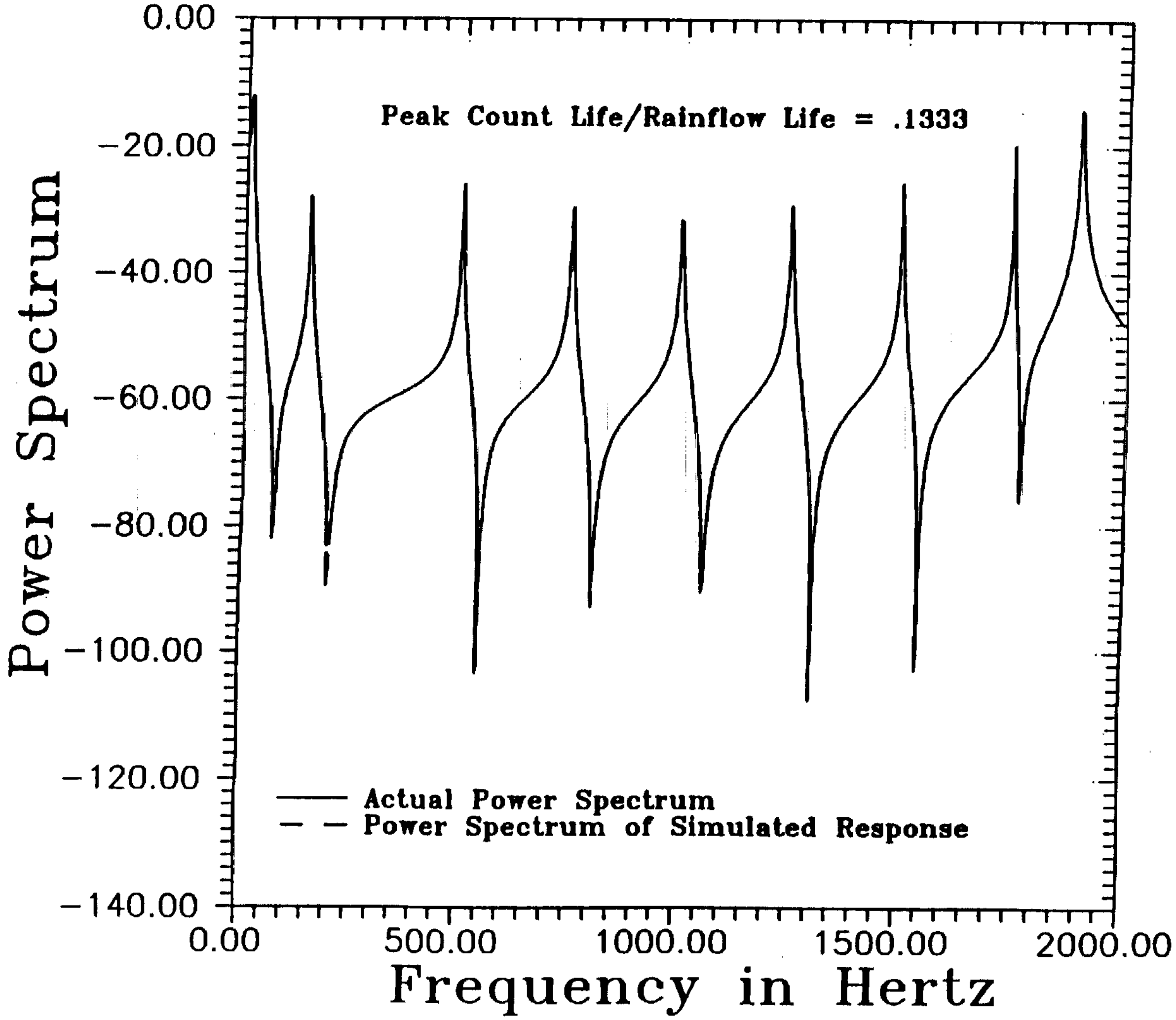

Figure VI.6 Simulated Time History

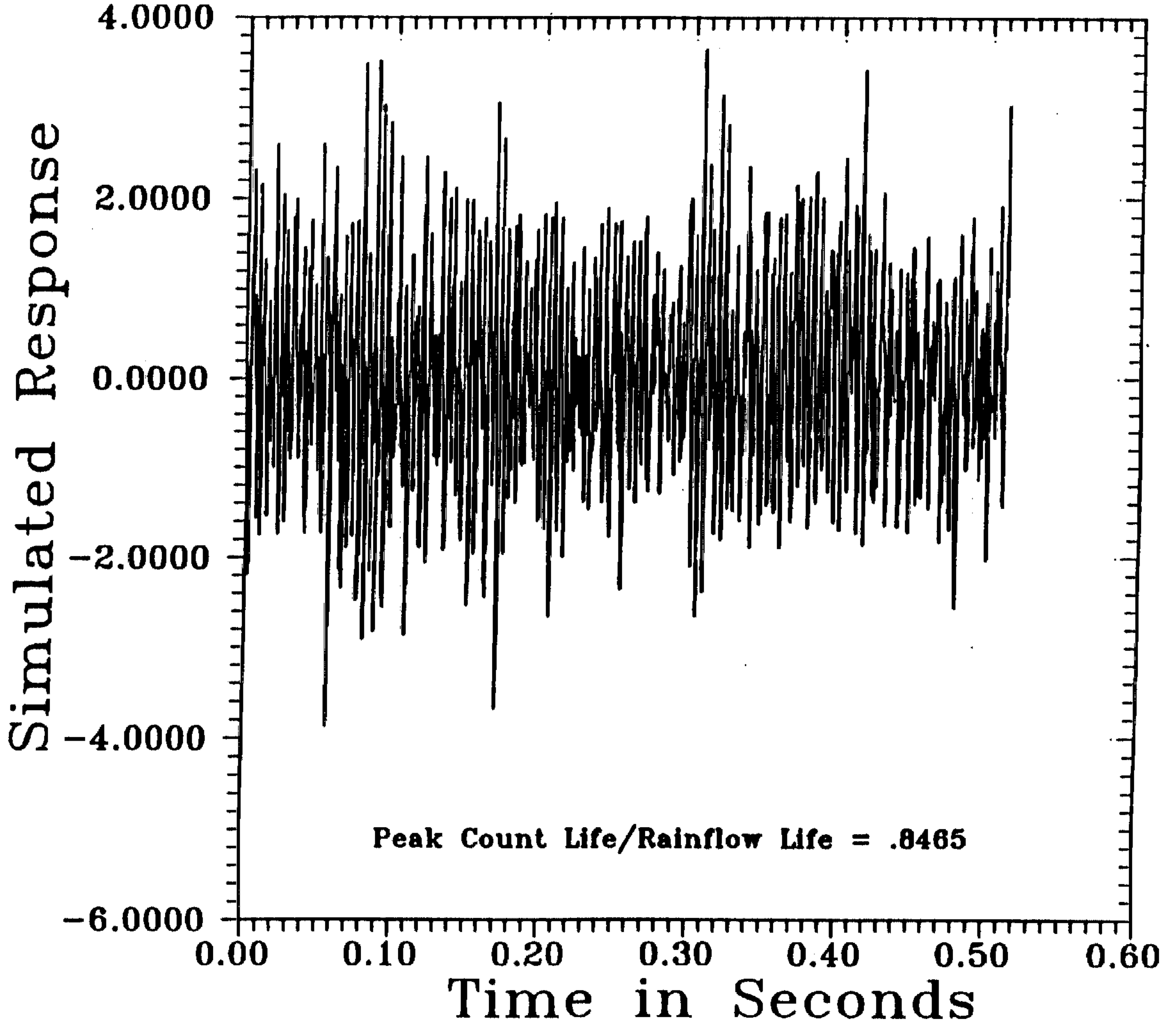

VII.1 Nonlinear Regression for Fatigue Parameter

Any fatigue prediction procedure requires certain empirically derived constants to characterize the structure's fatigue properties. In acoustic fatigue studies this data is usually obtained using a coupon test with narrowband random excitation. The S/N curve obtained from this test is then used to identify the fatigue constants. The application of this data to a broadband random load, as the structure is likely to experience in service, requires certain assumptions. The successful prediction requires that one is able to accurately account for the complex time histories encountered under broadband loading. The method of Rainflow counting as discussed in previous sections is intended to accomplish this.

Although Rainflow counting has been used successfully in accounting for complex loadings it seems more direct (and therefore more accurate) to acquire the fatigue constants using a load history that more closely resembles the service environment. A procedure that could identify the necessary constants when complex loadings are used could also be applied to determine fatigue properties from in-service failures. The goal of the present section is to develop a fatigue characterization method which can be applied with arbitrary loadings.

The fatigue characterization scheme examined in the present effort begins with sets of data consisting of the time to failure along with the corresponding stress or strain power spectral densities. This data could be obtained either in tests of complex structures or in tests of simple coupon samples. Suppose that the measured fatigue lives are T_j and the corresponding spectra are $\Phi_j(\omega)$. Using the methods of reference [3] one can construct a simulated random time history and perform cycle counting to obtain a histogram, P_{ij}, to describe the number of damaging events identified at each stress range, S_{ij}, for each power spectrum $\Phi_j(\omega)$. If the simulated time histories each have a duration τ, then the damage experienced by the structure should be

$$D_j = \tau / T_j. \tag{VII.1}$$

If there are M sets of fatigue lives and corresponding power spectra then the problem of estimating the fatigue coefficients, b and c, may be expressed as one of minimizing the total squared error,

$$e(b,c) = \sum_{j=1}^{M} \left(D_j - \sum_{i=1}^{N} \frac{S_{ij}^b}{c} P_{ij} \cdot \Delta S_i \right)^2 \tag{VII.2}$$

where, b and c are constants depending on the materials, and b typically varies from 1 to 6 while c from 10^{20} to 10^{30}.

The problem of identifying b and c to minimize the error in equation (VII.2) may be simplified by replacing c by a new unknown, v,

$$c = \frac{C_0}{v^b} \tag{VII.3}$$

where, C_0 is a suitable constant. The choice of C_0 will be discussed later.

Substituting equation (VII.3) into equation (VII.2) gives,

$$e(b,v)=\sum_{j=1}^{M}\left(D_j-\sum_{i=1}^{N}\frac{(v\cdot S_{ij})^b}{C_0}P_{ij}\cdot\Delta S_i\right)^2 \tag{VII.4}$$

or in general form,

$$e(x_1,x_2)=\sum_{j=1}^{M}\left(D_j-\sum_{i=1}^{N}\frac{(x_2\cdot S_{ij})^{x_1}}{C_0}P_{ij}\cdot\Delta S_i\right)^2 \tag{VII.5}$$

This is a modified mathematical model for identifying x_1 and x_2 (b and v) instead of b and c so that the property of the error function $e(b,c)$ can be improved.

To identify x_1 and x_2, a combined Newton-Powell method is used in this project because of the special property of the error function $e(x_1,x_2)$ (or $e(b,c)$) which will be discussed in the coming section of this report.

Given the nonlinear function $e(x_1,x_2)$, let

$$\mathbf{X}=(x_1,x_2)^T=\begin{pmatrix}x_1\\x_2\end{pmatrix}, \tag{VII.6}$$

The Newton method solves this problem by expanding $e(\mathbf{X})$ in a second order Taylor series about an estimate of the desired values of $(x_1,x_2)^T$, $\mathbf{X}^k=(x_1^k,x_2^k)^T$. This procedure will enable us to obtain an improved estimate $\mathbf{X}^{k+1}=(x_1^{k+1},x_2^{k+1})^T$. In matrix form,

$$e(\mathbf{X})=e(\mathbf{X}^k)+\nabla e^T(\mathbf{X}^k)\cdot(\mathbf{X}-\mathbf{X}^k)+\frac{1}{2}(\mathbf{X}-\mathbf{X}^k)^T\cdot\mathbf{A}(\mathbf{X}^k)\cdot(\mathbf{X}-\mathbf{X}^k) \tag{VII.7}$$

where, $e(\mathbf{X}^k)$ is the functional value of e at $\mathbf{X}^k$, and,

$$\nabla e(\mathbf{X}^k)=\left.\begin{pmatrix}\frac{\partial e(x_1,x_2)}{\partial x_1}\\ \frac{\partial e(x_1,x_2)}{\partial x_2}\end{pmatrix}\right|_{X=X^k}, \tag{VII.8}$$

$$\mathbf{A}(\mathbf{X}^k)=\left.\begin{pmatrix}\frac{\partial^2 e(x_1,x_2)}{\partial x_1^2} & \frac{\partial^2 e(x_1,x_2)}{\partial x_1\partial x_2}\\ \frac{\partial^2 e(x_1,x_2)}{\partial x_2\partial x_1} & \frac{\partial^2 e(x_1,x_2)}{\partial x_2^2}\end{pmatrix}\right|_{X=X^k} \tag{VII.9}$$

and,

$$\begin{aligned}\frac{\partial e(x_1,x_2)}{\partial x_1}=2\sum_{j=1}^{M}&\left(D_j-\sum_{i=1}^{N}\frac{(x_2\cdot S_{ij})^{x_1}}{C_0}P_{ij}\cdot\Delta S_i\right)\\ &\cdot\left(-\sum_{i=1}^{N}\frac{ln(x_2\cdot S_{ij})\cdot(x_2\cdot S_{ij})^{x_1}}{C_0}P_{ij}\cdot\Delta S_i\right)\end{aligned}, \tag{VII.11}$$

$$\frac{\partial e(x_1,x_2)}{\partial x_2} = 2\sum_{j=1}^{M}\left(D_j - \sum_{i=1}^{N}\frac{(x_2\cdot S_{ij})^{x_1}}{C_0}P_{ij}\cdot\triangle S_i\right) \cdot\left(-\sum_{i=1}^{N}\frac{(x_1\cdot S_{ij})\cdot(x_2\cdot S_{ij})^{x_1-1}}{C_0}P_{ij}\cdot\triangle S_i\right), \tag{VII.12}$$

$$\begin{aligned}\frac{\partial^2 e(x_1,x_2)}{\partial x_1^2} = 2\sum_{j=1}^{M}\Bigg[&\left(D_j - \sum_{i=1}^{N}\frac{(x_2\cdot S_{ij})^{x_1}}{C_0}P_{ij}\cdot\triangle S_i\right)\\ &\cdot\left(-\sum_{i=1}^{N}\frac{[ln(x_2\cdot S_{ij})]^2\cdot(x_2\cdot S_{ij})^{x_1}}{C_0}P_{ij}\cdot\triangle S_i\right)\\ &+\left(-\sum_{i=1}^{N}\frac{ln(x_2\cdot S_{ij})\cdot(x_2\cdot S_{ij})^{x_1}}{C_0}P_{ij}\cdot\triangle S_i\right)^2\Bigg],\end{aligned} \tag{VII.13}$$

$$\begin{aligned}\frac{\partial^2 e(x_1,x_2)}{\partial x_1\partial x_2} = 2\sum_{j=1}^{M}\Bigg[&\left(-\sum_{i=1}^{N}\frac{(x_1\cdot S_{ij})\cdot(x_2\cdot S_{ij})^{x_1-1}}{C_0}P_{ij}\cdot\triangle S_i\right)\\ &\cdot\left(-\sum_{i=1}^{N}\frac{ln(x_2\cdot S_{ij})\cdot(x_2\cdot S_{ij})^{x_1}}{C_0}P_{ij}\cdot\triangle S_i\right)\\ &+\left(D_j - \sum_{i=1}^{N}\frac{(x_2\cdot S_{ij})^{x_1}}{C_0}P_{ij}\cdot\triangle S_i\right)\\ &\cdot\left(-\sum_{i=1}^{N}\frac{[S_{ij}+x_1\cdot ln(x_2\cdot S_{ij})]\cdot(x_2\cdot S_{ij})^{x_1-1}}{C_0}P_{ij}\cdot\triangle S_i\right)\Bigg]\\ = \frac{\partial^2 e(x_1,x_2)}{\partial x_2\partial x_1}&\end{aligned} \tag{VII.14}$$

and,

$$\begin{aligned}\frac{\partial^2 e(x_1,x_2)}{\partial x_2^2} = 2\sum_{j=1}^{M}\Bigg[&\left(D_j - \sum_{i=1}^{N}\frac{(x_2\cdot S_{ij})^{x_1}}{C_0}P_{ij}\cdot\triangle S_i\right)\\ &\cdot\left(-\sum_{i=1}^{N}\frac{[x_1\cdot(x_1-1)\cdot S_{ij}^2]\cdot(x_2\cdot S_{ij})^{x_1-2}}{C_0}P_{ij}\cdot\triangle S_i\right)\\ &+\left(-\sum_{i=1}^{N}\frac{(x_1\cdot S_{ij})\cdot(x_2\cdot S_{ij})^{x_1-1}}{C_0}P_{ij}\cdot\triangle S_i\right)^2\Bigg]\end{aligned} \tag{VII.15}$$

To find the minimum point, let

$$\nabla e(\mathbf{X}) = \mathbf{A}(\mathbf{X}^k)\cdot(\mathbf{X}-\mathbf{X}^k)+\nabla e(\mathbf{X}^k) = 0, \tag{VII.16}$$

Solving equation (VII.16) for $\mathbf{X}$ leads to an iterative procedure to determine the next estimate $\mathbf{X}^{k+1}$,

$$\mathbf{X} = \mathbf{X}^{k+1} = \mathbf{X}^k - \mathbf{A}(\mathbf{X}^k)^{-1} \cdot \nabla e(\mathbf{X}^k), \tag{VII.17}$$

where, $\mathbf{A}(\mathbf{X}^k)^{-1}$ indicates the inverse of matrix $\mathbf{A}(\mathbf{X}^k)$. It is assumed that $\mathbf{A}(\mathbf{X}^k)$ is a positive definite matrix and its inverse exists.

As it will be discussed in the coming section, for the error function given in equation (VII.5), the matrix $\mathbf{A}(\mathbf{X}^k)$ will become singular when $\mathbf{X}^k$ is near the minimum point of $e(\mathbf{X})$. This suggests that, although the Newton method does an excellent job when $\mathbf{X}^k$ is far away from the minimum point for this problem, it will fail when $\mathbf{X}^k$ is near the optimum approximation of b and c. To obtain the optimum estimate of b and c, we use the Powell method [4] to find the optimum values of b and c when the Newton method begins to fail to do so.

Here is how Powell method goes:

Initialize the set of directions $\mathbf{S}^i$ to the base vectors,

$$\mathbf{S}^1 = (1,0,0,...,0)^T, \qquad \mathbf{S}^2 = (0,1,0,...,0)^T, \quad ..., \quad \mathbf{S}^N = (0,0,0,...,1)^T$$

Now repeat the following sequence of steps ("basic procedure") until the function stops decreasing:

- Save the initial estimation of $\mathbf{X}$ as $\mathbf{X}^0$.
- For $i = 1,...,N$, move $\mathbf{X}^{i-1}$ to the minimum along direction $\mathbf{S}^i$ and call this point $\mathbf{X}^i$.
- For $i = 1,...,N-1$, set $\mathbf{S}^i \leftarrow \mathbf{S}^{i+1}$.
- Set $\mathbf{S}^N \leftarrow \mathbf{X}^N - \mathbf{X}^0$.
- Move $\mathbf{X}^N$ to the minimum along direction $\mathbf{S}^N$ and call this point $\mathbf{X}^0$.

In addition, some modifications have been added to the basic procedure to ensure a reasonable rate of convergence.

VII.2 Identifiability of Parameters b and c

As mentioned in the previous section, the error function $e(b,c)$ possesses some special properties. This affects the identifiability of parameters b and c. First, we can make a simple observation. When carrying out a fatigue test, we excite a structure by using a random loading with a specified stress power spectrum, such as what was done in Clevenson's [5] and Ramesh's [6] fatigue tests in which each specimen was loaded at a constant root-mean-square stress level with a given shape of stress spectrum (as shown in figures (VII.1) through (VII.9)) until rupture occurred. In order to estimate the fatigue parameters b and c using the method developed in this project, the data of the root-mean-square stress and the stress spectral shape are used to construct the stress spectrum under this certain test condition. We will assume that a set of fatigue lives, $T_j, j = 1,2,...,M$, have been measured and that the corresponding stress power spectra, $S_j(\omega), j = 1,2,...,M$, are known. The methods of reference [3] are used to construct a simulated random time history during a record of duration τ (as shown in figures (VII.10) through (VII.18)) for each fatigue test. Rainflow cycle counting is then used to obtain a histogram of the levels of damaging cycles, P_{ij} (as shown in figures (VII.19) through (VII.27)), where the index i corresponds to the damage level and j indicates the test specimen number. The value of $P_{ij} \cdot \Delta S_i$, as in equation (VII.2)), describes the number of damaging events identified at each stress range S_{ij} during a record of duration τ. Therefore, b and c should be constants such that,

$$D_j = \frac{\tau}{T_j} = \sum_{i=1}^{N} \frac{S_{ij}^b}{c} P_{ij} \cdot \Delta S_i \qquad j = 1, 2, ..., M. \qquad \text{(VII.18)}$$

Since the fatigue characteristics of a given material are assumed to be described by the two constants, b and c, it is hoped that for any given set of test data, a unique pair of values of b and c may be determined. Unfortunately, due to the nature of fatigue measurements, an error in the determination of b can be partially off-set by adjusting c. This problem comes about when b and c are to be identified in tests conducted with simple deterministic load histories as well as in the more complicated situation considered here.

First consider the case where the load history consists of a pure tone so that the number of damaging cycles is easily determined. A typical S/N curve for sinusoidal loading [5] is shown in figure (VII.28).

Figure (VII.29) shows estimated fatigue curves having significantly different values of b and c. The values of b and c for each curve are shown in the figure. It is found that if one parameter, either b or c, is chosen incorrectly, then the other parameter may be adjusted to compensate for much of the error. Figure (VII.29) shows that values of c varying over two orders of magnitude can give reasonable results as long as b is adjusted accordingly.

A similar affect to that seen in figure (VII.29) is also observed in the more general loading case considered here. To illustrate the 'near' dependence of b and c in this case, consider the problem of finding b and c when there is only one set of measured fatigue test data. In this case equation (VII.2) becomes,

$$e(b,c) = \left(D_j - \sum_{i=1}^{N} \frac{S_{ij}^b}{c} P_{ij} \cdot \Delta S_i \right)^2, \qquad j = 1. \qquad \text{(VII.19)}$$

Figure (VII.30) shows the error, $e(b,c)$, as computed using equation(VII.19) for a range of values of b and c. The figure shows that for each value of b, a value of c may be found to cause the error to be zero. One can then use equation (VII.19) to construct a relationship between b and c which gives $e(b,c) = 0$, as shown in figure (VII.31). This relation between b and c may be obtained for each fatigue test specimen if a series of tests are conducted. Figure (VII.32) shows the relationships between b and c which give zero error for 4 different tests [5] having spectra identified as A, B, C and D. It would be ideal if all of the lines intersected at a particular combination of b and c. The figure shows that the lines indicating a relationship between b and c corresponding to the different fatigue tests are almost parallel. There is thus no ideal combination of b and c for this data. This results in the error function $e(b,c)$ being illconditioned.

Another way to illustrate the near dependence of b and c in typical test data is to plot the error as a function of b and c as in figure (VII.33). The minimum of $e(b,c)$ is seen to consist of a curve rather than a point. It is obvious that there exists a narrow region in which the value of error function is almost kept unchanged. The minimum values of the error function with respect to b and c are shown in figure (VII.34) and figure (VII.35), respectively, in which it can be found that the minimum value of $e(b,c)$ just changes very slightly while b varies from 3.5 to 5.5 and c from 10^{19} to 10^{28}. This results in the failure of Newton Method for this problem when the iteration point approaches this narrow region because where the matrix $\mathbf{A}(\mathbf{X}^k)$ will become near singular. This also suggests that a range of values of b and c will give almost equally good estimates to the data.

There are many situation where we can find some general empirical relationship between fatigue constants [7]. When the S/N curves for some steel alloys are plotted in nondimensional form using the endurance limit, S_e, and the ultimate strength, S_u, they tend to follow the same curve shown in figure (VII.36). A power relationship is recommended to be used to estimate the S/N curve for steel:

$$S = 10^C \cdot N^b (\text{for } 10^3 < N < 10^6) \tag{VII.20}$$

where the exponents, C and b, of the S/N curve are determined using the two defined point shown in figure (VII.37):

$$b = \frac{-1}{3} log_{10} \frac{S_{1000}}{S_e}, \qquad C = log_{10} \frac{(S_{1000})^2}{S_e} \tag{VII.21}$$

where, alternating stress level corresponding to a life of 1000 cycles, S_{1000}, can be determined as 0.9 times the ultimate strength, and when the estimate for S_e is made as $S_e = 0.5 S_u$, the S/N curve is defined as

$$S = 1.62 S_u N^{-0.085} \tag{VII.22}$$

This suggests that for certain kinds of steel, the S/N curve can be approximately defined as only depending on the ultimate strength S_u, which also suggests that fatigue constants are not strongly independent. This results in the ill-conditioning of the error function.

In order to overcome the ill-conditioning, it is necessary to make a dimensional transformation of variables. When using equation (VII.2) as the mathematical model for this problem, the contours of the error function (with b and c as two parameters) near the minimum point are often curved as in figure (VII.38) (b and c are both in linear scale because they behave like this when we estimate the parameters using Newton Method or Powell Method) . Here the projection of the contour has substantial length. After a nonlinear dimensional transformation

$$c = \frac{C_0}{v^b} \tag{VII.3}$$

is made as in Section VII.1, the contours of $e(b,v)$ near the minimum point of the error function are as shown in figure (VII.39). This makes the estimation of b and c much more stable than that before the transformation. It has been found that a suitable value of the constant, C_0, is $C_0 = 2\text{x}10^{22}$ in this case.

VII.3 Application to Existing Fatigue Data and Discussion

In order to show the advantage of the method developed in this project, it has been applied to some existing measured fatigue data published in both references [5] and [6], in which some statistical properties of the random loading are used to estimate the fatigue constants and to predict the fatigue lives of the structures studied.

Fatigue tests of aluminum-alloy specimens under stationary and Gaussian random loadings having a zero mean value were conducted in reference [5]. The random loadings were described by power spectral densities of the form $\Phi(\omega) = K_1\omega^{-2}, K_2\omega^0, K_3\omega^2$ in a certain frequency range, where K is an arbitrary constant (typical stress spectra are spectrum A, B, C, and D as shown in figure (VII.1) through (VII.4)) and the fatigue lives were determined for statistical parameters of the random loadings such as root-mean-square nominal applied stress, power spectral shape, mean number of zero crossings per unit time, and mean number of peak loads per unit time, etc. The corresponding fatigue data are listed in table (VII.1), which shows root-mean-square nominal applied stress, S_{rms}, in *psi*, fatigue lives , t_f, in seconds, α, the ratio of zero crossing rate to peak rate as defined later in equation (VII.27), and the corresponding stress spectrum used in the test.

The measured data in reference [6] were obtained by fatigue tests of a number of structural steel specimens. Five typical power spectral shapes were selected to generate various random loading wave forms and the idealized shapes are spectrum A, B, C, D, and E as shown in figures (VII.5) through (VII.9) by setting the filters in different ways. Fatigue tests were conducted under different power spectral shapes, measured on the basis of central frequencies, positive zero crossing frequencies, and frequencies of maxima. Table (VII.2) shows the corresponding fatigue data which gives power spectral shapes used, root-mean-square applied stress, S_{rms}, the fatigue lives, t_f, and the value of α.

To apply the method developed in this study, time histories for each power spectrum mentioned above are generated (as shown in figures (VII.10) through (VII.18)) and a Rainflow counting scheme is used to calculate the damage accumulation in each case investigated. Some typical plots of damaging densities of the stress ranges identified by Rainflow counting are shown in figures (VII.19) through (VII.27).

The simulated damage probability densities and corresponding measured fatigue lives may be processed as described in equations (VII.1) through (VII.5). By applying the scheme discussed in the previous section to some of the measured fatigue data in both references [5] and [6], fatigue constants b and c are identified and then used to estimate the fatigue lives for all other test specimens. Figures (VII.40) and (VII.41) indicate the predicted fatigue lives using the identified fatigue constants, which show that, with this method, the identification of fatigue constants and the prediction for fatigue lives based upon the Rainflow counting technique can be made with reasonable precision.

Some comparison are also made to show the efficiency of this method:

First, the effect of power spectral band width is considered. Let α be the ratio of zero crossing rate to peak rate. This may be computed if the power spectrum, $\Phi(\omega)$, is known,

$$\alpha = \frac{\int_{-\infty}^{\infty} \omega^2 \Phi(\omega) d\omega}{\left(\int_{\infty}^{\infty} \omega \Phi(\omega) d\omega \right)^{\frac{1}{2}} \left(\int_{\infty}^{\infty} \omega^4 \Phi(\omega) d\omega \right)^{\frac{1}{2}}}. \qquad \text{(VII.27)}$$

The α values for tests conducted in both references [5] and [6] vary from 0.586 to 0.992, as shown in tables (VII.1) and (VII.2). This indicates that the data corresponds to broadband and narrowband random loadings. A power spectrum with α=0.586 is considered to be a broadband random loading and when $\alpha = 1$, the loading is narrowband. The difference between narrowband and broadband spectra can be seen from typical time histories shown in figures (VII.12) and (VII.14), which have α values of 0.695 and 0.992, respectively, and the corresponding spectra are shown in figure (VII.42), where both spectra have the same unit root-mean-square stress value.

The application of the regression method to each power spectrum used in the tests is investigated. From table (VII.1), 32 sets of fatigue data are shown which are taken from reference [5]. The tests were conducted using four different spectrum shapes identified as A, B, C, and D. For spectrum shapes A, B, C, and D there are twelve, four, ten, and six measured fatigue lives, respectively.

Figures (VII.43) through (VII.46) show the different cases of fatigue life prediction. In each of these figures, data from one of the four spectrum shapes was used to identify b and c. The data used to perform the regression are shown as circles. In each figure, predictions of the fatigue lives for the data of the remaining three spectrum shapes are shown as squares. Figure (VII.43) shows twelve circles, representing a comparison of twelve predicted and measured fatigue lives obtained under spectrum A. These twelve circles indicate the fatigue test data used to identify b and c while the squares indicate predicted fatigue lives based on these constants for the rest of the fatigue data listed in table (VII.1). Figures (VII.44), (VII.45) and (VII.46) show predicted lives in the same way as in figure (VII.43), in which fatigue constants are identified from fatigue data obtained under the random loadings with spectra B, C, and D as shown in figures (VII.2), (VII.3), and (VII.4), respectively.

We can also find the similarity in predicting fatigue lives using identified fatigue constants from figures (VII.47) through (VII.51) in which, for fatigue tests conducted in reference [6], fatigue constants b and c are identified from those fatigue test data under random loadings with five different stress spectrum shapes A, B, C, D, and E, respectively. It can be found from figures (VII.43) through (VII.51) that, with this method, the prediction for fatigue lives under the random loading with certain power spectrum can be made almost equally well by using fatigue constants b and c estimated from fatigue tests under the loading with very different power spectral shapes even under narrow band random loading. Figures (VII.43) and (VII.47) show the extreme cases in which fatigue lives are predicted using fatigue constants identified from the test data measured under narrow band random loadings with α values of 0.92 and 0.99, respectively. It means if the fatigue constants b and c are determined using narrowband test data, the prediction can also work well for fatigue lives under broadband random loading.

Secondly, since Rainflow counting considers the effect of each stress level, it seems to be possible to identify fatigue constants b and c by using only one or a few more sets of fatigue test data instead of large amount of fatigue tests. Figures (VII.52) through (VII.60) show the predicted fatigue lives by using only one set of fatigue test data chosen for each type of spectrum. The results show very good agreement. It is expected that, on the consideration of economy and for the easy implementation of the fatigue test, one can conduct a fatigue test using only one spectrum shape which is specially designed so that damaging events occurs more evenly at each stress level.

The practical advantage of using Rainflow cycle counting to calculate the damage accumulation in predicting fatigue life can be pointed out here. By using the Rainflow counting technique, one can consider the effect of each stress level on fatigue life in both identification of fatigue constants and prediction of fatigue lives even if only one set of test data is available. Figure (VII.5) indicates a narrow band spectrum shape corresponding to a time history as shown in figure (VII.14) which can be found to be a typical narrow band random time history. But, from figure (VII.23), we can find that it includes as much information about damage events at each stress level as that in the broad band case. This is one reason that we can get almost equally good predictions of fatigue life by using fatigue constants estimated from fatigue tests under random loadings with very different power spectral shapes.

VII.4 Conclusions

The common method of applying narrowband random S/N data is to simply consider the structure under study to also respond in a narrowband, random fashion. In practice, however, a structure is expected to encounter a more complicated broadband random excitation. A primary goal of this effort has been to develop a method of identifying the fatigue constants when a realistic broadband random load is applied. It was felt that this would lead to more accurate predictions. We have found that when Rainflow counting is used to identify damaging events and when the fatigue prediction is performed using the methods outlined above, one can make reasonably accurate predictions of broadband fatigue life using narrowband fatigue data.

Because the success of the present method depends strongly on the accurate identification of damaging events in a complex time history, one can conclude that Rainflow counting can be used reliably. The regression procedure we have described can be useful in situations where narrowband fatigue data is not available such as when fatigue constants are to be determined from in-service data.

References

[1] J. W. Miles 1954 *Journal of the Aeronautical Sciences* **21**, 753-762. On structural fatigue under random loading.

[2] N. E. Dowling 1972 *Journal of Materials* **7**, 71-87. Fatigue failure predictions for complicated stress-strain histories.

[3] R. N. Miles 1991 *Journal of Sound and Vibration* , Effect of spectral shape on acoustic fatigue life estimates.

[4] L. Cooper and D. Steinberg 1970, Introduction to Methods of Optimization, W. B. Saunders Co.

[5] S. A. Clevenson and R. Steiner 1967 NASA TR R-266, Fatigue life under random loading for several power spectral shapes.

[6] T. Ramesh 1973 *Engineering Fracture Mechanics* **5**, 993-1007. On Fatigue Life under Stationary Gaussian Random Loads.

[7] J. A. Bannantine, J. J. Comer and J. L. Handrock 1990, Fundamentals of Metal Fatigue Analysis, Prentice-Hall Inc.

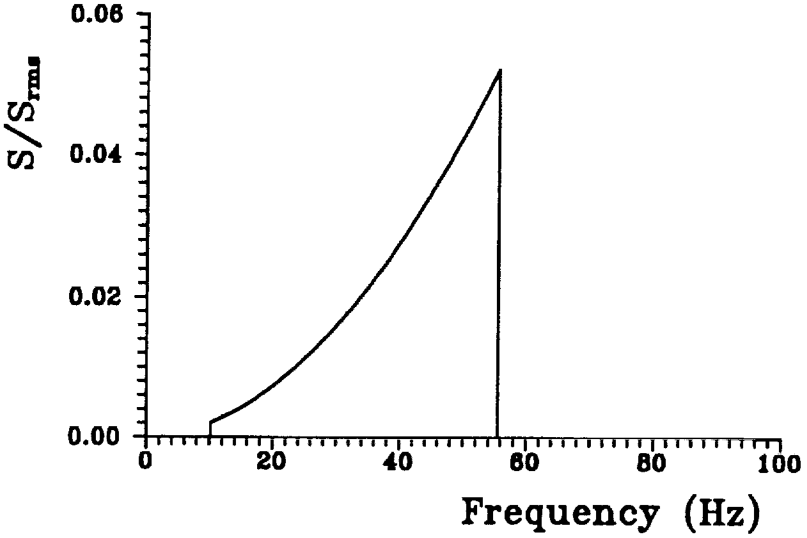

Figure VII.1 Power Spectrum A [5]

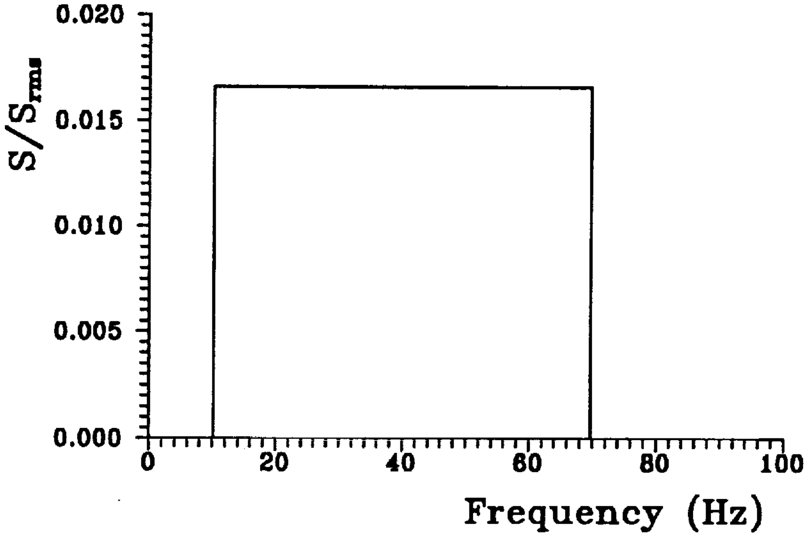

Figure VII.2 Power Spectrum B [5]

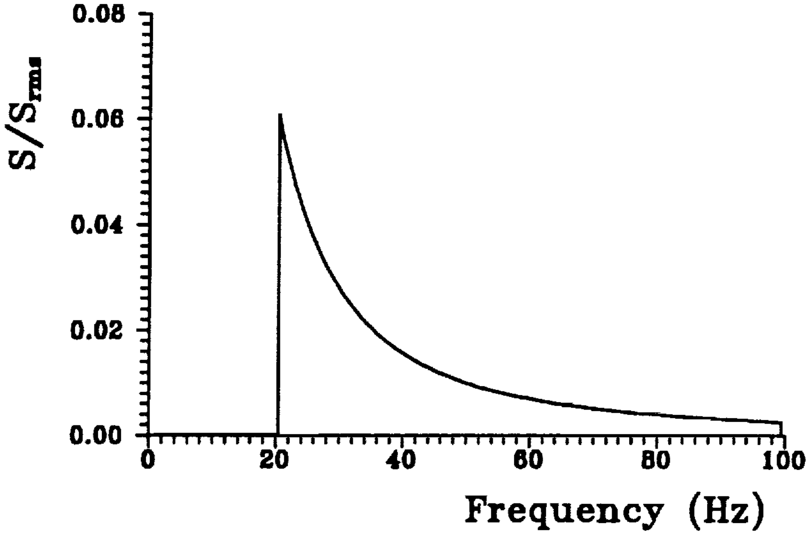

Figure VII.3 Power Spectrum C [5]

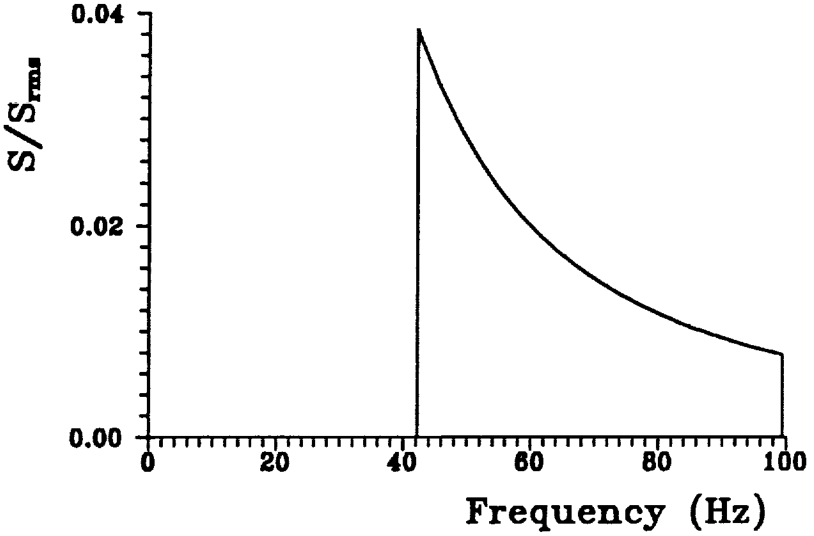

Figure VII.4 Power Spectrum D [5]

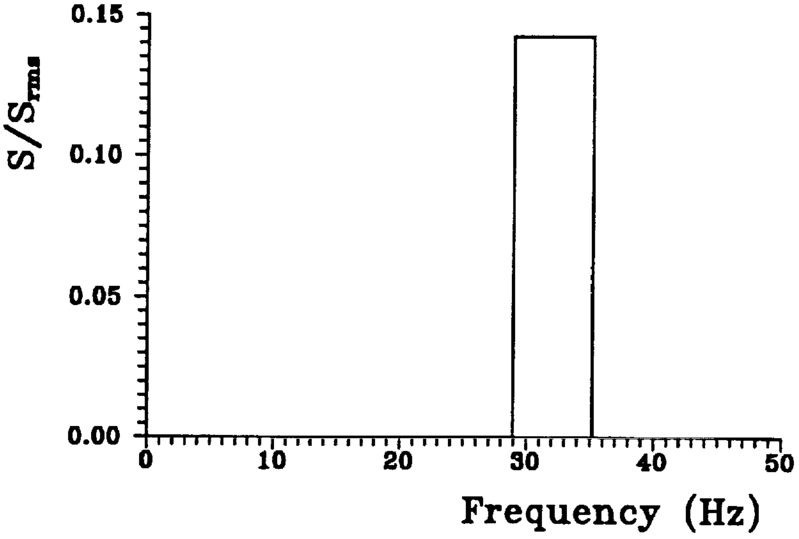

Figure VII.5 Power Spectrum A [6]

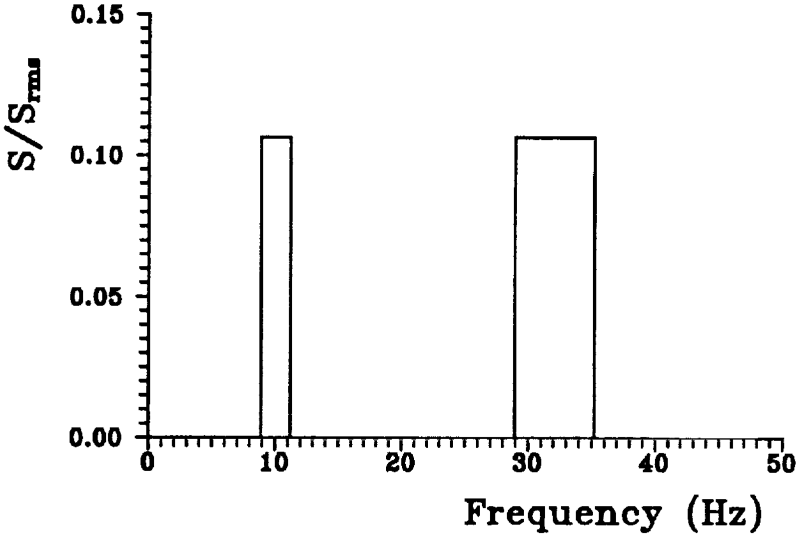

Figure VII.6 Power Spectrum B [6]

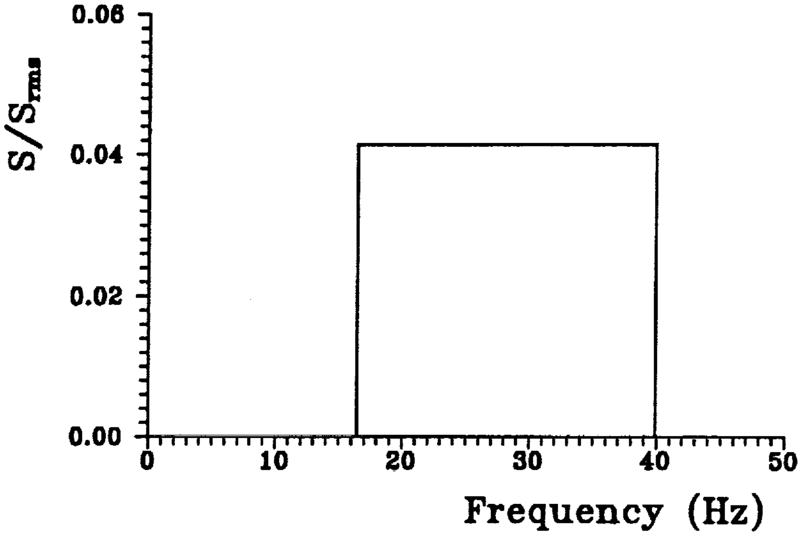

Figure VII.7 Power Spectrum C [6]

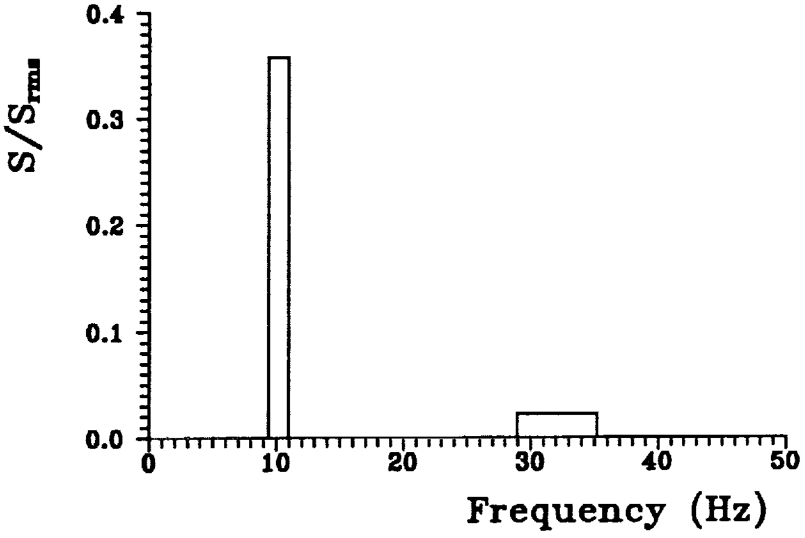

Figure VII.8 Power Spectrum D [6]

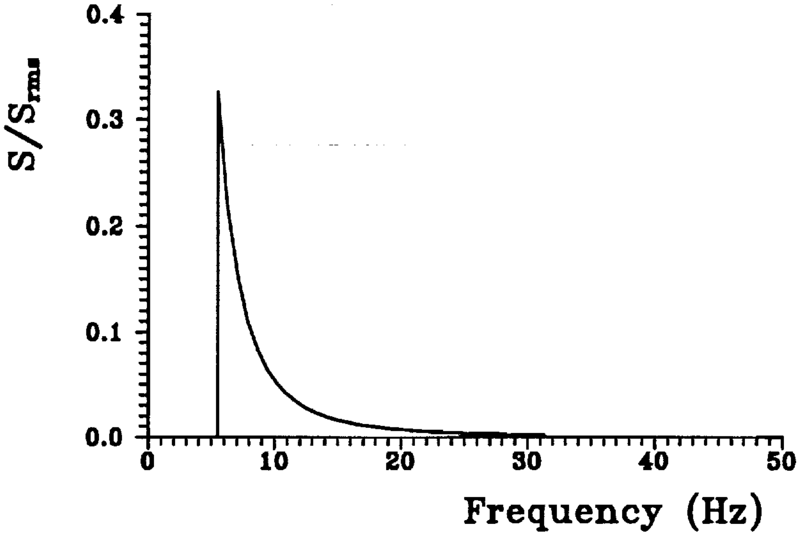

Figure VII.9 Power Spectrum E [6]

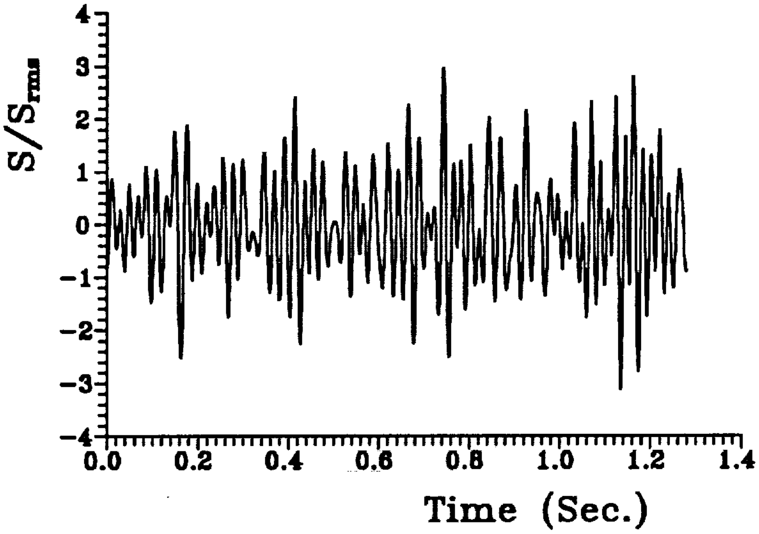

Figure VII.10 Time History of Spectrum A [5]

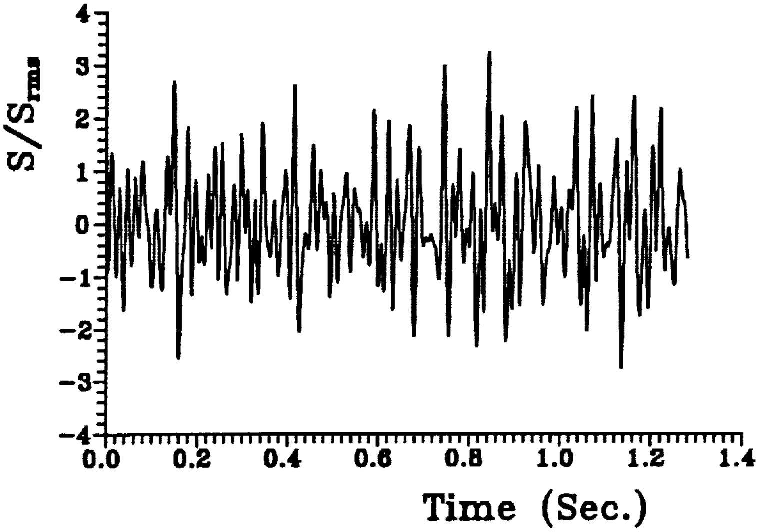

Figure VII.11 Time History of Spectrum B [5]

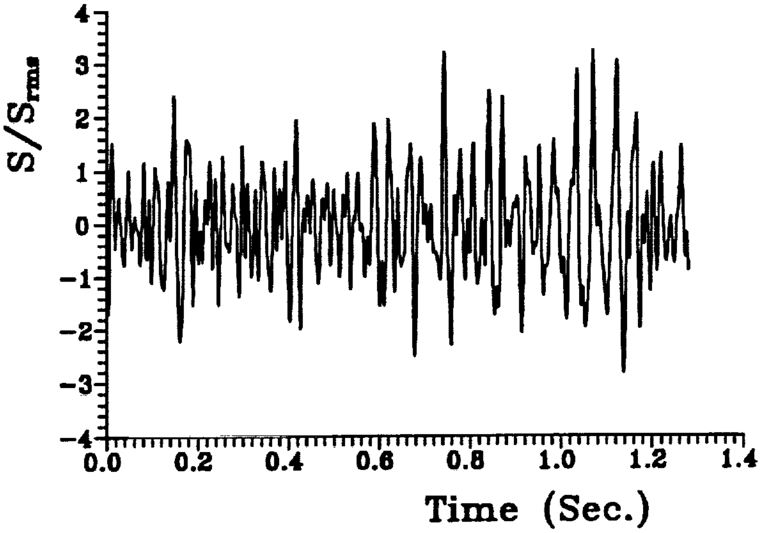

Figure VII.12 Time History of Spectrum C [5]

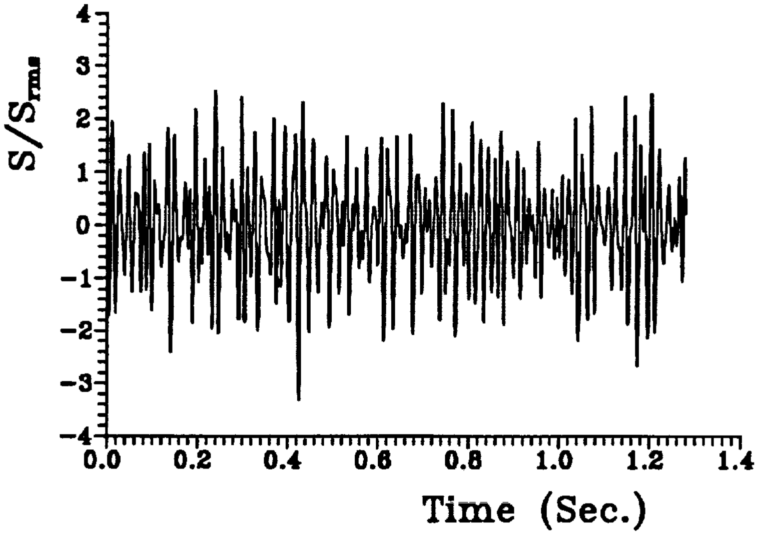

Figure VII.13 Time History of Spectrum D [5]

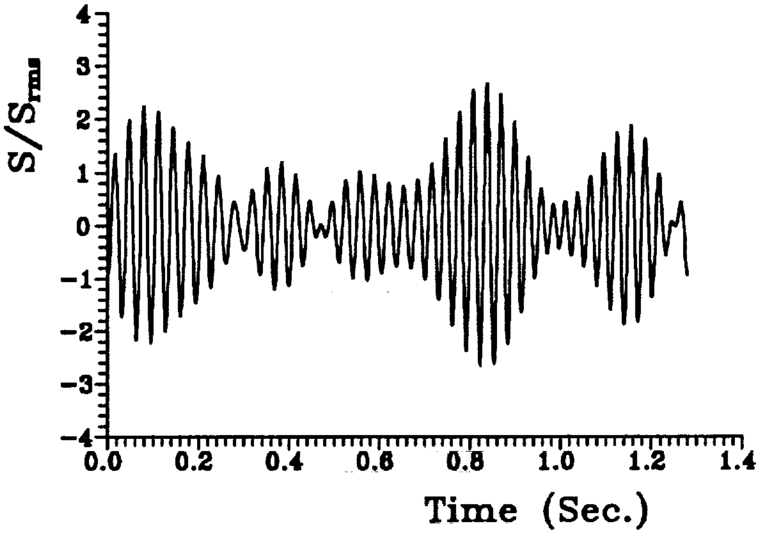

Figure VII.14 Time History of Spectrum A [6]

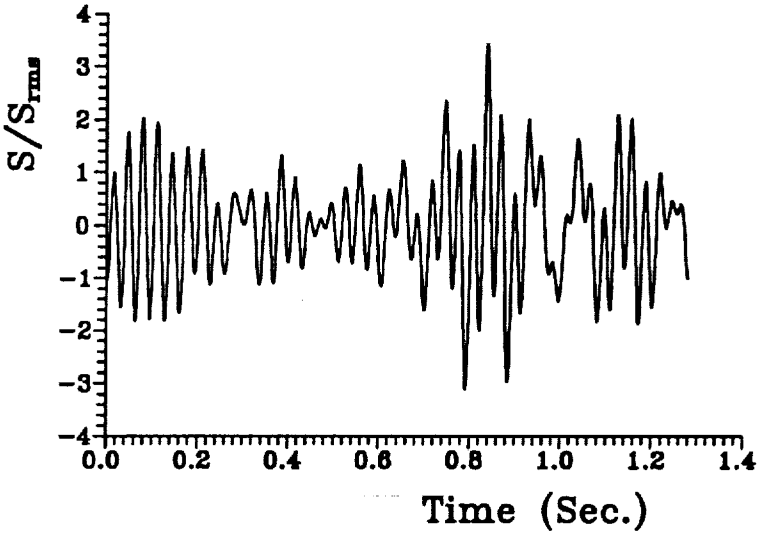

Figure VII.15 Time History of Spectrum B [6]

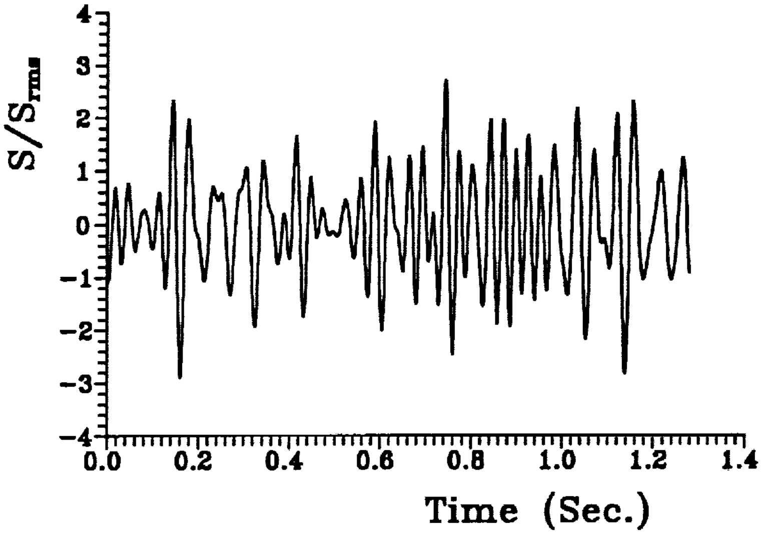

Figure VII.16 Time History of Spectrum C [6]

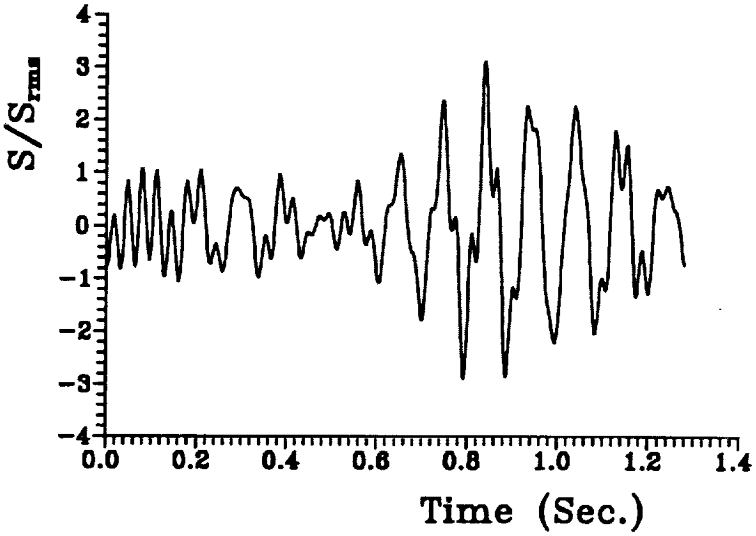

Figure VII.17 Time History of Spectrum D [6]

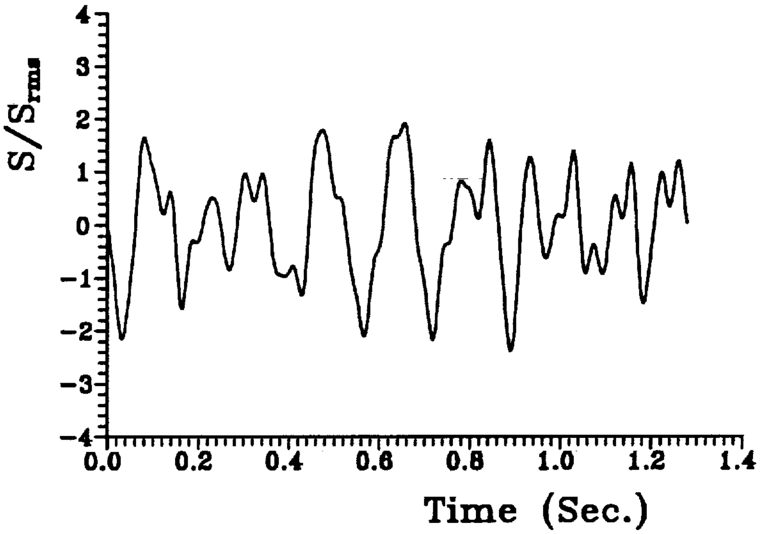

Figure VII.18 Time History of Spectrum E [6]

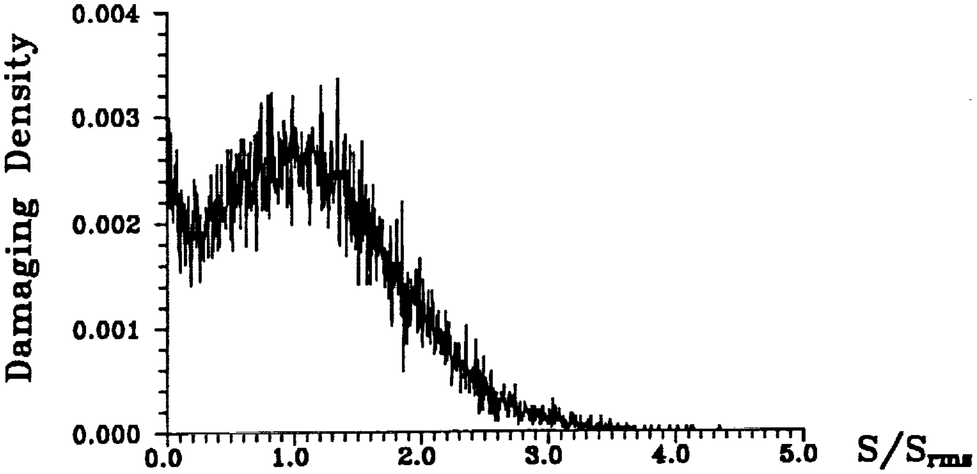

Figure VII.19 Damaging Probalility Density of Spectrum A [5]

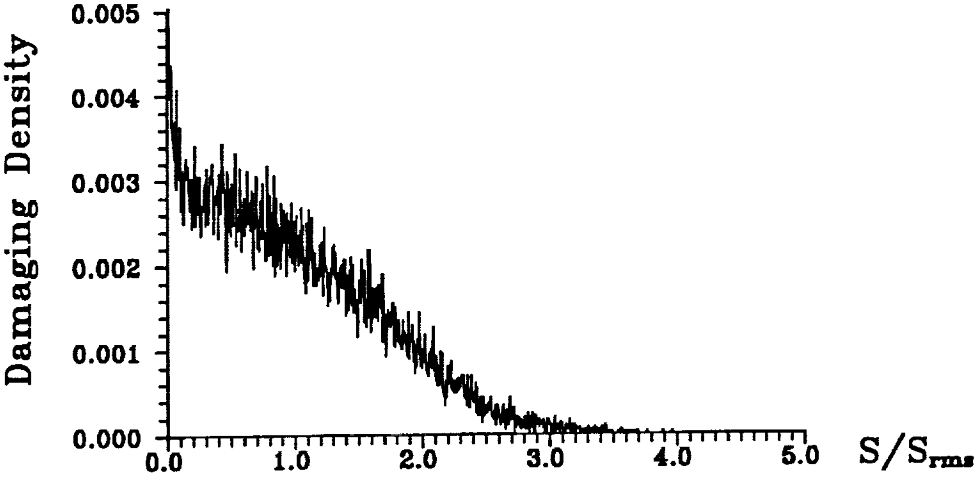

Figure VII.20 Damaging Probalility Density of Spectrum B [5]

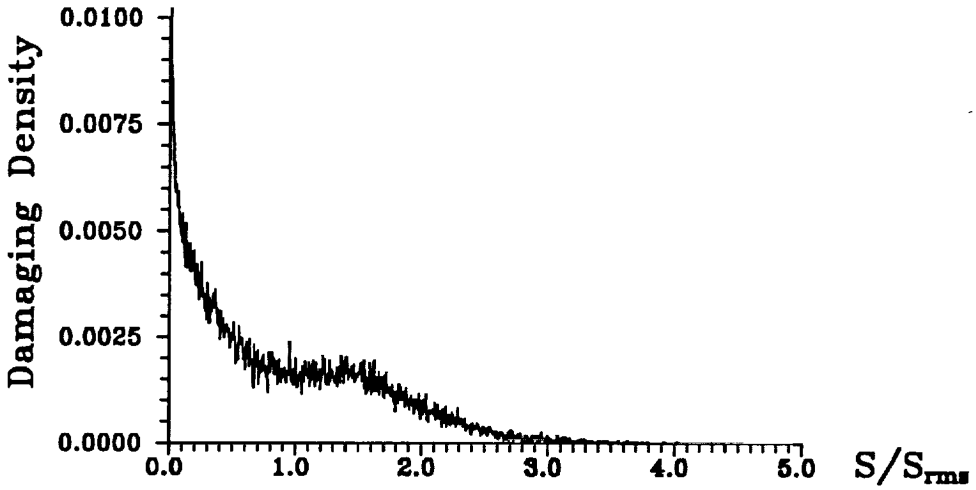

Figure VII.21 Damaging Probalility Density of Spectrum C [5]

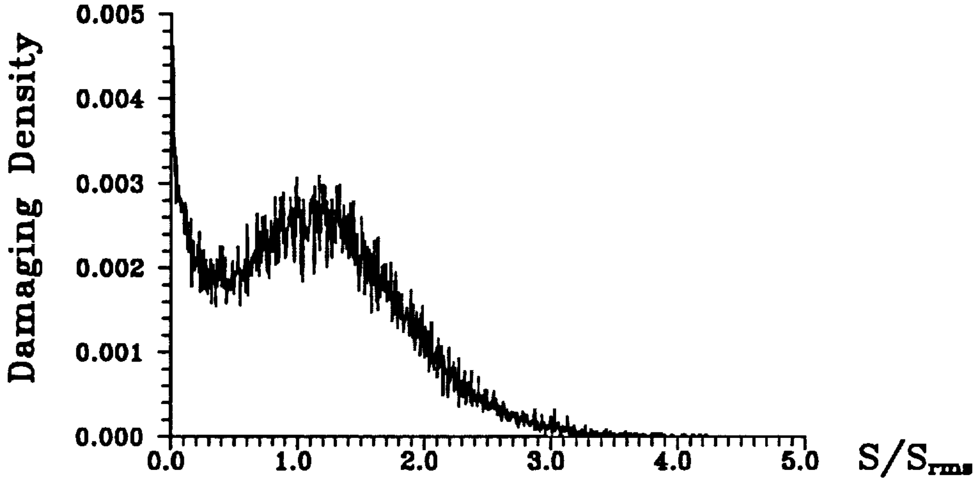

Figure VII.22 Damaging Probalility Density of Spectrum D [5]

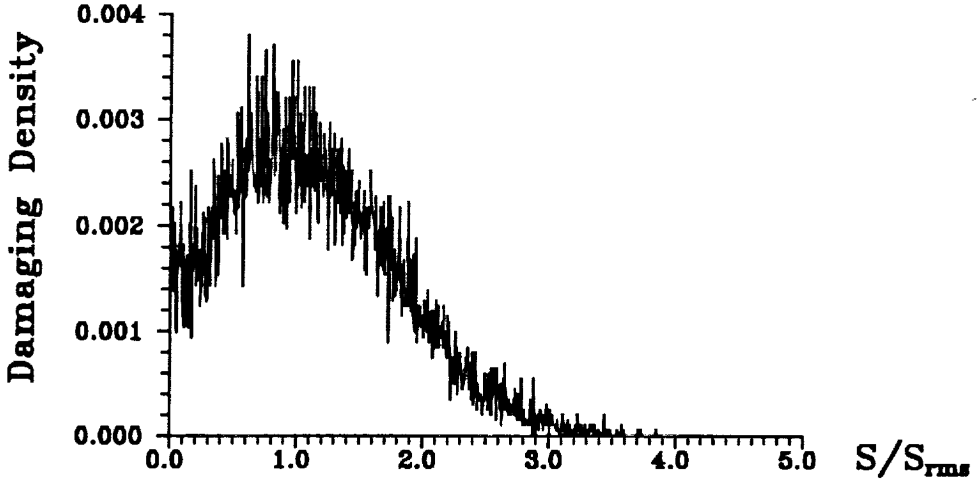

Figure VII.23 Damaging Probalility Density of Spectrum A [6]

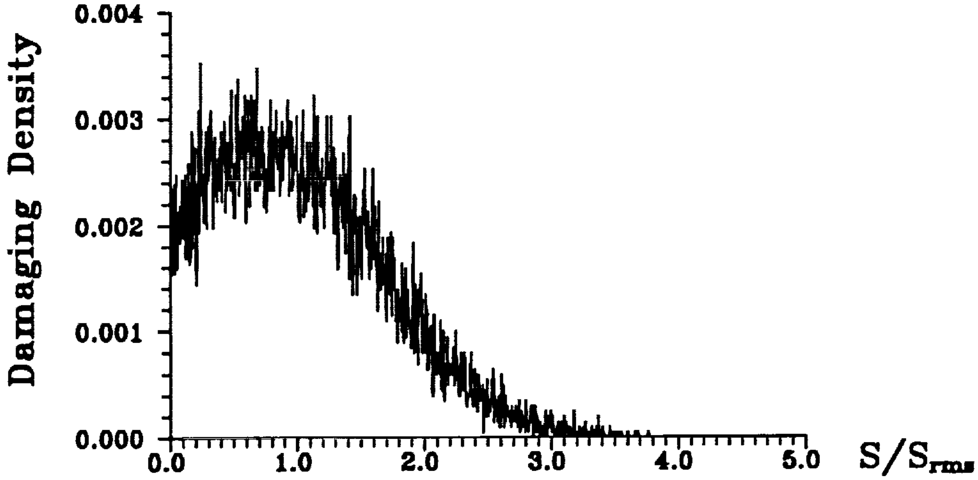

Figure VII.24 Damaging Probalility Density of Spectrum B [6]

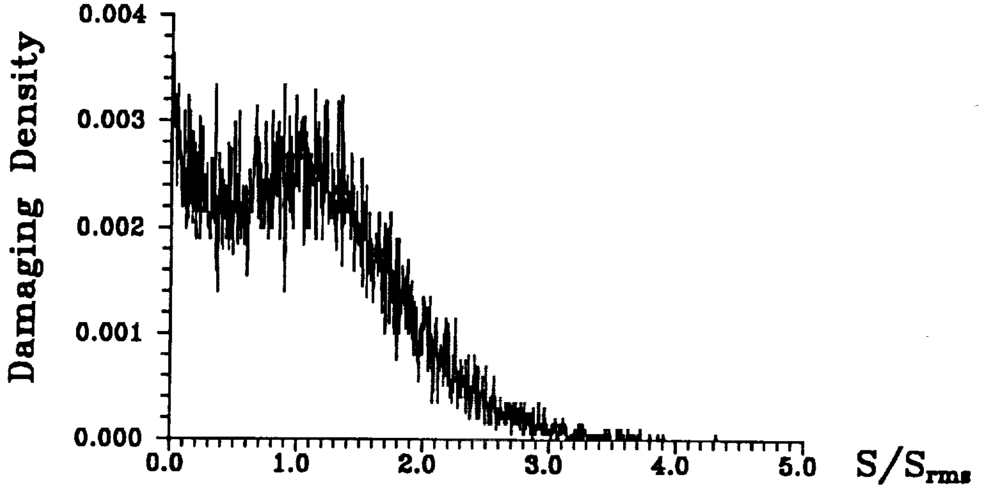

Figure VII.25 Damaging Probalility Density of Spectrum C [6]

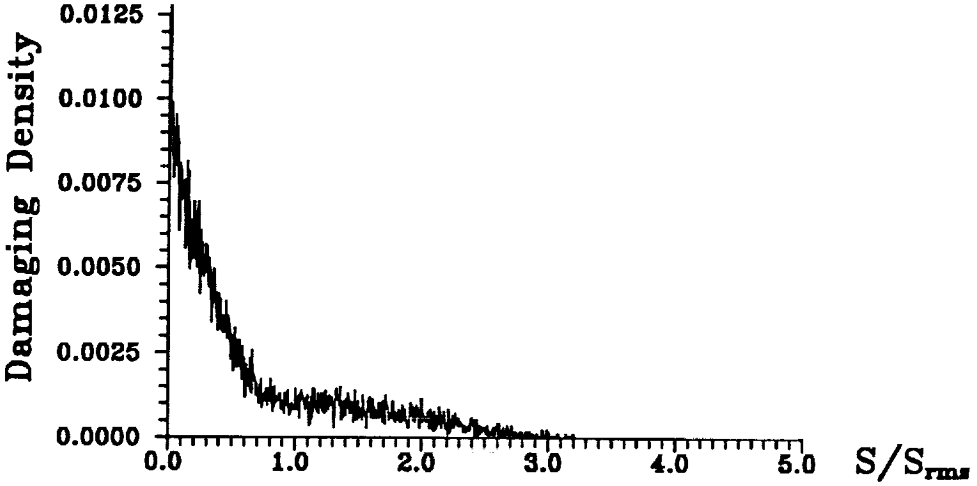

Figure VII.26 Damaging Probalility Density of Spectrum D [6]

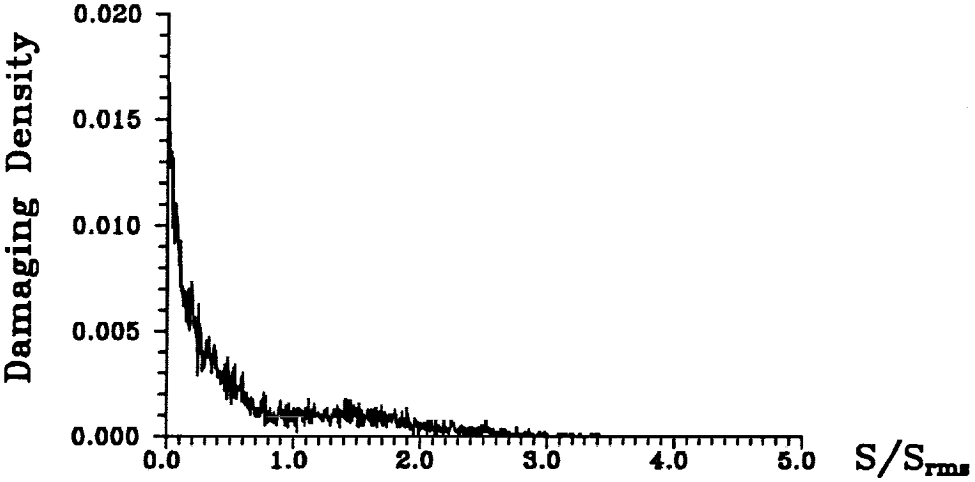

Figure VII.27 Damaging Probalility Density of Spectrum E [6]

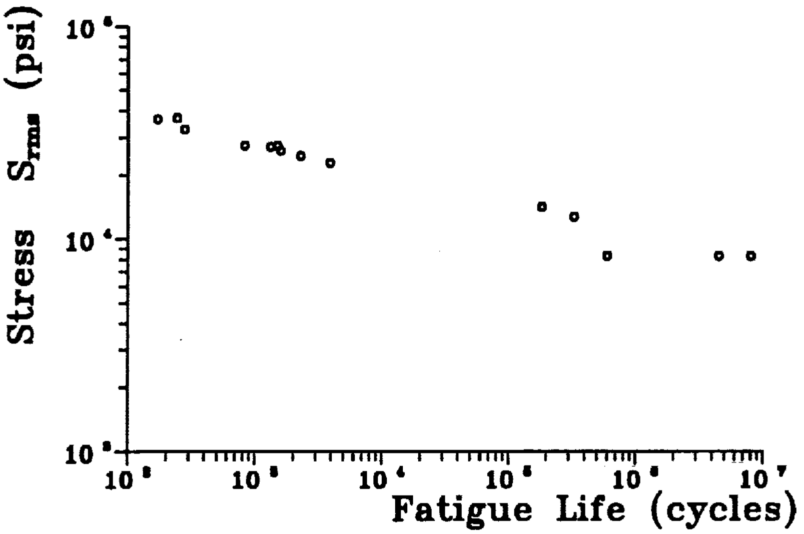

Figure VII.28 A Typical S/N Curve for Sinusoidal Loading [5]

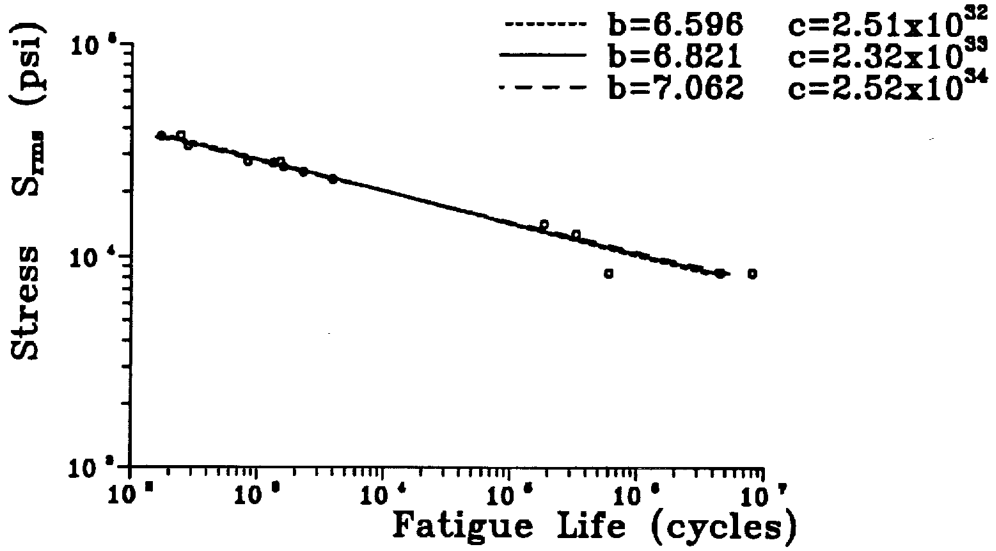

Figure VII.29 Estimated Fatigue Curves with Different Values of b and c

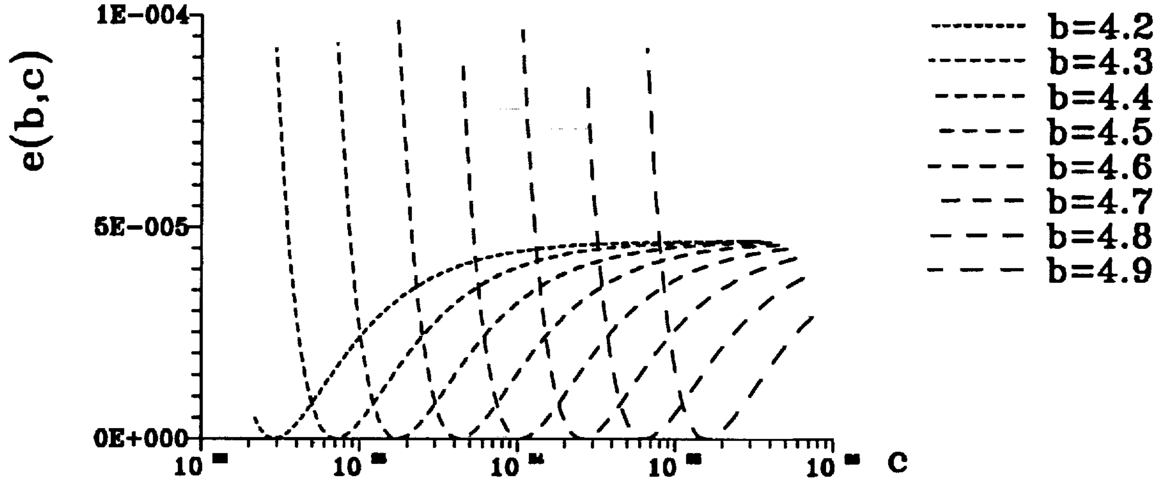

Figure VII.30 Error Functional Values vs. b and c

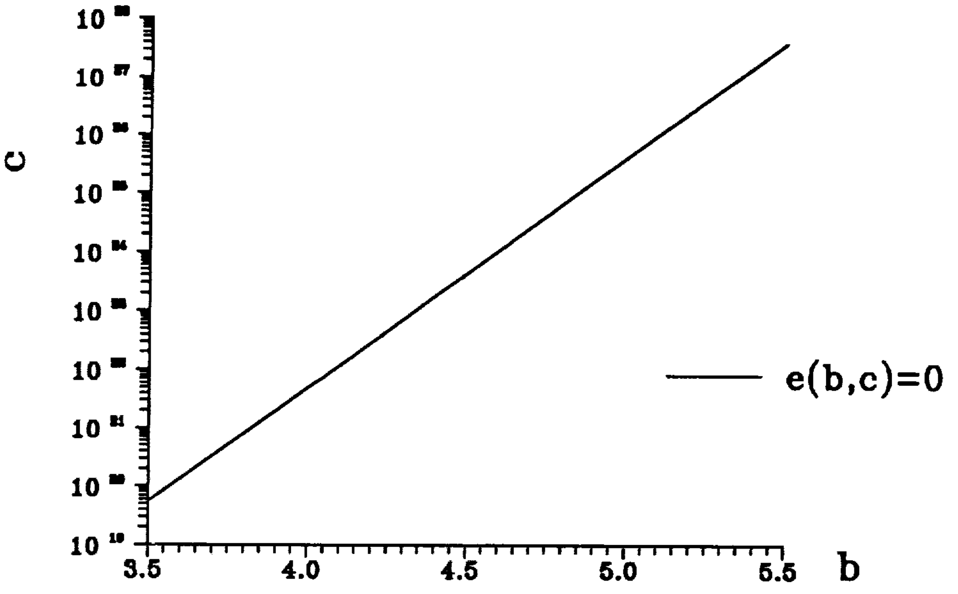

Figure VII.31 Relationship between b and c

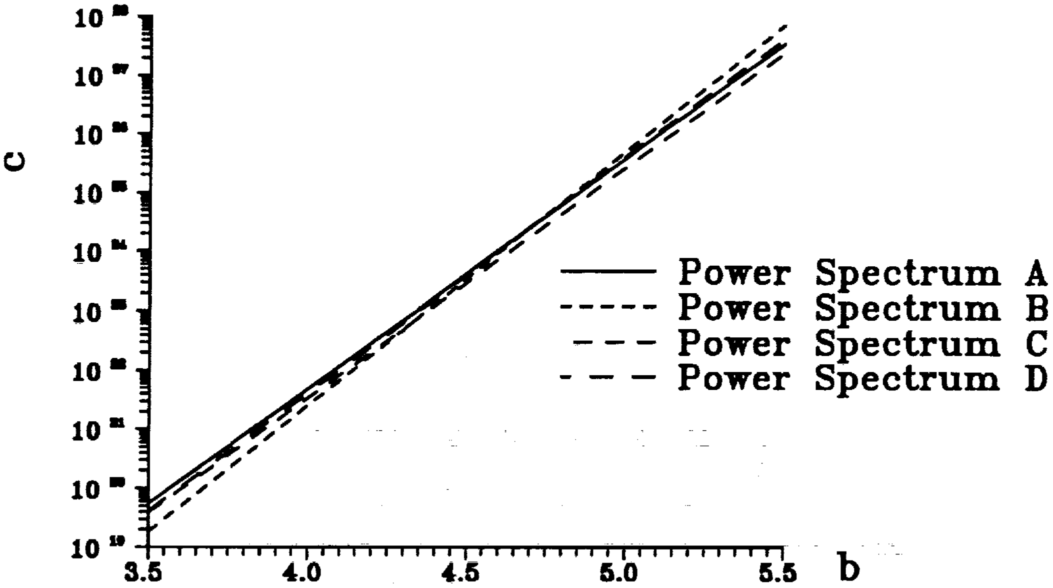

Figure VII.32 Zero Error for 4 Different Tests [5]

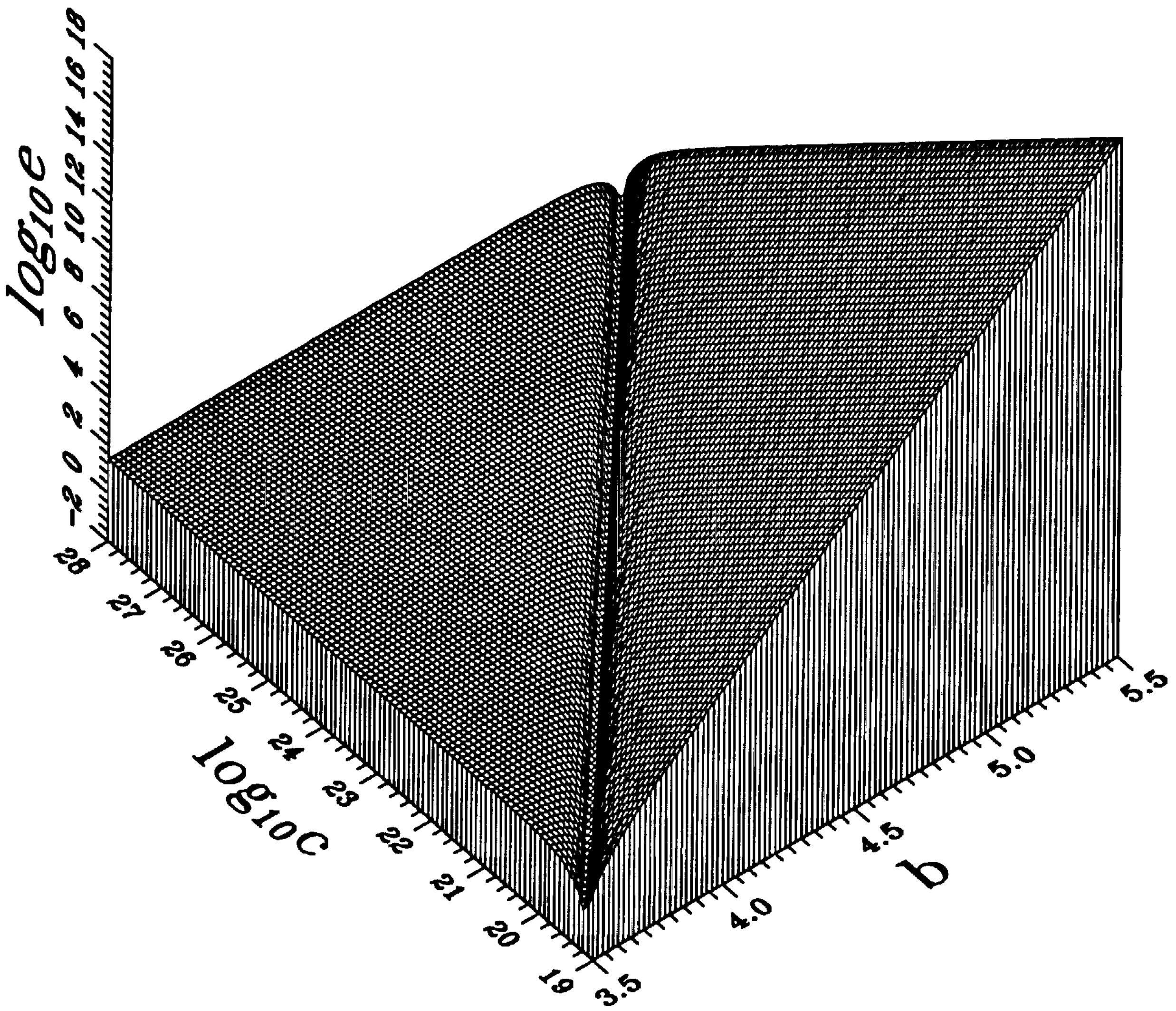

Figure VII.33 Error Functional Values vs. b and c

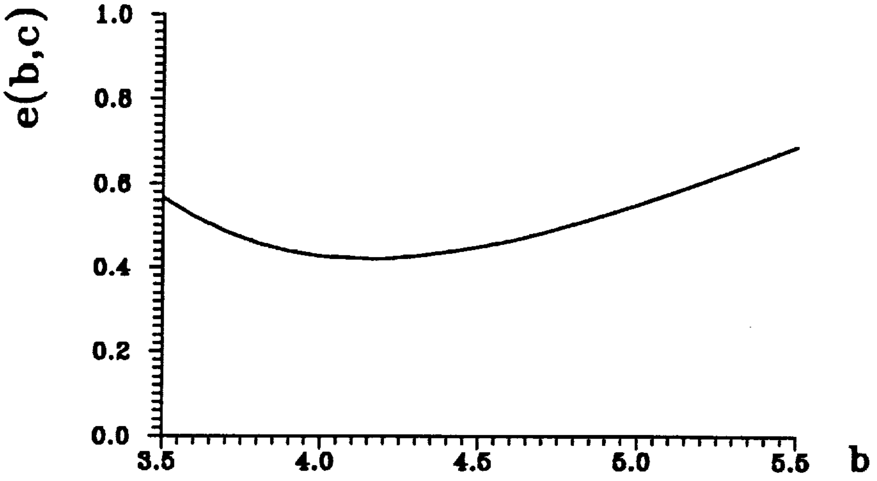

Figure VII.34 Error Functional Values vs. b

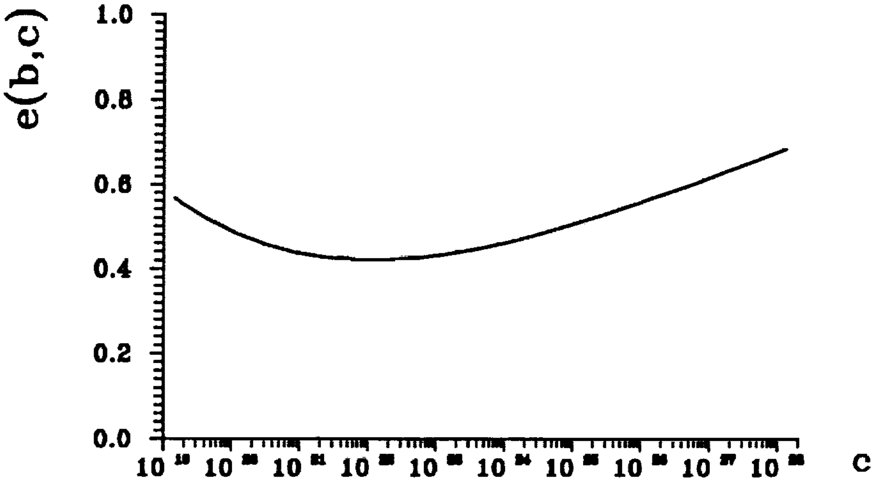

Figure VII.35 Error Functional Values vs. c

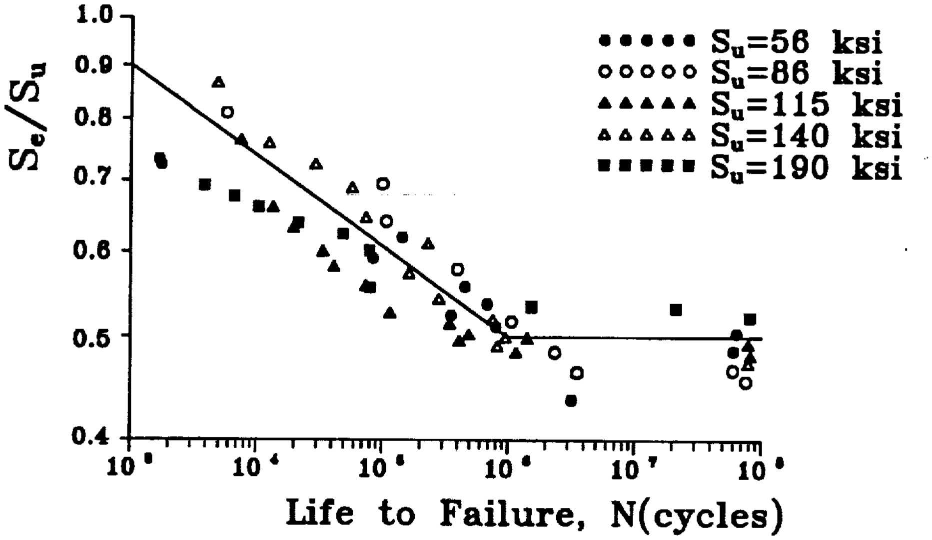

Figure VII.36 S/N Curves for Several Wrought Steels Plotted in Ratio Form (S_e/S_u) [7]

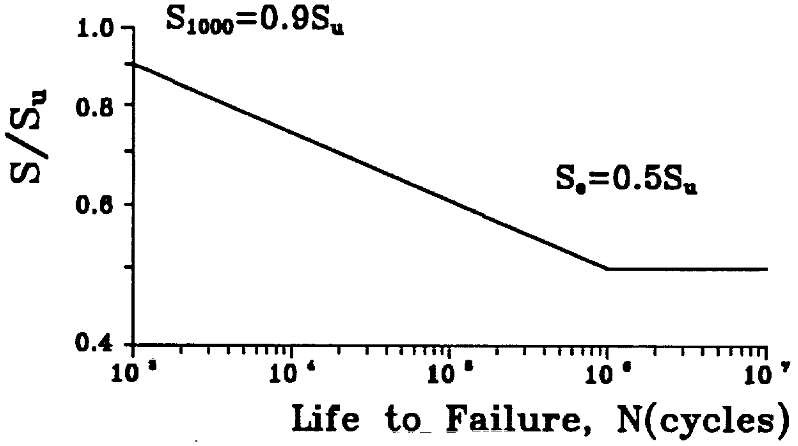

Figure VII.37 Generalized S/N Curve for Wrought Steels on Log-Log Plot [7]

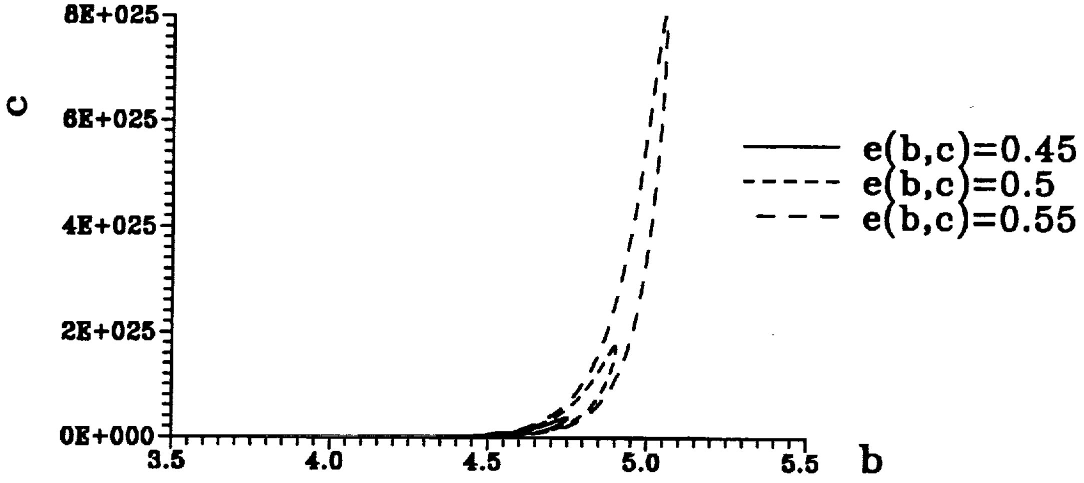

Figure VII.38 Contours of e(b,c)

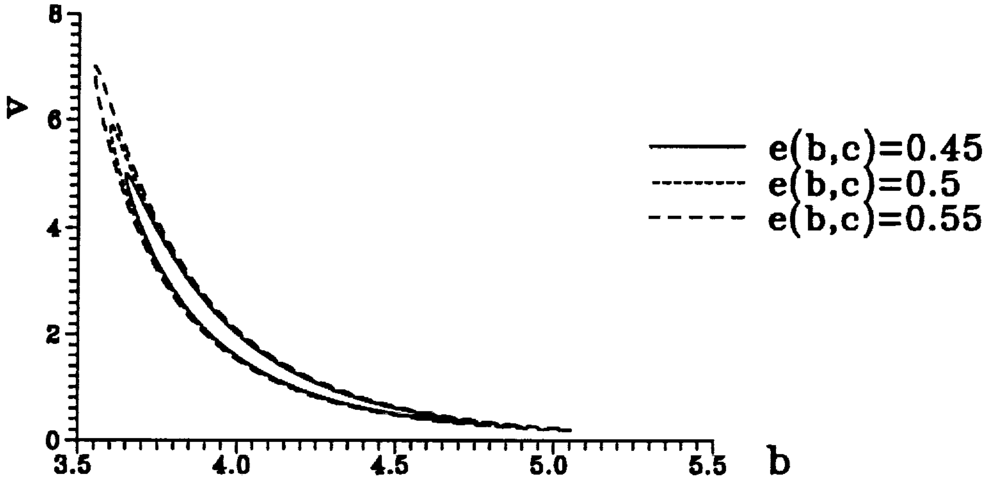

Figure VII.39 Contours of e(b,v)

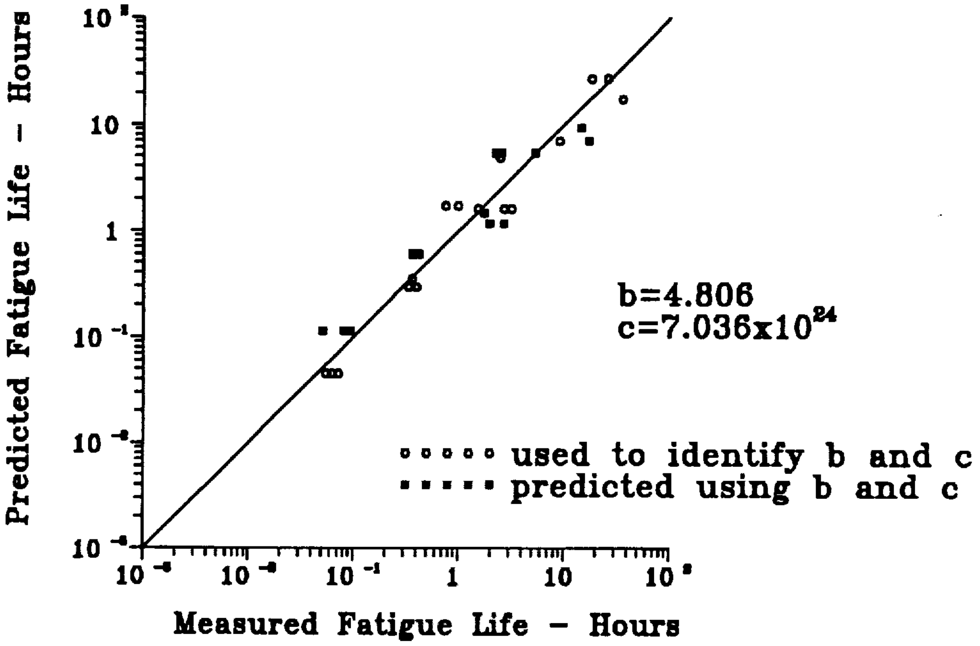

Figure VII.40 Measured and Predicted Fatigue Lives [5]

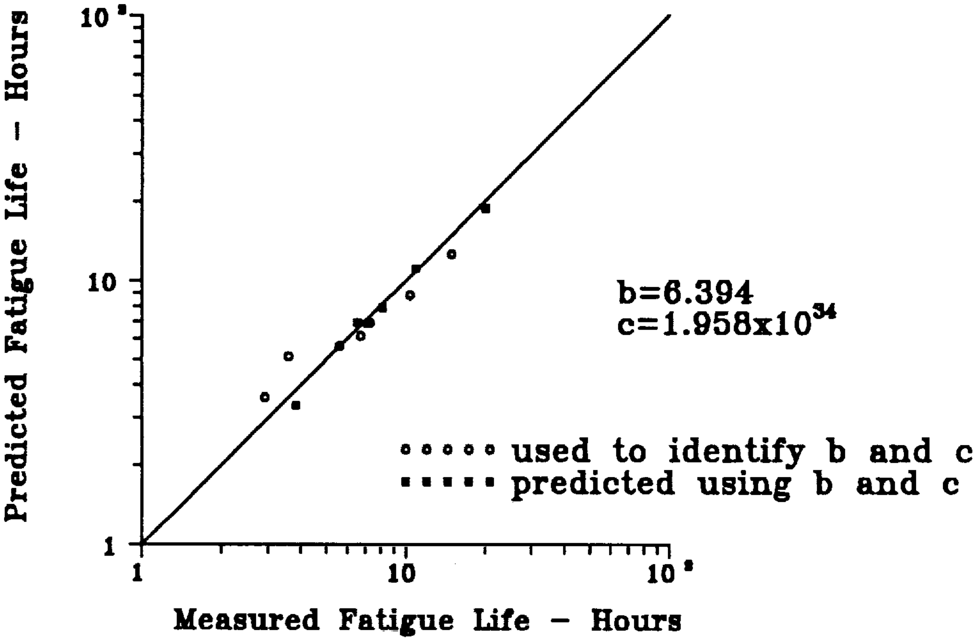

Figure VII.41 Measured and Predicted Fatigue Lives [6]

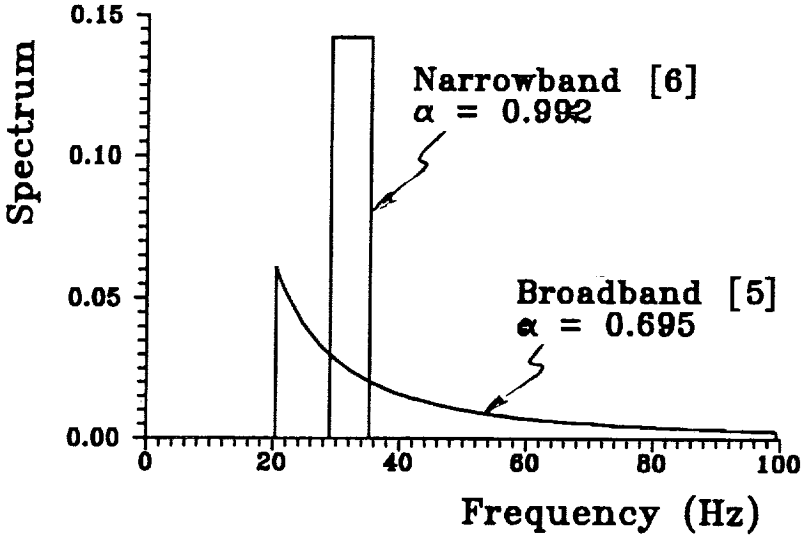

Figure VII.42 Samples of Broadband and Narrowband Spectra

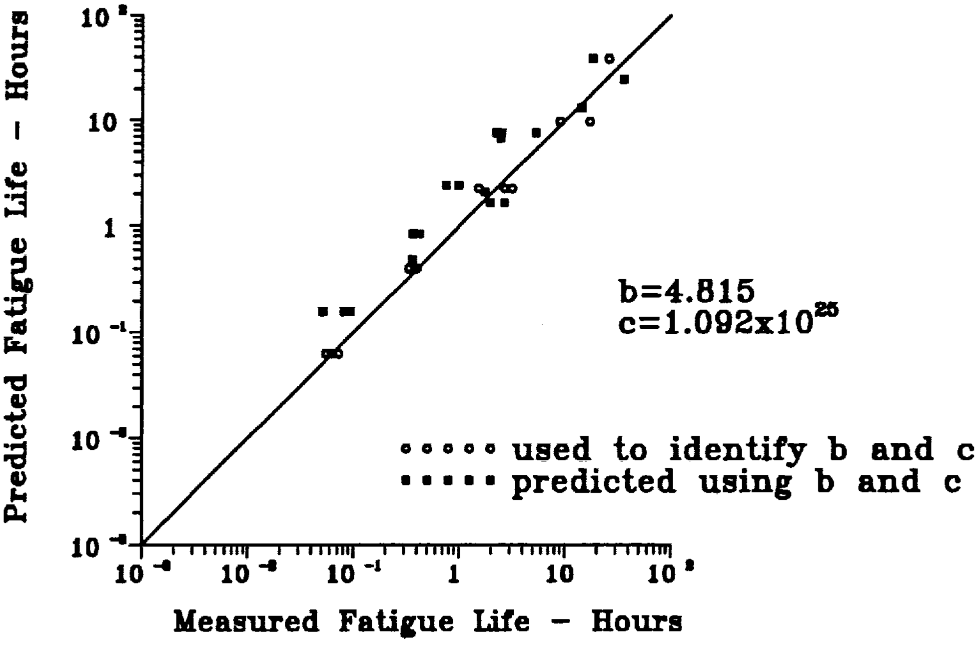

Figure VII.43 Measured and Predicted Fatigue Lives [5]

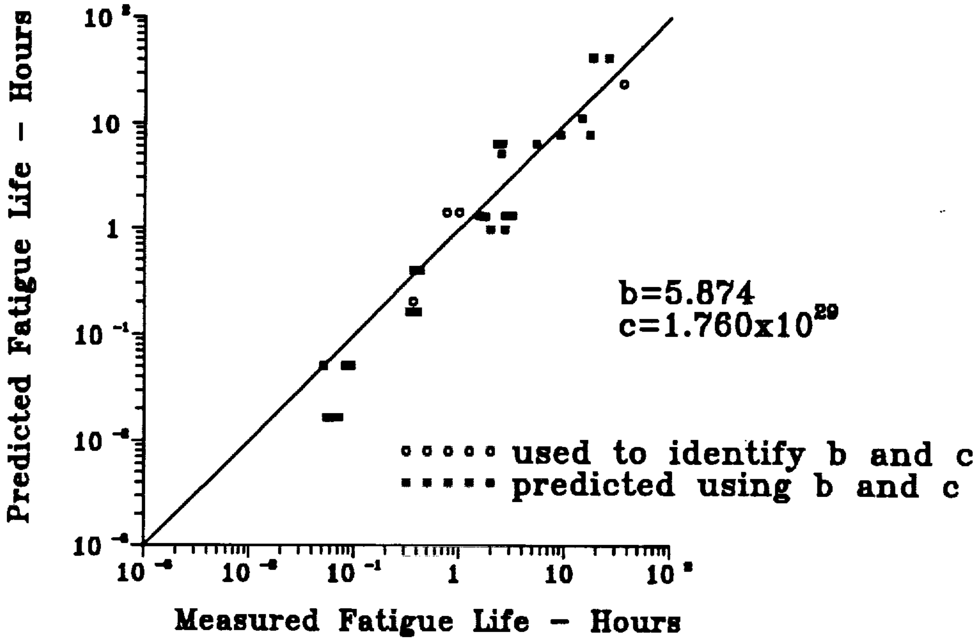

Figure VII.44 Measured and Predicted Fatigue Lives [5]

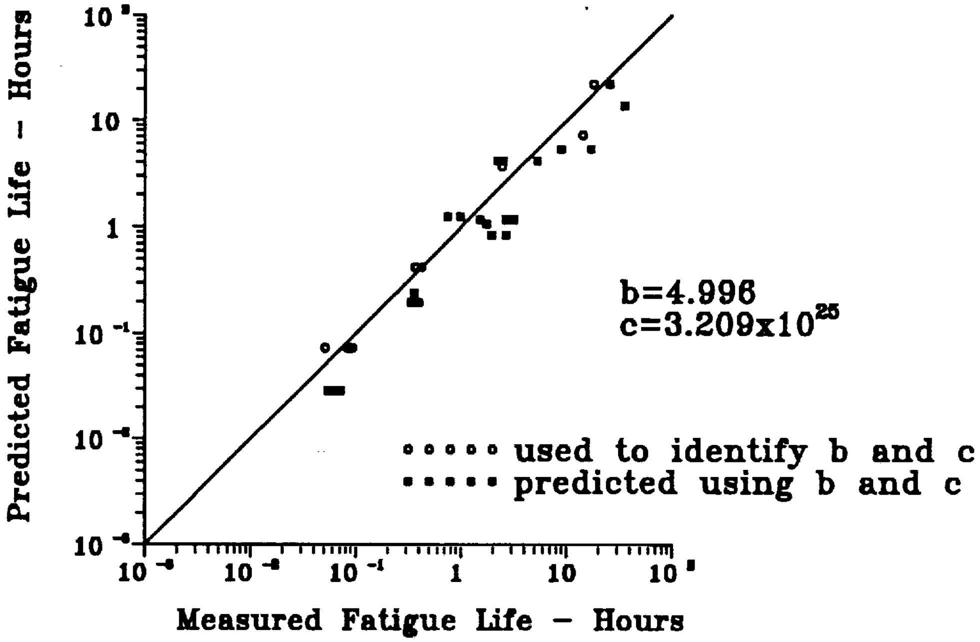

Figure VII.45 Measured and Predicted Fatigue Lives [5]

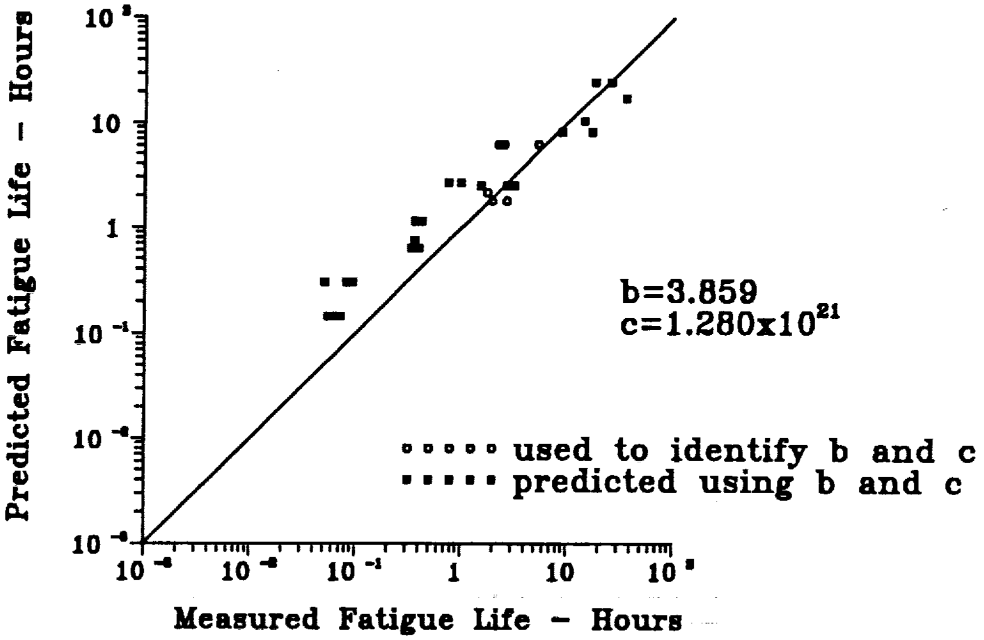

Figure VII.46 Measured and Predicted Fatigue Lives [5]

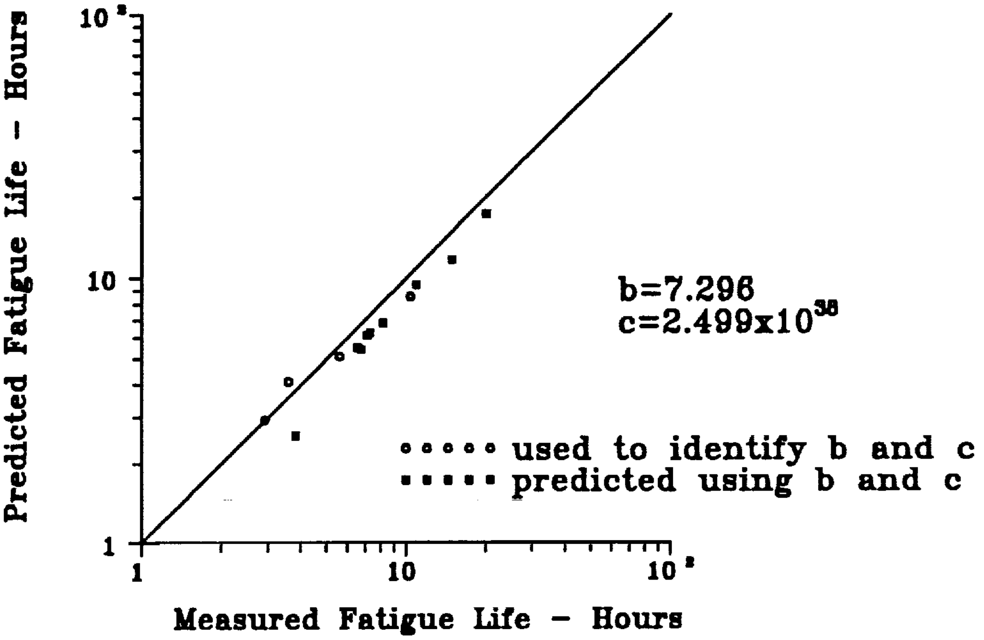

Figure VII.47 Measured and Predicted Fatigue Lives [6]

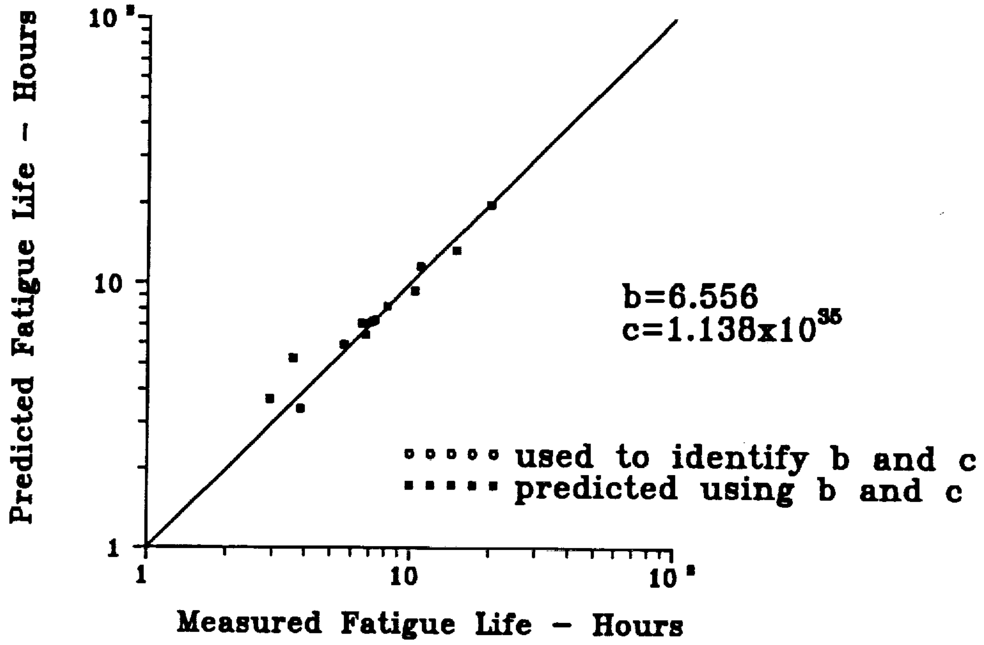

Figure VII.48 Measured and Predicted Fatigue Lives [6]

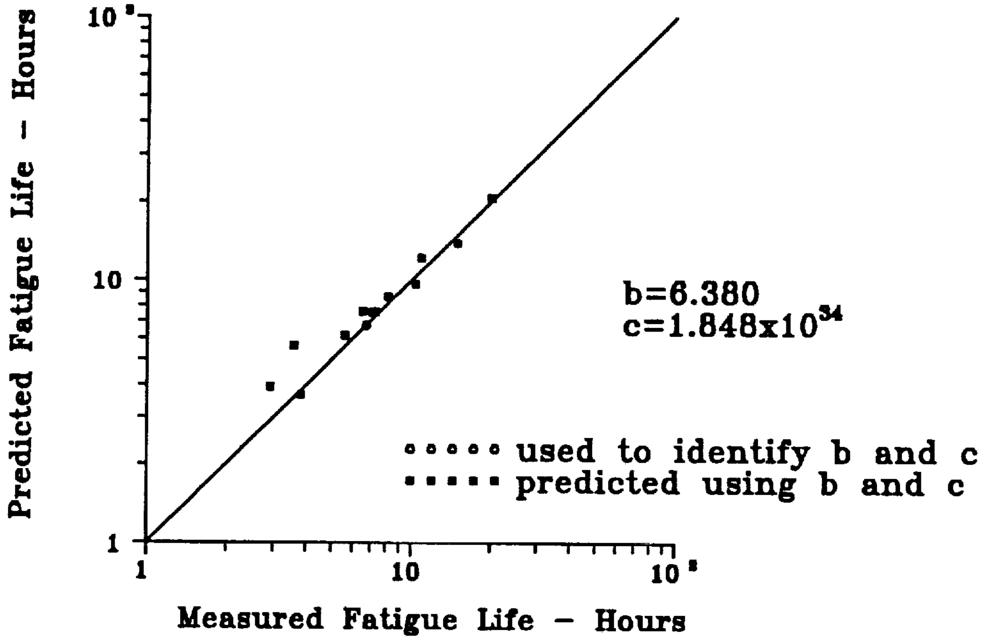

Figure VII.49 Measured and Predicted Fatigue Lives [6]

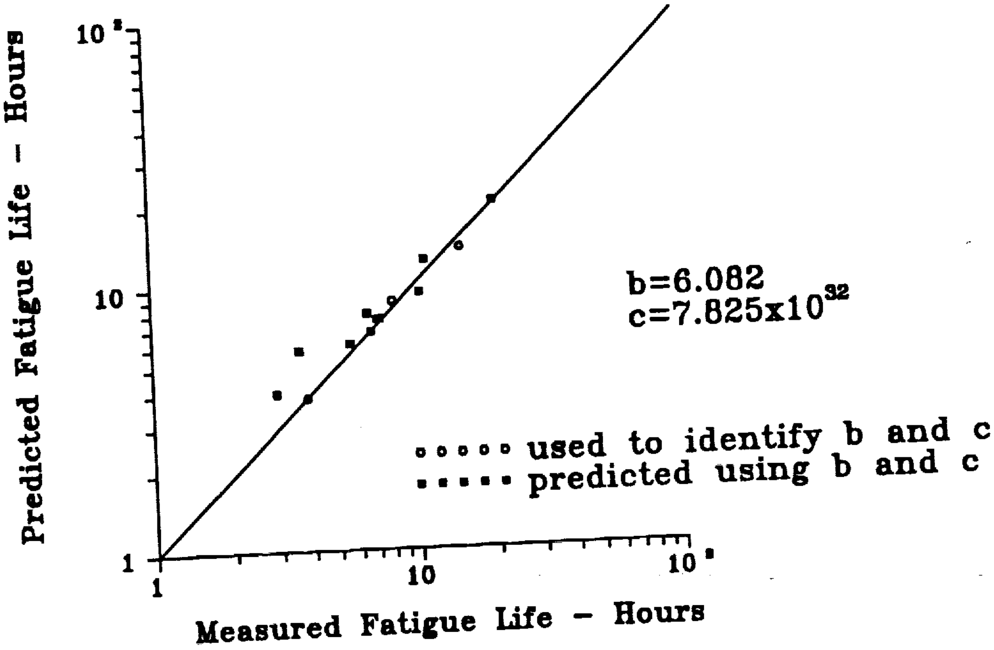

Figure VII.50 Measured and Predicted Fatigue Lives [6]

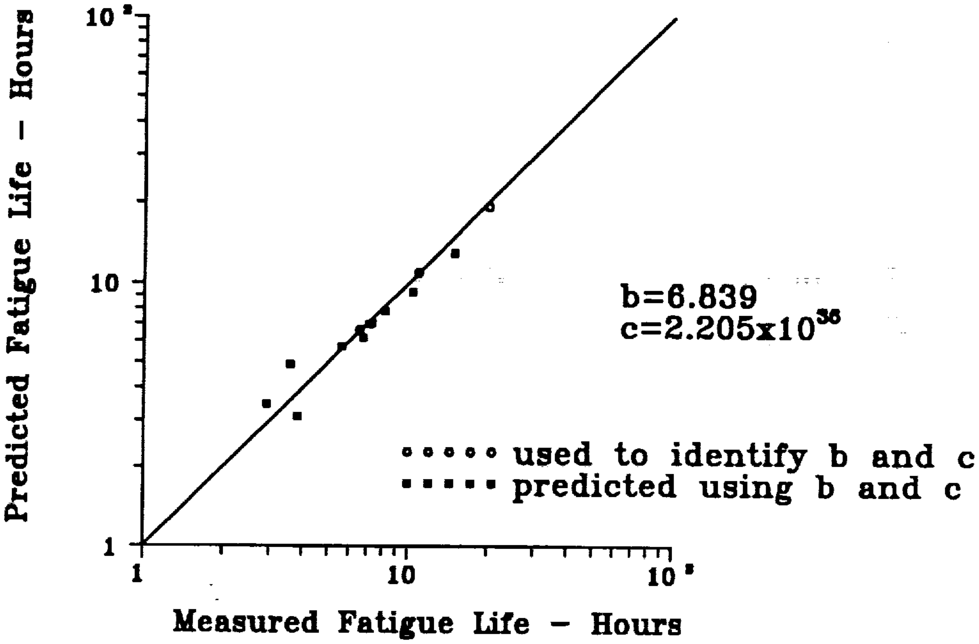

Figure VII.51 Measured and Predicted Fatigue Lives [6]

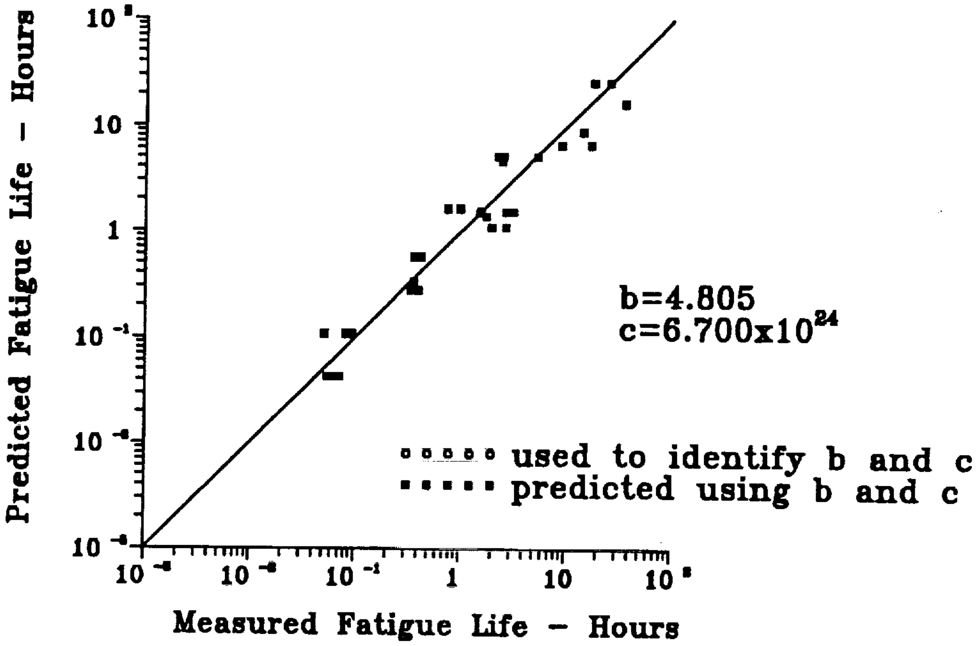

Figure VII.52 Measured and Predicted Fatigue Lives [5]

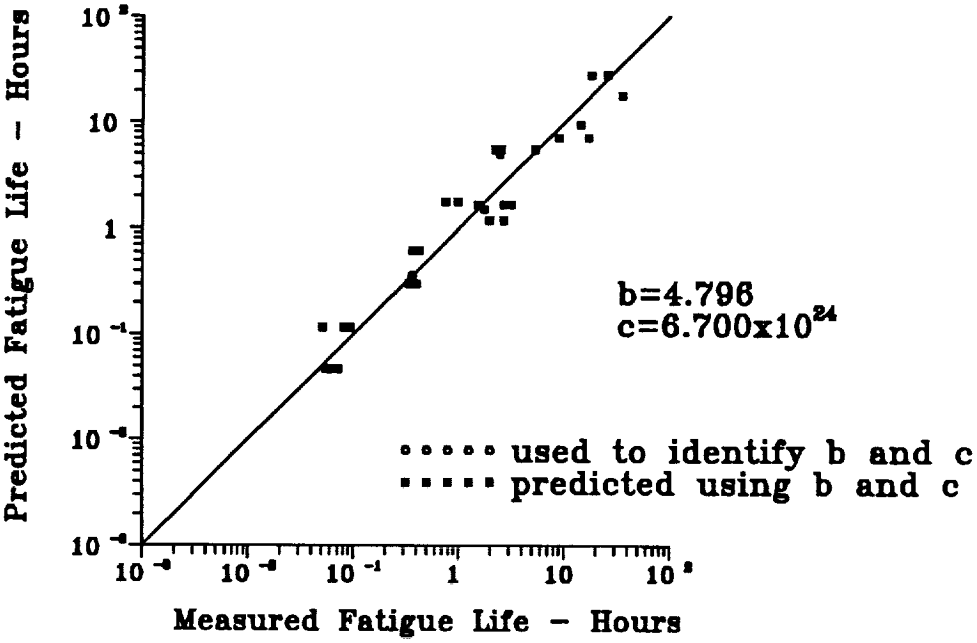

Figure VII.53 Measured and Predicted Fatigue Lives [5]

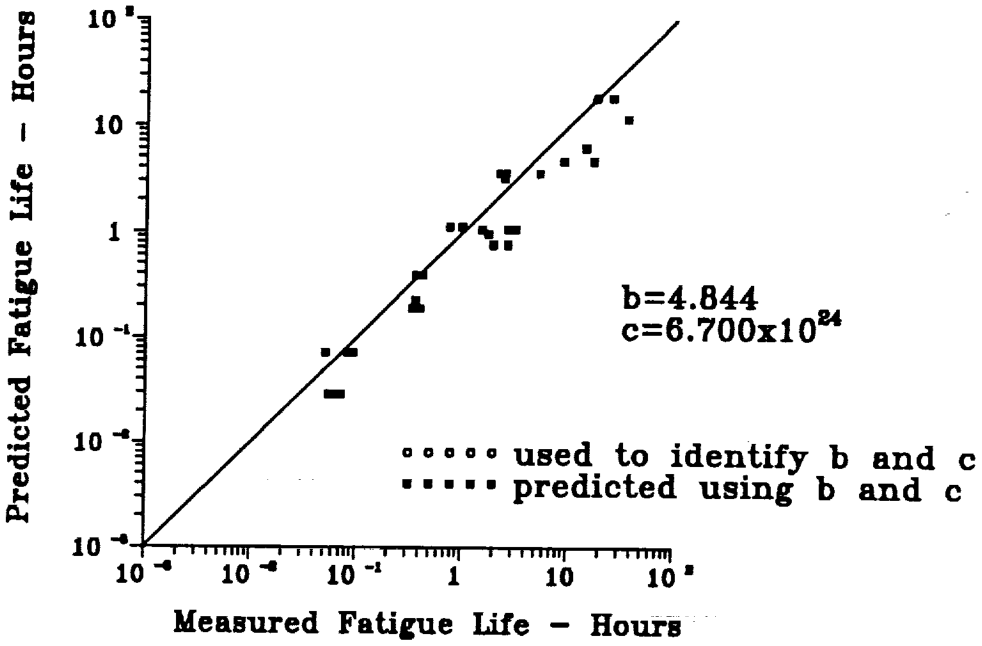

Figure VII.54 Measured and Predicted Fatigue Lives [5]

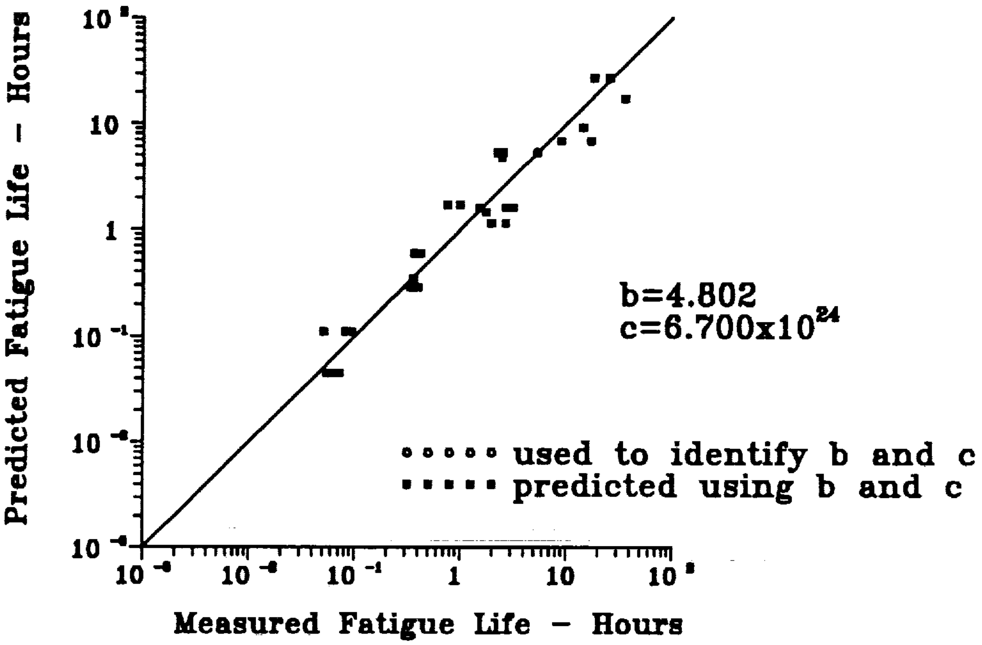

Figure VII.55 Measured and Predicted Fatigue Lives [5]

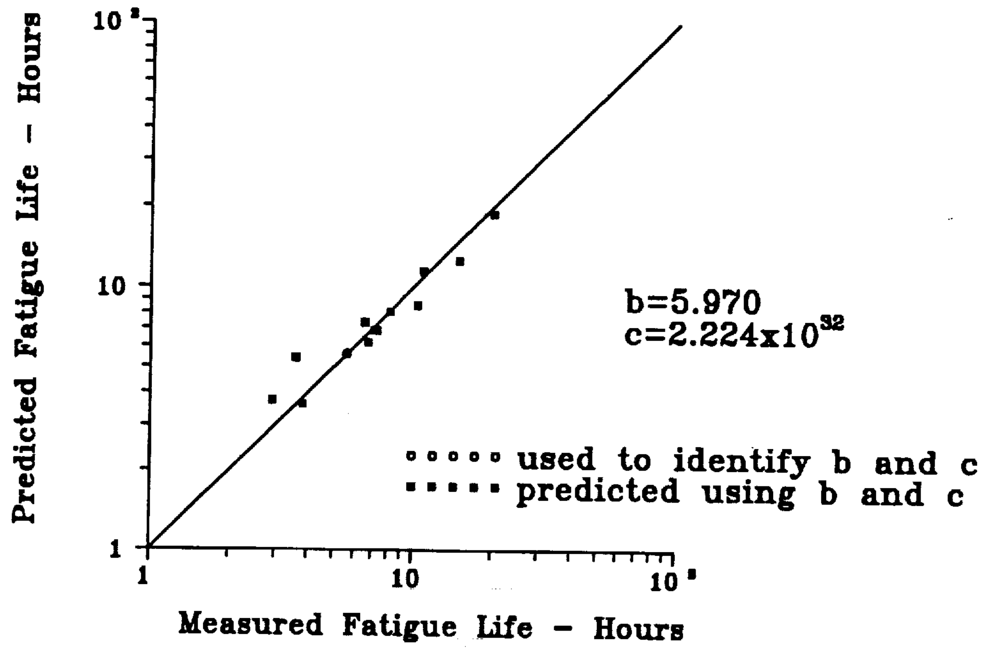

Figure VII.56 Measured and Predicted Fatigue Lives [6]

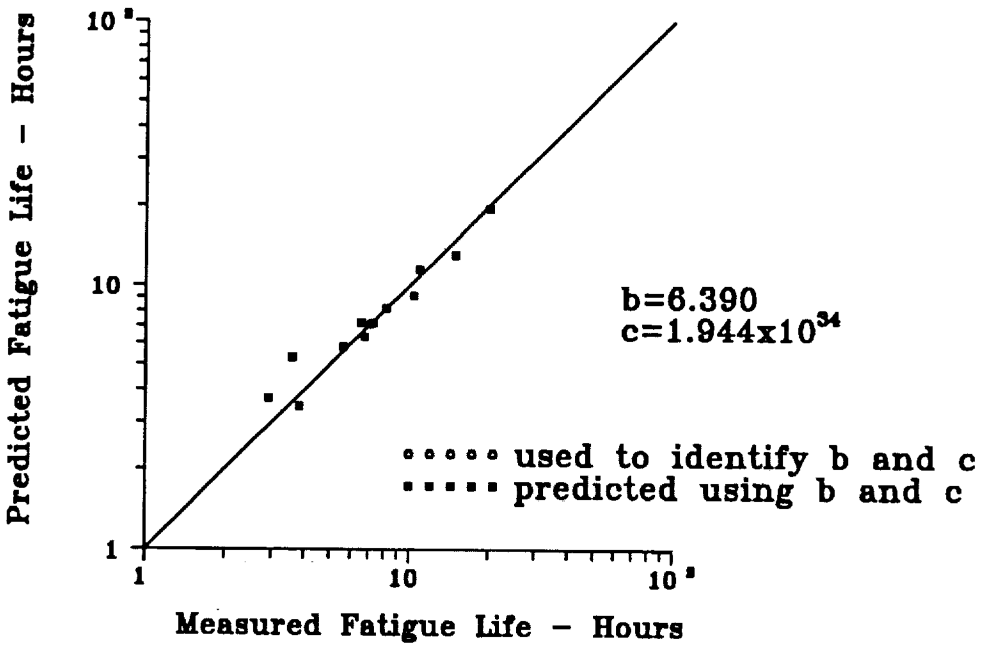

Figure VII.57 Measured and Predicted Fatigue Lives [6]

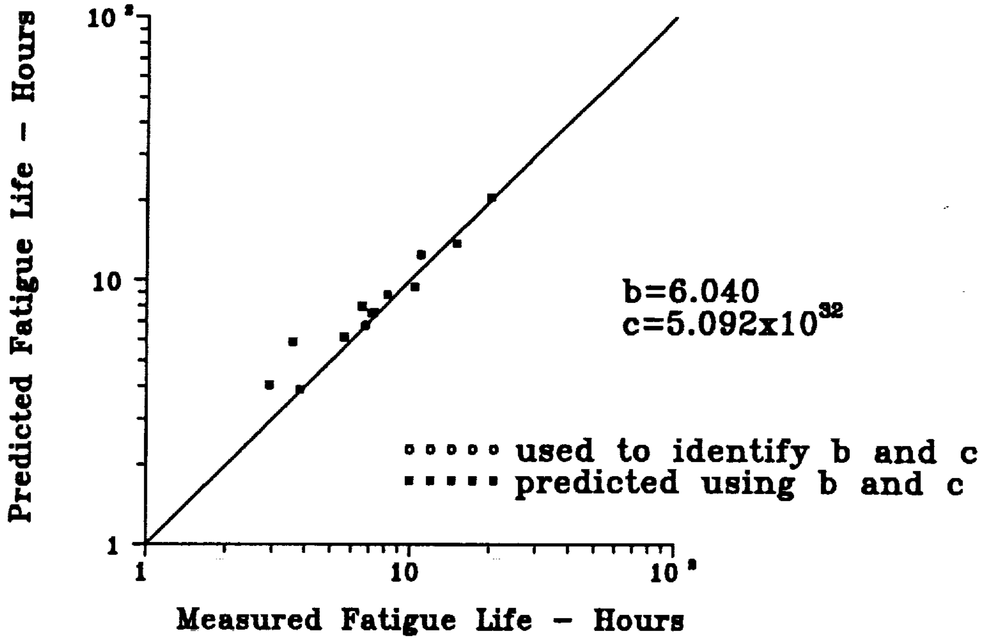

Figure VII.58 Measured and Predicted Fatigue Lives [6]

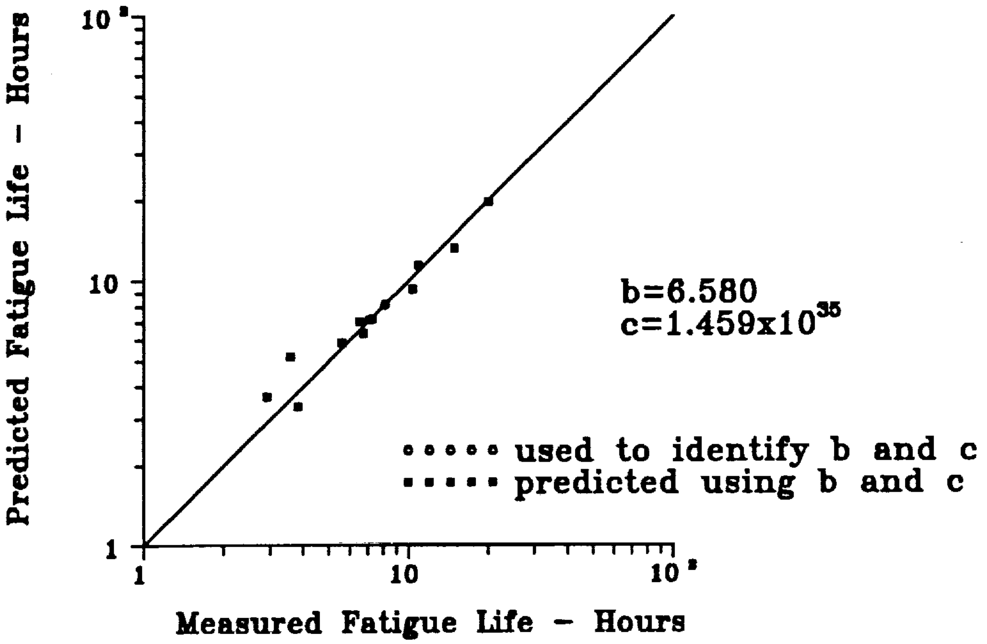

Figure VII.59 Measured and Predicted Fatigue Lives [6]

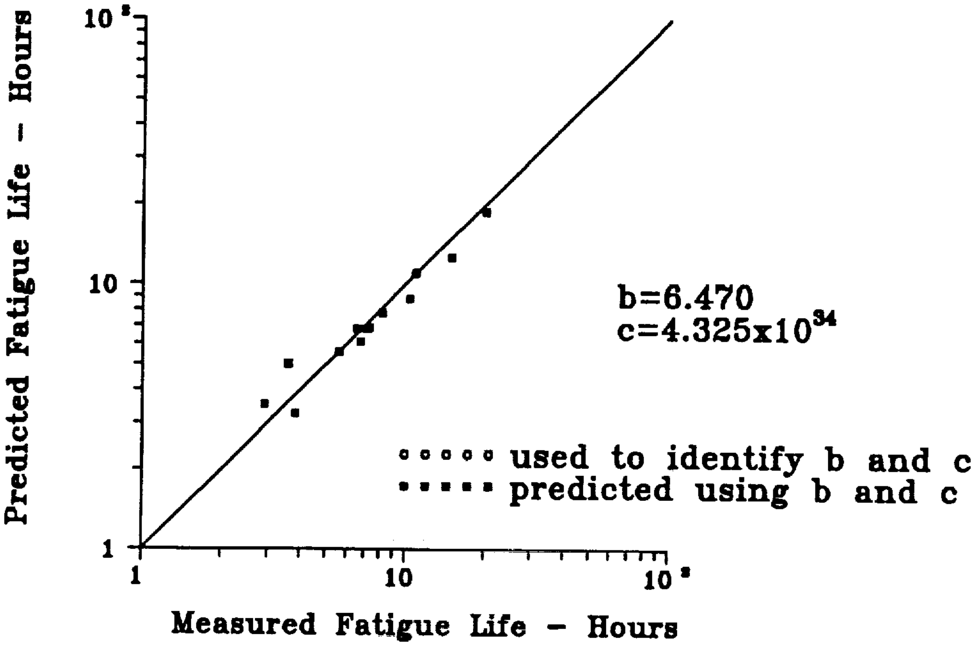

Figure VII.60 Measured and Predicted Fatigue Lives [6]

Table VII.1 Fatigue Data for Random Loading [5]

SPECTRUM	APPLIED STRESS S_{rms}, ksi	FATIGUE LIVES t_r, sec.	ZERO CROSSING RATE/ PEAK RATE
A	3.56	93360	0.916
A	4.74	61860	0.916
A	4.74	32340	0.916
A	6.42	11400	0.916
A	6.42	5490	0.916
A	6.42	9660	0.916
A	9.17	1440	0.916
A	9.17	1200	0.916
A	9.17	1410	0.916
A	13.50	259.8	0.916
A	13.50	225.0	0.916
A	13.50	198.0	0.916
B	3.95	128880	0.801
B	6.40	3540	0.801
B	6.40	2700	0.801
B	8.91	1302	0.801

Table VII.1 - Continued [5]

SPECTRUM	APPLIED STRESS S_{rms}, ksi	FATIGUE LIVES t_f, sec.	ZERO CROSSING RATE/ PEAK RATE
C	3.57	65580	0.695
C	4.47	51660	0.695
C	6.12	8850	0.695
C	7.90	1332	0.695
C	7.90	1320	0.695
C	7.90	1530	0.695
C	11.20	334.8	0.695
C	11.20	319.8	0.695
C	11.20	295.8	0.695
C	11.20	183.6	0.695
D	4.58	19080	0.889
D	4.58	9120	0.889
D	4.58	8040	0.889
D	6.00	6300	0.889
D	6.36	7020	0.889
D	6.36	9660	0.889

Table VII.2 Fatigue Data for Random Loading [6]

SPECTRUM	APPLIED STRESS S_{rms}, psi	FATIGUE LIVES t_f, sec.	ZERO CROSSING RATE/ PEAK RATE
A	13924	37394	0.992
A	14940	20170	0.992
A	16680	10522	0.991
A	17840	12924	0.990
B	14940	25680	0.886
B	14940	26330	0.898
C	14940	24320	0.904
D	14940	53870	0.586
D	16100	29390	0.586
D	18420	13770	0.586
E	15394	72480	0.593
E	16680	39384	0.593
E	17985	23590	0.593

Section VIII Powell's Method

Powell's method has the characteristic that when it is applied to a quadratic form, it choose *conjugate directions* (defined in the following paragraph) in which to move. Hence, the rate of convergence is fast when the method is used to minimize a general function. In addition, Powell has added a modification to the basic procedure to ensure a reasonable rate of convergence when the initial approximation is quite poor.

Conjugate Directions

Consider the problem of finding the minimum value of the quadratic function

$$f(\mathbf{X}) = \frac{1}{2}\mathbf{X}^T\mathbf{A}\mathbf{X} + \mathbf{B}^T\mathbf{X} + C, \qquad \text{(VIII.1)}$$

where, **A** is positive definite and symmetric. In two dimensions, the level curves $f(\mathbf{X}) = K$, for different values of K, are concentric ellipses as shown in figure (VIII.1). Suppose that we search for a minimum from the point $\mathbf{X}^0$ in the direction $\mathbf{S}^1$, that this minimum occurs at X^1 and that C is the optimal point. We say that the direction $\mathbf{X}^1 - C$ is *conjugate* to the direction $\mathbf{S}^1$ since, for any ellipse $f(\mathbf{X}) = K$, the diameter through $\mathbf{X}^1$ is conjugate (in the usual geometrical sense) to the diameter parallel to $\mathbf{S}^1$. The idea of conjugate directions is easily extended to n dimensions.

Let a set of non-zero search direction vectors $\mathbf{S}^1, \mathbf{S}^2, ..., \mathbf{S}^n$ be conjugate to a given positive definite matrix **A**, if the following condition is satisfied,

$$\mathbf{S}^{i^T} \cdot \mathbf{A} \cdot \mathbf{S}^j = 0, \qquad \text{for all} \qquad i \neq j, \qquad \text{(VIII.2)}$$

where the matrix **A** is as defined in equation (VIII.1).

We can reach the minimum in at most n exact one-dimensional searches, if the i-th estimate, $\mathbf{X}^i$, is generated by the initial guess,$\mathbf{X}^0$, and the conjugate directions $\mathbf{S}^1, \mathbf{S}^2, ..., \mathbf{S}^i$. The estimates of **X** at each iteration may be written in the form,

$$\mathbf{X}^2 = \mathbf{X}^1 + \alpha_2\mathbf{S}^2 = \mathbf{X}^0 + \alpha_1\mathbf{S}^1 + \alpha_2\mathbf{S}^2, \qquad \text{(VIII.3)}$$

$$\mathbf{X}^1 = \mathbf{X}^0 + \alpha_1\mathbf{S}^1,$$

$$\cdots \quad \cdots$$

$$\mathbf{X}^i = \mathbf{X}^{i-1} + \alpha_i\mathbf{S}^i = \mathbf{X}^0 + \sum_{j=1}^{i}\alpha_j\mathbf{S}^j,$$

where α_i are optimum step size it should go from $\mathbf{X}^{i-1}$ to $\mathbf{X}^i$ along direction $\mathbf{S}^i$.

A search technique which finds the minimum of $f(\mathbf{X})$ defined by equation (VIII.1) in a finite number of one-dimensional searches will have considerable merit for a general optimization problem, since it should converge rapidly once the optimum is approached. The basis for these methods can be seen in the geometric construction shown in figure

(VIII.1). Here any point, $\mathbf{X}^0$, is taken as the initial base point, and a search is made in an arbitrary direction (shown here as $\mathbf{S}^1$) until a minimum, $\mathbf{X}^1$, is found. A second point, $\mathbf{X}^2$, not on the line through $\mathbf{X}^0$ and $\mathbf{X}^1$, is now taken and a search carried out for a minimum, $\mathbf{X}^3$, on the line parallel to that through $\mathbf{X}^0$ and $\mathbf{X}^1$ ($\mathbf{S}^1$). If the contours are ellipsoidal, as defined by equation (VIII.1), a line connecting points $\mathbf{X}^1$ and $\mathbf{X}^3$ constructing a new direction, $\mathbf{S}^2$ will pass exactly through the true minimum. A one-dimensional search along this connecting line will then reveal the desired optimum. We can therefore find the optimum without further iteration, provided the objective function has the quadratic form given by equation (VIII.1). If the objective function is not quadratic, then of course convergence is not assured in a finite number of iterations, or even after a very large number of tries. Since most problems of interest are not expressed in terms of quadratic objective functions, we might inquire as to the value of quadratic convergence. Most functions, however, approach quadratic behavior in the neighborhood of their optimum, and since quadratic functions can have very elongated elliptical contours, quadratically convergent methods are capable of coping with such shapes. In essence, it seems very reasonable to expect a quadratically convergent procedure to be effective in searching nonquadratic object functions.

Powell's Basic Method

Initial directions in Powell's method are usually taken to be the coordinate directions,

$$\mathbf{S}^1 = (1,0,0,...,0)^T, \qquad \mathbf{S}^2 = (0,1,0,...,0)^T, \quad ..., \quad \mathbf{S}^n = (0,0,0,...,1)^T \qquad \text{(VIII.4)}$$

then repeat the following sequence of step until the function stops decreasing:

(1) Save the initial estimation of $\mathbf{X}$ as $\mathbf{X}^0$.

(2) For $i = 1, ..., n$, move $\mathbf{X}^{i-1}$ to the minimum along direction $\mathbf{S}^i$ and call this point $\mathbf{X}^i$.

(3) For $i = 1, ..., n-1$, set $\mathbf{S}^i \leftarrow \mathbf{S}^{i+1}$.

(4) Set $\mathbf{S}^n \leftarrow \mathbf{X}^n - \mathbf{X}^0$.

(5) Move $\mathbf{X}^n$ to the minimum along direction $\mathbf{S}^n$ and call this point $\mathbf{X}^0$.

But, if one uses Powell's method to solve

$$f(\mathbf{X}) = {x_1}^2 - x_1 x_2 + 3{x_2}^2 \qquad \text{(VIII.5)}$$

starting at the point $\mathbf{X}^0 = [1,2]$ with $\mathbf{S}^1 = [1,0]$, and $\mathbf{S}^2 = [0,1]$, then it will be found that when searching from $\mathbf{X}^0$ in the direction $\mathbf{S}^1$ for a minimum, it turns to be the point $\mathbf{X}^0$ itself. Thus $\mathbf{X}^1 = \mathbf{X}^0$ and the method breaks down: the directions of search in subsequent iterations are restricted to a subspace which does not contain the direction $\mathbf{S}^1$. The given problem can not therefore be solved by this method.

Powell's Method

Powell modified his basic method to overcome the type of difficulty encountered above by allowing a direction other than $\mathbf{S}^1$ to be discarded after each iteration. In this way, the n directions of search can be chosen so as to be always linearly independent; in some cases, the same n directions are used for two successive iterations. For each iteration starting with initial point $\mathbf{X}^0$ and n directions $\mathbf{S}^j$, $j = 1, 2, ..., n$, it proceeds as follows:

(1) For $i = 1, 2, ..., n$, search from $\mathbf{X}^{i-1}$ in the direction $\mathbf{S}^i$ for a minimum at $\mathbf{X}^i$.

(2) Find

$$\Delta = \max_{1 \leq i \leq n} [f(\mathbf{X}^{i-1}) - f(\mathbf{X}^i)] = f(\mathbf{X}^{q-1}) - f(\mathbf{X}^q) \tag{VIII.6}$$

i.e. q is the value of i which has a maximum value of Δ.

(3) Define

$$f_1 = f(\mathbf{X}^0) \qquad f_2 = f(\mathbf{X}^n) \tag{VIII.7}$$

and evaluate

$$f_3 = f(2\mathbf{X}^n - \mathbf{X}^0) \tag{VIII.8}$$

(4) If either

$$f_3 \geq f_1; \tag{VIII.9}$$

and/or

$$2(f_1 - 2f_2 + f_3)(f_1 - f_2 - \Delta)^2 \geq \Delta(f_1 - f_3)^2, \tag{VIII.10}$$

use the old directions $\mathbf{S}^i$, $i = 1, 2, ..., n$ for the next iteration and use $\mathbf{X}^n$ as the initial point of the next iteration, $\mathbf{X}^0$. Otherwise, use rule (5).

(5) Set $\delta = \mathbf{X}^n - \mathbf{X}^0$; move $\mathbf{X}^n$ to the minimum along the direction δ and call this point $\mathbf{X}^0$; and take the following sequence as the directions for the next iteration

$$\mathbf{S}^1, ..., \mathbf{S}^{q-1}, \mathbf{S}^{q+1}, ..., \mathbf{S}^n, \delta. \tag{VIII.11}$$

In (4), the first inequality considers the value of a tentative value of the objective function (error function) f_3 found by exploring ahead along the new search direction. Here Powell tests the objective function at the point $\mathbf{X} = 2\mathbf{X}^n - \mathbf{X}^0$, which is a point along the direction $\mathbf{S}^n$, located the same distance from $\mathbf{X}^n$ as the original base point $\mathbf{X}^0$. If this tentative point in the new direction does not produce a better value of the objective function than the original base point, the new direction is rejected without further tests as being a poor prospect.

The second inequality is used to determine if the function may not be rising sharply (when seeking a minimum) in the move from the point $\mathbf{X}^n$ to the tentative point $\mathbf{X}$ after dropping sharply from $\mathbf{X}^0$ to $\mathbf{X}^n$. In other words, the test is used to determine if the direction $\mathbf{S}^n$ is pointing across a deep valley, and if it is, we reject it as a reasonable direction of search, retaining the previous search directions for use in the new stage.

Reference

[1] L. Cooper and D. Steinberg 1970, Introduction to Methods of Optimization, W. B. Saunders Co.

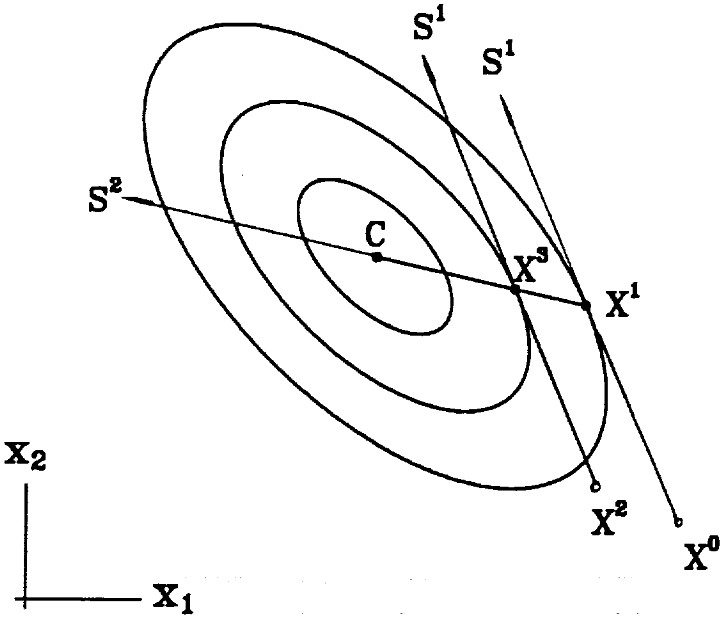

Figure VIII.1

IX.1 Governing Equation for a Nonlinear Beam - Rainflow Counting

The results presented in the following are part of an investigation of the effects of nonlinear vibration on the fatigue of structures. Nonlinear effects are important in fatigue studies because it is usually large deflection response that causes damage and nonlinearities are more prevalent when the deflections are large. While most structural systems are not subjected to sufficient excitations to elicit nonlinear response in service, it is not uncommon to perform experimental studies of the fatigue life with artificially high vibration levels. By testing at high vibration levels the rate of damage accumulation may be accelerated so that the test can simulate a long service life (say 10 to 20 years) during a normal 8 hour working day. In order to properly use the results of the accelerated test, however, it is important to know what influence nonlinearities may have on the results. The goals of the present investigation are to examine the impact of common nonlinear effects on fatigue life and to develop practical tools for including nonlinearities in fatigue predictions.

In the present section the method of Rainflow counting is applied to estimate the fatigue life of a nonlinear beam. The model of the response of the beam comprises an extension of the linear beam analysis presented in section II.2 to account for nonlinearities. The equation of motion for the deflection, W, of a base excited, elastic beam including the effect of nonlinear stretching strain at large deflection is

$$\begin{aligned}&\rho A\ddot{W}(x,t) + \frac{Ebh^3}{12}W_{xxxx} - \\ &\frac{Ebh}{l}W_{xx}\int_0^l W_x^2(\xi,t)d\xi + \eta\dot{W} = -\rho A\ddot{W}_o.\end{aligned} \tag{IX.1.1}$$

where ρ is the density, A is the constant cross sectional area, E is Young's modulus, b is the width, h is the thickness, l is the length, and η is a viscous damping coefficient. The subscript x denotes partial differentiation with respect to x and dots denote partial differentiation with respect to time, t. W is measured relative to the displacement of the beam ends which are assumed to have equal prescribed acceleration $\ddot{W}_o$, and have zero rotation. $\ddot{W}_o$ will be assumed to be stationary Gaussian white noise. In the derivation of equation (IX.1.1) it is assumed that there is no axial displacement at the beam ends. The derivation is presented in section IX.4.

The relation between the strain and displacement of the beam may be shown to be

$$\epsilon_{xx} = \frac{1}{2l}\int_0^l W_x^2(\xi,t)d\xi - z\frac{\partial^2 W(x,t)}{\partial x^2}, \tag{IX.1.2}$$

where z is the vertical distance from the mid-line of the beam. Since the boundaries prevent rotation at the beam ends, the maximum strain will occur at $x = 0$, and $x = l$ and at the extreme fibers at $z = \pm h/2$. The maximum strain is then

$$\epsilon = \frac{1}{2l}\int_0^l W_x^2(\xi,t)d\xi + \frac{h}{2}\frac{\partial^2 W(x,t)}{\partial x^2}, \tag{IX.1.3}$$

where $x = 0$ or $x = l$.

An approximate solution of equation (IX.1.1) may be developed by expanding the displacement response in a finite set of the eigenfunctions for a linear clamped-clamped beam, $\phi_i(x)$,

$$W(x,t) = \sum_{i=1}^{N} \alpha_i(t)\phi_i(x), \tag{IX.1.4}$$

where N is a finite integer and $\alpha_i(t)$ are unknown functions of time. For the linear beam, the eigenfunctions are given by

$$\begin{aligned}\phi_i(x) = \cos(p_i x/l) - \cosh(p_i x/l) + \\ D_i\big(\sin(p_i x/l) - \sinh(p_i x/l)\big)\end{aligned} \tag{IX.1.5}$$

where p_i and D_i are given in Table II.2.1 for the first six eigenfunctions.

Substitution of equation (IX.1.4) into (IX.1.1) leads to a coupled system of nonlinear ordinary differential equations for the $\alpha_i(t)$,

$$\ddot{\alpha}_i + \zeta\dot{\alpha}_i + \omega_i^2\alpha_i + Q(\underline{\alpha})\sum_{j=1}^{N} I_{ij}\alpha_j = F_i\ddot{W}_o(t), \;\; i = 1,2,\ldots N, \tag{IX.1.6}$$

where $\underline{\alpha}$ is a vector containing the $\alpha_i(t)$, and

$$Q(\underline{\alpha}) = \frac{E}{2\rho}\sum_{i=1}^{N}\sum_{j=1}^{N} I_{ij}\alpha_i\alpha_j, \tag{IX.1.7}$$

$$\zeta = \frac{\eta}{\rho A}, \tag{IX.1.8}$$

$$\omega_i^2 = \frac{Eh^2}{12\rho}\left(\frac{p_i}{l}\right)^4, \tag{IX.1.9}$$

$$I_{ij} = \frac{1}{l}\int_0^l \frac{\partial\phi_i(x)}{\partial x}\frac{\partial\phi_j(x)}{\partial x}dx, \tag{IX.1.10}$$

and

$$F_i = -\frac{1}{l}\int_0^l \phi_i(x)dx. \tag{IX.1.11}$$

Note that due to the symmetry of the beam F_i is zero if i is even. As a result, the steady-state response corresponding to even numbered modes is zero,

$$\lim_{t\to\infty} \alpha_i(t) = 0 \;\; \text{if } i \text{ is even.} \tag{IX.1.12}$$

Once the $\alpha_i(t)$ are determined, the displacement, $W(x,t)$, is obtained from equation (IX.1.4) and the maximum strain may be calculated using equation (IX.1.3).

IX.2 Quasi-Simulation for Multi-Mode Nonlinear Systems

In this section, we shall present the method of equivalent linearization for solving equation (IX.1.6). A simulation procedure of the resulting equivalent linear system is then developed to generate the maximum strain time history for the purpose of fatigue analysis.

The method of equivalent linearization consists of approximating equation (IX.1.6) by an equivalent linear system,

$$\ddot{\alpha}_i + \zeta\dot{\alpha}_i + \sum_{j=1}^{N} K_{ij}\alpha_i + e_i(\underline{\alpha}) = F_i\ddot{W}_o(t), \quad i = 1, 2, \ldots N, \tag{IX.2.1}$$

where the constants K_{ij} are chosen to minimize the error, $e_i(\underline{\alpha})$, in some sense. From equations (IX.1.6) and (IX.2.1), the error term $e_i(\underline{\alpha})$ can be written in a vector form

$$\mathbf{e} = \{e_i(\underline{\alpha})\} = \left\{ \sum_{j=1}^{N} K_{ij}\alpha_j - \omega_i^2\alpha_i - Q(\underline{\alpha})\sum_{j=1}^{N} I_{ij}\alpha_j \right\}. \tag{IX.2.2}$$

Minimization of the steady-state mean square value of the $\mathbf{e}$ with respect to K_{ij} leads to

$$\frac{\partial \mathrm{E}[\mathbf{e}^T\mathbf{e}]}{\partial K_{ij}} = 0. \tag{IX.2.3}$$

Expanding equation (IX.2.3), and using equation (IX.1.7) give

$$\begin{aligned} &\sum_{m=1}^{N} K_{im}\mathrm{E}[\alpha_m\alpha_j] = \omega_i^2\mathrm{E}[\alpha_i\alpha_j] + \\ &\frac{E}{2\rho}\sum_{m=1}^{N}\sum_{k=1}^{N}\sum_{l=1}^{N} I_{im}I_{kl}\mathrm{E}[\alpha_j\alpha_m\alpha_k\alpha_l]. \end{aligned} \tag{IX.2.4}$$

The solution for the α_i's from equation (IX.2.1) with the error term neglected is known to be jointly Gaussian. The fourth order moments in equation (IX.2.4) can thus be expressed in terms of lower order moments,

$$\begin{aligned} &\mathrm{E}[\alpha_j\alpha_m\alpha_k\alpha_l] = \mathrm{E}[\alpha_j\alpha_m]\mathrm{E}[\alpha_k\alpha_l] + \\ &\mathrm{E}[\alpha_j\alpha_k]\mathrm{E}[\alpha_m\alpha_l] + \mathrm{E}[\alpha_j\alpha_l]\mathrm{E}[\alpha_m\alpha_k]. \end{aligned} \tag{IX.2.5}$$

In deriving equation (IX.2.5), we have used the fact that all the odd order steady-state moments of the α_i's are zero. Substituting equation (IX.2.5) in equation (IX.2.4) gives

$$\begin{aligned} &\sum_{m=1}^{N} K_{im}\mathrm{E}[\alpha_m\alpha_j] = \omega_i^2\mathrm{E}[\alpha_i\alpha_j] + \frac{E}{2\rho}\times \\ &\sum_{m=1}^{N}\sum_{k=1}^{N}\sum_{l=1}^{N} I_{im}I_{kl}\{\mathrm{E}[\alpha_j\alpha_m]\mathrm{E}[\alpha_k\alpha_l] + 2\mathrm{E}[\alpha_j\alpha_k]\mathrm{E}[\alpha_m\alpha_l]\}. \end{aligned} \tag{IX.2.6}$$

Equation (IX.2.6) can be used to determine the components of K_{ij}. However, one has to solve simultaneously for $\mathrm{E}[\alpha_i\alpha_j]$ and K_{ij} using an iterative procedure as described in the following. To simplify the discussion, we introduce the following matrix notations:

$$\mathbf{R} = \{\mathrm{E}[\alpha_i\alpha_j]\}\,,\ \ \mathbf{K} = \{K_{ij}\}\,,\ \ \mathbf{I} = \{I_{ij}\}\,,$$
$$\boldsymbol{\Omega}^2 = \begin{pmatrix} \omega_1^2 & & & \\ & \omega_2^2 & & \\ & & \ddots & \\ & & & \omega_N^2 \end{pmatrix}. \tag{IX.2.7}$$

Equation (IX.2.6) may then be written in a compact form

$$\mathbf{K}\cdot\mathbf{R} = \boldsymbol{\Omega}^2\cdot\mathbf{R} + \frac{E}{2\rho}\left\{(\mathbf{I}\colon\mathbf{R})\mathbf{I}\cdot\mathbf{R} + 2(\mathbf{I}\cdot\mathbf{R})\cdot(\mathbf{I}\cdot\mathbf{R})\right\}, \tag{IX.2.8}$$

where

$$(\mathbf{K}\cdot\mathbf{R})_{ij} = \sum_{m=1}^{N} K_{im}R_{mj},\ \ (\mathbf{I}\colon\mathbf{R}) = \sum_{i=1}^{N}\sum_{j=1}^{N} I_{ij}R_{ij}.$$

Solving equation (IX.2.8) for $\mathbf{K}$, we have

$$\mathbf{K} = \boldsymbol{\Omega}^2 + \frac{E}{2\rho}\left\{(\mathbf{I}\colon\mathbf{R})\mathbf{I} + 2(\mathbf{I}\cdot\mathbf{R})\cdot\mathbf{I}\right\}. \tag{IX.2.9}$$

Notice that in general, $\mathbf{K}$ is not diagonal. Neglecting the error term, $e_i(\underline{\alpha})$, in equation (IX.2.1), then leads to a coupled system of linear ordinary differential equations. With $e_i(\underline{\alpha})$ neglected, equation (IX.2.1) may be solved using modal analysis.

Consider the equation

$$\ddot{\underline{\alpha}} + \mathbf{K}\underline{\alpha} = \mathbf{0}. \tag{IX.2.10}$$

Let γ_i^2 $(i = 1, 2, \ldots, N)$ be the eigenvalues of the matrix $\mathbf{K}$ in equation (IX.2.10) and let $\boldsymbol{\Phi}$ be the normalized matrix of eigenvectors such that

$$\boldsymbol{\Phi}^T\cdot\boldsymbol{\Phi} = \mathcal{I},\ \ \boldsymbol{\Phi}^T\cdot\mathbf{K}\cdot\boldsymbol{\Phi} = \begin{pmatrix} \gamma_1^2 & & & \\ & \gamma_2^2 & & \\ & & \ddots & \\ & & & \gamma_N^2 \end{pmatrix}. \tag{IX.2.11}$$

where $\mathcal{I}$ is the unit matrix. Also let

$$\underline{\alpha} = \boldsymbol{\Phi}\underline{\beta},\ \ \mathbf{f} = \boldsymbol{\Phi}^T\mathbf{F}. \tag{IX.2.12}$$

If the error term, $e_i(\underline{\alpha})$, is neglected, equations (IX.2.1) and (IX.2.12) lead to the equations for modal coordinates β_i

$$\ddot{\beta}_i + \zeta\dot{\beta}_i + \gamma_i^2\beta_i = f_i\ddot{W}_o,\ \ i = 1, 2, \ldots N. \tag{IX.2.13}$$

This uncoupled system of equations will be used in the following to simulate the time domain response of the nonlinear beam. Define a matrix of second order moments of the modal coordinates,

$$\mathcal{R} = \{\mathrm{E}[\beta_i \beta_j]\}, \tag{IX.2.14}$$

where the steady-state moment $\mathrm{E}[\beta_i \beta_j]$ can be obtained as

$$\mathrm{E}[\beta_i \beta_j] = \frac{\zeta f_i f_j G_{\ddot{W}_o}}{(\gamma_i^2 - \gamma_j^2)^2 + 2\zeta^2(\gamma_i^2 + \gamma_j^2)}, \tag{IX.2.15}$$

and where $G_{\ddot{W}_o}$ is the single sided power spectral density of $\ddot{W}_o$ with units of acceleration squared per Hertz. The matrices $\mathbf{R}$ and $\mathcal{R}$ are related by

$$\mathbf{R} = \mathbf{\Phi} \cdot \mathcal{R} \cdot \mathbf{\Phi}^T. \tag{IX.2.16}$$

Using equations (IX.2.9) through (IX.2.16), the iterative procedure for determining $\mathbf{R}$ and $\mathbf{K}$ may be stated as follows:

Step 1. (Zero order approximation) Assume that

$$\mathrm{E}[\alpha_i \alpha_j] = 0, \quad K_{ij} = 0 \quad \text{for } i \neq j.$$

Then, from equation (IX.2.6),

$$K_{ii} = \omega_i^2 + \frac{E}{2\rho} \sum_{j=1}^{N} (I_{ii} I_{jj} + 2 I_{ij}^2) \mathrm{E}[\alpha_j^2] \tag{IX.2.17}$$

By neglecting the error term, $e_i(\underline{\alpha})$ in equation (IX.2.1) and neglecting the off-diagonal elements of K_{ij}, we obtain

$$K_{ii} = \frac{F_i^2 G_{\ddot{W}_o}}{4\zeta \mathrm{E}[\alpha_i^2]}. \tag{IX.2.18}$$

Equations (IX.2.17) and (IX.2.18) can be readily solved iteratively by starting with an initial value of $K_{ii} = \omega_i^2$. Equation (18) may then be used to determine $\mathrm{E}[\alpha_i^2]$ and the result substituted into equation (IX.2.17). Evaluation of (IX.2.17) then produces an up dated value of K_{ii}. This process may be repeated until K_{ii} and $\mathrm{E}[\alpha_i^2]$ converge.

Step 2. Compute K_{ij} for $i \neq j$. Using the results from Step 1 in equation (IX.2.6) gives

$$K_{ij} = \frac{E}{2\rho} \sum_{k=1}^{N} (I_{ij} I_{kk} + 2 I_{ik} I_{jk}) \mathrm{E}[\alpha_k^2], \quad i \neq j. \tag{IX.2.19}$$

Step 3. Determine the eigenvalues and eigenvectors of the matrix $\mathbf{K}$ in equation (IX.2.10).

Step 4. Evaluate $\mathcal{R}$ and then $\mathbf{R}$ using equations (IX.2.14) through (IX.2.16). Let $\mathbf{R}_n$ and $\mathbf{K}_n$ denote the $\mathbf{R}$ and $\mathbf{K}$ matrices obtained in the n^{th} iteration. $\mathbf{K}_n$ is updated by using equation (IX.2.9) where $\mathbf{R}$ is replaced with $\mathbf{R}_n$.

Step 5. Check convergence. If

$$||\mathbf{R}_n - \mathbf{R}_{n-1}|| < \delta_R, \text{ or } ||\mathbf{K}_n - \mathbf{K}_{n-1}|| < \delta_K, \tag{IX.2.20}$$

then stop the iteration, otherwise, repeat the iteration from Step 3. In equation (IX.2.20) δ_R and δ_K are two given small numbers, and $|| \cdot ||$ denotes the norm of a matrix. The infinite norm

$$||\mathbf{R}||_\infty = \max_{i,j} |R_{ij}| \tag{IX.2.21}$$

is used in this study.

It should be pointed out that in additional to matrices $\mathbf{R}$ and $\mathbf{K}$, the eigenmatrix $\mathbf{\Phi}$ and eigenvalues γ_i^2 are also obtained at the end of the above iteration. These are the results we need for the subsequent fatigue analysis. Most applications of the method of equivalent linearization end at yielding the matrices $\mathbf{R}$ and $\mathbf{K}$.

We have thus far completed the description of the method of equivalent linearization for determining the response of the nonlinear beam under consideration. The general idea of this method applies equally well to other nonlinear structures. To analyze the fatigue damage of the beam, we need samples of the time history of $\alpha_i(t)$ to generate time histories of the strain or stress. It turns out that it is more efficient to do so if the strain is expressed in terms of modal coordinates $\beta_i(t)$. Using equations (IX.1.3) and (IX.1.4), the maximum strain of the beam at $x = 0$ or l can be written as

$$\epsilon = \mathbf{a}^T \underline{\alpha} + \frac{1}{2} \underline{\alpha}^T \mathbf{I}\, \underline{\alpha}, \tag{IX.2.22}$$

where

$$\mathbf{a} = \{a_i\} = \left\{ -\frac{h}{2} \frac{\partial^2 \phi_i(0)}{\partial x^2} \right\}, \tag{IX.2.23}$$

and $\mathbf{I}$ is defined in equation (IX.2.7). By substituting the first of equations (VI.12) into equation (IX.2.22) the maximum strain may be expressed in terms of the $\beta_i(t)$,

$$\epsilon = \hat{\mathbf{a}}^T \underline{\beta} + \frac{1}{2} \underline{\beta}^T \hat{\mathbf{I}}\, \underline{\beta}, \tag{IX.2.24}$$

where

$$\hat{\mathbf{a}} = \mathbf{a}^T \mathbf{\Phi}, \;\; \hat{\mathbf{I}} = \mathbf{\Phi}^T \mathbf{I}\, \mathbf{\Phi}. \tag{IX.2.25}$$

The modal responses of the equivalent linear system, $\beta_i(t)$, can be readily simulated from equation (IX.2.13). Equation (IX.2.24) then gives the strain time history. Once the strain time histories are generated, a fatigue damage model may be applied to estimate the fatigue life.

An efficient way of generating the time history of $\beta_i(t)$ is to integrate equation (IX.2.13) numerically using the central difference scheme:

$$\beta_i(t_{n+1}) = C_1 \beta_i(t_n) + C_2 \beta_i(t_{n-1}) + C_3 f_i \ddot{W}_o(t_n). \tag{IX.2.26}$$

where t_n is the value of t at the n^{th} time step, $t_n = n \cdot \Delta t$, where Δt is the time increment. The constants C_1, C_2, and C_3 are given by

$$C_1 = \frac{2 - \gamma_i^2 \Delta t^2}{\frac{1}{2}\zeta \Delta t + 1}, \; C_2 = \frac{\frac{1}{2}\zeta \Delta t - 1}{\frac{1}{2}\zeta \Delta t + 1}, \; C_3 = \frac{\zeta \Delta t^2 - 1}{\frac{1}{2}\zeta \Delta t + 1}. \tag{IX.2.27}$$

Note that because the calculations are performed in terms of uncoupled modal coordinates, the modal responses may be obtained using parallel processors with vectorization.

The local truncation error of the central difference scheme is of the order $O(\Delta t^2)$. The spectral stability condition of the scheme for each mode is given by [1]

$$0 \leq \Delta t \leq \frac{2}{\gamma_i}, \; i = 1, 2, \ldots, N. \tag{IX.2.28}$$

Hence, the stability condition for the entire system is given by

$$0 \leq \Delta t \leq \frac{2}{\gamma_N}, \tag{IX.2.29}$$

where γ_N^2 is the largest eigenvalue in equation (IX.2.11). The time step Δt in our simulation is chosen according to equation (IX.2.29). The time series of the white noise excitation $\ddot{W}_o(t_n)$ is simulated by using Rice's approach and the Fast Fourier Transform [2].

We shall refer to the method of fatigue analysis described in this section as the quasi-simulation approach. In summary, the method of equivalent linearization is used to obtain the eigenvalues and eigenmatrix of the uncoupled equivalent linear system, and then the time histories of the modal coordinates are simulated numerically to generate the strain time histories for the fatigue analysis. It should be noted that once the equivalent linear system is determined, the computational effort of simulating the time series of the response is identical to that required for a linear system and is independent of the type of nonlinearity. Since a large number of very long time series are required to obtain accurate fatigue estimates, the 'over-head' required in constructing the equivalent linear system is comparatively small.

IX.4 Numerical results

The quasi-simulation approach developed in the previous section has been applied to estimate the fatigue life of a nonlinear beam and the results compared to those obtained using a conventional numerical simulation. The comparisons were performed to identify the errors in the approximate method and to quantify the savings in computation time. The conventional simulations were obtained using a fourth order Runge-Kutta algorithm. The same time step, Δt, was used in all computations. The parameters of the beam used in the numerical study are:

$$E = 10^7 \#/in^2, \; \rho = .1 \#/in^3, \; h = .032in,$$
$$l = 15in, \; \eta = 3.016, \; b = 2, \; A = .064,$$

where the variables are defined in the discussion following equation (IX.1.1). The number of resonant modes was taken to be three.

Estimated fatigue lives are shown in figures IX.4.1 and IX.4.2 for the nonlinear beam modeled in the previous sections. In these figures the dots indicate results obtained using a full numerical simulation and the lines are the result of the approximate method. The estimated fatigue lives are found to be in excellent agreement for a range of excitation levels and for a range of values of the fatigue exponent, b, in equation (III.1.1).

In the results shown in figure IX.4.1, damage was assumed to occur at each stress maximum in the time domain. In figure IX.4.2 damage was accumulated only for the greatest stress maximum between zero crossings. Of course, as discussed above, one can accommodate any desired damage counting scheme in a simulation procedure.

Equation (III.1.1) was implemented in the simulations in the form

$$D_m \leftarrow D_m + \frac{|S|^b}{c}, \tag{IX.4.1}$$

where D_m is initially set to zero and S is the level of the stress maximum. The absolute value of the stress is taken to allow for positive contributions to damage due to negative maxima. b is the fatigue exponent which for most materials varies between 2 and 6. c is a material constant taken to be 6.56×10^{30}. The value of c has no effect on the comparison between the methods shown in figures IX.4.1 and IX.4.2.

Once the simulated damage is accumulated according to equation (IX.4.1) for a sufficiently long time, τ, the average damage rate is simply

$$\Delta = D_m/\tau, \tag{IX.4.2}$$

and the simulated mean fatigue life is

$$T = 1/\Delta. \tag{IX.4.3}$$

Figures IX.4.1 does not reveal the amount of nonlinearity in the system at the excitation levels used here. To indicate the influence of nonlinearity, the power spectral density of the stress time history was computed for three excitation levels. The results are shown in figures IX.4.3 through IX.4.5. In figure IX.4.3 it is clear that three resonant modes contribute to the response. In this figure the excitation level was not intense enough to elicit nonlinear behavior. As the excitation level is increased, the full simulation shows that the three dominant peaks are shifted to higher frequencies and become broadened. Additional peaks in the stress spectrum also become apparent at the higher excitation levels. Since the response is drastically different at the higher levels than at low excitation levels, nonlinear effects clearly play an important role. A further indication of the degree of nonlinearity in the response can be seen in figure IX.4.6 which shows the mean square displacement at the center of the beam with and without nonlinearities included. The figure shows that above roughly -35 dB (g^2/Hz) the nonlinearities are substantial.

The increase in resonant frequencies and the broadening of the resonant peaks are common behaviors of random systems with stiffness nonlinearities. The broadening of the resonant peaks has been shown to result from the fact that the resonant frequencies become random in a system where the stiffness depends on the random response amplitude [3]. It has also been shown (and can be seen in figures IX.4.3 through IX.4.5) that while equivalent linearization accounts for the increase in the resonant frequencies due to nonlinear stiffness, it does not depict the broadening behavior [4]. Although equivalent linearization does not accurately represent the response spectrum, it has been applied very successfully using a probabilistic approach to estimate fatigue life for a single degree of freedom system [5]. The results obtained in the present study show that equivalent linearization may also be used in a time domain approach to estimate fatigue lives for multi-degree of freedom nonlinear systems. Theoretical aspects, such as error analysis and convergence, of the method of equivalent linearization for the fatigue analysis of nonlinear structures await further studies.

Along with the shift and broadening of the resonant response peaks, figures IX.4.3 through IX.4.5 also show that the nonlinearities produce additional peaks in the stress spectrum. These added peaks arise from the nonlinear stress/displacement relationship in equation (IX.1.2) and from the nonlinear coupling in equation (IX.1.6).

As mentioned above, the numerical comparisons were performed to evaluate the accuracy of the approximate simulation and to determine the improvement in computational efficiency relative to conventional simulation methods. In the present effort, our purpose is not to conduct a comprehensive comparison of numerical simulation methods. The present results primarily serve to indicate the validity and potential of the approach. For the cases studied here where the beam was assumed to have three resonant modes, the quasi-simulations required roughly $(1/8)^{th}$ the computer time used to perform the full simulations.

All of the calculations were performed on an IBM 3090 computer using a single processor without vectorization. Since the present approach is well suited to parallel computation on multiple processor computers, even greater savings are achievable.

References

[1] T. J. R. Hughes 1987 *The Finite Element Method.* Englewood Cliffs, NJ: Prentice-Hall, Inc..

[2] M. Shinozuka 1972 *Computers and Structures* **2**, 855–874. Monte Carlo solution of structural dynamics.

[3] R. N. Miles 1989 *Journal of Sound and Vibration* **132**, 43–49. An approximate solution for the spectral response of Duffing's oscillator with random input.

[4] P. G. Reinhall and R. N. Miles 1989 *Journal of Sound and Vibration* **132**, 33–42. Effect of damping and stiffness on the random vibration of nonlinear periodic plates.

[5] R. N. Miles Equivalent linearization for fatigue life estimates of a nonlinear structure. *NASA* TM 101536.January1989

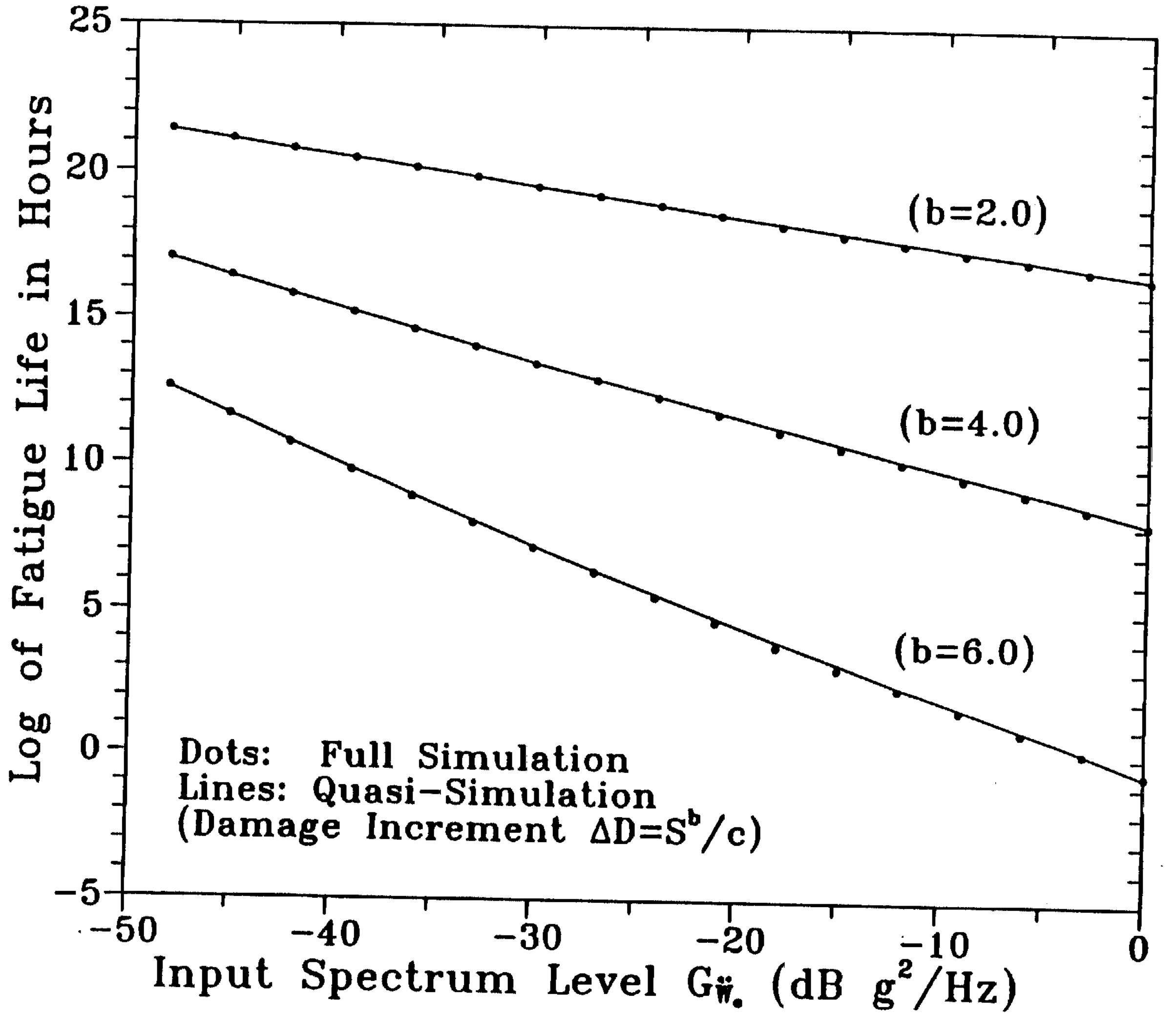

Figure IX.4.1
Predicted fatigue lives of a nonlinear beam having three resonant modes obtained using full numerical simulation and the present quasi−simulation method. The calculations were performed assuming that damage occurs at each stress maximum.

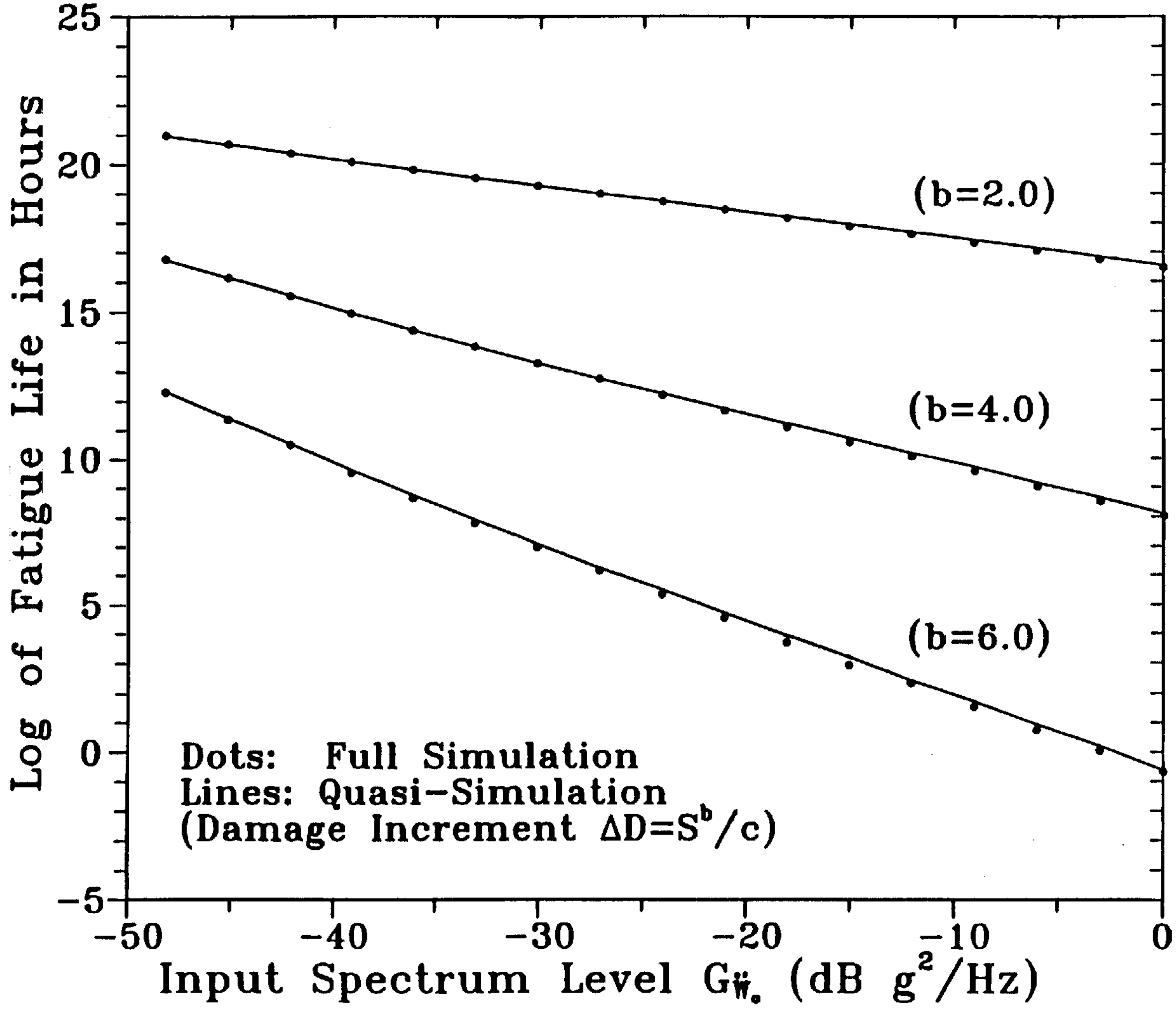

Figure IX.4.2 Predicted fatigue lives of a nonlinear beam having three resonant modes obtained using full numerical simulation and the present quasi−simulation method. The calculations were performed assuming that damage occurs at the maximum stress peak between each zero crossing.

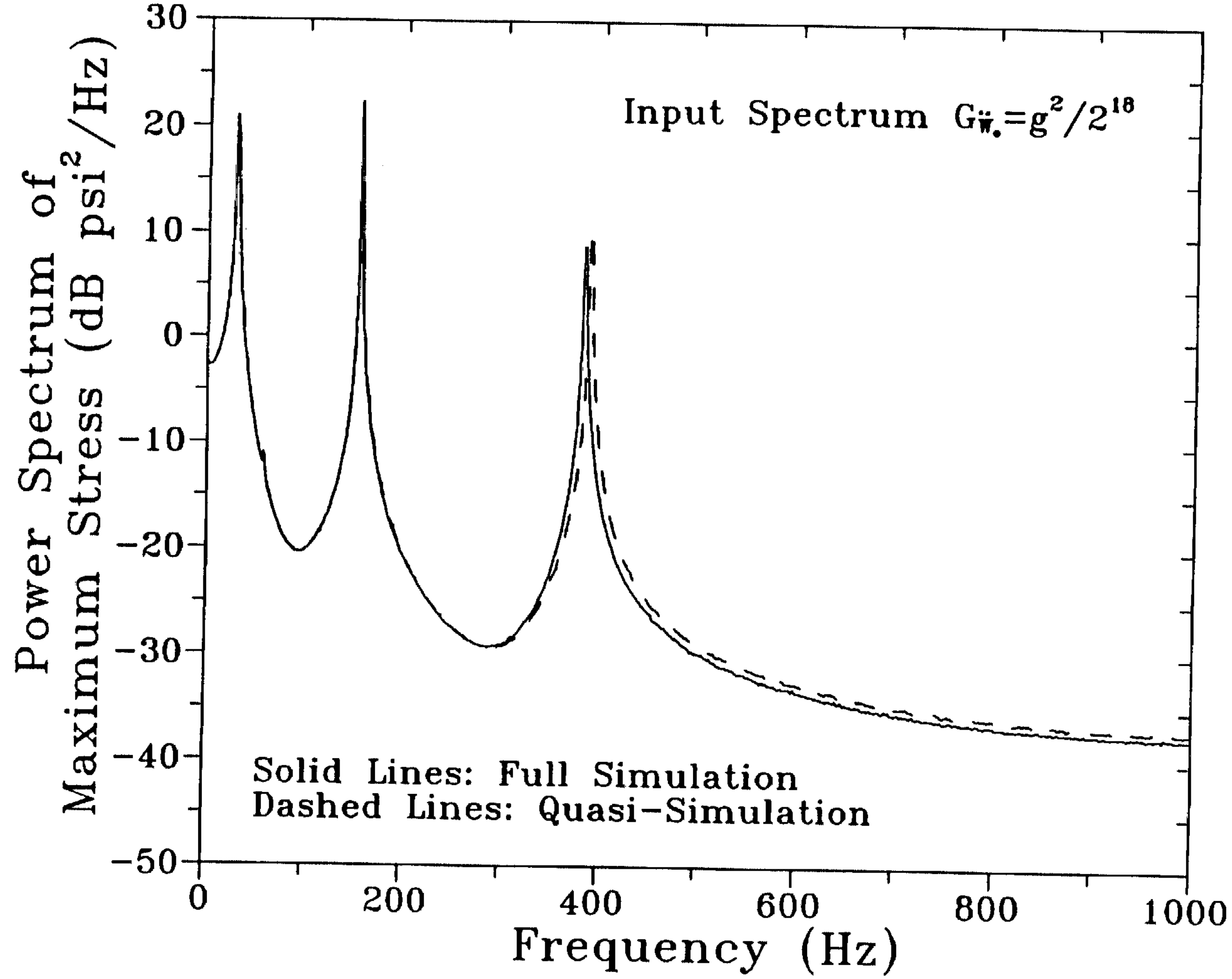

Figure IX.4.3
Comparison of stress spectra obtained using a full numerical simulation and the present quasi-simulation approach. g is the acceleration due to gravity.

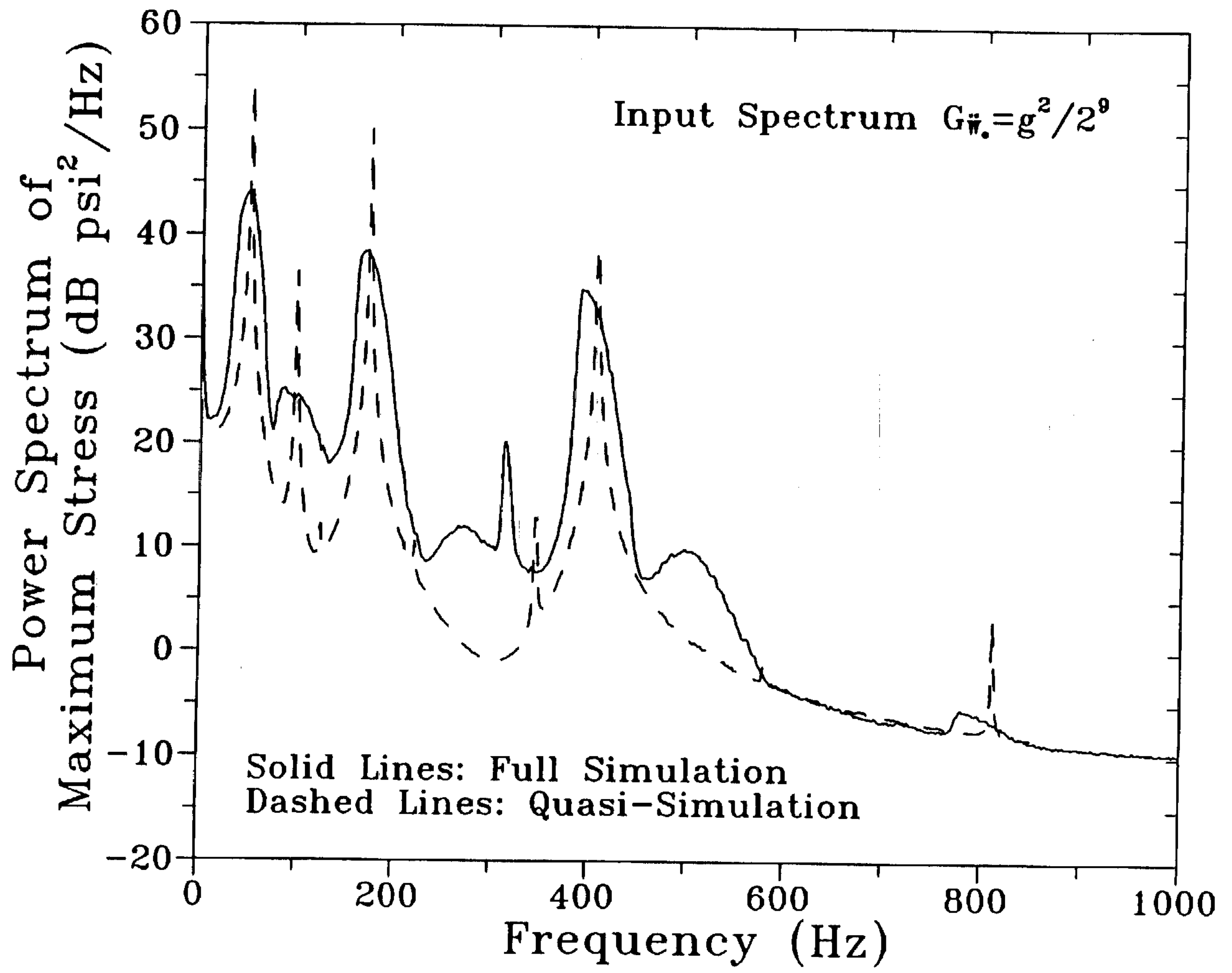

Figure IX.4.4 Comparison of stress spectra obtained using a full numerical simulation and the present quasi-simulation approach. g is the acceleration due to gravity.

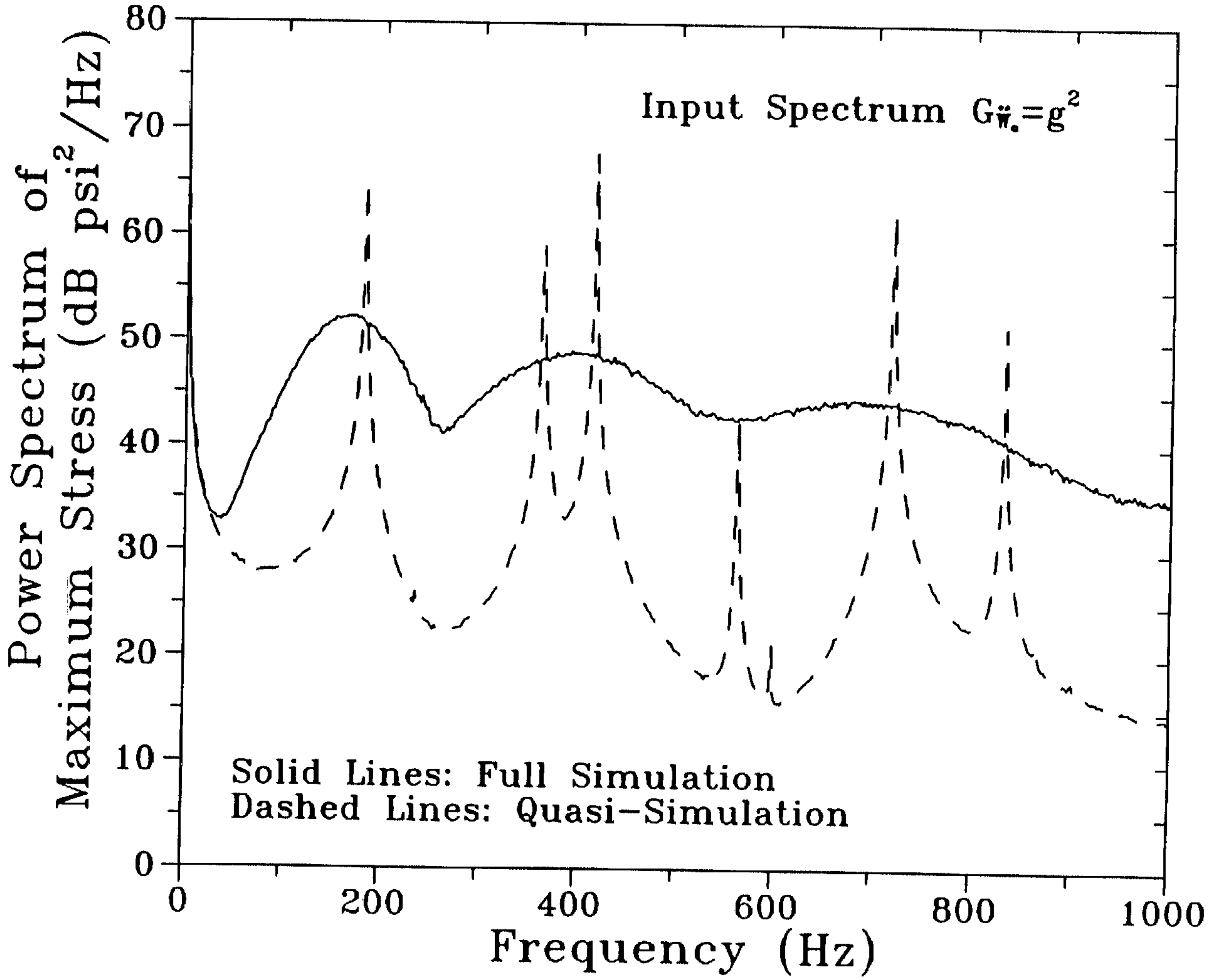

Figure IX.4.5
Comparison of stress spectra obtained using a full numerical simulation and the present quasi–simulation approach. g is the acceleration due to gravity.

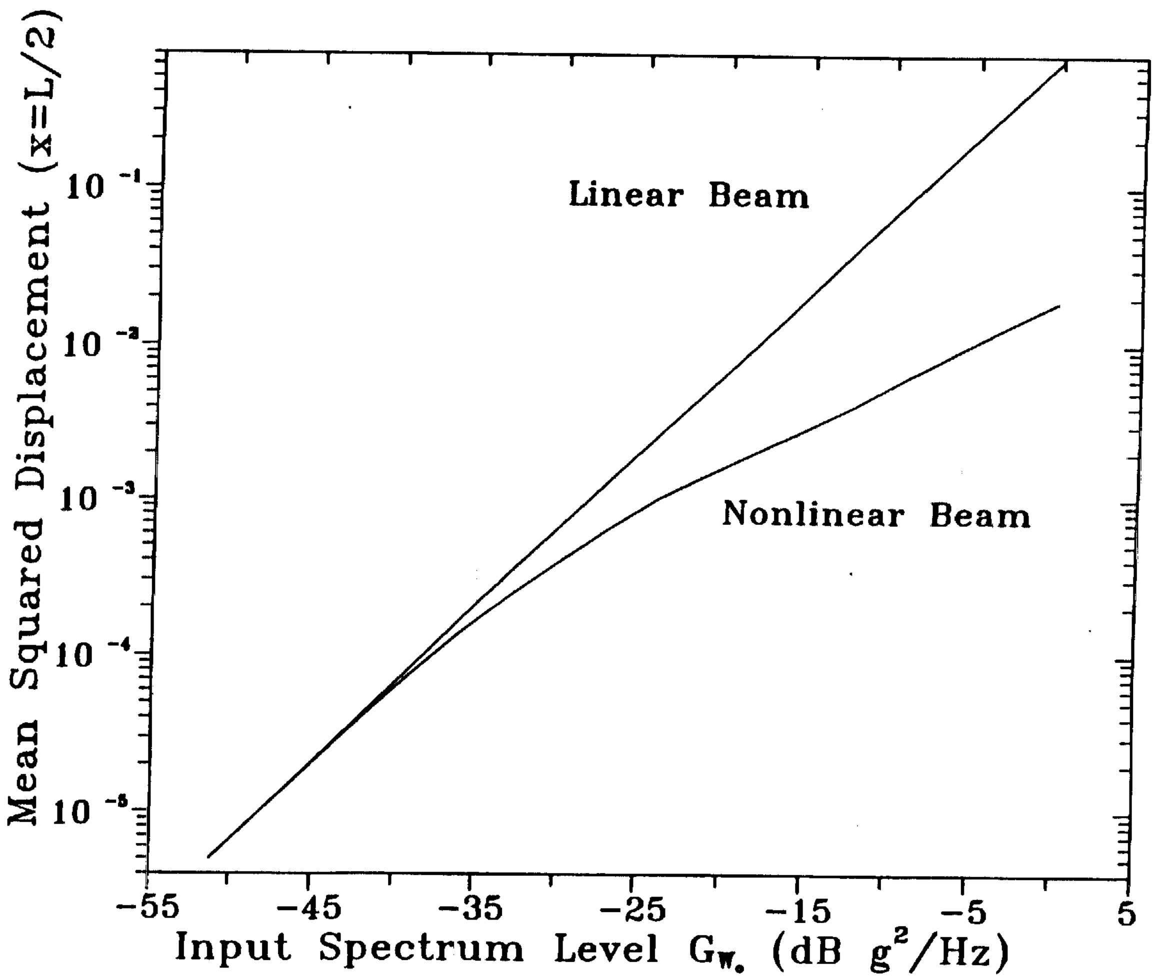

Figure IX.4.6 Comparison of the mean squared displacement at the center of a linear beam and a nonlinear beam.

X. Nonlinear Plates

In the previous section an application of equivalent linearization is developed to estimate the fatigue life of a simple beam with multiple resonant modes. The results indicate that the method is applicable to fatigue prediction in nonlinear structures. Because we are usually concerned with the problem of estimating the fatigue life of structures that are considerably more complicated than beams, the procedure has been applied to a nonlinear plate. The next logical application of the method should be on stiffened plates or shells such as fuselage structures. This extension of the method will be left to future studies.

In the present section, a model of a nonlinear plate is developed based on Von-Karmán plate theory and a governing equation for transverse motion only is derived by neglecting the in-plane inertia. As in the analysis of the nonlinear beam of the previous section, an equivalent linearization approach is used to approximate the nonlinear system with a equivalent linear system by selecting the damping properties and natural frequencies to minimize the mean square error between the approximate and original system. Further, the construction of the time domain response due to stationary Gaussian random excitation is relatively straight-forward and the geometrical nonlinearity which results in a nonlinear relationship between strain and displacement is considered. Because the plate we considered has multiple resonant modes, the response will be broad-band in nature. The Rain-Flow Cycle Counting scheme which is applicable to a broad-band process is used to estimated the fatigue life. The present approach is based on an analysis of the stress and strain in the time domain because the Rain-Flow Cycle Counting scheme is extremely difficult to incorporate in a probabilistic formulation.

It has been shown previously that although the equivalent linearization method is not appropriate for estimating the power spectral density and some other statistics, it yields reasonably accurate estimates of the mean square response. We have shown that the estimated fatigue lives of nonlinear beams are in excellent agreement with results obtained by more accurate techniques. The purpose of the present study is to extend these results to nonlinear plates.

Comparisons are presented of the estimated fatigue lives of a plate with multiple resonant modes and geometrical nonlinearity as obtained by present method and by a full numerical simulation. It is found that the fatigue lives agree very closely even when nonlinearities dominate the response. Since the major computational effort of the present approach is concentrated on constructing the time domain response of the equivalent linear system, the efficiency and complexity of the analysis are not affected by the nonlinearity of the structure. This feature makes the present approach a very practical method for fatigue study of highly complex structures. Further, the equivalent linearization approach is efficient enough to allow us to compute fatigue lives at a large number of points on a plate which is almost impossible to get by using full numerical simulation.

A comparison is presented of predicted fatigue lives with and without nonlinearities included in the model. It is found that although the predicted fatigue lives are in close agreement when excitation is low, the fatigue lives differ significantly when the excitation is high. This is because the geometrical nonlinearities which are caused by the stretching of the plate reduce the mean square stress response and increase the predicted fatigue lives. It is implied that we can not calculate the low excitation fatigue lives from the high excitation fatigue lives by using a simple linear extrapolation.

X.1. Nonlinear Plate

In this section, the governing equation for a nonlinear plate which is subject to random excitation is obtained, an equivalent linear approach is derived in detail and the maximum stress of the plate is computed in terms of the modal coordinates. It will be assumed that the plate is excited by the transverse motion of its boundaries.

X.1.1 Basic Assumptions for a Nonlinear Plate

The assumptions of the present investigation are based on the Von-Karmán plate theory. For a thin plate subject to large elastic deflection with small rotation, the following assumptions are made:

1. The plate is thin, the thickness h is much smaller than the wavelength of any vibration modes considered in the model.
2. The magnitude of the deflection W is of the same order as the thickness h of the plate.
3. The slope is everywhere small.
4. The in-plane displacements U and V are infinitesimal. In the strain-displacement relations, only those nonlinear terms involving $\frac{\partial W}{\partial x}, \frac{\partial W}{\partial y}$ are included, all other nonlinear terms are neglected.
5. All strain components are small so that Hook's law holds.
6. Kirchhoffe's hypotheses hold: Tractions on surfaces parallel to the middle surface are negligible, and strains vary linearly within the plate thickness.
7. The in-plane inertia is negligible compared with the transverse inertia.

X.1.2 Governing Equation for a Nonlinear Plate

Let $U(x,y,t), V(x,y,t)$,and $W(x,y,t)$(see Figure X.1) be the displacements of a point (x,y) at the middle plane of the plate relative to the motion at the boundaries at $x = 0, a,\ y = 0, b$. The displacements of an arbitrary point within the plate are given by,

$$\begin{aligned} U_x(x,y,z,t) &= U(x,y,t) - z\frac{\partial W(x,y,t)}{\partial x} \\ U_y(x,y,z,t) &= V(x,y,t) - z\frac{\partial W(x,y,t)}{\partial y} \\ U_z(x,y,z,t) &= W(x,y,t). \end{aligned} \tag{X.1.1}$$

The Green's strain components are given by,

$$\epsilon_{ij} = \frac{1}{2}(\frac{\partial U_i}{\partial x_j} + \frac{\partial U_j}{\partial x_i} + \sum_k \frac{\partial U_k}{\partial x_i}\frac{\partial U_k}{\partial x_j}), \tag{X.1.2}$$

where we have dropped the explicit dependence on x, y and t to simplify the notation.

Because we regard the thin plate as a plane stress problem, we can neglect the z components of the strain and stress. From equation (X.1.2) and Hook's law, we can get the relationships for strain ϵ and stress σ in terms of the displacements at the middle plane of the plate,

$$\begin{aligned}
\epsilon_{xx} &= \frac{\partial U}{\partial x} - z\frac{\partial^2 W}{\partial x^2} + \frac{1}{2}\left(\frac{\partial W}{\partial x}\right)^2 \\
\epsilon_{yy} &= \frac{\partial V}{\partial y} - z\frac{\partial^2 W}{\partial y^2} + \frac{1}{2}\left(\frac{\partial W}{\partial y}\right)^2 \\
\epsilon_{xy} &= \frac{1}{2}\left[\frac{\partial U}{\partial y} + \frac{\partial V}{\partial x} - 2z\frac{\partial^2 W}{\partial x \partial y} + \frac{\partial W}{\partial x}\frac{\partial W}{\partial y}\right],
\end{aligned} \tag{X.1.3}$$

$$\begin{aligned}
\sigma_{xx} &= \frac{E}{1-\nu^2}(\epsilon_{xx} + \nu\epsilon_{yy}) \\
\sigma_{yy} &= \frac{E}{1-\nu^2}(\epsilon_{yy} + \nu\epsilon_{xx}) \\
\sigma_{xy} &= \frac{E}{1+\nu}\epsilon_{xy},
\end{aligned} \tag{X.1.4}$$

where E, ν are Young's modulus and Poisson ratio of the material, respectively.

The kinetic energy $\mathcal{T}$ and strain energy $\mathcal{V}$ are given by,

$$\mathcal{T} = \frac{\rho}{2}\int_{-\frac{h}{2}}^{\frac{h}{2}}\int_0^b\int_0^a\left[\left(\frac{\partial U_x}{\partial t}\right)^2 + \left(\frac{\partial U_y}{\partial t}\right)^2 + \left(\frac{\partial U_z}{\partial t} + \frac{\partial W_0}{\partial t}\right)^2\right] dxdydz \tag{X.1.5}$$

$$\mathcal{V} = \frac{1}{2}\int_{-\frac{h}{2}}^{\frac{h}{2}}\int_0^b\int_0^a(\sigma_{xx}\epsilon_{xx} + \sigma_{yy}\epsilon_{yy} + 2\sigma_{xy}\epsilon_{xy})\, dxdydz, \tag{X.1.6}$$

where, a, b, h are the length, width and thickness of the plate, ρ is the mass density and W_0 is the prescribed motion of the boundaries. Substituting equations (X.1.1), (X.1.3) and (X.1.4) into (X.1.5) and (X.1.6), integrating with respect to z, gives,

$$\begin{aligned}
\mathcal{T} = {} & \frac{\rho h}{2}\int_0^b\int_0^a\left[\left(\frac{\partial U}{\partial t}\right)^2 + \left(\frac{\partial V}{\partial t}\right)^2 + \left(\frac{\partial W}{\partial t} + \frac{\partial W_0}{\partial t}\right)^2\right] dxdy \\
& + \frac{\rho h^3}{24}\int_0^b\int_0^a\left[\left(\frac{\partial^2 W}{\partial x \partial t}\right)^2 + \left(\frac{\partial^2 W}{\partial y \partial t}\right)^2\right] dxdy;
\end{aligned} \tag{X.1.7}$$

$$
\begin{aligned}
\mathcal{V} = {} & \frac{D}{2}\int_0^b\!\!\int_0^a \left[\left(\frac{\partial^2 W}{\partial x^2}\right)^2 + \left(\frac{\partial^2 W}{\partial y^2}\right)^2 + 2\nu\frac{\partial^2 W}{\partial x^2}\frac{\partial^2 W}{\partial y^2} + 2(1-\nu)\left(\frac{\partial^2 W}{\partial x \partial y}\right)^2\right] dxdy \\
& + \frac{B}{2}\int_0^b\!\!\int_0^a \left[\left(\frac{\partial U}{\partial x}\right)^2 + \left(\frac{\partial V}{\partial y}\right)^2 + 2\nu\frac{\partial U}{\partial x}\frac{\partial V}{\partial y}\right. \\
& \qquad \left. + \frac{1-\nu}{2}\left(\left(\frac{\partial U}{\partial y}\right)^2 + \left(\frac{\partial V}{\partial x}\right)^2 + 2\frac{\partial U}{\partial y}\frac{\partial V}{\partial x}\right)\right] dxdy \\
& + \frac{B}{8}\int_0^b\!\!\int_0^a \left[\left(\frac{\partial W}{\partial x}\right)^4 + \left(\frac{\partial W}{\partial y}\right)^4 + 2\left(\frac{\partial W}{\partial x}\right)^2\left(\frac{\partial W}{\partial y}\right)^2\right] dxdy \\
& + \frac{B}{2}\int_0^b\!\!\int_0^a \left[\frac{\partial U}{\partial x}\left(\frac{\partial W}{\partial x}\right)^2 + \frac{\partial V}{\partial y}\left(\frac{\partial W}{\partial y}\right)^2 + \nu\left[\frac{\partial U}{\partial x}\left(\frac{\partial W}{\partial y}\right)^2 + \frac{\partial V}{\partial y}\left(\frac{\partial W}{\partial x}\right)^2\right]\right. \\
& \qquad \left. + (1-\nu)\left(\frac{\partial U}{\partial y} + \frac{\partial V}{\partial x}\right)\frac{\partial W}{\partial x}\frac{\partial W}{\partial y}\right] dxdy,
\end{aligned}
\tag{X.1.8}
$$

where,

$$
D = \frac{Eh^3}{12(1-\nu^2)} \qquad\qquad B = \frac{Eh}{1-\nu^2}. \tag{X.1.9}
$$

The second term of (X.1.7) represents the rotational inertia and it will be neglected because it only influences the very high frequency responses. This will cause the mass matrix to be diagonal. The first term of (X.1.8) will generate the linear term of the stiffness matrix of the transverse motion, the second term will generate the linear term of the stiffness matrix of the in-plane motion, the third term will generate the nonlinear term of the stiffness matrix of the transverse motion and the fourth term accounts for the coupling between transverse motion and in-plane motion.

The virtual work done by the non-conservative forces may be written as,

$$
\delta\mathcal{W} = -\int_0^b\!\!\int_0^a c(x,y)\frac{\partial W}{\partial t}\delta W \, dxdy, \tag{X.1.10}
$$

where $c(x,y)$ is the viscous damping coefficient.

Now, we assume the displacement responses $U, V \& W$ can be expanded in a finite set orthogonal functions,

$$
\begin{aligned}
U(x,y,t) &= \sum_{\tilde{I}=1}^{M} \alpha_i(x)\beta_j(y)U_{\tilde{I}}(t) \\
V(x,y,t) &= \sum_{\tilde{I}=1}^{M} \gamma_i(x)\eta_j(y)V_{\tilde{I}}(t) \\
W(x,y,t) &= \sum_{I=1}^{N} \phi_i(x)\psi_j(y)W_I(t),
\end{aligned}
\tag{X.1.11}
$$

where $\alpha_i(x), \beta_j(y), \gamma_i(x), \eta_j(y)$ are the functions used to describe the in-plane motion, $\phi_i(x), \psi_j(y)$ are the functions for the transverse motion, M, N are the number of terms used for the in-plane and transverse motion, respectively, and $\tilde{}$ denotes the index relative to the in-plane motion. $U_{\tilde{I}}(t), V_{\tilde{I}}(t)$, and $W_I(t)$ are unknown functions of time. i, j are selected so that any desired number of half waves is included in each direction. The relationships between the indices are

$$
\begin{aligned}
I &= (i-1)\times n_j + j \\
&\qquad \text{for } i = 1,2,\cdots n_i, \qquad j = 1,2,\cdots n_j, \\
\text{and,}\quad & \\
\tilde{I} &= (i-1)\times \tilde{n}_j + j \\
&\qquad \text{for } i = 1,2,\cdots \tilde{n}_i, \qquad j = 1,2,\cdots \tilde{n}_j
\end{aligned}
\tag{X.1.12}
$$

where n_i, n_j are the number of modes for transverse motion in the x and y direction, respectively, and $\tilde{n}_i, \tilde{n}_j$ are the number of modes for in-plane motion in x and y direction, respectively, and

$$
\begin{aligned}
N &= n_i \times n_j \\
M &= \tilde{n}_i \times \tilde{n}_j.
\end{aligned}
\tag{X.1.13}
$$

An example is given in table X.1.1 to show the relationship between $\tilde{I}$ and i, j for $U(x,y,t)$ with $\tilde{n}_i = \tilde{n}_j = 3$,

$\tilde{I}$	i	j
1	1	1
2	1	2
3	1	3
4	2	1
5	2	2
6	2	3
7	3	1
8	3	2
9	3	3

Table X.1.1 An Example of Index Relationship

In the present study, the boundary conditions for in-plane motion are taken to be fixed and for transverse motion they are assumed to be clamped-clamped. A reasonable choice for the shape functions used in equations (X.1.11) is the set of eigenfunctions for a fully fixed beam,

$$
\begin{aligned}
&\alpha_i(x) = sin\frac{2i\pi x}{a}\\
&\beta_j(y) = sin\frac{j\pi y}{b}\\
&\gamma_i(x) = sin\frac{i\pi x}{a}\\
&\eta_j(y) = sin\frac{2j\pi y}{b}\\
&\phi_i(x) = cos(\frac{p_i x}{a}) - cosh(\frac{p_i x}{a}) + D_i\big(sin(\frac{p_i x}{a}) - sinh(\frac{p_i x}{a})\big)\\
&\psi_j(y) = cos(\frac{p_j y}{b}) - cosh(\frac{p_j y}{b}) + D_j\big(sin(\frac{p_j y}{b}) - sinh(\frac{p_j y}{b})\big),
\end{aligned}
\tag{X.1.14}
$$

where p_i and D_i are given in the table X.1.2 for the first six eigenfunctions.

i	p_i	D_i
1	4.730040745	-0.982502215
2	7.853204624	-1.000777312
3	10.99560784	-0.999966450
4	14.13716549	-1.000001450
5	17.27875996	-1.000000000
6	20.42035225	-1.000000000

Table X.1.2 Eigenfunction Coefficients for a Clamped-Clamped Beam

Introduce following notations,

$$
\begin{aligned}
M(I,J) &= \rho h\int_0^b\int_0^a(\phi_i\psi_j\phi_k\psi_l)\,dxdy\\
Q(I) &= \rho h\int_0^b\int_0^a(\phi_i\psi_j)\,dxdy\\
m_U(\tilde{I},\tilde{J}) &= \rho h\int_0^b\int_0^a(\alpha_i\beta_j\alpha_k\beta_l)\,dxdy\\
m_V(\tilde{I},\tilde{J}) &= \rho h\int_0^b\int_0^a(\gamma_i\eta_j\gamma_k\eta_l)\,dxdy,\\
k_W(I,J) &= D\int_0^b\int_0^a(\phi_i''\psi_j\phi_k''\psi_l + \phi_i\psi_j''\phi_k\psi_l'' + 2\phi_i'\psi_j'\phi_k'\psi_l')\,dxdy\\
k_U(\tilde{I},\tilde{J}) &= B\int_0^b\int_0^a(\alpha_i'\beta_j\alpha_k'\beta_l + \frac{1-\nu}{2}\alpha_i\beta_j'\alpha_k\beta_l')\,dxdy
\end{aligned}
\tag{X.1.15}
$$

$$k_V(\tilde{I},\tilde{J}) = B\int_0^b\int_0^a (\gamma_i\eta'_j\gamma_k\eta'_l + \frac{1-\nu}{2}\gamma'_i\eta_j\gamma'_k\eta_l)\,dxdy$$

$$k_{UV}(\tilde{I},\tilde{J}) = \frac{B}{2}\int_0^b\int_0^a 2\nu\alpha'_i\beta_j\gamma_k\eta'_l + (1-\nu)\alpha_i\beta'_j\gamma'_k\eta_l)\,dxdy \tag{X.1.16}$$

$$\begin{aligned}k_{WW}(I,J,K,L) = \frac{B}{2}\int_0^b\int_0^a (&\phi'_i\psi_j\phi'_k\psi_l\phi'_m\psi_n\phi'_r\psi_s + \phi_i\psi'_j\phi_k\psi'_l\phi_m\psi'_n\phi_r\psi'_s \\ &+ 2\phi'_i\psi_j\phi'_k\psi_l\phi_m\psi'_n\phi_r\psi'_s)\,dxdy\end{aligned}$$

$$k_{WU}(\tilde{K},I,J) = B\int_0^b\int_0^a (\phi'_i\psi_j\phi'_k\psi_l\alpha'_m\beta_n + \nu\phi_i\psi'_j\phi_k\psi'_l\alpha'_m\beta_n + (1-\nu)\phi'_i\psi_j\phi_k\psi'_l\alpha_m\beta'_n)\,dxdy$$

$$k_{WV}(\tilde{K},I,J) = B\int_0^b\int_0^a (\phi_i\psi'_j\phi_k\psi'_l\gamma_m\eta'_n + \nu\phi'_i\psi_j\phi'_k\psi_l\gamma_m\eta'_n + (1-\nu)\phi'_i\psi_j\phi_k\psi'_l\gamma'_m\eta_n)\,dxdy,$$

and

$$C(I,J) = \int_0^b\int_0^a c(x,y)\phi_i\psi_j\phi_k\psi_l\,dxdy, \tag{X.1.17}$$

where $'$ denotes the derivative with respect to the spatial variable. Then the energy expression can be written in a compact way. Substituting equations (X.1.11) through (X.1.17) into equations (X.1.7) and (X.1.8) gives,

$$\begin{aligned}\mathcal{T} = \frac{1}{2}\,(&\sum_{I=1}^{N}\sum_{J=1}^{N} M(I,J)\dot{W}_I\dot{W}_J \\ &+\sum_{\tilde{I}=1}^{M}\sum_{\tilde{J}=1}^{M}(m_U(\tilde{I},\tilde{J})\dot{U}_{\tilde{I}}\dot{U}_{\tilde{J}} + m_V(\tilde{I},\tilde{J})\dot{V}_{\tilde{I}}\dot{V}_{\tilde{J}}) \\ &+2\sum_{I=1}^{N} Q(I)\dot{W}_I\dot{W}_0 \;+\; ab\dot{W}_0^2)\end{aligned} \tag{X.1.18}$$

$$\begin{aligned}\mathcal{V} = \frac{1}{2}\,(&\sum_{I=1}^{N}\sum_{J=1}^{N} k_W(I,J)W_IW_J \\ &+\sum_{\tilde{I}=1}^{M}\sum_{\tilde{J}=1}^{M}(k_U(\tilde{I},\tilde{J})U_{\tilde{I}}U_{\tilde{J}} + k_V(\tilde{I},\tilde{J})V_{\tilde{I}}V_{\tilde{J}} + 2k_{UV}(\tilde{I},\tilde{J})U_{\tilde{I}}V_{\tilde{J}}) \\ &+\frac{1}{2}\sum_{I=1}^{N}\sum_{J=1}^{N}\sum_{K=1}^{N}\sum_{L=1}^{N} k_{WW}(I,J,K,L)W_IW_JW_KW_L\end{aligned} \tag{X.1.19}$$

$$+2\sum_{\tilde{K}=1}^{M}\sum_{I=1}^{N}\sum_{J=1}^{N}(k_{WU}(\tilde{K},I,J)W_IW_JU_{\tilde{K}}+k_{WV}(\tilde{K},I,J)W_IW_JV_{\tilde{K}})),$$

where we have dropped the explicit time dependence of $U_{ij}(t), V_{ij}(t)$, and $W_{ij}(t)$ to simplify the notation.

The Ritz Method will be used in this model to find the mass and stiffness matrices and the response of the plate by using Hamilton's Principle,

$$\delta\int_{t_1}^{t_2}[\mathcal{T}-\mathcal{V}+\mathcal{W}]\,dt \;=\; 0, \tag{X.1.20}$$

where δ is the variational operator. Note that the base excitation, W_0, is a known function, so that,

$$\delta W_0 \;=\; \delta\dot{W}_0 \;=\; 0. \tag{X.1.21}$$

Applying the variational operation to equation (X.1.18) and (X.1.19) gives,

$$\delta\mathcal{T} =(\sum_{J=1}^{N}M(I,J)\dot{W}_J+Q(I)\dot{W}_0)\delta\dot{W}_I+\sum_{\tilde{J}=1}^{M}(m_U(\tilde{I},\tilde{J})\dot{U}_{\tilde{J}}\delta\dot{U}_{\tilde{I}}+m_V(\tilde{I},\tilde{J})\dot{V}_{\tilde{J}}\delta\dot{V}_{\tilde{I}}) \tag{X.1.22}$$

$$\begin{aligned}\delta\mathcal{V} \;=\; &(\sum_{J=1}^{N}k_W(I,J)W_J+\sum_{J=1}^{N}\sum_{K=1}^{N}\sum_{L=1}^{N}k_{WW}(I,J,K,L)W_JW_KW_L\\
&+2\sum_{J=1}^{N}\sum_{\tilde{K}=1}^{M}(k_{WU}(\tilde{K},I,J)W_JU_{\tilde{K}}+k_{WV}(\tilde{K},I,J)W_JV_{\tilde{K}}))\delta W_{ij}\\
&+(\sum_{\tilde{J}=1}^{M}k_U(\tilde{I},\tilde{J})U_{\tilde{J}}+\sum_{\tilde{J}=1}^{M}k_{WU}(\tilde{I},\tilde{J})V_{\tilde{J}}+\sum_{J=1}^{N}\sum_{K=1}^{N}k_{WU}(\tilde{I},J,K)W_JW_K)\delta U_{\tilde{I}} \qquad (\text{X.1.23})\\
&+(\sum_{\tilde{J}=1}^{M}k_V(\tilde{I},\tilde{J})V_{\tilde{J}}+\sum_{\tilde{J}=1}^{M}k_{WV}(\tilde{I},\tilde{J})U_{\tilde{J}}+\sum_{J=1}^{N}\sum_{K=1}^{N}k_{WV}(\tilde{I},J,K)W_JW_K)\delta V_{\tilde{I}}.\end{aligned}$$

Substituting equations (X.1.11) and (X.1.17) into equation (X.1.10) gives,

$$\delta\mathcal{W}=-\sum_{J=1}^{N}C(I,J)\dot{W}_J\delta W_I. \tag{X.1.24}$$

Substituting equations (X.1.22) through (X.1.24) into (X.1.20), we can get the governing equations for W_I, $U_{\tilde{I}}$ and $V_{\tilde{I}}$ in the expansions in equations (X.1.11),

$$\sum_{J=1}^{N}M(I,J)\ddot{W}_J+\sum_{J=1}^{N}C(I,J)\dot{W}_J+\sum_{J=1}^{N}k_W(I,J)W_J+\sum_{J=1}^{N}\sum_{K=1}^{N}\sum_{L=1}^{N}k_{WW}(I,J,K,L)W_JW_KW_L$$

$$+2\sum_{J=1}^{N}\sum_{\tilde{K}=1}^{M}\left(k_{WU}(\tilde{K},I,J)U_{\tilde{k}}W_J + k_{WV}(\tilde{K},I,J)V_{\tilde{K}}W_J\right) = -Q(I)\ddot{W}_0, \qquad \text{(X.1.25)}$$

$$\text{for } I = 1,2,\cdots,N$$

$$\sum_{\tilde{J}=1}^{M} m(\tilde{I},\tilde{J})\ddot{U}_{\tilde{J}} + \sum_{\tilde{J}=1}^{M} k_U(\tilde{I},\tilde{J})U_{\tilde{J}} + \sum_{\tilde{J}=1}^{M} k_{UV}(\tilde{I},\tilde{J})V_{\tilde{J}} + \sum_{J=1}^{N}\sum_{K=1}^{N} k_{WU}(\tilde{I},J,K)W_J W_K \qquad \text{(X.1.26)}$$

$$\text{for } \tilde{I} = 1,2,\cdots,M$$

$$\sum_{\tilde{J}=1}^{M} m(\tilde{I},\tilde{J})\ddot{V}_{\tilde{J}} + \sum_{\tilde{J}=1}^{M} k_V(\tilde{I},\tilde{J})V_{\tilde{J}} + \sum_{\tilde{J}=1}^{M} k_{UV}(\tilde{I},\tilde{J})V_{\tilde{J}} + \sum_{J=1}^{N}\sum_{K=1}^{N} k_{WV}(\tilde{I},J,K)W_J W_K \qquad \text{(X.1.27)}$$

$$\text{for } \tilde{I} = 1,2,\cdots,M$$

From previous analysis, we know $[M(I,J)]$ is a diagonal matrix having diagonal elements M_I, if we assume $c(x,y)$ is a constant, $[C(I,J)]$ will also be a diagonal matrix having diagonal elements C_I. In the present study, the general terms of the stiffness matrix have been evaluated by using the symbolic computer program MACSYMA.

According to the assumption of the Von-Karmán plate, we can neglect the in-plane inertia, $\ddot{U}_{\tilde{J}}$and$\ddot{V}_{\tilde{J}}$ and solve for $U_{\tilde{I}}, V_{\tilde{I}}$ by using (X.1.26),(X.1.27),

$$\begin{pmatrix} \{U(\tilde{I})\} \\ \{V(\tilde{I})\} \end{pmatrix} = -\begin{bmatrix} [k_U(\tilde{I},\tilde{J})] & [k_{UV}(\tilde{I},\tilde{J})] \\ [k_{UV}(\tilde{I},\tilde{J})] & [k_V(\tilde{I},\tilde{J})] \end{bmatrix}^{-1} \begin{pmatrix} \{\sum_{K=1}^{N}\sum_{L=1}^{N} k_{WU}(\tilde{J},K,L)W_K W_L\} \\ \{\sum_{K=1}^{N}\sum_{L=1}^{N} k_{WV}(\tilde{J},K,L)W_K W_L\} \end{pmatrix}, \qquad \text{(X.1.28)}$$

where $\{U(\tilde{I})\}$ is a vector having elements $U(\tilde{I})$ for $\tilde{I} = 1,2,\cdots,M$, etc. and $[k_U(\tilde{I},\tilde{J})]$ is a matrix having elements $k_U(\tilde{I},\tilde{J})$

Equations (X.1.25) through (X.1.28) may be manipulated to obtain the governing equation which depends on the transverse displacement W only,

$$M_I\ddot{W}_I + C_I\dot{W}_I + \sum_{J=1}^{N} k_W(I,J)W_J + \sum_{J=1}^{N}\sum_{K=1}^{N}\sum_{L=1}^{N} k_N(I,J,K,L)W_J W_K W_L = -Q_I\ddot{W}_0, \qquad \text{(X.1.29)}$$

where $k_W(I,J)$ is the linear part of the stiffness matrix and $k_N(I,J,K,L)$ is the nonlinear part.

X.1.3 Equivalent Linearization

In order to predict the fatigue life, a sufficiently long time history of the response under random excitation is needed. Because of the nonlinear term in (X.1.29), it is not practical to solve for the response in the time domain using full numerical simulation methods if N is large. The numerical effort in evaluating equation (X.1.29) is roughly proportional to N^4. In this section, we shall present the method of equivalent linearization for solving equation(X.1.29). This will lead to an approximate solution to equation (X.1.29) in which the numerical effort is proportional to N^2 rather than N^4. This makes it practical to include a large number of terms.

The method of equivalent linearization consists of approximating equation (X.1.29) by an equivalent linear system,

$$\ddot{W}_I + \xi_I \dot{W}_I + \frac{1}{M_I}\sum_{J=1}^{N} k_e(I,J)W_J + e_I(\underline{W}) = q(I)\ddot{W}_0, \qquad (\text{X.1.30})$$

with

$$\xi_I = \frac{C_I}{M_I} \qquad q_I = -\frac{Q_I}{M_I} \qquad (\text{X.1.31})$$

where $k_e(I,J)$ is the equivalent linear stiffness matrix and $e_I(\underline{W})$ is the error term which can be written in a vector form,

$$\begin{aligned} \mathrm{e} &= \{e_I(\underline{W})\} \\ &= \left\{\sum_{J=1}^{N} k_e(I,J)W_J - \sum_{J=1}^{N} k_W(I,J)W_J - \sum_{J=1}^{N}\sum_{K=1}^{N}\sum_{L=1}^{N} k_N(I,J,K,L)W_J W_K W_L\right\}, \end{aligned} \qquad (\text{X.1.32})$$

where the index I indicates the row of the vector.

The elements $k_e(I,J)$ are chosen to minimize the steady-state mean square value of e,

$$\frac{\partial \mathrm{E}\left[\mathrm{e}^T \mathrm{e}\right]}{\partial k_e(I,J)} = 0, \qquad (\text{X.1.33})$$

where E[·] denotes the expected value.

Expanding (X.1.33), and using (X.1.32) give,

$$\begin{aligned} \sum_{M=1}^{N} k_e(I,M)\mathrm{E}[W_M W_J] &= \sum_{M=1}^{N} k_W(I,M)\mathrm{E}[W_M W_J] \\ &+ \sum_{M=1}^{N}\sum_{K=1}^{N}\sum_{L=1}^{N} k_N(I,M,K,L)\mathrm{E}[W_J W_M W_K W_L]. \end{aligned} \qquad (\text{X.1.34})$$

$$\text{for } I = 1, 2, \cdots, N.$$

Now we assume $\ddot{W}_0$ is Gaussian white noise, so the solution for the W_I is known to be jointly Gaussian and all the odd order steady-state moments of the W_I are zero. The fourth order moments in equation (X.1.33) can be expressed in terms of lower order moments,

$$\begin{aligned} &\mathrm{E}[W_J W_M W_K W_L] = \mathrm{E}[W_I W_M]\mathrm{E}[W_K W_L] + \\ &\mathrm{E}[W_J W_K]\mathrm{E}[W_M W_L] + \mathrm{E}[W_J W_L]\mathrm{E}[W_M W_K]. \end{aligned} \qquad (\text{X.1.35})$$

Substituting (X.1.35) into (X.1.34) gives,

$$k_e(I,J) = k_W(I,J) + \sum_{K=1}^{N}\sum_{L=1}^{N}(k_N(I,J,K,L) + 2k_N(I,K,L,J))R_W(K,L), \quad \text{(X.1.36)}$$

where,

$$R_W(K,L) \;=\; \mathrm{E}[W_K W_L] \quad \text{(X.1.37)}$$

is the steady-state correlation matrix for $W_K, K = 1, 2, \cdots, N$.

Equation (X.1.36) can be used to determine the components of $k_e(I,J)$. However, one has to solve for $[k_e]$ and $[R_W]$ simultaneously. An iterative procedure is described in the following. Let $\Phi(I,J)$ be a matrix whose columns are eigenvectors for

$$\ddot{W}_I + \frac{1}{M_I}\sum_{J=1}^{N} k_e(I,J)W_J \;=\; 0. \quad \text{(X.1.38)}$$

$\Phi(I,J)$ is a normalized modal column matrix with the following properties,

$$\begin{aligned} [\Phi]^T[\Phi] &= \mathrm{I} \\ [\Phi]^T[M]^{-1}[k_e][\Phi] &= \Omega^2, \end{aligned} \quad \text{(X.1.39)}$$

where,

$$\mathrm{I} = \begin{pmatrix} 1 & 0 & \dots & 0 \\ 0 & 1 & \dots & 0 \\ \vdots & \vdots & \ddots & \vdots \\ 0 & 0 & \dots & 1 \end{pmatrix} \qquad \Omega^2 = \begin{pmatrix} \omega_1^2 & 0 & \dots & 0 \\ 0 & \omega_2^2 & \dots & 0 \\ \vdots & \vdots & \ddots & \vdots \\ 0 & 0 & \dots & \omega_N^2 \end{pmatrix}, \quad \text{(X.1.40)}$$

and ω_I is the Ith natural frequency. Define a transformation to modal coordinates, B_J,

$$\begin{aligned} W_I &= \sum_{J=1}^{N} \Phi(I,J)B_J \\ f_I &= \sum_{J=1}^{N} \Phi(I,J)q_J. \end{aligned} \quad \text{(X.1.41)}$$

Substituting (X.1.40) into (X.1.30) and neglecting the error term leads to an uncoupled set of differential equations,

$$\ddot{B}_I + \xi_I\dot{B}_I + \omega_I^2 B_I \;=\; f_I\ddot{W}_0. \quad \text{(X.1.42)}$$

Assume $\ddot{W}_0(t)$ is Gaussian white noise with single-side power spectral density $G_{\ddot{W}}$. We define the steady-state correlation matrix for the modal coordinates B_I,

$$R_B(I,J) \;=\; E[B_I B_J]. \quad \text{(X.1.43)}$$

From equations (X.1.41) and (X.1.42) it can be shown that

$$E[B_I B_J] = \frac{\xi f_I f_J G_{\bar{W}_0}}{(\omega_I^2 - \omega_J^2)^2 + 2\xi^2(\omega_I^2 + \omega_J^2)}. \tag{X.1.44}$$

The correlation matrices $[R_W]$ and $[R_B]$ having elements $R_W(I,J)$ and $R_B(I,J)$, respectively, are related by

$$[R_W] = [\Phi][R_B][\Phi]^T. \tag{X.1.45}$$

Using equations (X.1.38) through (X.1.45), the iterative procedure to determine $[k_e]$ and $[R_W]$ may be stated as follows:

Step 1. (Zero order approximation) Assume that

$$R_B(I,J) = 0. \tag{X.1.46}$$

Then

$$\begin{aligned} R_W(I,J) &= 0 \\ k_e(I,J) &= k_W(I,J). \end{aligned} \tag{X.1.47}$$

Step 2. Determine the eigenvalue and eigen matrix of equation (X.1.38).

Step 3. Evaluate R_B and then R_W using equation (X.1.43) through (X.1.45). Then $[k_e]$ is updated by using (X.1.36).

Step 4. Check convergence. We will stop the iteration if the convergence conditions are satisfied, otherwise, repeat the iteration from Step 2.

It should be pointed out that in addition to the matrices $[R_W]$, $[R_B]$ and $[k_e]$, the eigen matrix Φ and equivalent linear natural frequencies ω_I are also obtained at the end of the above iteration. These are the results we need for the subsequent analysis.

X.1.4 Stress Calculation

In order to predict the fatigue life, we need the stress or strain expressions in terms of the equivalent linear modal coordinates. The stress and strain should include both linear bending and nonlinear stretching components. Substituting equation (X.1.3) and (X.1.11) into equation (X.1.4) gives,

$$
\begin{aligned}
\sigma_{xx} = \frac{E}{1-\mu^2} & (\sum_{\bar{I}=1}^{M} (\alpha_i'(x)\beta_j(y)U_{\bar{I}} + \mu\gamma_i(x)\eta_j'(y)V_{\bar{I}}) \\
& -z\sum_{I=1}^{N} (\phi_i''(x)\psi_j(y) + \mu\phi_i(x)\psi_j''(y))W_I \\
& +\frac{1}{2}\sum_{I=1}^{N}\sum_{J=1}^{N} (\phi_i'(x)\psi_j(y)\phi_k'(x)\psi_l(y) + \mu\phi_i(x)\psi_j'(y)\phi_k(x)\psi_l'(y))W_IW_J) \\
\sigma_{yy} = \frac{E}{1-\mu^2} & (\sum_{\bar{I}=1}^{M} (\gamma_i(x)\eta_j'(y)V_{\bar{I}} + \mu\alpha_i'(x)\beta_j(y)U_{\bar{I}}) \\
& -z\sum_{I=1}^{N} (\phi_i(x)\psi_j''(y) + \mu\phi_i''(x)\psi_j(y))W_I \\
& +\frac{1}{2}\sum_{I=1}^{N}\sum_{J=1}^{N} (\phi_i(x)\psi_j'(y)\phi_k(x)\psi_l'(y) + \mu\phi_i'(x)\psi_j(y)\phi_k'(x)\psi_l(y))W_IW_J) \\
\sigma_{xy} = \frac{E}{2(1+\mu)} & (\sum_{\bar{I}=1}^{M} (\alpha_i(x)\beta_j'(y)U_{\bar{I}} + \gamma_i'(x)\eta_j(y)V_{\bar{I}}) \\
& -2z\sum_{I=1}^{N} \phi_i'(x)\psi_j'(y)W_I \\
& +\sum_{I=1}^{N}\sum_{J=1}^{N} \phi_i'(x)\psi_j(y)\phi_k(x)\psi_l'(y)W_IW_J).
\end{aligned}
\tag{X.1.48}
$$

From equation (X.1.48), we know that the stress of the plate is multiaxial and an equivalent stress approach should be developed to calculate the fatigue life. But, because the equivalent stress has different directions at different points, it is difficult to construct and count the stress cycles when using a cycle counting scheme to predict fatigue life. According to the basic plate theory, the maximum stress will occur at the boundary if the boundary condition is clamped and either σ_{xx} or σ_{yy} will dominate along the boundary. So in this project we simply calculate the fatigue life by using σ_{xx} and σ_{yy} separately. Along the boundary, the maximum σ_{xx} will occur at the middle of the edge in y direction while the maximum σ_{yy} will occur at the middle of the edge in x direction. If we assume the width b is greater than the length a, then

$$\sigma_{max} = \sigma_{xx}(x = 0, y = \frac{b}{2}, z = \pm\frac{1}{2}h), \tag{X.1.49}$$

where ± means we can choose either the upper plane or bottom plane of the plate and it will come up with the same solution. Define

$$\begin{aligned}
S_U(\tilde{I}) &= \frac{E}{1-\mu^2}\alpha_i'(0)\beta_j(\frac{b}{2}) \\
S_V(\tilde{I}) &= \frac{E}{1-\mu^2}\gamma_i(0)\eta_j'(\frac{b}{2}) \\
S_W(I) &= \frac{Eh}{2(1-\mu^2)}(\phi_i''(0)\psi_j(\frac{b}{2}) + \mu\phi_i(0)\psi_j''(\frac{b}{2})) \\
S_{WW}(I,J) &= \frac{E}{2(1-\mu^2)}(\phi_i'(0)\psi_j(\frac{b}{2})\phi_k'(0)\psi_l(\frac{b}{2}) + \mu\phi_i(0)\psi_j'(\frac{b}{2})\phi_k(0)\psi_l'(\frac{b}{2})).
\end{aligned} \tag{X.1.50}$$

Substituting equation (X.1.48) and (X.1.50) into (X.1.49) gives,

$$\sigma_{max} = \sum_{\tilde{I}=1}^{M}(S_U(\tilde{I})U_{\tilde{I}} + \mu S_V(\tilde{I})V_{\tilde{I}}) \pm \sum_{I=1}^{N} S_W(I)W_I + \sum_{I=1}^{N}\sum_{J=1}^{N} S_{WW}(I,J)W_I W_J. \tag{X.1.51}$$

Recalling the modal transformation equation (X.1.41), we can express equation (X.1.51) as,

$$\begin{aligned}
\sigma_{max} =& \sum_{\tilde{I}=1}^{M}(S_U(\tilde{I})U_{\tilde{I}} + \mu S_V(\tilde{I})V_{\tilde{I}}) \pm \sum_{I=1}^{N}\sum_{J=1}^{N} S_W(I)\Phi(I,J)B_J \\
&+ \sum_{I=1}^{N}\sum_{J=1}^{N}\sum_{K=1}^{N}\sum_{L=1}^{N} S_{WW}(I,J)\Phi(I,K)\Phi(J,L)B_K B_L,
\end{aligned} \tag{X.1.52}$$

where $U_{\tilde{I}}$, $V_{\tilde{I}}$ are given by equation (X.1.27) and can also be expanded as an expression in terms of the equivalent linear modal coordinates B_I.

X.2. Quasi-Simulation and Fatigue Estimates for Multi-mode Nonlinear Plate

As in previous sections, we will assume that the relation between the stress amplitude, S, and the number of the cycles to failure, N, is given by the well known equation,

$$N = c/S^b, \tag{X.2.1}$$

where c and b are experimentally obtained constants for a given materials. For most material b varies between 2 to 6 and c is taken to be 6.56×10^{30} here. For the purpose of estimating high cycle random fatigue life, the Palmgren-Miner linear damage accumulation rule may be applied. In this theory, the total damage D, is written as the sum of the damage due to all damage events,

$$D = \sum_i \Delta D_i. \tag{X.2.2}$$

Failure is predicted to occur when $D = 1$. The fatigue lifetime is then the amount of time it takes for this to happen.

The damage increment due to one cycle, ΔD, is given by,

$$\Delta D = |S_i|^b/c, \tag{X.2.3}$$

where S_i is the stress amplitude of the ith damaging event determined by the cycle counting scheme. In our study, because the band width of the response of the multi-modes nonlinear plate is very wide, we use Rain-flow Cycle Counting scheme.

Equation (X.2.2) may be implemented in a simulation of the damage accumulation in the form

$$D \leftarrow D + \frac{|S|^b}{c}, \tag{X.1.4}$$

where D is initially set to zero. Once the simulated damage is accumulated according to equation (X.2.4) for a sufficiently long time, τ, the average damage rate is

$$\Delta = D/\tau, \tag{X.2.5}$$

and the simulated mean fatigue life is

$$T = 1/\Delta. \tag{X.2.6}$$

Before counting the damage, a sufficiently long applied force time history should be simulated, then the time history of the modal responses B_I are calculated using equation (X.1.42) by the central difference method. Finally, the time history of the stress is calculated by equation (X.1.52). It should be noted that once the equivalent linear system is determined, the computational effort of simulating the time series of the response is identical to that required for a linear system, and is independent of the type of non-linearity. So the computational time is significantly reduced compared to the direct simulation of the nonlinear system.

X.3. Numerical Results

The approach developed in the previous section has been applied to estimate the fatigue life of a nonlinear plate, and the results compared to those obtained using a conventional numerical simulation. The comparisons were performed to identify the errors in the approximate method and to quantify the savings in computation time. The same time step, Δt, was used in all computations. The parameters of the plate used in the numerical study are:

$$E = 10^7\#/in^2, \qquad \rho = 0.1\#/in^3, \qquad h = 0.032in,$$
$$a = 10in, \qquad b = 15in, \qquad \mu = 0.3,$$

where the geometry of the plate is shown in Figure X.1. The number of resonant modes for transverse motion, N, was taken to be 9 and the number of resonant modes for in-plane motion, M, was taken to be 256.

The estimated fatigue lives for each point of the plate under different excitation levels are shown in Figures X.2 to X.4, which are calculated assuming that σ_{xx} is the only significant stress component. The location of the minimum fatigue life is found to be at the middle of the longest edge, where the maximum stress occurs. Because of the computational time limitation, it is almost impossible to get a similar figure by using full simulation. The comparison of the approximate results and those obtained using the full system in equations (X.1.29) is performed at the point where the minimum fatigue life happens.

Estimated fatigue lives at the middle point of the width under different excitation levels are shown in Figure X.5. Results obtained using the full simulation and the equivalent linearization methods are found to be in excellent agreement for a range of excitation levels. To indicate the influence of the non-linearity, results are compared in figure X.5 between a nonlinear plate and a plate which is assumed to respond linearly. The figure shows for input excitation levels $\ddot{W}_0(t)$ above -30dB g^2/Hz, the plate response is highly non-linear and the mean square responses and fatigue lives deviate substantially from that of a linear system. This is because the geometry nonlinearities reduce the mean square values of the displacement and the stress and increase the predicted fatigue lives. So it is unreasonable to calculate the low excitation fatigue lives from high excitation data only by using a simple linear extrapolation. Another observation we found here is although we considered both bending stress and membrane stress in our stress model, the results from Figure X.5 show that the bending stress is totally dominant at the middle point of the edges. We can understand it from equation (X.1.52) and recall that the boundary conditions we assumed are clamped-clamped.

As mentioned above, along with the comparisons of the accuracy, the computation time was compared. In the present effort, the quasi-simulations required roughly one-hundredth of the computer time used to perform the full simulation. It is expected for more complex systems with more modes, the present method would prove to be even more advantageous.

As expected, while the power spectral density of the stress has very good agreement between full simulation and equivalent linearization method at low excitation levels, they are totally different when excitation level is high. This is because we approximate a nonlinear system by a linear system and assume the response is Gaussian when excitation is Gaussian white noise. Comparisons of the power spectrum of the stress are shown in Figure X.6 to Figure X.8. Although peak shifts are found and agree very closely from both methods, the peak broadness, which is a major feature of a high nonlinear system, is very obvious in the full simulation solution when excitation level is high but can not be found in the equivalent linearization solution. Also, some extra peaks are found in the equivalent linearization solution at high excitation levels at the points where resonant frequencies are doubled. This is caused by the nonlinear stress terms in equation (X.1.52). This phenomenon is not obvious in the full simulation solution because of the peak broadness.

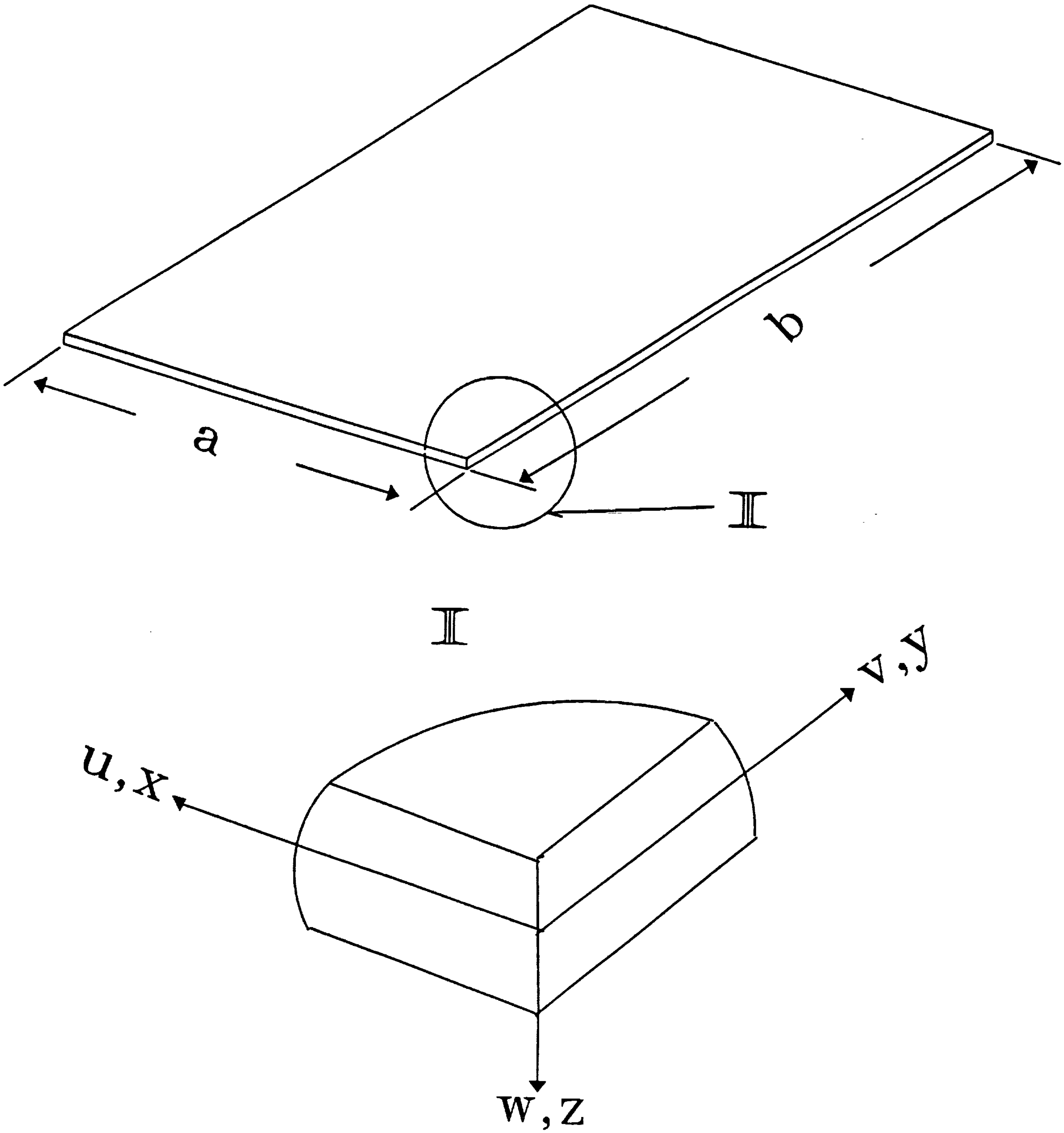

Figure X.1

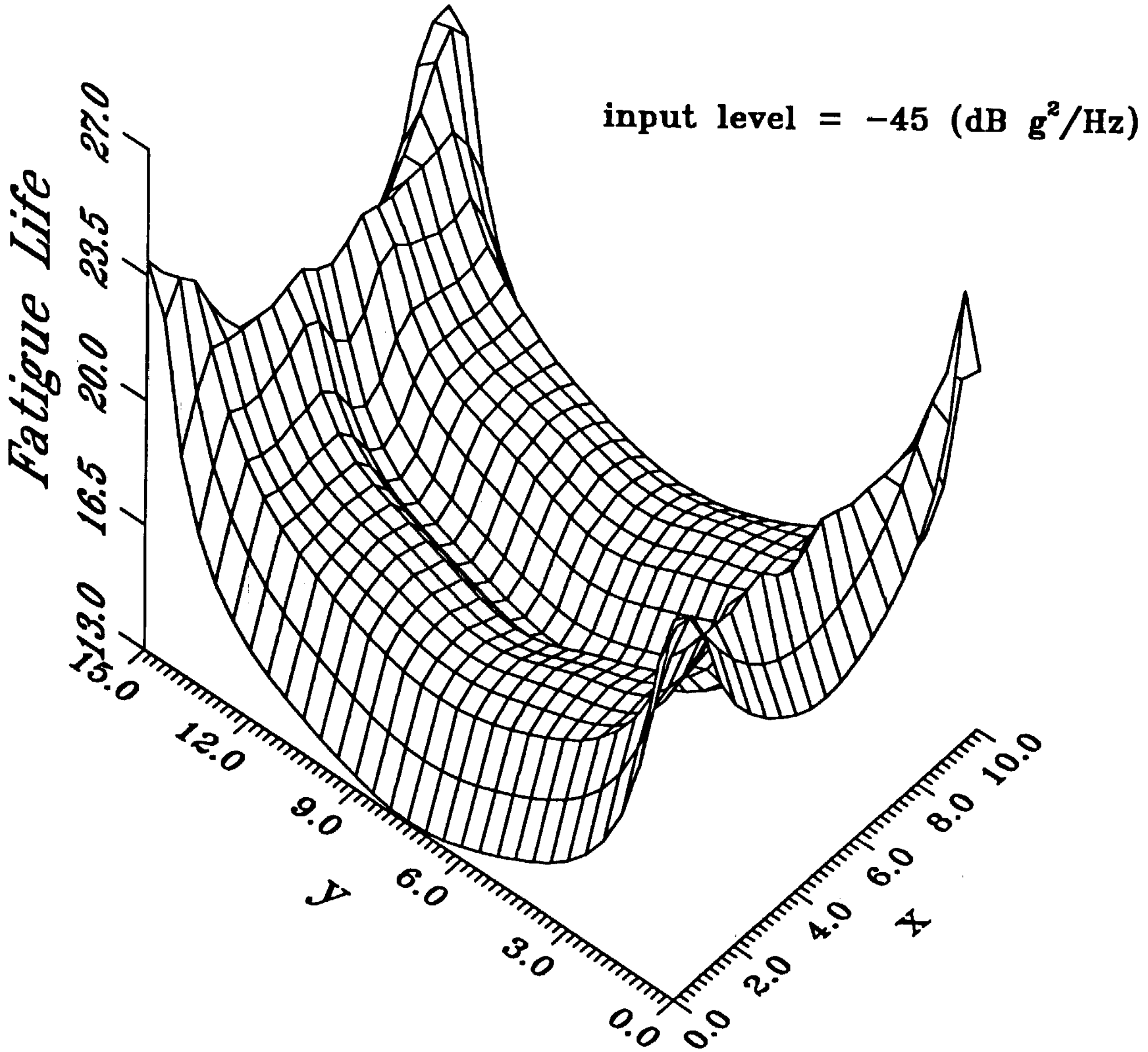
input level = −45 (dB g²/Hz)
Fatigue Life
13.0
16.5
20.0
23.5
27.0
y
15.0
12.0
9.0
6.0
3.0
0.0
x
0.0
2.0
4.0
6.0
8.0
10.0

Figure X.2

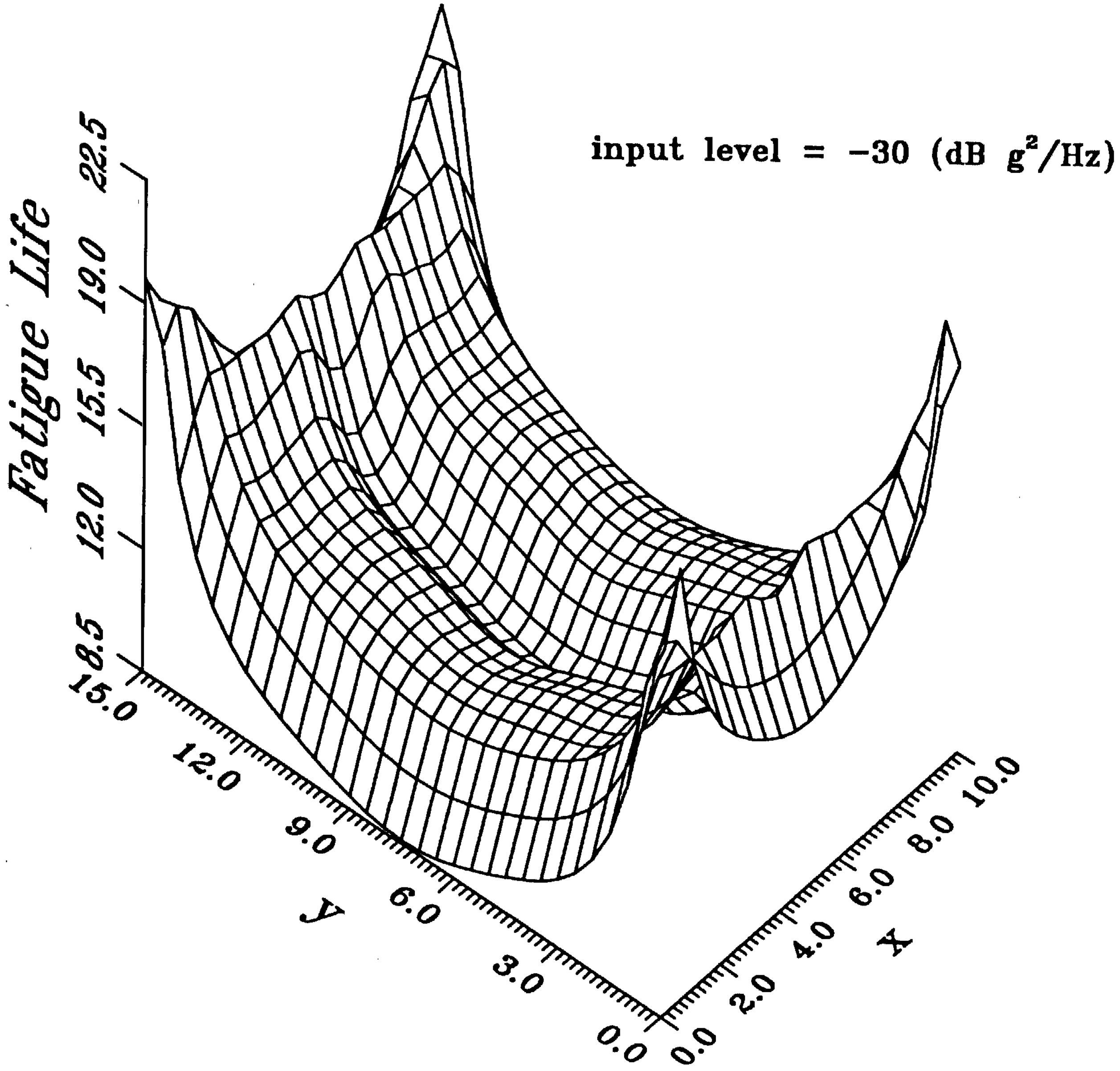
input level = −30 (dB g^2/Hz)

Figure X.3

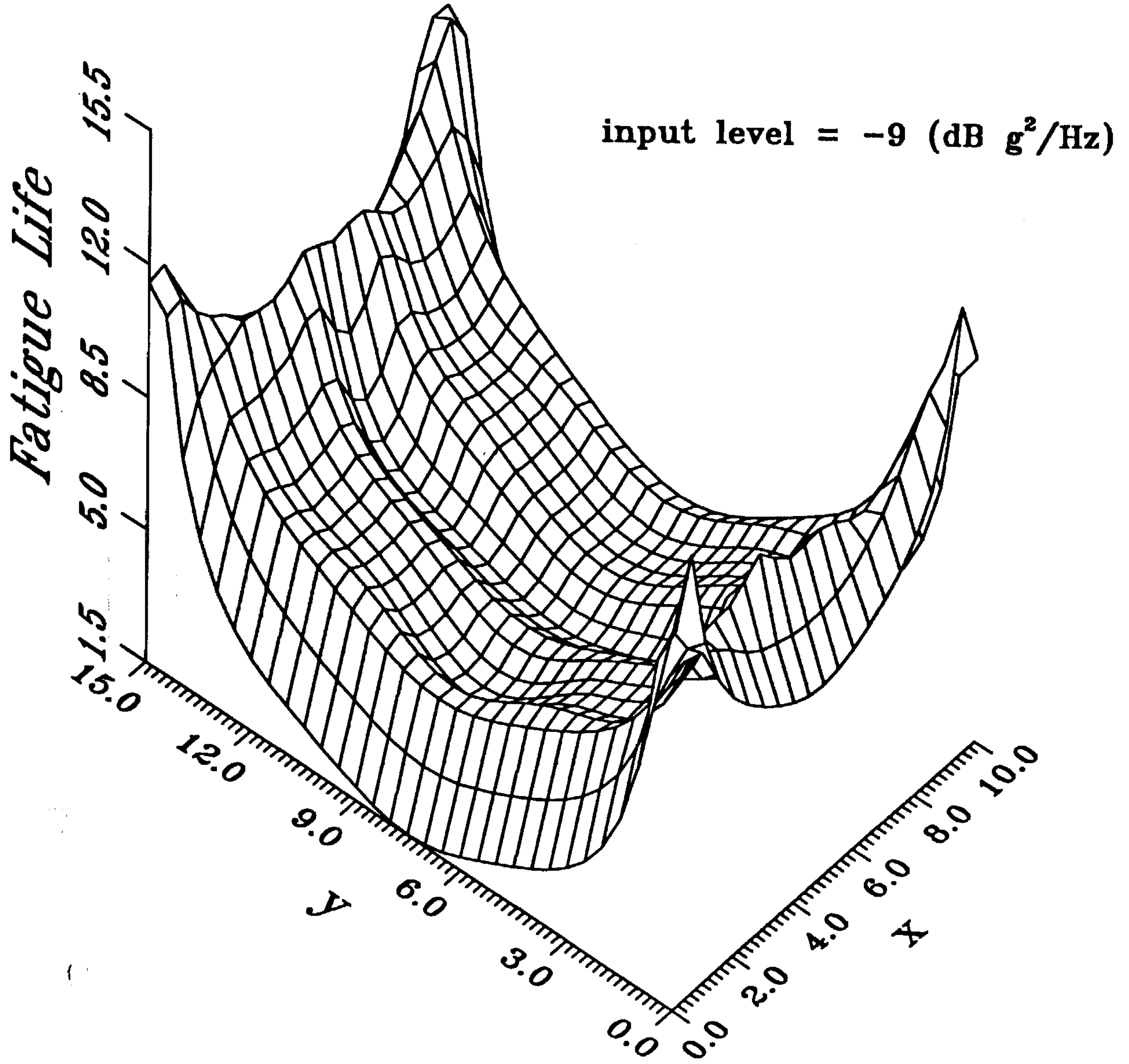
input level = −9 (dB g²/Hz)
Fatigue Life
15.5
12.0
8.5
5.0
1.5
15.0
12.0
9.0
y
6.0
3.0
0.0
0.0
2.0
4.0
6.0
8.0
10.0
X

Figure X.4

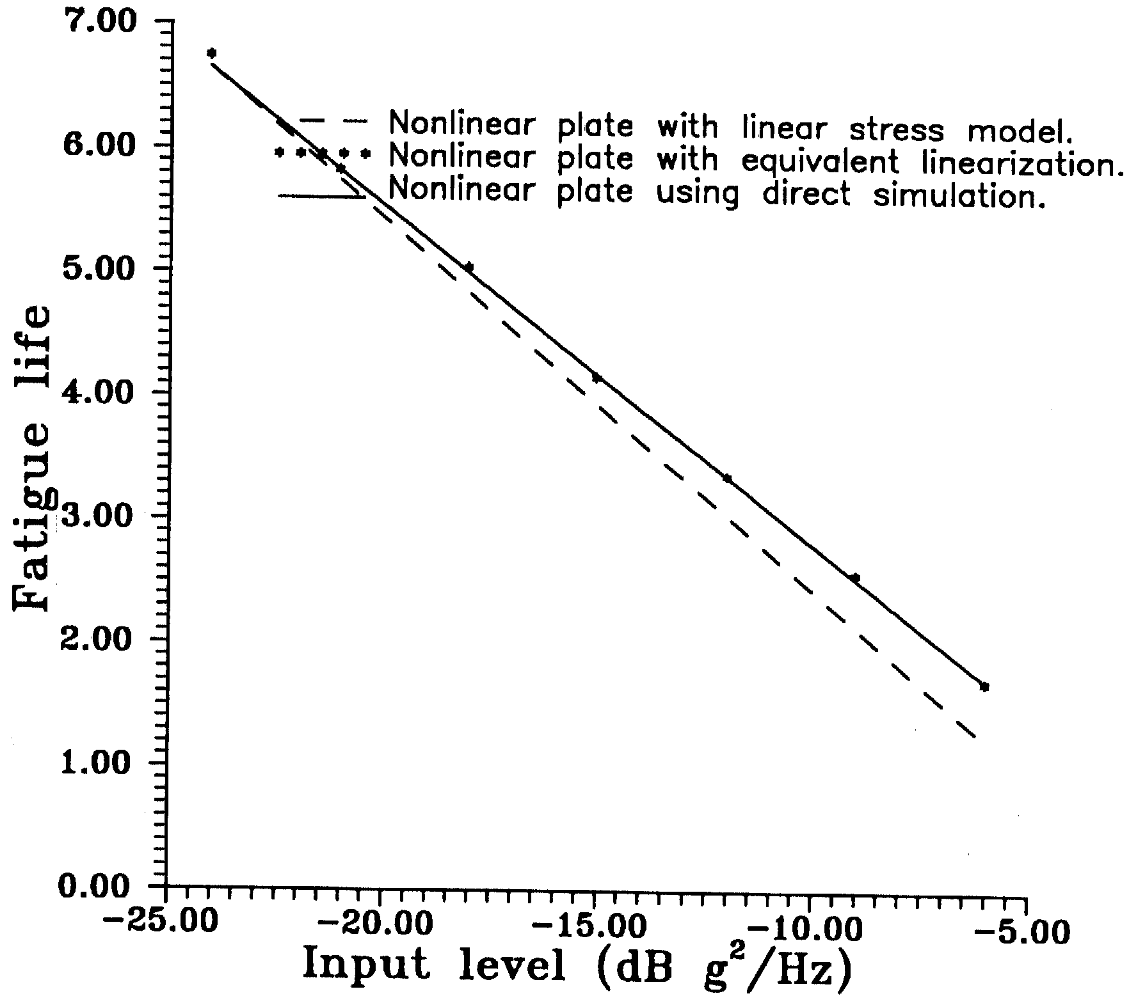
7.00
6.00
5.00
4.00
3.00
2.00
1.00
0.00
Fatigue life
−25.00
−20.00
−15.00
−10.00
−5.00
Input level (dB g²/Hz)
Nonlinear plate with linear stress model.
Nonlinear plate with equivalent linearization.
Nonlinear plate using direct simulation.

Figure X.5

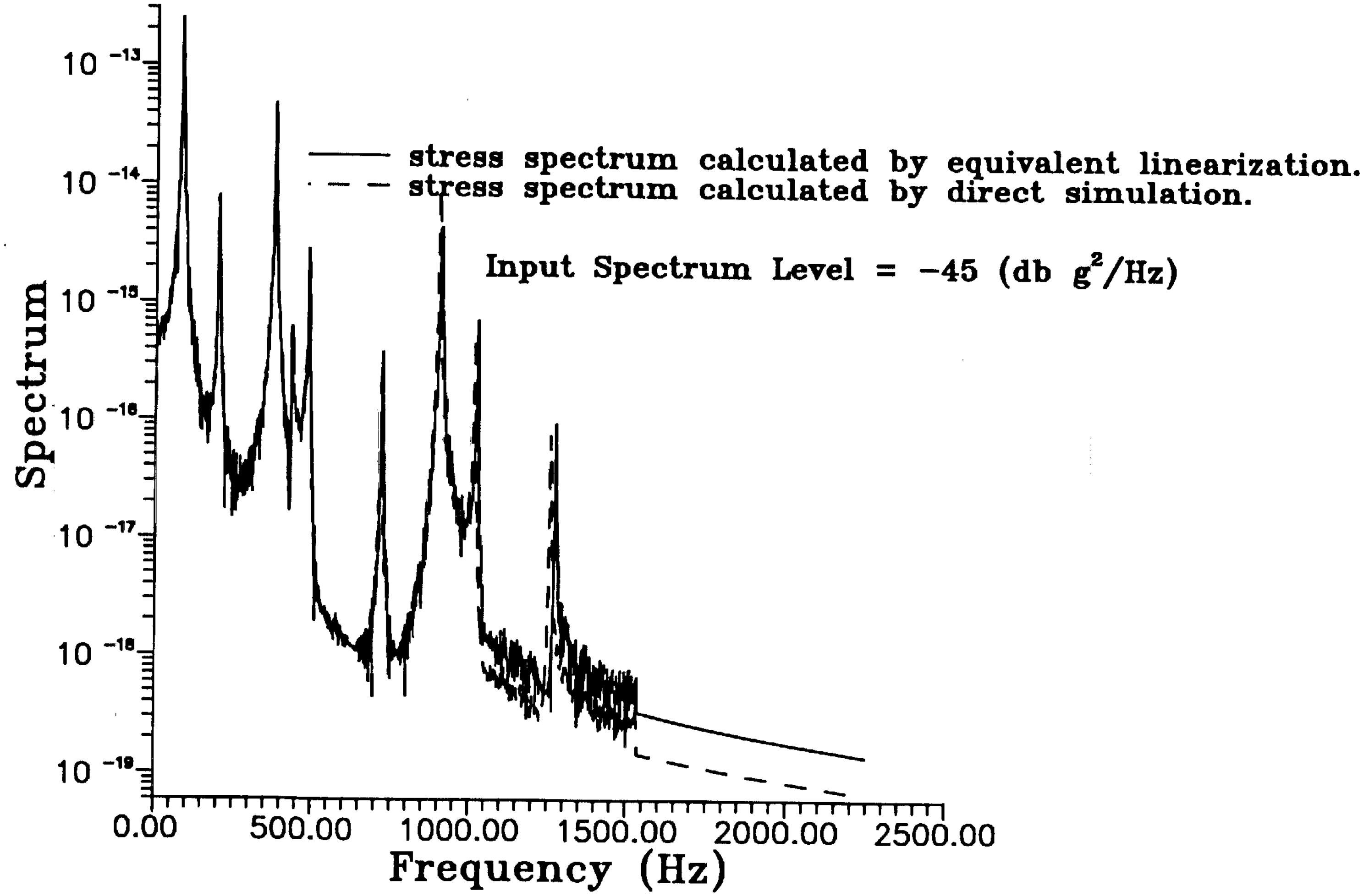Spectrum
10 $^{-13}$
10 $^{-14}$
10 $^{-15}$
10 $^{-16}$
10 $^{-17}$
10 $^{-18}$
10 $^{-19}$
0.00
500.00
1000.00
1500.00
2000.00
2500.00
Frequency (Hz)
stress spectrum calculated by equivalent linearization.
stress spectrum calculated by direct simulation.
Input Spectrum Level = −45 (db g^2/Hz)

Figure X.6

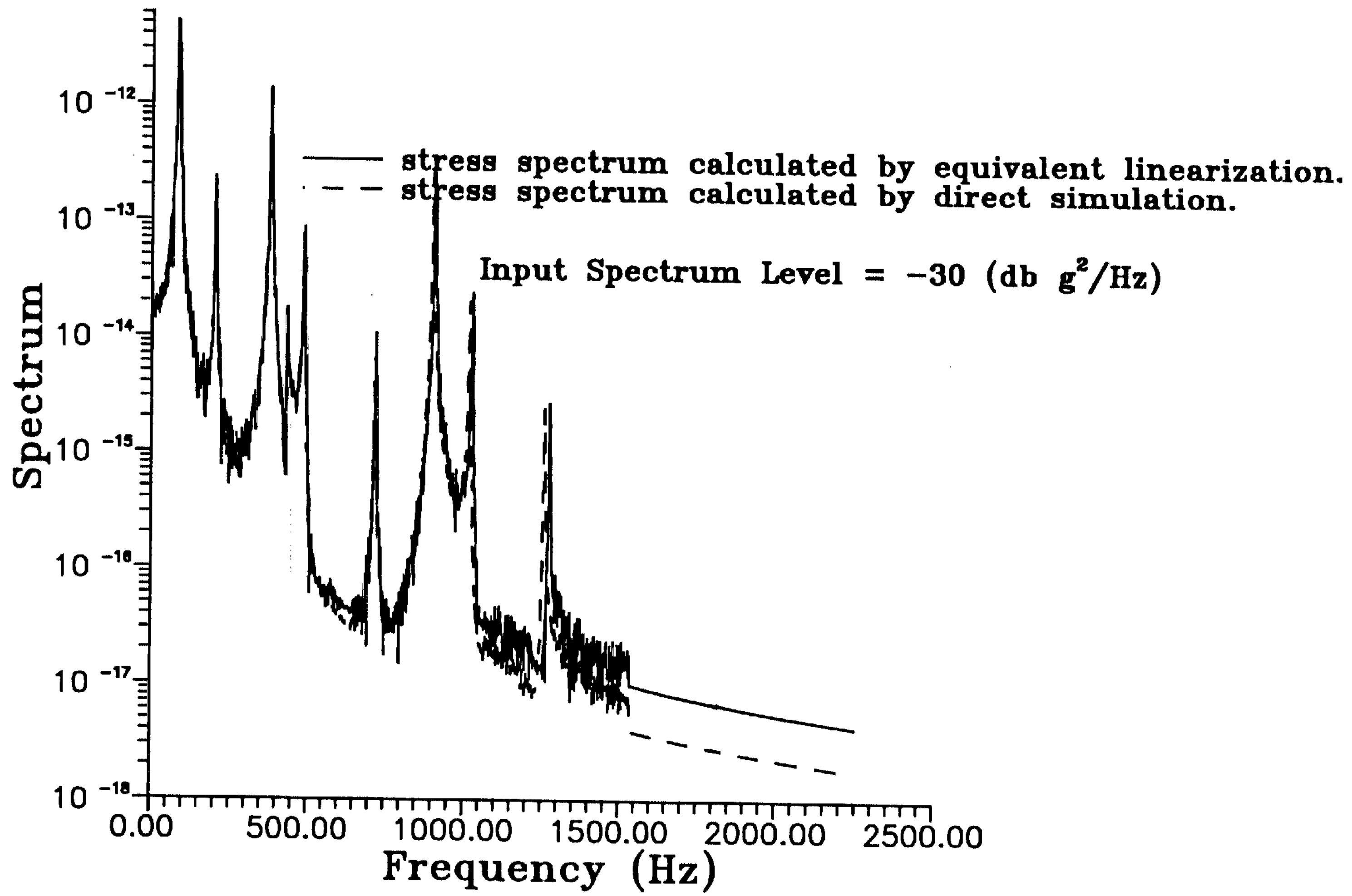
stress spectrum calculated by equivalent linearization.
stress spectrum calculated by direct simulation.
Input Spectrum Level = −30 (db g²/Hz)
Spectrum
10 −12
10 −13
10 −14
10 −15
10 −16
10 −17
10 −18
0.00
500.00
1000.00
1500.00
2000.00
2500.00
Frequency (Hz)

Figure X.7

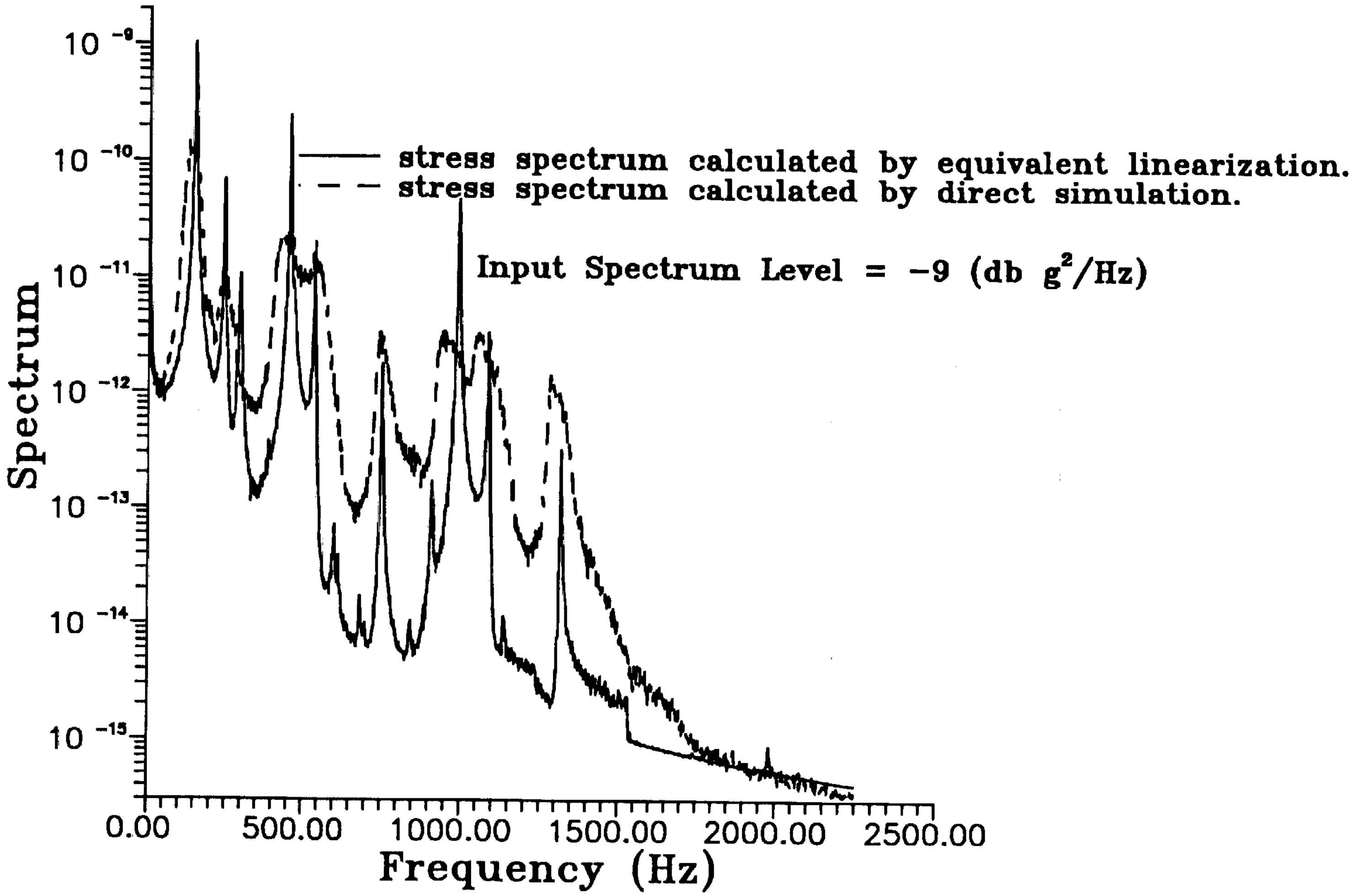
10 $^{-9}$
10 $^{-10}$
10 $^{-11}$
10 $^{-12}$
10 $^{-13}$
10 $^{-14}$
10 $^{-15}$
Spectrum
0.00
500.00
1000.00
1500.00
2000.00
2500.00
Frequency (Hz)
stress spectrum calculated by equivalent linearization.
stress spectrum calculated by direct simulation.
Input Spectrum Level = -9 (db g^2/Hz)

Figure X.8

XI.1 Effect of Nonlinearity on Spectral Shape

In previous sections we have examined the effect of spectral shape on the predicted fatigue lives of linear structures using several damage counting methods and have developed simulation methods to estimate the fatigue lives of nonlinear structures. It has also been pointed out that nonlinearities in a structure can have a pronounced influence on the response power spectrum in structures that are driven with random excitation. Although there is no simple way to estimate the fatigue life from the power spectrum of a nonlinear structure, it is important to understand the how the spectrum can be affected by nonlinear effects. In the present section, we present an approximate method of calculating the power spectrum of nonlinear systems.

In experimental studies of the response of structures to random excitations it is very common to characterize the response by measuring the power spectral density. Vibration engineers are usually very familiar with this representation of the structural behavior and, in a glance, can gain considerable insight into the system being studied. One can easily see how many resonant modes contribute to the response by looking at the resonant peaks in the spectrum and one can also determine whether the system is heavily or lightly damped. There are situations, however, where nonlinear effects in the structure influence the measured power spectrum in a manner that precludes straight-forward interpretation. In cases where the response has sufficient amplitude to elicit nonlinear behavior, the resonant response peaks in the power spectrum can take a dramatically different form than that observed in linear systems. The main goal of the present investigation is to propose a new approximate scheme for describing the influence of structural nonlinearities on the response power spectrum. It is hoped that the present study will provide a better understanding of the random response of nonlinear systems.

The present approximate representation of the spectrum is applied to a bilinear oscillator in which the nonlinearity has a very pronounced influence on the response spectrum. Comparisons are presented of the estimated power spectral density obtained using the present approximate scheme and by direct numerical simulation of the governing equation. Excellent agreement is observed between the two methods.

The effect of nonlinearities on the response power spectral density has been studied by a number of investigators. Early approximate analytical methods have been presented that are based on either a perturbation approach [1] or equivalent linearization [2,3]. These methods are found to give reasonable results only for very small nonlinearities. Other studies based on numerical simulations have shown that in the case of a Duffing oscillator, where the stiffness contains a cubic nonlinearity and the damping is assumed to be linear, the resonant response peak in the power spectral density tends to broaden and increase in frequency as the level of the random excitation is increased [4-6]. This behavior has been observed experimentally in studies of the high level random response of beams and plates [7,8].

An approximate analytical procedure was proposed by the author to estimate the response power spectrum of a Duffing oscillator with linear viscous damping [9]. The method is based on an adaptation of the method of equivalent linearization where the resonant frequency of the equivalent linear system is assumed to be random. This provided very accurate estimates of the spectrum when compared to results obtained using numerical simulations. It has not been possible, however, to extend the method to more general nonlinear random systems. The main purpose of the present study is to propose an approximate scheme that may be applicable to a wider class of nonlinear systems than studied previously.

The basic assumption of the method proposed in reference [9] is that the response spectrum is strongly influenced by nonlinearities in the system because in a nonlinear system, the stiffness, and hence, the natural frequency, depend on the response amplitude. In a system with sufficiently light damping, the random response will behave as a narrow-band process with an oscillation period that will vary randomly. The random variation of the oscillation period is a direct result of the fact that the response amplitude varies randomly. The random fluctuation of the dominant oscillation frequency will lead to a broadened resonant response peak in the power spectrum. It is reasonable to assume, therefore, that if certain statistics are known concerning the random amplitude fluctuations, and if the relationship between the system resonant frequency and amplitude is known, then one should be able to approximate the response spectrum.

The procedure presented in the following is based on assuming that the nonlinear system may be approximated as a linear system having a natural frequency that varies with the response amplitude in the same manner as that predicted when the nonconservative forces are not present. It is assumed that in the damped system with random excitation, the natural frequency depends on the envelope of the response of the original nonlinear system. The present method thus depends on knowledge of the statistics of the response envelope of the original nonlinear system being studied. The probability density of the response envelope is known for several classes of nonlinear systems [10]. The random fluctuations in the natural frequency are then assumed to occur much more slowly than the fluctuations in the response. This leads to a simple formula for the response spectrum in the form of an integration over the probability density of the envelope of the response of the original nonlinear oscillator.

The present approach has been applied to a bilinear oscillator where the restoring force is assumed to be equal to the deflection (stiffness = 1) for small deflections and is equal to twice the deflection (stiffness = 2) when the amplitude of the deflection is greater than unity. The damping is assumed to be linear viscous damping. This system is highly nonlinear when the random response spends a significant amount of time crossing over between the two stiffness regimes. Numerical simulations of the random response have shown that this bilinear stiffness characteristic has a pronounced effect on the predicted power spectrum. It is hoped that if accurate spectral estimates can be obtained for this rather difficult system, then the approximate method may be applicable to a fairly broad class of oscillators. Comparisons of spectra obtained using the present approximate scheme with those obtained using numerical simulations are presented and show excellent agreement.

As discussed above, the main purpose of the present study is to propose a description of the influence of nonlinearities on the power spectra of random structures with random excitation. Although the basic assumptions of the approach are plausible, a detailed error analysis has yet to be conducted. The validity of the approach is investigated here through a single example, the bilinear oscillator. A more detailed investigation of the influence of a number of approximations in the procedure will be performed in a future study.

XI.2. Approximate Representation of the Nonlinear System

Consider a nonlinear oscillator governed by

$$\ddot{x} + {\omega_0}^2(x + \epsilon g(x)) + c\dot{x} = f(t) \tag{XI.1}$$

where $f(t)$ is Gaussian white noise, $g(x)$ is a nonlinear restoring force, ω_0 is the natural frequency in the absence of nonlinear effects, ϵ is a constant and c is a viscous damping coefficient. For the present investigation we consider only systems having conservative nonlinearities. The function $g(x)$ does not depend on velocity, $\dot{x}$. Nonlinear damping effects will be left for future studies. It is also assumed that $g(x)$ is an odd function of x, i.e. $g(x) = -g(-x)$.

To develop a representation of the nonlinear random response, consider the behavior of a conservative nonlinear system. It is well known that in the case of conservative nonlinear systems, where c and $f(t)$ are zero, the solution of equation (XI.1), $x(t)$, will consist of an oscillation having a period that depends on the amplitude of the motion. The exact solution for the period, T, corresponding to an oscillation amplitude, a, is given by

$$T(a) = 4\int_0^a [2\int_x^a {\omega_0}^2(u + \epsilon g(u))du]^{-1/2}dx \tag{XI.2}$$

In the case of the damped system with random excitation described by equation (XI.1), if the damping coefficient, c, is sufficiently small the response may be considered to be a narrowband random process. The period of the oscillation cycles can be taken to be the time duration between occurrences of zero crossings with positive slope. The time required for one such cycle will depend on some measure of the oscillation amplitude. This follows from the fact that the stiffness of the nonlinear system, and hence, the effective natural frequency, depend on the response amplitude.

One can also view the response in the phase plane. In the case of the conservative system where c and $f(t)$ are zero, the amplitude of a given orbit in the phase plane determines the oscillation frequency. If the damping and excitation are sufficiently small, during one cycle the orbit of the nonconservative system will consist of a small fluctuation about that of the conservative system. If the amplitudes of the conservative and nonconservative orbits are nearly the same, the time duration of the cycles will also be similar.

During the forced, damped response of the system described by equation (XI.1), the amplitude of the motion will vary randomly and, based on the above discussion, we can also expect the oscillation period to vary accordingly. An approximate representation of the response of the system described by equation (XI.1) may then be obtained by idealizing it as a linear system having a natural frequency that depends on the response amplitude.

This amplitude dependent natural frequency is taken to be identical to that obtained for the conservative system,

$$\omega(a) = 2\pi/T(a), \tag{XI.3}$$

where $T(a)$ is given in equation (XI.2). The oscillation frequency is thus regarded as an intrinsic property of the system; it does not depend explicitly on the excitation or the damping as long as the damping is sufficiently light. During the forced, damped response, the oscillation frequency depends only on the amplitude of the motion as in the case of the conservative system. The amplitude, a, is a random quantity which for the present study is taken to be equal to the envelope of the random response of the original system in equation (XI.1). If $f(t)$ is Gaussian white noise, then the probability density of the envelope of the solution to equation (XI.1) may be determined [10]. Equation (XI.1) may then be approximated by

$$\ddot{x} + \omega^2(a)x + c\dot{x} = f(t). \tag{XI.4}$$

XI.3 Estimates of the Response Power Spectral Density

Having a representation of the nonlinear system of equation (XI.1) in the form of a linear system with a randomly varying natural frequency as in equation (XI.4) allows the estimation of the response power spectral density. This may be obtained by taking the Fourier transform of the autocorrelation function of the stationary response, $E[x(t)x(t+\tau)]$, where $E[\cdot]$ denotes the expected value. The solution of equation (XI.4) may be written in the form of a convolution integral,

$$x(t) = \int_0^t h(t-\tau)f(\tau)d\tau, \tag{XI.5}$$

where $h(t)$ is the impulse response which is assumed to depend on the randomly varying natural frequency, $\omega(a)$, given in equation (XI.3). The estimation of the power spectral density proceeds in the usual manner (see for example reference [10]) with the exception that we must account for the random nature of the envelope, a. It is assumed that although a varies randomly, it varies much more slowly than $x(t)$. An approximate expression for $h(t)$ in equation (XI.5) may be obtained by solving

$$\ddot{h} + \omega^2(a)h + c\dot{h} = \delta(t), \tag{XI.6}$$

with initial conditions, $h(0) = \dot{h}(0) = 0$, and where $\delta(\cdot)$ is the Dirac delta function. This is equivalent to

$$\ddot{h} + \omega^2(a)h + c\dot{h} = 0, \tag{XI.7}$$

with initial conditions, $h(0) = 0, \dot{h}(0) = 1$. If we assume that $\omega^2(a)$ varies much more slowly than $h(t)$, the solution of equation (XI.7) may be approximated by

$$h(t) = \frac{e^{-ct/2}sin(t\sqrt{\omega^2(a) - (c/2)^2})}{\sqrt{\omega^2(a) - (c/2)^2}}, t > 0. \tag{XI.8}$$

Given $h(t)$, one can calculate the autocorrelation function as

$$R_{xx}(\tau) = E[x(t)x(t+\tau)] = E[(\int_0^t h(\tau')f(t-\tau')d\tau')(\int_0^{t+\tau} h(\tau'')f(t+\tau-\tau'')d\tau'')]. \quad \text{(XI.9)}$$

Since the impulse response in equation (XI.8) is zero for negative values of t, the lower limits of integration may be set to $-\infty$. Because we are interested in the stationary response, the value of t is set to ∞. The upper limits of integration are then set to ∞. By assuming that the impulse response and the white noise excitation are uncorrelated, equation (XI.9) may be written as

$$R_{xx}(\tau) = \int_{-\infty}^{\infty}\int_{-\infty}^{\infty} E[h(\tau')h(\tau'')]E[f(t-\tau')f(t+\tau-\tau'')]d\tau' d\tau''. \quad \text{(XI.10)}$$

It is assumed that $f(t)$ is stationary Gaussian white noise so that

$$E[f(t-\tau')f(t+\tau-\tau'')] = 2\pi\Phi_f\delta(\tau+\tau'-\tau''), \quad \text{(XI.11)}$$

where $\delta(\cdot)$ is the Dirac delta function and Φ_f is the power spectral density of the excitation. The integration over τ'' in equation (XI.10) then gives

$$R_{xx}(\tau) = 2\pi\Phi_f \int_{-\infty}^{\infty} E[h(\tau')h(\tau+\tau')]d\tau'. \quad \text{(XI.12)}$$

The power spectral density of $x(t)$ is equal to the Fourier transform of $R_{xx}(\tau)$,

$$\begin{aligned}\Phi_x(\omega) &= \frac{1}{2\pi}\int_{-\infty}^{\infty} R_{xx}(\tau)e^{-i\omega\tau}d\tau \\ &= \Phi_f \int_{-\infty}^{\infty}\int_{-\infty}^{\infty} E[h(\tau')h(\tau+\tau')]e^{-i\omega\tau}d\tau' d\tau,\end{aligned} \quad \text{(XI.13)}$$

where i is $\sqrt{-1}$. If the integrand is multiplied by $e^{i\omega\tau'}e^{-i\omega\tau'}$, equation (XI.13) becomes

$$\Phi_x(\omega) = \Phi_f \int_{-\infty}^{\infty}\int_{-\infty}^{\infty} E[h(\tau')e^{i\omega\tau'}h(\tau+\tau')e^{-i\omega(\tau+\tau')}]d\tau' d\tau \quad \text{(XI.14)}$$

carrying out the integration first over τ and then τ' gives

$$\Phi_x(\omega) = \Phi_f E[H(\omega)H^*(\omega)], \quad \text{(XI.15)}$$

where $(\cdot)^*$ denotes the complex conjugate and,

$$H(\omega) = \int_{-\infty}^{\infty} h(\tau)e^{-i\omega\tau}d\tau. \quad \text{(XI.16)}$$

Substituting equation (XI.8) into equations (XI.15) and (XI.16) gives the response spectrum in the form

$$\Phi_x(\omega) = E[\frac{\Phi_f}{(\omega^2(a) - \omega^2)^2 + (c\omega)^2}], \tag{XI.17}$$

where in the evaluation of equation (XI.16) we have again assumed that $\omega^2(a)$ is slowly varying in comparison to $x(t)$.

The calculation of the expected value in equation (XI.17) is possible if the probability density of the envelope response, a, is known. The exact expression for the probability density of the envelope of the solution to equation (XI.1) is [10]

$$P(a) = [\omega_0^2(x + \epsilon g(x))2\pi/(c_n\omega(a))]e^{-\mathcal{V}(a)/\sigma_0^2}, \tag{XI.18}$$

where c_n is a normalization constant so that

$$\int_{-\infty}^{\infty} P(a)da = 1, \tag{XI.19}$$

and $\mathcal{V}(a)$ is the potential energy of the system corresponding to the response amplitude a,

$$\mathcal{V}(a) = \omega_0^2(a^2/2 + \epsilon \int_0^a g(x)dx). \tag{XI.20}$$

σ_0^2 is the mean square response of equation (XI.1) when $\epsilon = 0$,

$$\sigma_0^2 = \frac{\Phi_f \pi}{c\omega_0^2} \tag{XI.21}$$

The approximate response spectrum is then given by

$$\Phi_x(\omega) = \int_0^{\infty} \frac{\Phi_f}{(\omega^2(a) - \omega^2)^2 + (c\omega)^2} P(a)da. \tag{XI.22}$$

XI.4 Numerical Results for a Bilinear Oscillator

Equation (XI.22) has been applied to estimate the response spectrum of a bilinear system having a nonlinear restoring force as shown in figure XI.1. The restoring force shown in figure XI.1 is equal to $\omega_0^2(x+\epsilon g(x))$ in equation (XI.1). In the present calculations the system is assumed to have a linear force/deflection characteristic with unit slope when the amplitude of the response is less than unity. For greater response amplitudes, the stiffness of the system is assumed to be doubled as shown in the figure. The viscous damping coefficient, c, in equation (XI.1) is taken to be .005 .

The results of applying equation (XI.22) for a range of input force spectrum levels, Φ_f are shown in figures XI.2 A) through D). The figures also show the estimated spectra obtained by direct numerical simulation of the response of equation (XI.1). This was computed by calculating the time domain response and estimating the spectrum by a Fast Fourier Transform. The figures show that the power spectrum exhibits a broadened shape when the nonlinearity is significant. The effect of the nonlinear restoring force on the spectrum shape is depicted extremely well by the approximate method of equation (XI.22).

The primary discrepancy appears in figures XI.2 C) and XI.2 D) where the approximate expression in equation (XI.22) predicts a significant peak a 1 rad/sec. Since neither solution is exact it is desirable to employ a third solution method to examine this effect.

XI.5 References

[1] S. Crandall 1963 *Journal of the Acoustical Society of America* **35**, 1700–1705. Perturbation techniques for random vibration on nonlinear systems.

[2] T. K. Caughey 1963 *Journal of the Acoustical Society of America* **35**, 1706–1711. Equivalent linearization techniques.

[3] C. Mei and C. B. Prasad 1987 *Journal of Sound and Vibration* **117**, 173–186. Effects of nonlinear damping on random response of beams to acoustic loading.

[4] R. N. Miles, 1987 Nonlinear Periodic Structures, Ph. D. thesis, University of Washington

[5] P. G. Reinhall and R. N. Miles 1989 *Journal of Sound and Vibration* **132**, 33–42. Effect of damping and stiffness on the random vibration of nonlinear periodic plates.

[6] J. Robinson, 1990 *AIAA 12th Aeroacoustics Conference, April 10-12, 1989, San Antonio, TX. AIAA 89-1104*. The influence of nonlinear damping on the random response of panels by time domain simulation.

[7] I. Holehouse 1980 *Sonic Fatigue Design Techniques for Advanced Composite Aircraft Structures*. AFWAL-TR-80-3019: U. S. Air Force.

[8] C. Mei and K. R. Wentz, 1982 *AIAA/ASME/AHS 23rd Structures, Structural Dynamics and Materials Conference, New Orleans, LA, May 1982*. Analytical and experimental nonlinear response of rectangular panels to acoustic excitation.

[9] R. N. Miles 1989 *Journal of Sound and Vibration* **132**, 43–49. An approximate solution for the spectral response of Duffing's oscillator with random input.

[10] Y. K. Lin 1976 *Probabilistic Theory of Structural Dynamics*. Malabar, Florida: Robert E. Krieger Publishing Company.

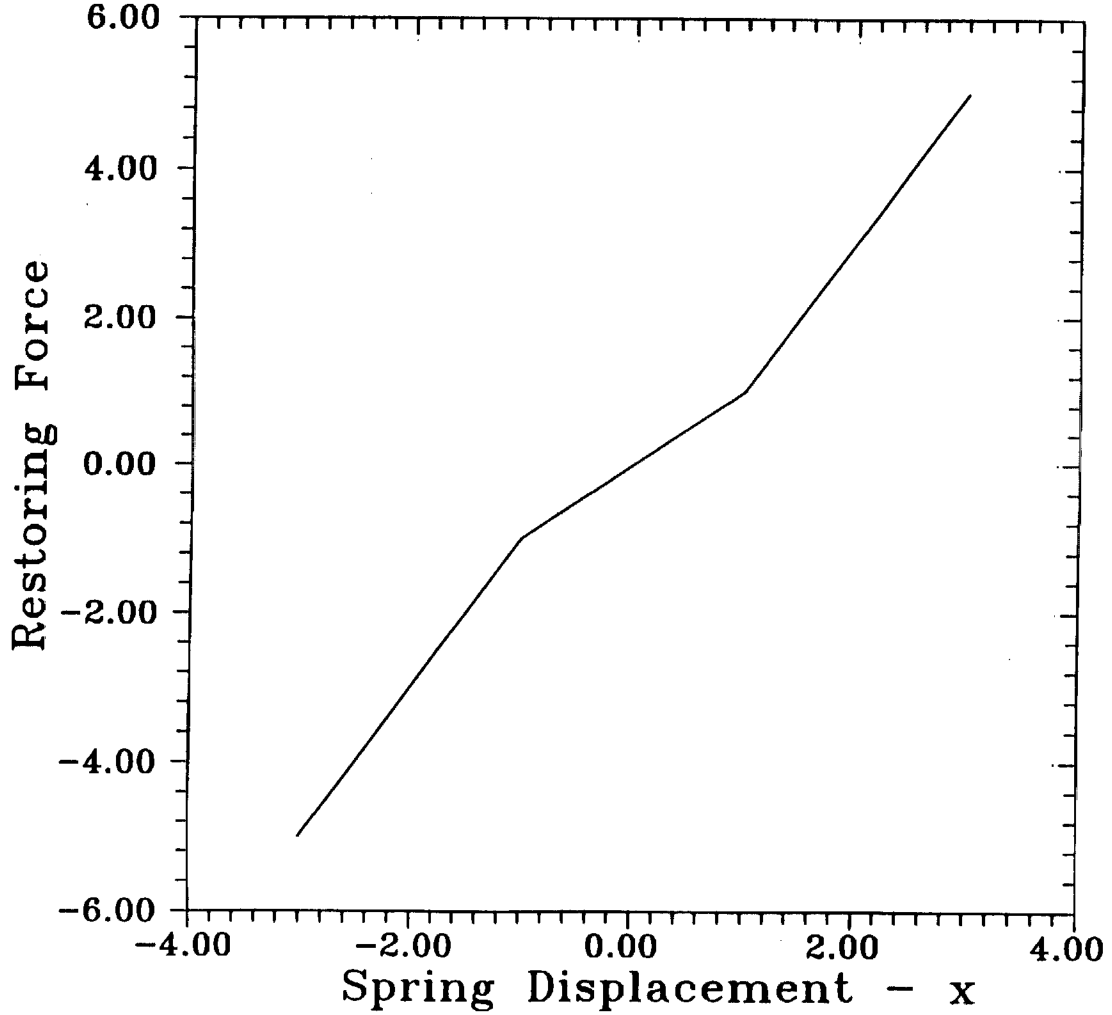
6.00
4.00
2.00
0.00
−2.00
−4.00
−6.00
Restoring Force
−4.00
−2.00
0.00
2.00
4.00
Spring Displacement − x

Figure XI.1

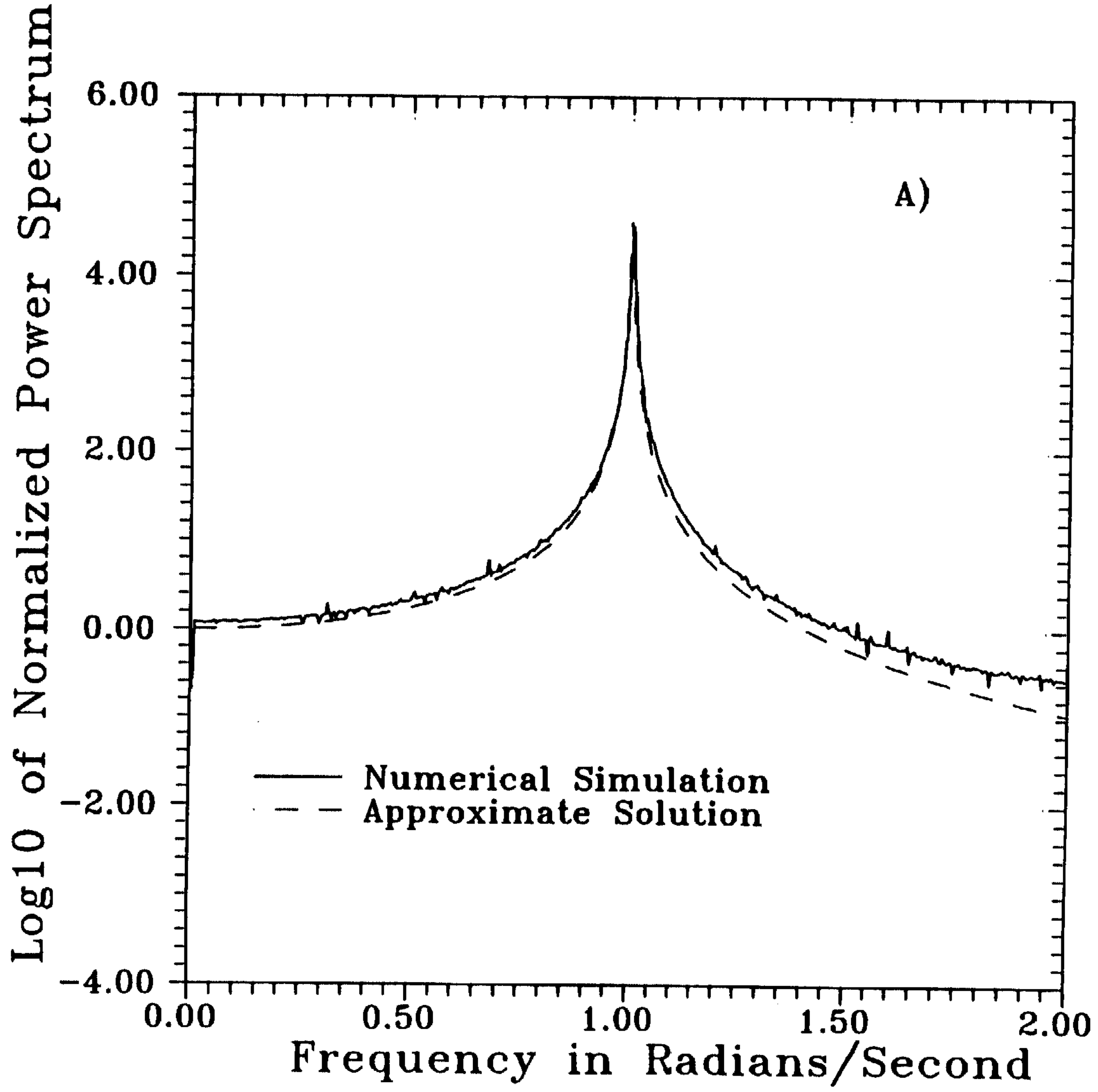

6.00
4.00
2.00
0.00
-2.00
-4.00
Log10 of Normalized Power Spectrum
A)
Numerical Simulation
Approximate Solution
0.00
0.50
1.00
1.50
2.00
Frequency in Radians/Second

Figure XI.2 A)

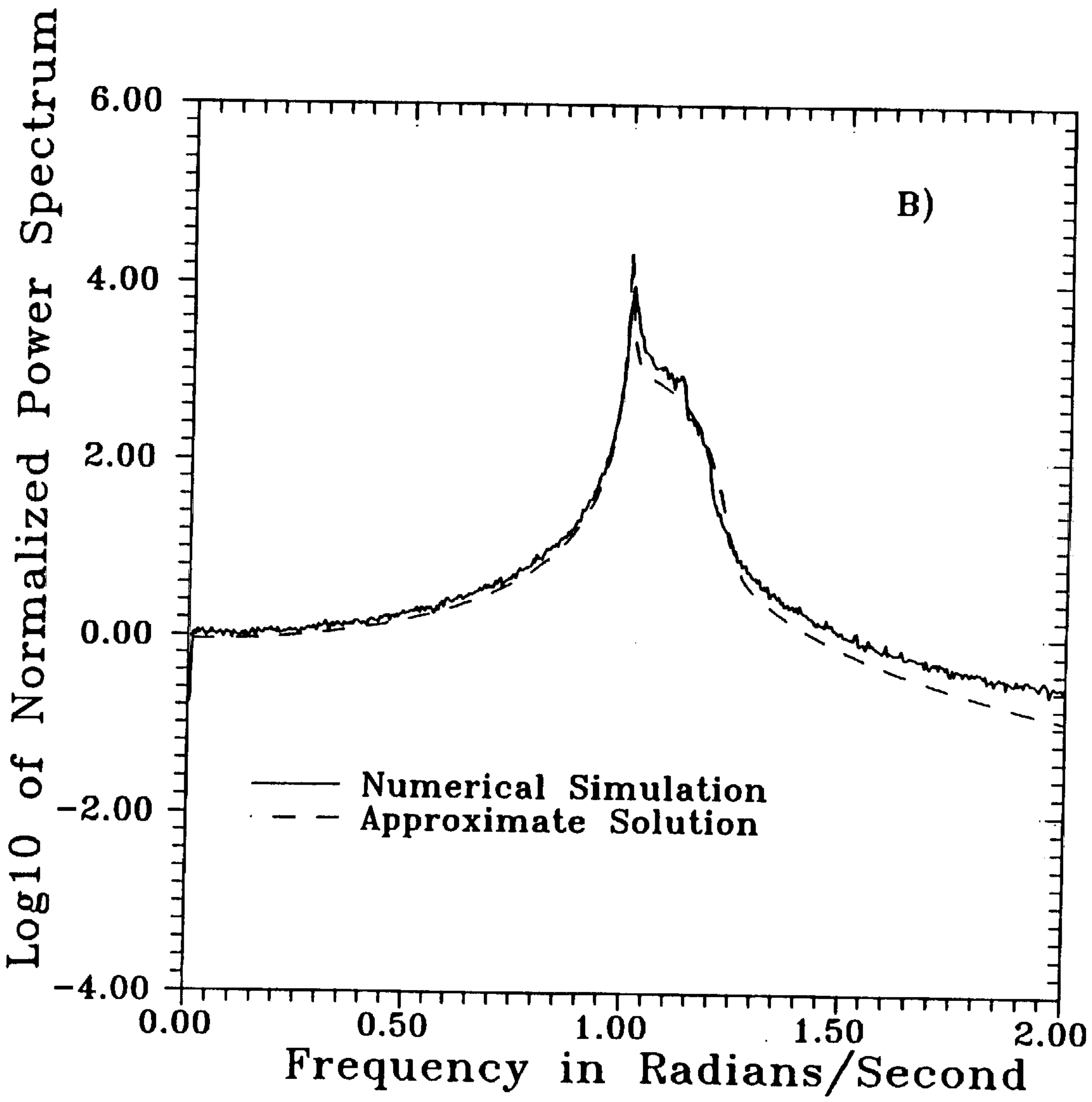
B)
6.00
4.00
2.00
0.00
−2.00
−4.00
Log10 of Normalized Power Spectrum
0.00
0.50
1.00
1.50
2.00
Frequency in Radians/Second
Numerical Simulation
Approximate Solution

Figure XI.2 B)

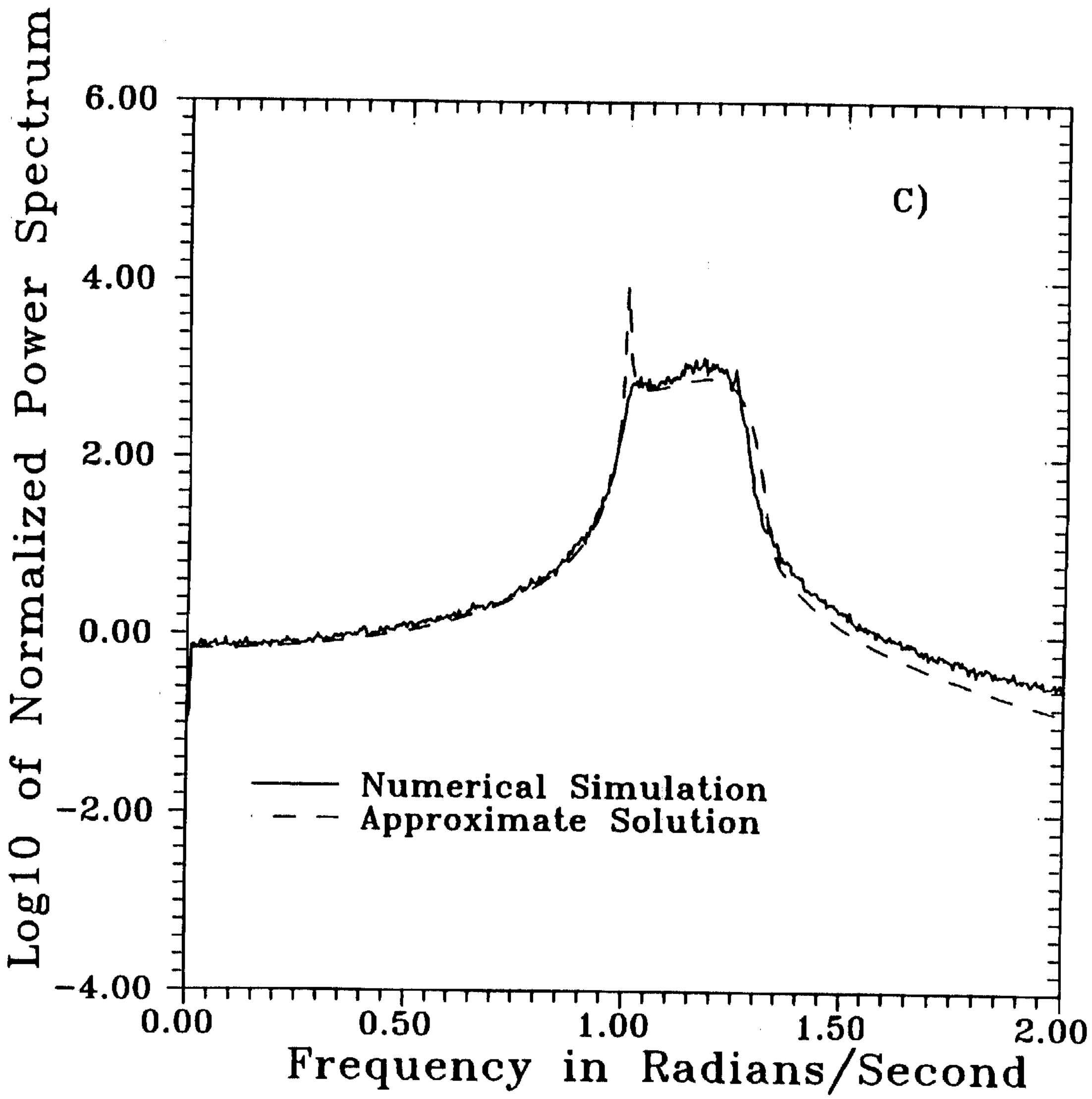
6.00
4.00
2.00
0.00
−2.00
−4.00
Log10 of Normalized Power Spectrum
0.00
0.50
1.00
1.50
2.00
Frequency in Radians/Second
C)
Numerical Simulation
Approximate Solution

Figure XI.2 C)

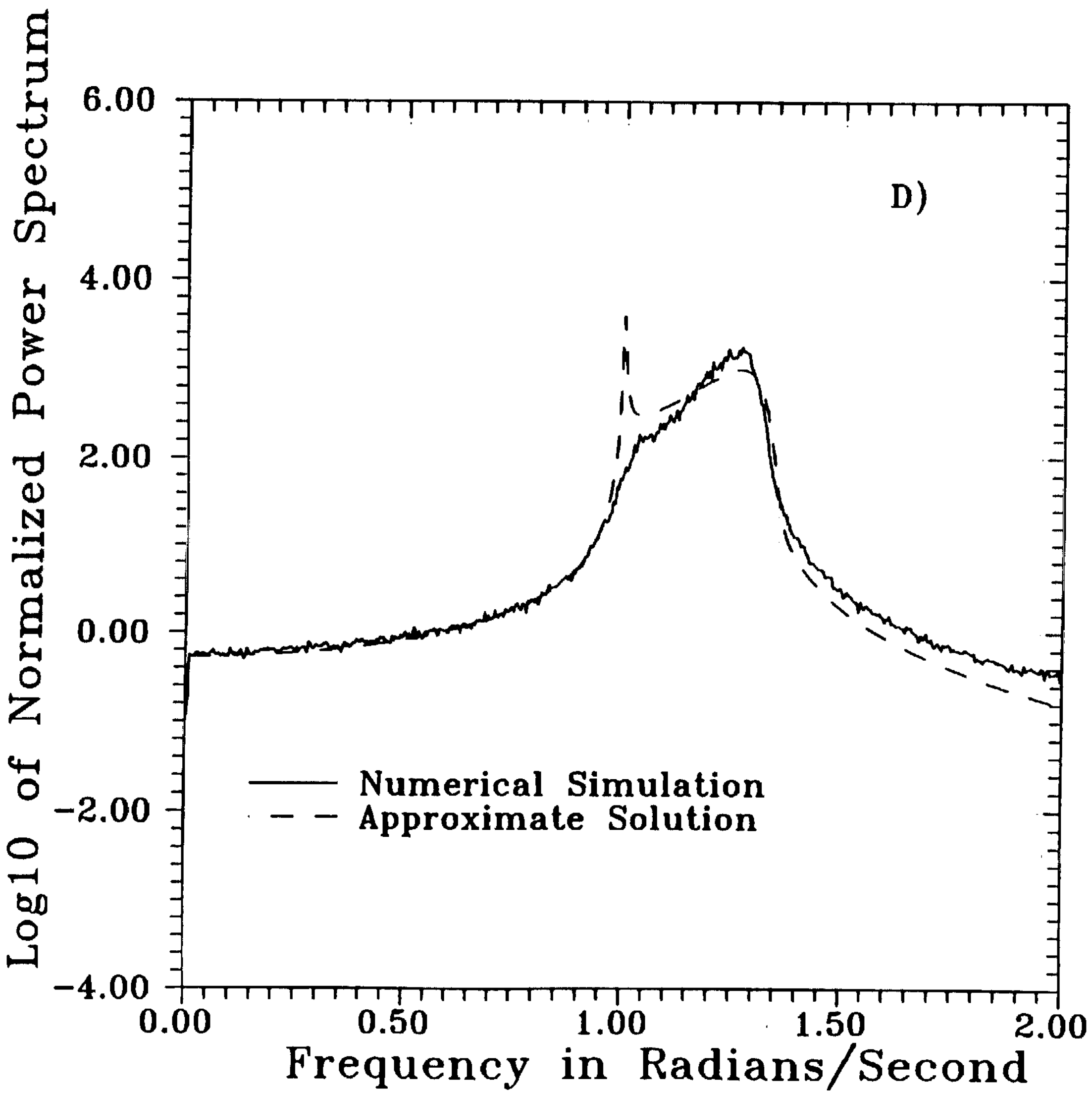
6.00
4.00
2.00
0.00
−2.00
−4.00
Log10 of Normalized Power Spectrum
0.00
0.50
1.00
1.50
2.00
Frequency in Radians/Second
D)
Numerical Simulation
Approximate Solution

Figure XI.2 D)

XII Conclusions

Several analytical methods have been developed to facilitate the prediction of the fatigue lives of structures that are subjected to acoustic loadings. In sections II through XI, time domain methods were presented for performing fatigue predictions based on knowledge of the power spectral density of the random strain response. It is suggested that procedures such as those presented here will lead to much more reliable fatigue predictions than methods that are commonly used.

Because any fatigue prediction procedure relies on empirical data to characterize material fatigue properties, in section VII we present a technique for estimating the necessary constants using either narrowband random loads or realistic broadband loads as encountered in service. One advantage of this procedure is that it enables one to identify fatigue constants from tests of complex structures with multiple resonant modes rather than simplified coupons.

Another contribution of the present study has been to construct a method of accounting for nonlinear response in random fatigue predictions. This can be helpful in situations where the in service loads are sufficiently intense to elicit nonlinear response or where nonlinear effects are found to be significant in accelerated tests which employ artificially high excitation levels. The approximate procedure is applied to nonlinear beams and plates and excellent agreement is observed between results using the approximate method and using a detailed numerical simulation. Conventional numerical simulation methods are not practical for random fatigue predictions for nonlinear structures because the nonlinearities drastically complicate the calculations. It is found that the approximate method makes it practical to analyze the fatigue lives of highly complex nonlinear structures. This is because the numerical effort required using the approximate procedure is roughly the same as for a linear structure.

The final contribution of this effort has been to identify the effect of nonlinearities on the power spectral density of the random response. The power spectral density is commonly used in the analysis of random vibration. When nonlinear effects contribute to the response, the power spectrum is influenced in a manner that is far from obvious. An explanation of this effect is proposed and an approximate analytical method is presented to predict the power spectrum of nonlinear random systems. Excellent agreement is observed between the approximate method and numerical simulations.